UNIVERSIDAD NACIONAL DEL LITORAL

Diseño computacional de metamateriales mecánicos y acústicos

Rolando Yera Moreno

FICH

FACULTAD DE INGENIERÍA Y CIENCIAS HÍDRICAS

INTEC

INSTITUTO DE DESARROLLO TECNOLÓGICO PARA LA INDUSTRIA QUÍMICA

CIMEC

CENTRO DE INVESTIGACIÓN DE MÉTODOS COMPUTACIONALES

sinc(i)

INSTITUTO DE INVESTIGACIÓN EN SEÑALES, SISTEMAS E INTELIGENCIA COMPUTACIONAL

Tesis de Doctorado **2022**

UNIVERSIDAD NACIONAL DEL LITORAL

Facultad de Ingeniería y Ciencias Hídricas

Centro de Investigación de Métodos Computacionales

Diseño computacional de metamateriales mecánicos y acústicos

Rolando Yera Moreno

Tesis remitida al Comité Académico del Doctorado
como parte de los requisitos para la obtención
del grado de
DOCTOR EN INGENIERÍA
Mención Mecánica Computacional
de la
UNIVERSIDAD NACIONAL DEL LITORAL

2022

Comisión de Posgrado, Facultad de Ingeniería y Ciencias Hídricas, Ciudad Universitaria,
Paraje “El Pozo”, S3000, Santa Fe, Argentina.

Declaración legal del autor

Esta Tesis ha sido remitida como parte de los requisitos para la obtención del grado de Doctor ante la Universidad Nacional del Litoral y ha sido depositada en la Biblioteca de la Facultad de Ingeniería y Ciencias Hídricas para que esté disponible a sus lectores bajo las condiciones estipuladas por el Reglamento de la mencionada Biblioteca.

Citaciones breves de esta disertación son permitidas sin la necesidad de un permiso especial, en la suposición de que la fuente sea correctamente citada. Solicitudes de permiso para una citación extendida o para la reproducción de este manuscrito en un todo o en parte serán exigidas por el portador legal del derecho de propiedad intelectual de la misma.

Rolando Yera Moreno

Agradecimientos

En primer lugar, quiero agradecer a las instituciones que hicieron posible la realización de la presente Tesis; al Consejo Nacional de Investigaciones Científicas y Técnicas (CONICET), que me financió la beca de estudio de doctorado; a la Facultad de Ingeniería y Ciencias Hídricas (FICH-UNL), donde he realizado el doctorado, al Centro de Investigación de Métodos Computacionales (CIMEC) que me dio un lugar de trabajo.

Deseo expresar mi eterna gratitud a mis directores de beca y Tesis, el Dr. Alfredo Huespe y el Dr. Victor Fachinotti, por lo mucho que me han enseñado y por todo el apoyo que siempre me han brindado, sin el cuál, realizar esta tesis hubiese sido imposible.

Agradezco también a todos los compañeros del CIMEC, que he tenido el honor de conocer y forjar vínculos de amistad.

Finalmente, nada de esto hubiese sido posible sin las alegrías que me ha dado Analia, ni sin el apoyo incondicional de mi esposa Yaima, de mis padres, de mi hermano y en general de toda mi familia, pues a lo largo de toda mi vida siempre me han ayudado. Gracias ahora y siempre.

Resumen

En la presente Tesis se describen metodologías y técnicas numéricas para realizar el diseño de metamateriales mecánicos y matamateriales acústicos.

El diseño de los metamateriales mecánicos se realiza mediante una técnica de homogeneización inversa formulada como un problema de optimización topológica. Particularmente, se optimizan compuestos elásticos bifásicos periódicos, en dos y tres dimensiones, con el objetivo de obtener materiales con propiedades efectivas isotrópicas cercanas a sus límites teóricos.

El algoritmo de optimización se basa en los conceptos de derivada topológica y función level-set. Este algoritmo se integra con la imposición de simetrías de cristales preestablecidas. Se evalúa el impacto que tienen diferentes simetrías en las topología diseñadas.

Para los compuestos 3D, la homogeneización computacional de las propiedades elásticas de realiza usando una técnica numérica basada en la transformada de Fourier, la cual, fue extendida para ser usada en dominios no ortogonales.

El diseño de la microarquitectura de los cristales fonónicos y de los materiales localmente resonantes se realiza mediante un algoritmo de optimización topológica, también basado en los conceptos de derivada topológica y función level-set, cuyo objetivo es maximizar el bandgap entre dos bandas de dispersión adyacentes. El algoritmo de optimización sigue un esquema de Lagrangiano aumentado basado en un método de punto proximal.

Se evalúan las propiedades de convergencia de distintos métodos, basados en elementos finitos, de cálculo de la relación de dispersión (estructura de bandas del material). Se validan numéricamente de las expresiones analíticas obtenidas para la derivada topológica.

Se presenta un modelo de homogeneización para evaluar las propiedades dinámicas efectivas de compuestos periódicos en problemas de propagación de ondas que podría ser usado como una herramienta adicional para el diseño de metamateriales acústicos. Dicho modelo es validado comparando nuestros resultados con los resultados previamente publicados en la literatura.

Abstract

Methodologies and numerical techniques for designing mechanical and acoustic metamaterials are presented in this Thesis.

The mechanical metamaterials design is performed using an inverse homogenization technique formulated as a topological optimization problem. Particularly, periodic biphasic elastic composites, in two and three dimensions, are optimized to obtain materials with effective isotropic properties close to their theoretical limits.

The optimization algorithm is based on the topological derivative and level-set function concepts. This algorithm is integrated with the imposition of pre-established crystal symmetries. An evaluation of the impact that different symmetries have on the designed topologies is presented.

For the 3D composites, the computational homogenization of the elastic properties is performed using a numerical technique based on the Fourier transform, which was extended to non-orthogonal domains.

A topological optimization algorithm, which is also based on the topological derivative and level-set function concepts, is developed for the phononic crystals and the locally resonant materials microarchitecture design. The goal is to maximize the bandgap between two adjacent dispersion bands. The optimization algorithm follows an augmented Lagrangian scheme based on a proximal point method.

The convergence properties of different methods, based on finite elements, for calculating the dispersion relation (band structure of the material) are evaluated. The obtained topological derivative expressions are validated numerically.

A homogenization model to evaluate the effective dynamic properties of periodic composites in wave propagation problems is presented. This model could be an additional tool for the design of acoustic metamaterials. The results of this model are validated by comparing them with previously reported results in the literature.

Índice general

Índice de figuras

Capítulo 1

Introducción

Preliminares

En el presente trabajo de Tesis se presenta el desarrollo y aplicación de metodologías para el diseño computacional de metamateriales mecánicos y acústicos. Dichas metodologías se fundamentan en técnicas de optimización topológica (Bendsøe y Sigmund, 2003) basadas en los conceptos de función *level-set* (Amstutz y Andrä, 2006) y de derivada topológica (Novotny y Sokołowski, 2012). También, es estudiado el efecto que la imposición de diferentes grupos de simetría tiene sobre el diseño de la topología. Además, se presenta un modelo de homogeneización para evaluar las propiedades elastodinámicas efectivas de medios periódicos en problemas de propagación de ondas, el cual, podría utilizarse como una herramienta adicional para el diseño de metamateriales acústicos.

Un metamaterial es un material compuesto, diseñado para tener propiedades específicas, que no son encontradas en la naturaleza (Dong et al., 2017; Zheng et al., 2014). Ejemplos típicos están asociados al diseño y desarrollo de materiales que sirven de recubrimiento para hacer invisible, o camuflar, objetos ante la propagación de ondas acústicas o electromagnéticas; manejo, inversión, concentración o guía del flujo térmico; etc. El área de la física e ingeniería que se dedica al diseño de nuevos metamateriales tiene un alto potencial de desarrollo futuro, con un amplio rango de aplicaciones tecnológicas. Las microestructuras características de los metamateriales, obtenidos mediante optimización topológica, usualmente presentan un alto grado de complejidad y detalle. Los recientes avances en tecnologías de impresión 3D amplían las posibilidades de fabricar y producir estos compuestos.

1.1. Optimización topológica

Mediante el diseño de las microestructuras se han obtenido materiales con propiedades extraordinarias como, relaciones de Poisson negativas (Bückmann et al., 2012), (Babaee et al., 2013), compresibilidad negativa (Bückmann et al., 2014) y ultra rigidez a ultra bajo peso (Zheng et al.,

2014). La optimización topológica es una de las técnicas empleadas para diseñar metamateriales. Consiste en encontrar la distribución de dos o mas materiales dentro de un dominio, tal que minimice (maximice) cierta función objetivo y cumpla con restricciones impuestas.

Particularmente, el diseño de materiales mediante optimización topológica se basa en la idea de que las variables de diseño corresponden a algunas características micro o meso-estructurales, o más específicamente, a la distribución y topología del material al nivel de la micro-estructura.

Actualmente existen múltiples paradigmas para realizar optimización topológica, por ejemplo, en Huang et al. (2011) los autores utilizan un algoritmo de optimización estructural basado en evolución bidireccional (*Bidirectional Evolutionary Structural Optimization* - BESO), otro ejemplo es el presentado por Sigmund y Jensen (2003), donde los autores realizan el diseño de materiales fonónicos mediante el algoritmo de optimización *Solid Isotropic Material with Penalization - SIMP*.

En el presente trabajo de Tesis, se abordan dos objetivos fundamentales:

i) El diseño de metamateriales mecánicos mediante el uso de una técnica de homogeneización inversa (Sigmund, 1994), formulada matemáticamente como un problema de optimización topológica, con el objetivo de obtener compuestos bifásicos con propiedades isotrópicas efectivas cercanas a sus límites teóricos, los cuales, son definidos para compuestos 2D por los límites de Cherkaev-Giabiansky (CG-bounds) (Cherkaev y Gibiansky, 1993), o, en el caso de compuestos 3D por los límites de Hashin-Shtrikman (HS-bounds) (Hashin y Shtrikman, 1963).

ii) El diseño de los metamateriales acústicos mediante el diseño de la microestructura de un material periódico a través del cual se transmite una onda acústica, elástica. Como se analiza con más detalle en el Capítulo 2, en materiales periódicos es sabido que existe dispersión de las ondas elásticas, esto es, una dependencia de la velocidad de propagación de ondas admitidas con el número de onda k. El objetivo del diseño es el de maximizar el ancho del bandgap entre dos bandas de dispersión, $\omega_j(\mathbf{k})$ y $\omega_{j+1}(\mathbf{k})$, adyacentes (Jensen y Pedersen, 2006). En el presente trabajo el cálculo de la relación de dispersión se realiza mediante el método de elementos finitos (FEM). En el Capítulo 2 se presentan tres estrategias, basadas en el método de elementos finitos, para obtener la relación de dispersión $\omega(\mathbf{k})$.

Nuestro objeto de estudio son materiales periódicos representados por una celda de periodicidad Ω_μ, ver Figura 1.1. Por tanto, nuestros problemas de optimización topológica consisten fundamentalmente en diseñar la microestructura de la celda unidad, Ω_μ, constituida por dos fases elásticas e isotrópicas, M_1 y M_2, con el objetivo de que éste exhiba cierta propiedad requerida.

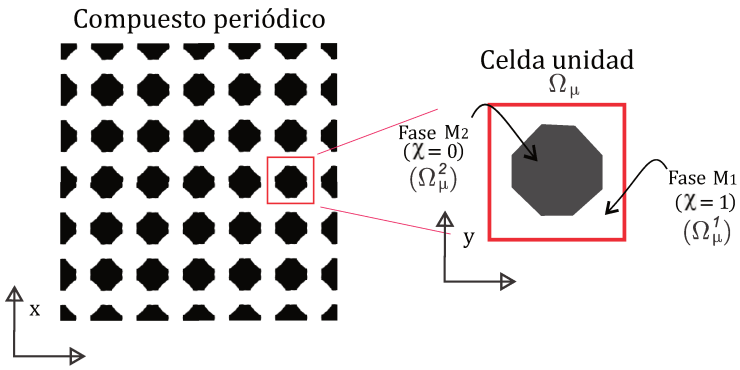

Figura 1.1: Función característica, χ, definida en el dominio de diseño, $\Omega_\mu = \Omega_\mu^1 \cup \Omega_\mu^2$, de un material periódico.

Para ésto, se define la función característica, $\chi(\mathbf{y})$, en los dominios Ω_μ^1 y Ω_μ^2 que determinan la distribución de las fases M_1 y M_2 en el dominio de diseño, $\Omega_\mu = \Omega_\mu^1 \cup \Omega_\mu^2$, ver Figura 1.1. La función característica, $\chi(\mathbf{y})$, será la variable de diseño de nuestros problemas:

$$\chi(\mathbf{y}) = \begin{cases} 1 & \forall \mathbf{y} \in \Omega_\mu^1 \\ 0 & \forall \mathbf{y} \in \Omega_\mu^2 \end{cases} . \tag{1.1}$$

Para resolver los problemas de optimización utilizamos el método presentado por Amstutz y Andrä (2006), donde se aplican los conceptos de función *level-set* y de derivada topológica. Esta técnica, ha sido aplicada en contribuciones tales como el diseño inverso de microestructuras Amstutz et al. (2010), diseño estructural sujeto a restricciones de tensión Amstutz et al. (2012) o diseño de materiales piezoeléctricos Amigo et al. (2016), pero, a conocimiento del autor, nunca ha sido empleada en el diseño de materiales fonónicos.

A continuación se describe brevemente la formulación matemática de los problemas de optimización topológica resueltos en el presente trabajo para cada uno de los objetivos, i) y ii), antes mencionados. Posteriormente, en los respectivos capítulos 3 y 4 se desarrollan con mas detalle ambos temas.

1.1.1. Diseño de compuestos bifásicos con propiedades efectivas isotrópicas cercanas a los límites teóricos

El diseño topológico mediante técnicas de homogeneización inversa está bien establecido en la literatura, el gran número de trabajos enfocados en este tópico (ver por ejemplo Amstutz et al. (2010), Amigo et al. (2016), Torquato (2010), Osanov y Guest (2016)) representan una indicación clara del poder de esta técnica para la obtención de nuevas microarquitecturas.

Las técnicas de homogeneización inversa pueden ser formuladas matemáticamente como problemas de optimización topológica planteados en el dominio espacial Ω_μ, que representa la celda unidad del material periódico, cuyas soluciones proporcionan las topologías óptimas, o distribuciones espaciales de material, que satisfacen los objetivos propuestos. Una descripción general de estas técnicas para diferentes problemas puede ser encontrada en el libro de Bendsøe y Sigmund

(2003) y un trabajo que ha sido significativo para llevar adelante esta linea de investigación ha sido el de Amstutz et al. (2010).

En el presente trabajo se diseñan microestructuras de compuestos periódicos constituidos por dos fases isotrópicas , M_1 y M_2, y una fracción de volumen dada f_1 de M_1. Se suponen dos escalas de longitud, ver Fig. 1.2, la escala de la estructura (macroescala), ℓ, y la escala de la microestructura (microescala), ℓ_μ, donde se define la configuración geométrica de la distribución de fases. Asumimos que la relación $\ell \gg \ell_\mu$ se satisface.

A nivel de la macroescala las propiedades efectivas del compuesto pueden ser descritas mediante el tensor de elasticidad homogeneizado, $\mathbf{C}^h$, que relaciona las macro-deformaciones $\boldsymbol{E}$ con las macro-tensiones $\boldsymbol{\sigma}$. Una celda representativa Ω_μ de la microestructura es usada para determinar $\mathbf{C}^h$. Para los compuestos 3D que presentan respuestas elásticas efectivas isotrópicas, $\mathbf{C}^h$ es completamente caracterizado por el módulo volumétrico efectivo κ^h (módulo plano efectivo, K^h, para compuestos 2D) y por el módulo de corte efectivo G^h.

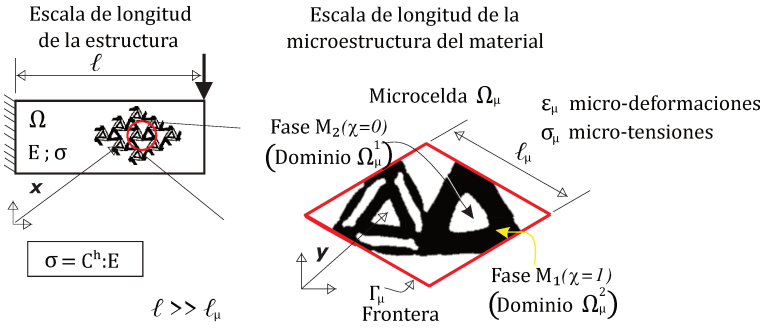

Figura 1.2: El diseño del material se realiza mediante una técnica de homogeneización inversa, formulada como un problema de optimización topológica, involucrando dos escalas de longitud características, ℓ en la macroescala y ℓ_μ en la microescala. La región Ω_μ se define como dominio de diseño para la optimización topológica.

Técnica de homogeneización inversa

El diseño óptimo de la topología de microarquitecturas 3D cuyas propiedades efectivas objetivo son los puntos en los límites inferiores de Hashin-Shtrikman , ver Fig. 1.3b, se obtienen resolviendo un conjunto de n problemas de optimización topológica formulados de la siguiente manera:

$$\begin{aligned} &\min_{\chi} \; G^h(\chi); \\ &\text{tal que:} \quad \kappa^h(\chi) - \kappa_j^* = 0 \\ &\qquad\qquad \mathbf{C}^h(\chi) \text{ is isotropic} \\ &\qquad\qquad f_1(\chi) - f_1^* = 0 \end{aligned} \tag{1.2}$$

donde κ_j^* (con $1 \leq j \leq n$) es el $j-$th modulo volumétrico objetivo del compuesto. definido dentro del intervalo $\hat{\kappa}^l \leq \kappa_j^* \leq \hat{\kappa}^u$ y f_1^* es la fracción de volumen objetivo de la fase M_1. El

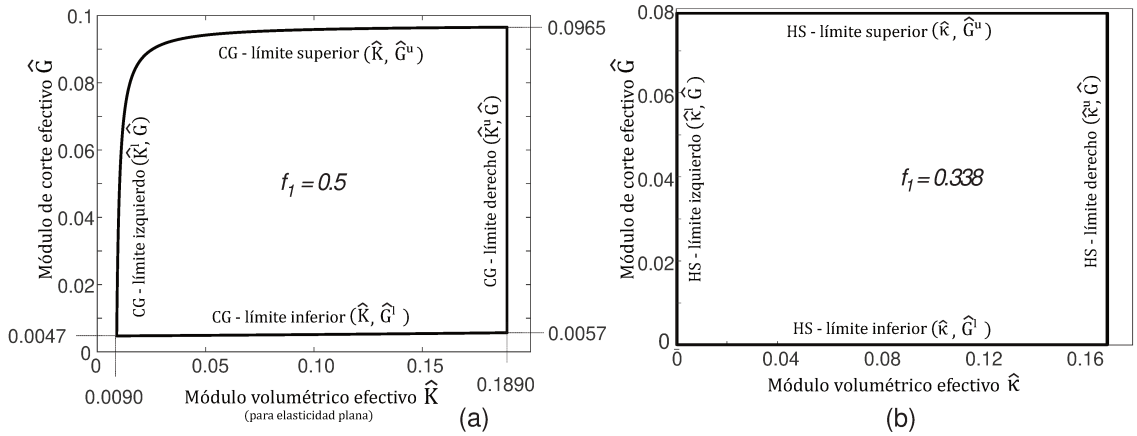

Figura 1.3: Límites analíticos de las propiedades efectivas de compuestos bifásicos isotrópicos. a) Elasticidad plana. Límites acordes a Cherkaev y Gibiansky (1993) (CG-bounds). Las propiedades de las fases M_1 y M_2 son $K_1 = 5/7$; $K_2 = K_1/200$; $G_1 = 5/13$; $G_2 = G_1/200$. La fracción de volumen de la fase M_1 es $f_1 = 0.5$. b)Límites elásticos 3D acordes a Hashin y Shtrikman (1963) (HS-bounds). Las propiedades de las fases M_1 y M_2 son $\kappa_1 = 1.667$, $G_1 = 0.3571$, $\kappa_2 = \gamma\kappa_1$, $G_2 = \gamma G_1$, factor de contraste $\gamma = 10^{-4}$, fracción de volumen $f_1 = 0.338$.

problema (1.2) implica que el mínimo del módulo de corte efectivo, G^h, se busca variando la función característica χ dentro de Ω_μ.

Análogamente, el límite superior de Hashin-Strikman se busca maximizando $G^h(\chi)$, con las misma restricciones del problema (1.2).

Alternativamente, las topologías próximas al límite izquierdo de Hashin-Strikman se obtienen resolviendo los problemas:

$$\begin{aligned} &\min_{\chi} \kappa^h(\chi); \\ &\text{tal que:} \quad G^h(\chi) - G_j^* = 0 \\ &\qquad\qquad \mathbf{C}^h(\chi) \text{ is isotropic} \\ &\qquad\qquad f_1(\chi) - f_1^* = 0 \end{aligned} \tag{1.3}$$

donde ahora, el modulo de corte efectivo objetivo G_j^* del $j-$th problema de optimización es elegido dentro del intervalo $\hat{G}^l \leq G_j^* \leq \hat{G}^u$. Los compuestos extremos en el límite H-S derecho se obtienen maximizando $\kappa^h(\chi)$ con las misma restricciones del problema (1.3).

El diseño inverso de microestructuras 2D (elasticidad plana) cuyo objetivo es alcanzar un material isotrópico extremo, ver Fig. 1.3a, también se realiza mediante un algoritmo de optimización topológica con una formulación ligeramente diferente a las indicadas en (1.2) o (1.3). En este caso, los problemas se formulan imponiendo simetría hexagonal a la arquitectura lo que garantiza la isotropía de las propiedades efectivas (incluyendo la respuesta elástica efectiva). Con ésto, no se requiere imponer explícitamente la restricción de isotropía en el problema matemático de optimización inversa.

Un aspecto clave de la técnica matemática que hemos seguido, es utilizar la derivada topológi-

ca para identificar direcciones de descenso del algoritmo de optimización. Esta derivada ha sido tomada del trabajo Amstutz et al. (2010).

En el Capítulo 3 se presentan dos ejemplos de diseño topológico, el diseño de un material auxético y el de un material con rigidez máxima, y se exponen brevemente aspectos fundamentales del algoritmo de optimización topológica para resolver los problemas (1.2) y (1.3) que es presentado detalladamente en el anexo A.

1.1.2. Diseño de cristales fonónicos mediante la maximización del bandgap entre dos bandas de dispersión adyacentes

La frecuencia ω de las ondas elásticas que se propagan en medios periódicos, como se muestra en el Capítulo 2, dependen del vector de onda $\mathbf{k}$. Este fenómeno induce un efecto dispersivo que posibilita la aparición de bandas de frecuencias prohibidas, o bandgaps, en el espectro de este medio (Kushwaha, 1996). En estas frecuencias las ondas no se pueden propagar.

Microestructuras periódicas diseñadas específicamente para promover la generación, ensanchamiento, o manipulación de los bandgaps se conocen como cristales fonónicos y también como metamateriales acústicos. La distinción entre cristal fonónico y metamaterial es ilustrada por Croënne et al. (2011), quien también describe tres mecanismos, denominados Bragg, hibridación, y efectos de acoplamiento elástico débil, que inducen la ocurrencia de los bandgaps. Además, la formación de bandgaps a bajas frecuencias y longitudes de ondas largas pueden ser originados a través de mecanismos localmente resonantes y que típicamente inducen (o abren) dicho bandgap en un rango de frecuencias que originalmente constituía una banda de dispersión.

Las propiedades presentes en la estructura de bandas, específicamente los bandgaps, dependen de la microarquitectura del medio, la cual determina el ancho y la frecuencia de los bandgaps.

En el presente trabajo de Tesis, la relación de dispersión, $\omega(\mathbf{k})$, de las ondas que se propagan en un medio periódico se realiza mediante el modelado por Elementos Finitos de la celda unidad, Ω_μ, que caracteriza a la estructura periódica con condiciones de borde que satisfacen la condición de Bloch, ver Fig. 1.4,. En el capitulo 2 se presentan diferentes estrategias para realizar esta tarea.

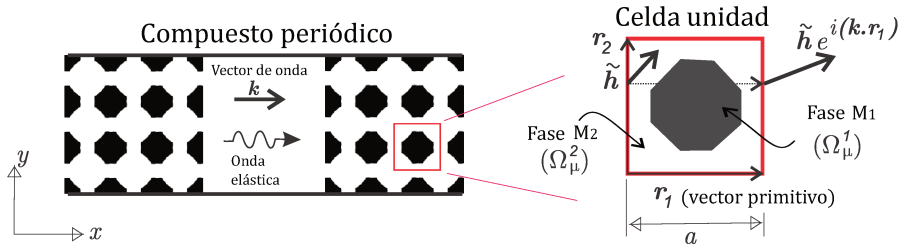

Figura 1.4: Onda elástica propagándose en un medio periódico. Celda unidad con condiciones de borde de Bloch.

Para el caso del diseño de los materiales fonónicos el objetivo es obtener la microarquitectura

de una estructura periódica, tal que, el ancho del bandgap entre dos bandas adyacentes, a priori seleccionadas, sea máximo

$$\max_{\chi} \left(\min_{\mathbf{k}} \omega_{j+1}^2(\mathbf{k}, \chi) - \max_{\mathbf{k}} \omega_j^2(\mathbf{k}, \chi) \right); \tag{1.4}$$

donde ω_{j+1} y ω_j son las frecuencias de las bandas $j+1$ y j, respectivamente. La variable de diseño en (1.4) es la misma función característica χ definida en (1.1). Por lo tanto, se examina todo el espacio de configuraciones de fase para encontrar la solución óptima.

En el Capítulo 4 se muestran ejemplos de microestructuras obtenidas al resolver el problema de optimización topológica (1.4) mediante el algoritmo descrito en el anexo C

1.2. Propiedades efectivas de medios periódicos en problemas de elastodinámica

La evaluación de las propiedades efectivas de elasticidad y densidad en un problema elastodinámico de propagación de ondas elásticas, en materiales heterogéneos periódicos, es el caso más típico en metamateriales donde pueden surgir situaciones no convencionales, como se muestra en Dong et al. (2017). Por ejemplo, una discusión interesante sobre la obtención de propiedades efectivas no convencionales en materiales heterogéneos fue reportada por Milton y Willis (2007). Estos autores discuten las consecuencias que estas propiedades efectivas imponen sobre las respuestas fundamentales de los cuerpos en la mecánica clásica, en particular, el impacto que tienen sobre la segunda ley de Newton. Una densidad efectiva tensorial no isotrópica, densidades y rigideces negativas son resultados típicos que se pueden obtener en estos casos (materiales doblemente negativos). En este trabajo, se propone un modelo numérico, ver anexo D, para evaluar las propiedades efectivas de un metamaterial acústico. Estas propiedades efectivas se obtienen mediante un procedimiento de promediado que involucra la respuesta constitutiva que conecta las magnitudes mecánicas observadas en la macroescala: tensiones ($\boldsymbol{\Sigma}$), cantidad de movimiento ($\boldsymbol{P}$), deformaciones ($\boldsymbol{E}$) , desplazamientos ($\boldsymbol{U}$) y velocidades ($\dot{\boldsymbol{U}}$), con los observados a microescala: tensiones ($\boldsymbol{\sigma}$), cantidad de movimiento ($\boldsymbol{p}$), desplazamientos ($\mathbf{u}$) y velocidades ($\dot{\mathbf{u}}$). Nuestro procedimiento se basa en los trabajos de Willis, (Willis, 1997) y (Willis, 2012), para encontrar la forma general de relaciones constitutivas en medios dinámicos con microestructura.

1.3. Organización del documento

La Tesis está organizada bajo el formato de *tesis por compilación*. Por lo tanto, en el cuerpo principal de la monografía sólo se presenta una descripción global y sucinta de la temática estudiada, mientras que los detalles de cada tema son direccionados a los trabajos presentados en los

Anexos. Allí se podrán encontrar todos los desarrollos que han sido necesarios para alcanzar los resultados presentados en la monografía.

En el Capítulo 2 se repasan temas sobre propagación de ondas en medios periódicos, se describen distintas estrategias para calcular la relación de dispersión $\omega(\mathbf{k})$, empleando el método de elementos finitos.

En el Capítulo 3 se presentan dos ejemplos, el diseño de un material auxético y de un material con rigidez máxima, de aplicación de diseño inverso en $\mathbb{R}^3$. La optimización topológica se realiza mediante el algoritmo presentado en el anexo A.

En el Capítulo 4 se presentan ejemplos de diseño de cristales fonónicos, en estructuras con simetrías p4mm y p6mm. La optimización topológica se realiza mediante el algoritmo presentado en el anexo C. Además, se presentan ejemplos de determinación de propiedades efectivas a materiales que exhiben mecanismos de resonancia local mediante el uso del modelo descrito en el anexo D.

Por último, el Capítulo 5 consiste en el desarrollo de las conclusiones generales. Además se realiza un recuento de las contribuciones científicas derivadas del trabajo realizado en la presente Tesis.

1.3.1. Anexos

En los Anexos se encuentran los artículos científicos en los que se fundamentan los temas expuestos en el cuerpo principal de la Tesis. En el artículo presentado en el anexo A se describe el algoritmo de optimización topológica utilizado en el diseño de materiales extremos.

En el artículo presentado en el anexo B se evalúan los efectos de la imposición de distintas simetrías de cristales en el diseño de materiales extremos. La optimización topológica se realiza mediante el algoritmo descrito en el artículo presentado en el anexo A.

En el artículo presentado en el anexo C se describe un algoritmo de optimización topológica para el diseño de metamateriales acústicos mediante la maximización del bandgap de dos bandas de dispersión adyacentes.

En el artículo presentado en el anexo D se presenta un modelo numérico para evaluar las propiedades efectivas de los medios periódicos en problemas de elastodinámica.

Capítulo 2

Propagación de ondas en medios periódicos

2.1. Introducción

En el estudio de la propagación de ondas en medios periódicos juega un papel central la teoría de Bloch, o teoría de bandas, desarrollada por Bloch (1929). La teoría de Bloch dio forma al concepto de bandas de energía de los electrones en cristales. Además, ha sido fundamental en el estudio las propiedades eléctricas, magnéticas, ópticas y térmicas de los sólidos cristalinos.

El estudio de la propagación de ondas de Bloch ha cobrado aún mas interés con introducción de nuevas estructuras periódicas. En 1987 Yablonovitch (1987) y John (1987) propusieron el concepto de lo que hoy conocemos como cristales fotónicos. Unos años después, a inicio de la década de los noventa, surge el concepto de cristal fonónico, cuando Sigalas y Economou demostraron la existencia de bandgaps en la estructura de bandas, para ondas acústicas y elásticas, en una estructura tridimensional compuesta por un arreglo periódico de esferas idénticas (M.M. Sigalas, 1992) y en un sistema bidimensional fluido-sólido constituido por un arreglo periódico de inclusiones cilíndricas en una matriz (M.M. Sigalas, 1993).

Estos materiales periódicos pueden ser diseñados, en particular en el presente trabajo de Tesis (ver Capítulo 4) se realiza el diseño de cristales fonónicos 2D con el objetivo de maximizar el bandgap entre dos bandas de dispersión adyacentes. El concepto de bandgap es fundamental para aplicaciones de control y filtrado de vibraciones (Richards y Pines, 2003), (Hussein et al., 2006), (Policarpo et al., 2010).

Naturalmente, el cálculo de la estructura de bandas (relación de dispersión) es central para cualquiera de las aplicaciones de la teoría de Bloch. Típicamente, la relación de dispersión consiste en un plot de las frecuencias ω versus el vector de onda $\mathbf{k}$ que corresponden a aquellas ondas no forzadas que pueden ser transmitidas a través del material. Para determinar la estructura de bandas existen varios métodos, por ejemplo, el método de expansión de onda plana, el método de

dispersiones múltiples, el método de elementos finitos, el método basado en wavelet, entre otros.

En el presente Capítulo, se describen tres estrategias para calcular la estructura de bandas, todas basadas en el método de elementos finitos. Además, se presentan algunos conceptos básicos de simetría de cristales que están estrechamente relacionados con el análisis de propagación de ondas de Bloch.

2.2. Propagación de ondas en medios periódicos

Para un medio sólido, modelado como un continuo, la ecuación de movimiento (ecuación de Cauchy) es:

$$\nabla \cdot \boldsymbol{\sigma} = \rho \ddot{\mathbf{u}}, \tag{2.1}$$

donde $\boldsymbol{\sigma}$ es el tensor de tensiones, $\mathbf{u}$ representa el campo de desplazamientos, ρ es la densidad y $\ddot{\mathbf{u}}$ es la segunda derivada respecto al tiempo del campo de desplazamientos. La relación entre las tensiones $\boldsymbol{\sigma}$ y los desplazamientos $\mathbf{u}$, para un medio elástico lineal, viene dado por:

$$\boldsymbol{\sigma} = \mathbf{C} : \boldsymbol{\varepsilon} = \mathbf{C} : \nabla^s \mathbf{u}, \tag{2.2}$$

donde $\mathbf{C}$ es el tensor de elasticidad, $\boldsymbol{\varepsilon}$ el tensor de deformaciones y ∇^s representa el operador gradiente simétrico, $\nabla^s \mathbf{u} = \frac{1}{2}(\nabla \mathbf{u} + (\nabla \mathbf{u})^T)$.

Sustituyendo la expresión (2.2) en la ecuación (2.1) tenemos:

$$\nabla \cdot \mathbf{C} : \nabla^s \mathbf{u} = \rho \ddot{\mathbf{u}}, \tag{2.3}$$

que representa la ecuación general de la elástodinamica en su forma fuerte para un medio infinito.

Para medios periódicos infinitos, el teorema de Bloch explicita que: cualquier autofunción puede expresare como la propagación de una onda plana modulada por una función periódica. Por lo que la ecuación (2.3) tiene solución tipo Bloch, ver (Gazalet et al., 2013):

$$\mathbf{u} = \widetilde{\mathbf{u}}(\mathbf{x}) e^{i(\mathbf{k}\cdot\mathbf{x} - \omega t)} = \left[\widetilde{\mathbf{u}} e^{i\mathbf{k}\cdot\mathbf{x}}\right] e^{-i\omega t} \tag{2.4}$$

donde $\mathbf{k}$ es el vector de onda, t es el tiempo, ω es la frecuencia angular y el término $\widetilde{\mathbf{u}}(\mathbf{x})$, acorde con el teorema de Bloch, es una función periódica que reproduce la simetría de traslación del medio

2.3. Cálculo de la relación de dispersión

Para el cálculo de la estructura de bandas del material se presentan a continuación distintas metodologías numéricas alternativas. Diferenciamos dos aproximaciones básicas:

i) En el primer caso evaluamos la frecuencia en términos del número de onda (valores reales), $\omega(\mathbf{k})$, (subsecciones 2.3.1 y 2.3.2) mediante dos aproximaciones de elementos finitos diferentes, sea imponiendo condiciones de Bloch a nodos de contorno en la microcelda (subsección 2.3.1), o alternativamente, imponiendo el formato de la función de Bloch a la función de interpolación de elementos finitos (subsección 2.3.2).

ii) En el segundo caso (subsección 2.3.3), evaluamos el número de onda en términos de la frecuencia, $\mathbf{k}(\omega)$, siendo una aproximación que se puede utilizar inclusive para evaluar el par $(\omega, \mathbf{k})$ en las zonas de bandgap. En dichas zonas los número de onda resultan vectores complejos.

2.3.1. Solución $\omega(\mathrm{k})$ con condiciones de borde de Bloch

Una forma de resolver el problema (2.3) mediante el método de elementos finitos es expresando las solución de Bloch (2.4) como la siguiente expresión armónica en el tiempo:

$$\mathbf{u} = \widetilde{\boldsymbol{h}}(\mathbf{x})e^{-i\omega t} \tag{2.5}$$

donde $\widetilde{\boldsymbol{h}}(\mathbf{x})$ es una función desconocida. Sustituyendo la expresión (2.5) en la ecuación (2.3) y derivando respecto al tiempo, luego de cancelar los términos armónicos $e^{-i\omega t}$ de la ecuación, tenemos:

$$\nabla \cdot \mathbf{C} : \nabla^s \widetilde{\boldsymbol{h}} = -\rho\omega^2 \widetilde{\boldsymbol{h}}, \tag{2.6}$$

El material periódico puede ser modelado considerando solamente una celda unidad, Ω_μ. Por tanto, resolveremos el problema (2.6) mediante el método de elemento finitos con condiciones de borde que satisfacen el teorema de Bloch para medios periódicos, $\tilde{\boldsymbol{h}}(\mathbf{x} + \boldsymbol{r}) = \tilde{\boldsymbol{h}}(\mathbf{x})e^{i\mathbf{k}\cdot\boldsymbol{r}}$, donde $\boldsymbol{r}$ es el vector primitivo de la red de Bravais subyacente del material periódico, ver Figura 2.1. La forma débil de ecuación 2.6 es:

$$\int_{\Omega_\mu} \overline{\nabla^s \widetilde{\boldsymbol{w}}} : \mathbf{C} : \nabla^s \widetilde{\boldsymbol{h}} d\Omega_\mu = \omega^2 \int_{\Omega_\mu} \rho \overline{\widetilde{\boldsymbol{w}}} \cdot \widetilde{\boldsymbol{h}} d\Omega_\mu, \ \forall \widetilde{\boldsymbol{w}} \text{ admisible} \tag{2.7}$$

donde $\overline{\nabla^s \widetilde{\boldsymbol{w}}}$ es el gradiente complejo conjugado de la función de prueba $\widetilde{\boldsymbol{w}}$. Notar que la función de prueba $\widetilde{\boldsymbol{w}}$ también satisface que $\widetilde{\boldsymbol{w}}(\mathbf{x} + \boldsymbol{r}) = \widetilde{\boldsymbol{w}}(\mathbf{x})e^{i\mathbf{k}\cdot\boldsymbol{r}}$.

La función $\widetilde{\boldsymbol{h}}$ y $\widetilde{\boldsymbol{w}}$ en Ω_μ se interpolan usando elementos finitos tradicional:

$$\widetilde{\boldsymbol{h}}(\mathbf{x}) = \boldsymbol{N}(\mathbf{x})\widehat{\boldsymbol{h}}; \tag{2.8}$$

$$\nabla\widetilde{\boldsymbol{h}} = \mathbf{B}\widehat{\boldsymbol{h}}; \tag{2.9}$$

$$\widetilde{\boldsymbol{w}}(\mathbf{x}) = \boldsymbol{N}(\mathbf{x})\widehat{\boldsymbol{w}}; \tag{2.10}$$

$$\nabla\widetilde{\boldsymbol{w}} = \mathbf{B}\widehat{\boldsymbol{w}}; \tag{2.11}$$

donde $\boldsymbol{N}$ es la matriz de funciones de forma y $\widehat{\boldsymbol{h}} \in \mathbb{R}^{ndof}$ es el vector de parámetros de interpolación (desplazamientos nodales) del campo de desplazamientos interpolado por las funciones de elementos finitos. El número total de grados de libertad (DOFs) es denotado $ndof$. El operador ∇ y la matriz $\mathbf{B}$ definen respectivamente al gradiente y a la matriz de deformación-desplazamiento de elementos finitos convencionales.

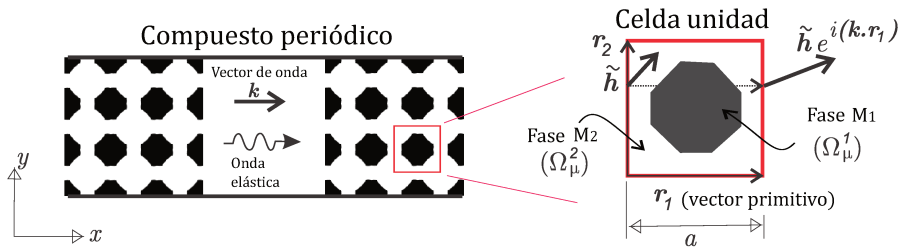

Figura 2.1: Onda elástica propagándose en un medio periódico. Celda unidad con condiciones de borde de Bloch.

Imposición de las condiciones de borde tipo Bloch a través de matrices proyección.

Introduciendo las ecuaciones (2.8), (2.9), (2.10) y (2.11) en (2.7), obtenemos el sistema discreto:

$$\overline{\widehat{\boldsymbol{w}}} \left[\int_{\Omega_\mu} (\overline{\mathbf{B}}\mathbf{C}\mathbf{B} d\Omega_\mu - \omega^2 \int_{\Omega_\mu} \rho \boldsymbol{N}^T \boldsymbol{N} d\Omega_\mu \right] \widehat{\boldsymbol{h}} = \mathbf{0} \; ; \; \forall \widehat{\boldsymbol{w}} \;\; \text{admisible} \; , \tag{2.12}$$

El sistema discreto (2.12) con las condiciones de contorno explicitadas es escrito en forma compacta como:

$$\overline{\mathbb{P}}(\mathbf{k}) \left[\mathbb{K} - \omega^2 \mathbb{M} \right] \mathbb{P}(\mathbf{k}) \widehat{\boldsymbol{h}}_r = \mathbf{0} \; , \tag{2.13}$$

donde $\mathbb{K} = \int_{\Omega_\mu} \overline{\mathbf{B}}\mathbf{C}\mathbf{B} d\Omega_\mu$ y $\mathbb{M} = \int_{\Omega_\mu} \rho \boldsymbol{N}^T \boldsymbol{N} d\Omega_\mu$ son las matrices no restringidas de rigidez y de masa. La matriz $\overline{\mathbb{P}}$ es la transpuesta conjugada de $\mathbb{P}$ que impone las condiciones de borde de Bloch a los grados de libertad de la frontera:

$$\widehat{\boldsymbol{h}} = \mathbb{P} \widehat{\boldsymbol{h}}_r \quad ; \quad \widehat{\boldsymbol{w}} = \mathbb{P} \widehat{\boldsymbol{w}}_r \; , \tag{2.14}$$

Considerando la malla de elementos finitos de la celda unidad mostrada en la Figura 2.2, los término de la expresión (2.14) son representados como:

$$\widehat{\boldsymbol{h}} = \begin{bmatrix} \widehat{\boldsymbol{h}}_I \\ \widehat{\boldsymbol{h}}_L \\ \widehat{\boldsymbol{h}}_R \\ \widehat{\boldsymbol{h}}_B \\ \widehat{\boldsymbol{h}}_T \\ \widehat{\boldsymbol{h}}_{BL} \\ \widehat{\boldsymbol{h}}_{BR} \\ \widehat{\boldsymbol{h}}_{TR} \\ \widehat{\boldsymbol{h}}_{TL} \end{bmatrix} \quad ; \quad \mathbb{P} = \begin{bmatrix} \mathbf{I}_I & \mathbf{0} & \mathbf{0} & \mathbf{0} \\ \mathbf{0} & \mathbf{I}_L & \mathbf{0} & \mathbf{0} \\ \mathbf{0} & \xi_1 \mathbf{I}_L & \mathbf{0} & \mathbf{0} \\ \mathbf{0} & \mathbf{0} & \mathbf{I}_B & \mathbf{0} \\ \mathbf{0} & \mathbf{0} & \xi_2 \mathbf{I}_B & \mathbf{0} \\ \mathbf{0} & \mathbf{0} & \mathbf{0} & \mathbf{I}_{BL} \\ \mathbf{0} & \mathbf{0} & \mathbf{0} & \xi_1 \mathbf{I}_{BL} \\ \mathbf{0} & \mathbf{0} & \mathbf{0} & \xi_1 \xi_2 \mathbf{I}_{BL} \\ \mathbf{0} & \mathbf{0} & \mathbf{0} & \xi_2 \mathbf{I}_{BL} \end{bmatrix} \quad ; \quad \widehat{\boldsymbol{h}}_r = \begin{bmatrix} \widehat{\boldsymbol{h}}_I \\ \widehat{\boldsymbol{h}}_L \\ \widehat{\boldsymbol{h}}_B \\ \widehat{\boldsymbol{h}}_{BL} \end{bmatrix} \; , \tag{2.15}$$

donde los subíndices I, L, R, B, T, BL, BR, TR y TL en (2.15) identifican a los conjuntos de grados de libertad indicados en la Figura 2.2. $\mathbf{I}_I$, $\mathbf{I}_L$, $\mathbf{I}_B$ y $\mathbf{I}_{BL}$ son matrices identidad con dimensiones dadas por el numero de grados de libertad de los vectores $\widehat{\boldsymbol{h}}_I$, $\widehat{\boldsymbol{h}}_L$, $\widehat{\boldsymbol{h}}_B$ y $\widehat{\boldsymbol{h}}_{BL}$, respectivamente. Los coeficientes ξ_1 y ξ_2 son iguales a: $\xi_1 = e^{i(\mathbf{k}\cdot\boldsymbol{r}_1)}$ y $\xi_2 = e^{i(\mathbf{k}\cdot\boldsymbol{r}_2)}$, $\boldsymbol{r}_1$ y $\boldsymbol{r}_2$ son los vectores primitivos de traslación de la red.

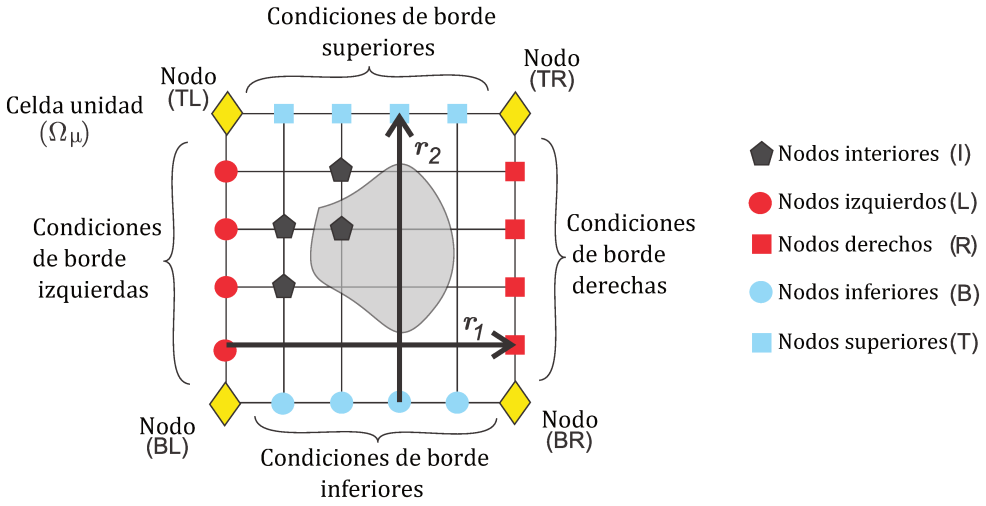

Figura 2.2: Malla de elementos finitos de la celda unidad Ω_μ. Denominación de los diferentes conjuntos de nodos.

Debido a las propiedades de simetría de la celda unidad, tal como se esquematiza en la Figura 2.3 para un caso específico de simetría p4mm, para calcular la relación de dispersión debemos resolver el problema de autovalores generalizados (2.13) solo para los vectores de onda $\mathbf{k}$ pertenecientes a la zona irreducible de Brillouin (IBZ), ver (Brillouin, 1953). Para celdas unidad con simetrías de alto orden, i.e p4mm, p6mm, el dominio de solución para los vectores de onda $\mathbf{k}$ puede ser reducido al contorno de la zona irreducible de Brillouin, ver (Maurin et al., 2018).

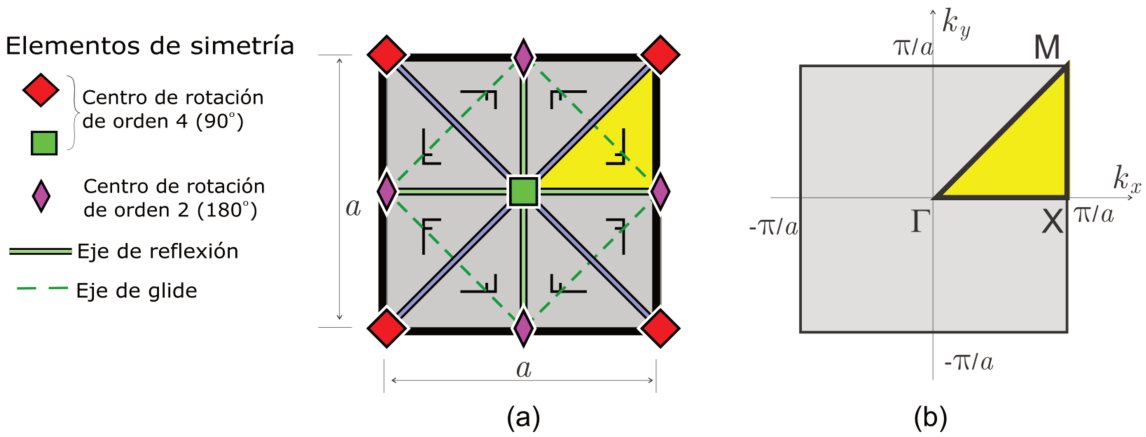

Figura 2.3: Cristal fonónico con simetría p4mm. (a) Elementos de simetría de la celda unidad y región asimétrica (en azul). (b) Celda unidad de la red reciproca. Primera Zona de Brillouin (FBZ en gris) y zona irreducible de Brillouin (IBZ en amarrillo); contorno de la zona irreducible de Brillouin $[\Gamma - X - M - \Gamma]$.

Esta estrategia para calcular la estructura de bandas es usada en al artículo presentado en el

anexo C y en el Capítulo 4 para realizar el diseño de materiales fonónicos mediante optimización topológica.

2.3.2. Solución $\omega(\mathrm{k})$ con condiciones de borde de periódicas

Alternativamente, otra vía de solución, mediante elementos finitos, se basa en resolver la función $\widetilde{u}$ de la expresión (2.4), periódica en la celda, mediante la transformación del operador de Bloch de la ecuación diferencial (2.3). Este operador de Bloch se obtiene sustituyendo la expresión (2.4) en la ecuación (2.3). Cancelando el término $e^{i(\mathbf{k}\cdot\mathbf{x}-\omega t)}$ y usando los principios variacionales tenemos:

$$\int_{\Omega_\mu} \overline{(\nabla^s \widetilde{\boldsymbol{w}} + i\mathbf{k}\otimes^s \widetilde{\boldsymbol{w}})} : \mathbf{C} : (\nabla^s \widetilde{\mathbf{u}} + i\mathbf{k}\otimes^s \widetilde{\mathbf{u}}) d\Omega_\mu = \omega^2 \int_{\Omega_\mu} \rho \overline{\widetilde{\boldsymbol{w}}}\cdot\widetilde{\mathbf{u}} d\Omega_\mu \ ; \ \forall \widetilde{\boldsymbol{w}} \ \text{ periódico}, \quad (2.16)$$

donde $\widetilde{\boldsymbol{w}}$ es una función de prueba periódica en la microcelda.

Los desplazamientos $\widetilde{\mathbf{u}}$ en Ω_μ se interpolan usando elementos finitos tradicional:

$$\widetilde{\mathbf{u}}(\mathbf{x}) = \boldsymbol{N}(\mathbf{x})\widehat{\mathbf{u}}, \quad (2.17)$$

$$\nabla_k \widetilde{\mathbf{u}} = \mathbf{B}\widehat{\mathbf{u}} + i\mathbf{k}\otimes^s \boldsymbol{N}\widehat{\mathbf{u}} = \mathbf{B}_k\widehat{\mathbf{u}}, \quad (2.18)$$

$$\widetilde{\boldsymbol{w}}(\mathbf{x}) = \boldsymbol{N}(\mathbf{x})\widehat{\boldsymbol{w}}, \quad (2.19)$$

$$\nabla_k \widetilde{\boldsymbol{w}} = \mathbf{B}\widehat{\boldsymbol{w}} + i\mathbf{k}\otimes^s \boldsymbol{N}\widehat{\boldsymbol{w}} = \mathbf{B}_k\widehat{\boldsymbol{w}}, \quad (2.20)$$

donde $\boldsymbol{N}$ es la matriz de funciones de forma y $\widehat{\mathbf{u}} \in \mathbb{R}^{ndof}$ es el vector compuesto por todos los valores de desplazamiento en nodos que componen la malla de elementos finitos. El número total de grados de libertad (DOFs) es denotado $ndof$. $\mathbf{B}$ es la matriz de deformación-desplazamiento convencional de elementos finitos y ∇_k es el operador de Bloch.

Los valores de $\widehat{\mathbf{u}}$ son los autovectores del siguiente problema de autovalores discreto:

$$\overline{\widehat{\boldsymbol{w}}}\left[\int_{\Omega_\mu} \overline{(\mathbf{B} + i\mathbf{k}\otimes^s \boldsymbol{N})}\mathbf{C}(\mathbf{B} + i\mathbf{k}\otimes^s \boldsymbol{N}) d\Omega_\mu - \omega^2 \int_{\Omega_\mu} \rho \boldsymbol{N}^T\boldsymbol{N} d\Omega_\mu\right]\widehat{\mathbf{u}} = 0 \ ; \ \forall \widehat{\boldsymbol{w}} \ \text{ periódico}, \quad (2.21)$$

El problema (2.21) es complementado con condiciones de borde periódicas impuestas mediante la matriz $\boldsymbol{P}$.

$$\widehat{\mathbf{u}} = \boldsymbol{P}\widehat{\mathbf{u}}_r \quad (2.22)$$

los términos de la expresión (2.22) vienen dados por:

$$\widehat{\mathbf{u}} = \begin{bmatrix} \widehat{\mathbf{u}}_I \\ \widehat{\mathbf{u}}_L \\ \widehat{\mathbf{u}}_R \\ \widehat{\mathbf{u}}_B \\ \widehat{\mathbf{u}}_T \\ \widehat{\mathbf{u}}_{BL} \\ \widehat{\mathbf{u}}_{BR} \\ \widehat{\mathbf{u}}_{TR} \\ \widehat{\mathbf{u}}_{TL} \end{bmatrix} \quad ; \quad \boldsymbol{P} = \begin{bmatrix} \mathbf{I}_I & \mathbf{0} & \mathbf{0} & \mathbf{0} \\ \mathbf{0} & \mathbf{I}_L & \mathbf{0} & \mathbf{0} \\ \mathbf{0} & \mathbf{I}_L & \mathbf{0} & \mathbf{0} \\ \mathbf{0} & \mathbf{0} & \mathbf{I}_B & \mathbf{0} \\ \mathbf{0} & \mathbf{0} & \mathbf{I}_B & \mathbf{0} \\ \mathbf{0} & \mathbf{0} & \mathbf{0} & \mathbf{I}_{BL} \\ \mathbf{0} & \mathbf{0} & \mathbf{0} & \mathbf{I}_{BL} \\ \mathbf{0} & \mathbf{0} & \mathbf{0} & \mathbf{I}_{BL} \\ \mathbf{0} & \mathbf{0} & \mathbf{0} & \mathbf{I}_{BL} \end{bmatrix} \quad ; \quad \widehat{\mathbf{u}}_r = \begin{bmatrix} \widehat{\mathbf{u}}_I \\ \widehat{\mathbf{u}}_L \\ \widehat{\mathbf{u}}_B \\ \widehat{\mathbf{u}}_B L \end{bmatrix} . \tag{2.23}$$

El sistema discreto de ecuaciones obtenido se expresa como:

$$\boldsymbol{P}^T \left[\widehat{\mathbb{K}}(\mathbf{k}) - \omega^2 \mathbb{M} \right] \boldsymbol{P} \widehat{\mathbf{u}}_r = \mathbf{0} \, , \tag{2.24}$$

donde $\widehat{\mathbb{K}}(\mathbf{k}) = \int_{\Omega_\mu} \overline{(\mathbf{B} + i\mathbf{k} \otimes^s \boldsymbol{N})} \mathbf{C} (\mathbf{B} + i\mathbf{k} \otimes^s \boldsymbol{N}) d\Omega_\mu$ es la matriz de rigidez asociada al operador de Bloch y $\mathbb{M} = \int_{\Omega_\mu} \rho \boldsymbol{N}^T \boldsymbol{N} d\Omega_\mu$ es la matriz de masa tradicional obtenida mediante el método de elementos finitos.

La relación de dispersión se obtiene resolviendo el problema de autovalores generalizados (2.24) para cada uno de los vectores de onda $\mathbf{k}$ de la zona irreducible de Brillouin. Esta formulación es utilizada en el desarrollo del modelo de homogeneización para la determinación de las propiedades efectivas de los metamateriales acústicos en problemas de propagación de ondas, presentado en el anexo D.

2.3.3. Solución $\mathbf{k}(\omega)$

La relación de dispersión se puede calcular, como se presentó en la secciones 2.3.1 y 2.3.2, escaneando los vectores de onda $\mathbf{k}$ de la zona irreducible de Brillouin y resolviendo, para cada valor de $\mathbf{k}$, el problema 2.13 o el problema 2.24. Pero, para estudiar las propiedades efectivas del medio en la región de bandgap, donde los vectores de onda $\mathbf{k}$ son imaginarios, se requiere de un método que permita escanear el espacio de frecuencias y obtener la relación $\mathbf{k}(\omega)$. Una discusión mas detallada del método presentado en la presente sección se puede encontrar en (Collet et al., 2011).

Expandiendo la ecuación (2.21) tenemos:

$$\begin{aligned} \Bigg[\int_{\Omega_\mu} & (\mathbf{B}^T \mathbf{C} \mathbf{B} - \omega^2 \rho \boldsymbol{N}^T \boldsymbol{N} + i[\mathbf{B}^T \mathbf{C} (\mathbf{k} \otimes^s \boldsymbol{N}) - (\boldsymbol{N} \otimes^s \mathbf{k}) \mathbf{C} \mathbf{B}] - \\ & - (\boldsymbol{N} \otimes^s \mathbf{k}) \mathbf{C} (\mathbf{k} \otimes^s \boldsymbol{N})) d\Omega_\mu \Bigg] \widehat{\mathbf{u}} = 0 \end{aligned} \tag{2.25}$$

En particular, asumiendo que la parte real e imaginaria del vector de onda $\mathbf{k}$ son colineales, para problemas 2D (de forma análoga para problemas 3D) el vector de onda $\mathbf{k}$ puede ser expresado como $\mathbf{k} = k\boldsymbol{\Phi} = k\left[\cos(\theta)\mathbf{e}_x + \sin(\theta)\mathbf{e}_y\right]$, donde θ representa el ángulo de dirección en la red reciproca. Sustituyendo esta expresión para $\mathbf{k}$ en la ecuación 2.25 tenemos:

$$\left[\int_{\Omega_\mu}(\mathbf{B}^T\mathbf{C}\mathbf{B}-\omega^2\rho\boldsymbol{N}^T\boldsymbol{N}+ik[\mathbf{B}^T\mathbf{C}(\boldsymbol{\Phi}\otimes^s\boldsymbol{N})-(\boldsymbol{N}\otimes^s\boldsymbol{\Phi})\mathbf{C}\mathbf{B}]- \right.$$
$$\left.-k^2(\boldsymbol{N}\otimes^s\boldsymbol{\Phi})\mathbf{C}(\boldsymbol{\Phi}\otimes^s\boldsymbol{N}))d\Omega_\mu\right]\widehat{\mathbf{u}}=0 \tag{2.26}$$

Aplicando las condiciones de borde periodicas, (2.22), la expresión (2.26) se puede expresar de manera compacta como:

$$\boldsymbol{P}^T\left[(\mathbb{K}-\omega^2\mathbb{M})+\lambda\mathbb{L}-\lambda^2\mathbb{H}\right]\boldsymbol{P}\widehat{\mathbf{u}}_r=\mathbf{0}\,, \tag{2.27}$$

donde $\lambda=ik$, $\mathbb{K}=\int_{\Omega_\mu}\mathbf{B}^T\mathbf{C}\mathbf{B}d\Omega_\mu$ y $\mathbb{M}=\int_{\Omega_\mu}\rho\boldsymbol{N}^T\boldsymbol{N}d\Omega_\mu$ son las matrices simétricas de rigidez (semidefinida positiva) y de masa (definida positiva) respectivamente, $\mathbb{L}=\int_{\Omega_\mu}[\mathbf{B}^T\mathbf{C}(\boldsymbol{\Phi}\otimes^s\boldsymbol{N})-(\boldsymbol{N}\otimes^s\boldsymbol{\Phi})\mathbf{C}\mathbf{B}]d\Omega_\mu$, es una matriz antisimétrica y $\mathbb{H}=\int_{\Omega_\mu}(\boldsymbol{N}\otimes^s\boldsymbol{\Phi})\mathbf{C}(\boldsymbol{\Phi}\otimes^s\boldsymbol{N})d\Omega_\mu$, es una matriz simétrica semidefinida positiva. La $\boldsymbol{P}$ está dada por la ecuación (2.23). Los autovalores λ son obtenidos fijando la frecuencia ω y la dirección de propagación de la onda $\boldsymbol{\Phi}$.

El problema de autovalores cuadrático (2.27) puede ser linealizado de la siguiente manera:

$$\begin{bmatrix}\boldsymbol{P}^T\mathbb{L}\boldsymbol{P} & \boldsymbol{P}^T(\mathbb{K}-\omega^2\mathbb{M})\boldsymbol{P}\\ \mathbb{I} & \mathbf{0}\end{bmatrix}\begin{bmatrix}\lambda\widehat{\mathbf{u}}_r\\ \widehat{\mathbf{u}}_r\end{bmatrix}-\lambda\begin{bmatrix}\boldsymbol{P}^T\mathbb{H}\boldsymbol{P} & \mathbf{0}\\ \mathbf{0} & \mathbb{I}\end{bmatrix}\begin{bmatrix}\lambda\widehat{\mathbf{u}}_r\\ \widehat{\mathbf{u}}_r\end{bmatrix}=\mathbf{0} \tag{2.28}$$

donde $\mathbb{I}$ es la matriz identidad de dimensión igual al número de grados de libertad reducido del problema original. La ecuación (2.28) se corresponde con un problema de autovalores generalizados que puede ser resuelto mediante métodos tradicionales.

En el Capítulo 4 se muestran ejemplos donde se utiliza el método descrito en 2.3.1 para realizar la optimización topológica de cristales fonónicos y los métodos presentados en 2.3.2 y 2.3.3 para determinar las propiedades efectivas de metamateriales acústicos.

2.4. Estudio de convergencia para distintas aproximaciones y tipos de elementos finitos

En la presente sección se comparan los métodos para el calculo de la estructura de bandas descritos en las secciones 2.3.1 y 2.3.2. Los resultados presentados en esta sección son inéditos. En la Figura 2.4 se muestra la celda unidad cuadrada (con simetría p4mm) de $1.00\ m$ de longitud de un compuesto bifásico que se utiliza para modelar la estructura de bandas con las dos aproximaciones de elementos finitos mencionadas en la secciones 2.3.1 y 2.3.2 presentadas anteriormente. También se comparan las estructuras de banda al ser modeladas con elementos finitos triangulares lineales y cuadrilaterales bilineales. En todos los casos utilizamos mallas estructuradas observando que la interface entre ambos materiales se modela en forma geométricamente exacta. La fase rígida, M_2, del material tiene un módulo de Young, $E_2=300\ GPa$ y una densidad, $\rho_2=8000\ kg/m^3$,

mientras que la fase blanda, M_1, tiene un módulo de Young, $E_1 = 3.00\ GPa$ y una densidad, $\rho_1 = 1180\ kg/m^3$, ver Figura 2.4, ambas fases tienen un coeficiente de Poisson, $\nu = 0.30$.

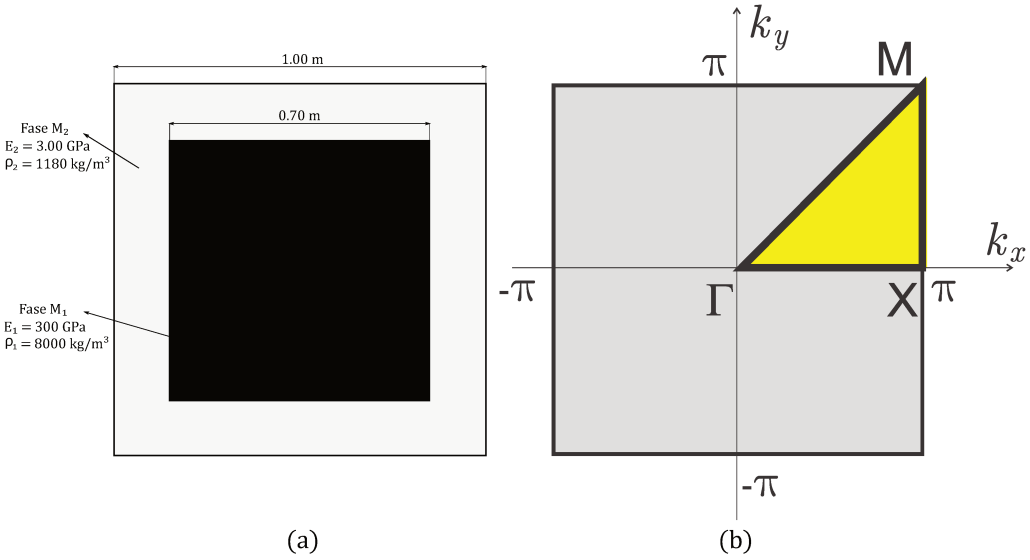

Figura 2.4: Celda unidad con simetría p4mm (a) y contorno zona irreducible de Brillouin $[\Gamma - X - M - \Gamma]$ (b) del compuesto bifásico para el cual se determina la estructura de bandas mediante los métodos descritos en las secciones 2.3.1 y 2.3.2.

Para todos los casos analizados se comparan las primeras cinco bandas de menor frecuencia, determinadas para ondas in-plane. Las gráficas muestran la dependencia entre la frecuencia expresada en Hz (eje Y) y los vectores de onda $\mathbf{k}$ (eje X) discretizados sobre el contorno de la zona irreducible de Brillouin $[\Gamma - X - M - \Gamma]$, ver Figura 2.4.

En la Figura 2.5a se muestra la comparación de las estructuras de bandas calculadas con el método descrito en la sección 2.3.1 usando mallas de 800 y 20000 elementos finitos triangulares. El mayor error relativo de la solución con la malla de 800 elementos finitos respecto a la de 20000 elementos corresponde a la tercera banda y es de solo el $1.3\,\%$, por lo que adoptaremos las relaciones de dispersión obtenidas mediante este método como nuestras soluciones de referencia. En las Figuras 2.5b, 2.5c, 2.5d y 2.5e se muestra la comparación de las estructuras de bandas calculadas mediante los métodos descritos en las secciones 2.3.1 y 2.3.2 para mallas de 800, 3200, 12800 y 20000 elementos finitos triangulares respectivamente. Podemos apreciar que el método que emplea condiciones de borde periódicas y matrices de elementos finitos obtenidas mediante el operador de Bloch, sección 2.3.2, presenta una velocidad de convergencia notablemente inferior que el método descrito en la sección 2.3.1 que emplea matrices de elementos finitos tradicionales y condiciones de borde de Bloch. El error es de $40.6\,\%$, $12.6\,\%$, $3.3\,\%$ y $2.1\,\%$ para las mallas de 800, 3200, 12800 y 20000 elementos finitos respectivamente.

En la Figura 2.6 se muestra un estudio similar al mencionado en el parágrafo previo pero utilizando una malla de elementos finitos cuadrilaterales (con interpolación bilineal). Se aprecia que la

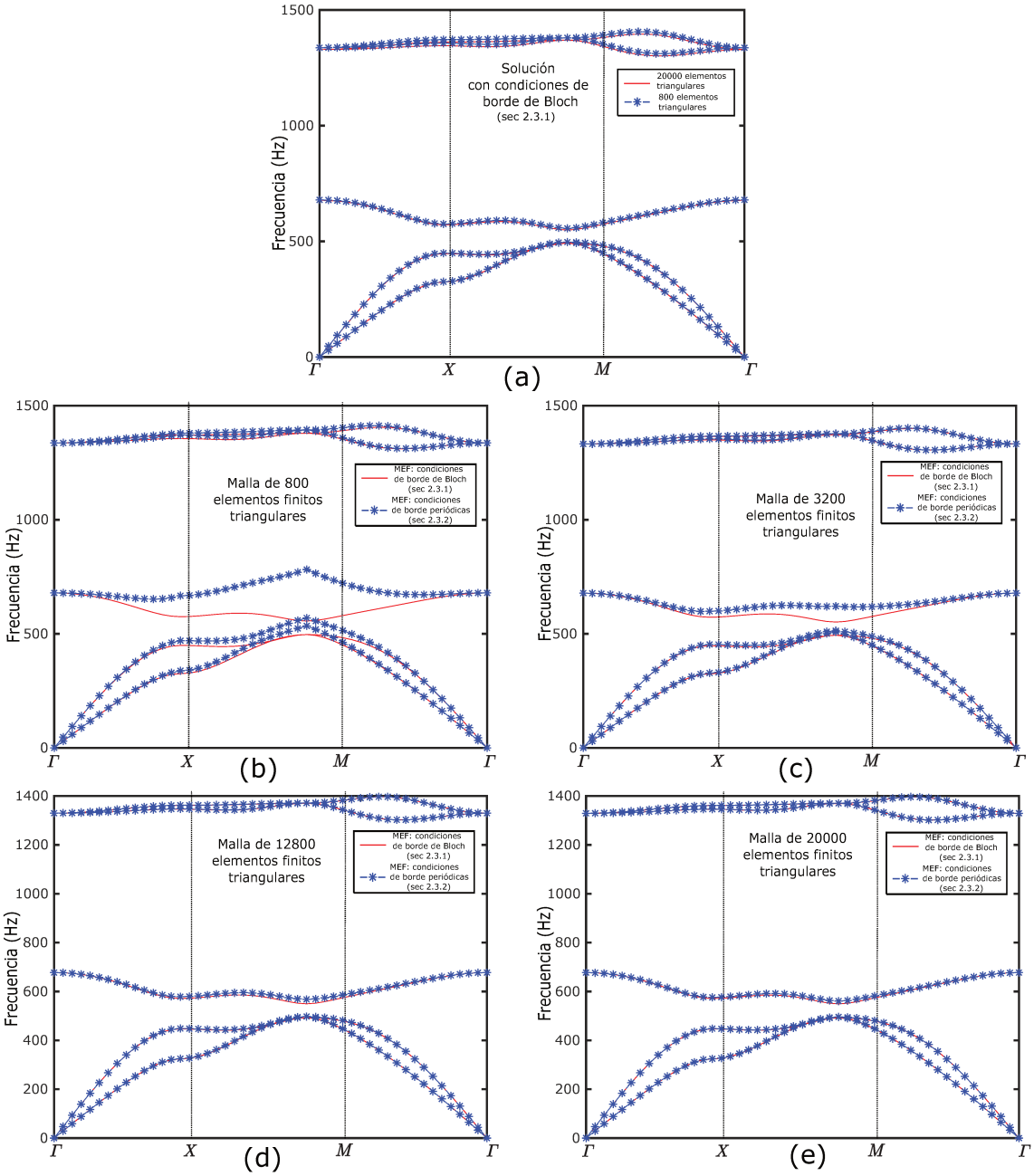

Figura 2.5: Estructura de bandas de ondas in-plane para la el material periódico cuya celda unidad esta esquematizado en la Figura 2.4. Comparación entre los métodos de cálculo de estructura de bandas descritos en las secciones 2.3.1 y 2.3.2 usando mallas de elementos finitos triangulares. (a) Comparación de soluciones obtenidas con mallas de 800 y 20000 elementos finitos mediante el método descrito en la sección 2.3.1. (b) Comparación de las soluciones obtenidas con mallas de 800 elementos. (c) Comparación de las soluciones obtenidas con mallas de 3200 elementos. (d) Comparación de las soluciones obtenidas con mallas de 12800 elementos. (e) Comparación de las soluciones obtenidas con mallas de 20000 elementos.

convergencia de los métodos con este tipo de elementos es mejor que con elementos triangulares. El error relativo de las solución con 400 respecto a la de 10000 elementos finitos, ver Figura 2.6a, obtenida mediante el método descrito en la sección 2.3.1 es de $0.4\,\%$. En cuanto a la comparación entre los dos métodos las soluciones para las mallas de 400, 1600, 6400 y 10000 elementos, ver Figuras 2.6b, 2.6c, 2.6d y 2.6e, tienen errores relativos del $18.1\,\%$, $4.8\,\%$, $1.1\,\%$ y $0.8\,\%$ respec-

tivamente. Los mayores errores se registran para las tres bandas de frecuencias mas bajas y el máximo error relativo siempre se obtuvo para la tercera banda, ver Figuras 2.5 y 2.6.

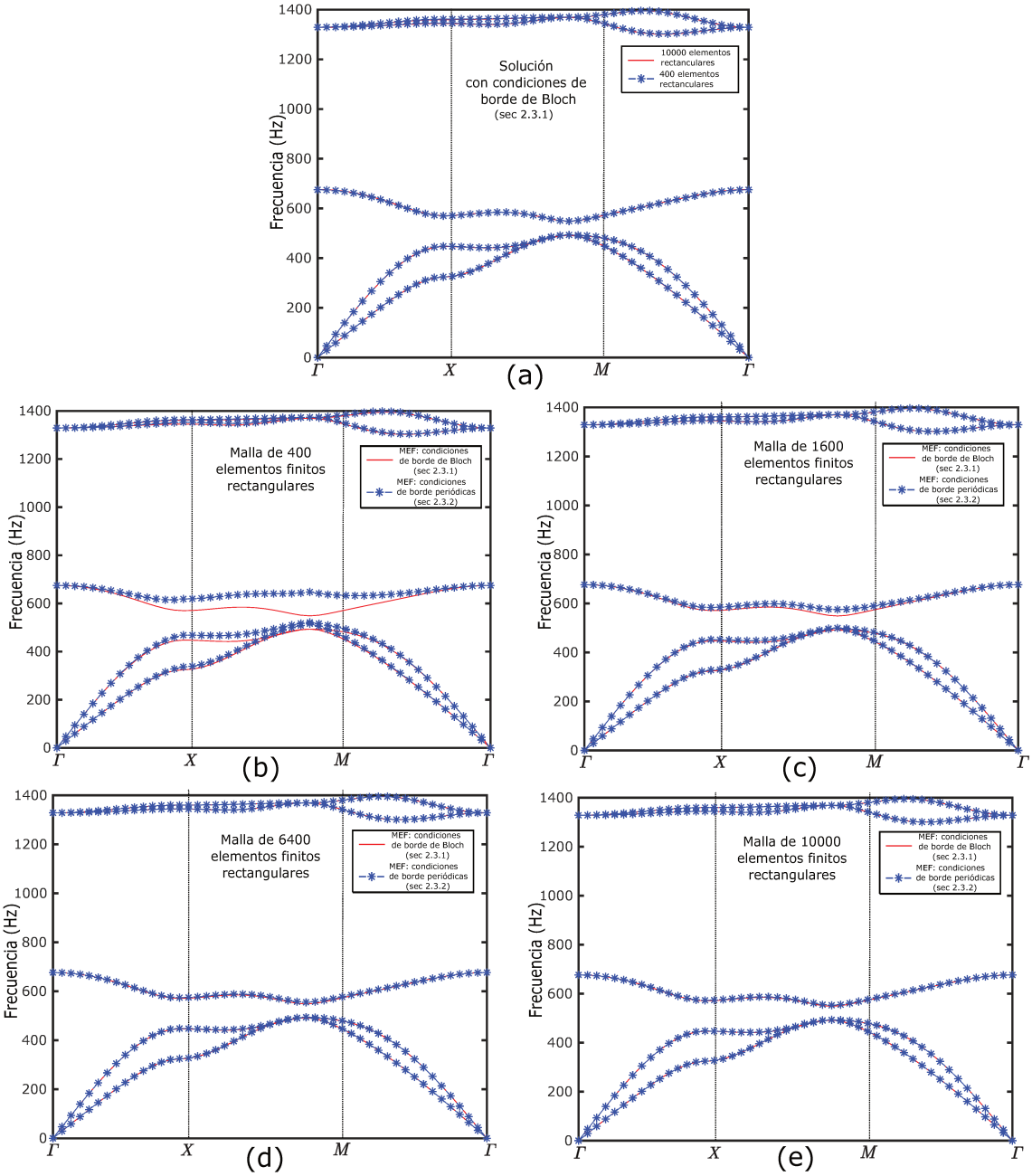

Figura 2.6: Estructura de bandas de ondas in-plane para la el material periódico cuya celda unidad esta esquematizado en la Figura 2.4. Comparación entre los métodos de cálculo de estructura de bandas descritos en las secciones 2.3.1 y 2.3.2 usando mallas de elementos finitos rectangulares. (a) Comparación de soluciones obtenidas con mallas de 400 y 10000 elementos finitos mediante el método descrito en la sección 2.3.1. (b) Comparación de las soluciones obtenidas con mallas de 400 elementos. (c) Comparación de las soluciones obtenidas con mallas de 1600 elementos. (d) Comparación de las soluciones obtenidas con mallas de 6400 elementos. (e) Comparación de las soluciones obtenidas con mallas de 10000 elementos.

Se investigó la hipótesis de que los problemas de convergencia del método descrito en la sección 2.3.2 se debieran a un posible problema de bloqueo (locking), pero esta hipótesis fue desestimada al realizar un test subintegrando con cuatro puntos de Gauss para las mallas de elementos

quadrilaterales bilineales y observar que los errores relativos fueron de $15.4\,\%$, $4.0\,\%$, $1.0\,\%$ y $0.6\,\%$ muy similares a los errores reportados anteriormente cuando se realiza integración exacta para las malla de 400, 1600, 6400 y 10000 elementos finitos respectivamente.

2.5. Conclusiones

En el presente Capítulo presentamos los aspectos teóricos fundamentales de los métodos empleados en el presente trabajo de tesis para el cálculo de la estructura de bandas de cristales fonónicos y metamateriales acústicos. El método descrito en la sección 2.3.1 se utiliza en el algoritmo presentado en el anexo C para realizar optimización topológica. El método descrito en la sección 2.3.2 es utilizado en el modelo numérico presentado en el anexo D para calcular las propiedades dinámicas efectivas de los cristales fonónicos y los metamateriales acústicos. El método descrito en la sección 2.3.3 se utiliza para obtener la relación de dispersión $\mathbf{k}(\omega)$ en la zona de bandgap y de esta manera poder determinar las propiedades dinámicas efectivas de los materiales en esta región. Los resultados obtenidos en la sección 2.4 muestran que los métodos asociados con el operador de Bloch y condiciones de borde periódicas, secciones 2.3.2 y 2.3.3, presentan una velocidad de convergencia inferior a la del método con elementos finitos tradicionales y condiciones de borde de Bloch, sección 2.3.1, por lo que, con estos métodos se deben usar mallas más finas y preferiblemente de elementos finitos rectangulares, el test donde se realiza subintegración con cuatro puntos de Gauss mejora marginalmente los resultados obtenidos con integración exacta, por lo que se desestima la hipótesis de que el problema de convergencia sea debido a un fenomeno de bloqueo inducido por el operador de Bloch (locking).

Capítulo 3

Diseño topológico de materiales elásticos con propiedades isotrópicas cercanas a sus límites teóricos

3.1. Introducción

En el presente Capítulo se presentan las metodologías numéricas desarrolladas para realizar el diseño inverso de la microestructura de compuestos elásticos bifásicos isotrópicos en tres dimensiones. Se estudian dos problemas particulares del diseño de micrarquitecturas de materiales con propiedades efectivas cercanas a sus límites teóricos. En el primer caso se desea desarrollar una microestructura cuyo comportamiento efectivo muestre un coeficiente de Poisson negativo. En el segundo caso se diseña una microestructura cuyo comportamiento efectivo muestre rigidez máxima. En problemas 3D los límites teóricos son determinados por los límites de Hashin-Shtrikmann (Hashin y Shtrikman, 1963).

En el anexo A se expone con mayor detalle el algoritmo empleado para obtener los resultados mostrados en el presente Capítulo.

3.2. Metodología

La metodología desarrollada para diseñar compuestos periódicos elásticos bifásicos 3D con propiedades efectivas isotrópicas cercanas a los límites teóricos es formulada como un problema de optimización topológica (Bendsøe y Sigmund, 2003) cuya implementación se basa en los conceptos de función *level-set* (Amstutz y Andrä, 2006) y de derivada topológica (Novotny y Sokołowski, 2012) cuya evaluación es una medida de la sensibilidad de un determinado funcional respecto a una perturbación singular infinitesimal del dominio, tales como, inserciones de agujeros o de inclusiones. Una característica fundamental de esta metodología es la imposición de simetrías de cristales preestablecidas a las topologías de las microarquitecturas diseñadas. La homogeneización computacional para evaluar las propiedades elásticas efectivas de los compuestos

se fundamenta en una técnica basada en Tranformada de Fourier (Eyre y Milton, 1999) la cual fue extendida para dominios no ortogonales (anexo A).

3.2.1. Elección del dominio de diseño Ω_μ. Imposición de simetrías de cristales

Una característica fundamental de la metodología presentada es la imposición de simetrías de cristales predefinidas a las microarquitectura diseñadas. La imposición de una simetría predefinida restringe el espacio de solución de nuestro problema, en consecuencia, impacta positivamente en la velocidad de convergencia del algoritmo de optimización topológica, pero, al limitar el espacio de búsqueda también condiciona qué tan extremas son las propiedades efectivas del material diseñado. En el artículo presentado en el anexo B se muestra un estudio sobre las simetrías más convenientes a utilizar de acuerdo al punto de los límites de HS a alcanzar (Hashin y Shtrikman, 1963), ver Figura 3.1. Las simetrías impuestas deben ser compatibles con la simetría elástica efectiva objetivo del problema. El principio de Neumann (Nye, 2006) vincula la simetría de la microarquitectura con la simetría de las propiedades físicas efectivas mostradas por el material.

3.2.2. Homogeneización computacional mediante un método basado en Transformada de Fourier

Las técnicas de homogeneización basadas en Transformada de Fourier para calcular el tensor de tensiones homogeneizado, $\mathbf{C}^h$, de compuestos con composición arbitraria fueron introducidas por Moulinec y Suquet (1998). Posteriormente, estas técnicas han sido mejoradas por diversos autores. Particularmente, Eyre y Milton (1999) presentaron un algoritmo que exhibe mejores propiedades de convergencia para la homogeneización de compuestos con mayor relación de contraste entre las fases constituyentes. Nuestra implementación se basa en este último algoritmo, el cuál, como se muestra en el anexo A fue extendido a dominios no ortogonales. En el artículo presentado en el anexo A se valida nuestra implementación de esta técnica comparando sus resultados y velocidad de convergencia contra un método basado en elementos finitos donde pudimos apreciar que en dependencia de los contrastes entre las fases, la técnica basada en Transformada de Fourier puede presentar un rendimiento superior.

3.3. Diseño de la microarquitectura de compuestos elásticos isotrópicos

3.3.1. Límites de las propiedades elásticas efectivas de compuestos isotrópicos bifásicos

Consideremos el conjunto de compuestos periódicos con propiedades elásticas isotrópicas efectivas y dos fases elásticas isotrópicas M_1 y M_2 cuyos módulos volumétricos son κ_1, κ_2, con

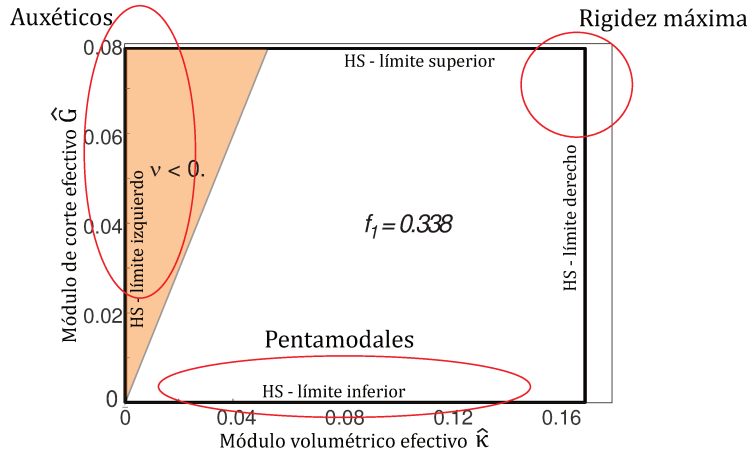

Figura 3.1: Límites teóricos de propiedades efectivas para compuestos 3D isotrópicos de dos fases según Hashin y Shtrikman (1963) (HS-bounds). Propiedades de las fases M_1 y M_2 son $\kappa_1 = 1.667$, $G_1 = 0.3571$, $\kappa_2 = \gamma\kappa_1$, $G_2 = \gamma G_1$, factor de contraste $\gamma = 10^{-4}$, fracción de volumen $f_1 = 0.338$.

$\kappa_2 < \kappa_1$, y módulos volumétricos G_1, G_2, con $G_2 < G_1$, respectivamente, y una fracción de volumen para M_1 igual a f_1. Entonces, las propiedades efectivas de estos compuestos, típicamente los módulos efectivos de volumen y corte, $\hat{\kappa}$ y $\hat{G}$, están acotados: $\hat{\kappa}^l \leq \hat{\kappa} \leq \hat{\kappa}^u$, $\hat{G}^l \leq \hat{G} \leq \hat{G}^u$, donde $\hat{\kappa}^u$ y $\hat{\kappa}^l$ son los límites superior e inferior del módulo volumétrico efectivo , y, $\hat{G}^u$ y $\hat{G}^l$ son los límites superior e inferior del módulo de corte efectivo. Estos límites se han estimado teóricamente con las expresiones derivadas de[1] Hashin y Shtrikman (1963) como:

$$\hat{\kappa}^u = \kappa_1 + \frac{1-f_1}{\frac{1}{\kappa_2-\kappa_1} + 3\frac{f_1}{3\kappa_1+4G_1}} \quad ; \quad \hat{\kappa}^l = \kappa_2 + \frac{f_1}{\frac{1}{\kappa_1-\kappa_2} + 3\frac{1-f_1}{3\kappa_2+4G_2}} \; ; \tag{3.1}$$

$$\hat{G}^u = G_1 + \frac{1-f_1}{\frac{1}{G_2-G_1} + \frac{6(\kappa_1+2G_1)f_1}{5G_1(3\kappa_1+4G_1)}} \quad ; \quad \hat{G}^l = G_2 + \frac{f_1}{\frac{1}{G_1-G_2} + \frac{6(\kappa_2+2G_2)(1-f_1)}{5G_2(3\kappa_2+4G_2)}} \; .$$

Para compuestos constituidos por dos fases caracterizadas por $\kappa_1 = 1.667$, $G_1 = 0.3571$, $\kappa_2 = \gamma\kappa_1$, $G_2 = \gamma G_1$, con factor de contraste $\gamma = 10^{-4}$, y fracción de volumen $f_1 = 0.338$, estos límites son: $\hat{\kappa}^u = 0.170$; $\hat{\kappa}^l = 2.8 \times 10^{-4}$; $\hat{G}^u = 0.789$; $\hat{G}^l = 7.3 \times 10^{-5}$ los cuales se muestran en la Fig. 3.1 y se denominan como los límites de Hashin-Shtrikmann (HS-bounds).

La Figura 3.1, además de identificar los límites de HS en el plano $(\widehat{\kappa}, \widehat{G})$, muestra una serie de propiedades efectivas límites admisibles que identifican compuestos que manteniendo una misma fracción de volumen del componente denso, poseen cualidades tales como :

i) Auxéticos, esto es, compuestos que experimentan un módulo de Poisson negativo.

ii) Pentamodales, denominados de este modo porque el tensor de elasticidad tiene cinco autovalores nulos (de ahí el nombre de pentamodal, y que se debe a un módulo de corte aproximadamente cero).

[1] Límites mas ajustados han sido reportados por Berryman y Milton (1988). Sin embargo, estos límites coinciden con los de Hashin-Shtrikmann cuando una de las fases es vacío.

iii) Los compuesto de máxima rigidez, con máximo valor de kappa y G respectivamente.

Cada uno de estos tipos de compuestos tienen aplicaciones relevantes en diversos tipos de problemas. Por ejemplo, materiales pentamodales se pueden utilizar para alcanzar camuflaje (acústico y mecánico), los materiales auxéticos para diversas utilidades estructurales, y obviamente los compuestos de máxima rigidez tienen también aplicaciones tecnológicas de valor evidente.

3.3.2. Problemas de optimización topológica

El objetivo es diseñar dos compuestos bifásicos con una fracción de volumen predefinida, cuyas propiedades efectivas son isotrópicas. Particularmente, buscamos obtener un material auxético y un material con rigidez máxima, (ver Figura 3.1).

Reintroduciendo la función característica $\chi(\mathbf{y})$ que determina la distribución de material dentro del dominio de diseño $\Omega_\mu = \Omega_\mu^1 \cup \Omega_\mu^2$, ver Figura 1.1.

$$\chi(\mathbf{y}) = \begin{cases} 1 & \forall \mathbf{y} \in \Omega_\mu^1 \\ 0 & \forall \mathbf{y} \in \Omega_\mu^2 \end{cases} . \tag{3.2}$$

La formulación matemática para el diseño del material auxético es:

$$\begin{aligned} &\min_{\chi} \kappa^h(\chi); \\ &\text{tal que:} \quad G^h(\chi) - G_j^* = 0 \\ &\qquad\qquad \mathbf{C}^h(\chi) \text{ is isotropic} \\ &\qquad\qquad f_1(\chi) - f_1^* = 0 \end{aligned} \tag{3.3}$$

con módulo de corte y fracción de volumen objetivos dados, $G^* = 0.03$ y $f_1^* = 0.338$, respectivamente.

Para el diseño del material con rigidez máxima:

$$\begin{aligned} &\max_{\chi} \; G^h(\chi); \\ &\text{tal que:} \quad \kappa^h(\chi) - \kappa_j^* = 0 \\ &\qquad\qquad \mathbf{C}^h(\chi) \text{ is isotropic} \\ &\qquad\qquad f_1(\chi) - f_1^* = 0 \end{aligned} \tag{3.4}$$

con módulo volumétrico y fracción de volumen objetivos $\kappa^* = 0.167$ y $f_1^* = 0.338$ respectivamente.

Las microestructuras con un sistema de simetría de cristales cúbico tienen respuestas elásticas efectivas con simetría cúbica (ver tabla A.1), por tanto, los coeficientes de sus matrices de elasticidad satisfacen las identidades: $C_{11}^h = C_{22}^h = C_{33}^h$; $C_{12}^h = C_{13}^h = C_{23}^h$; $C_{44}^h = C_{55}^h = C_{66}^h$.

Los coeficientes restantes son iguales a cero. Además, los coeficientes de cualquier tensor elástico isotrópico satisfacen las siguientes relaciones: *a)* $C^h_{44} = 2G$, *b)* $C^h_{12} + \frac{1}{3}C^h_{44} = \kappa$, *c)* $C_{11} + 2C_{12} = 3\kappa$, y *d)* $C_{11} - C_{12} + 3C_{44}/2 = 5G$; donde κ y G son los respectivos módulos volumétrico y de corte del material.

Por lo tanto, siempre que se garantice que la microestructura presenta un sistema de simetría cúbico y la isotropía del material sea un objetivo, los problemas de optimización topológica (3.3)–(3.4) pueden ser reescritos en términos de los coeficientes de la matriz de elasticidad como:

$$\min_{\psi \in C^0} (C^h_{12} + \frac{1}{3}C^h_{44}); \tag{3.5}$$

$$\text{tal que:} \quad h_1 = C^h_{11} - C^h_{12} + \frac{3}{2}C^h_{44} - 5G^* = 0$$
$$h_2 = C^h_{11} - C^h_{12} - C^h_{44} = 0$$
$$h_3 = f_1(\chi) - {f_1}^* = 0$$

$$\min_{\psi \in C^0} \; C^h_{44}; \tag{3.6}$$

$$\text{tal que:} \quad h_1 = C^h_{11} + 2C^h_{12} - 3\kappa^* = 0$$
$$h_2 = C^h_{11} - C^h_{12} - C^h_{44} = 0$$
$$h_3 = f_1(\chi) - {f_1}^* = 0$$

3.4. Resultados y discusión

3.4.1. Material auxéticos

Para este caso, el objetivo es lograr un compuesto isotrópico con una relación de Poisson mínima para un módulo de corte objetivo relativamente alto. La formulación del problema (3.5) es usada en este caso con un módulo de corte objetivo $G^* = 0.03$. Soluciones reportadas en el anexo B y por Andreassen y Lazarov (2014) muestran que es posible obtener coeficientes de Poisson más negativos usando módulos de corte objetivo G^* menores. Pero, el desafío fundamental en el diseño de nuevas microarquitecturas consiste en obtener materiales auxéticos con módulos de corte relativamente altos.

La microarquitectura diseñada ha sido resuelta con la imposición del grupo espacial $I23$ del sistema de simetría cubico de cristales. La Figura 3.2 muestra la topología optimizada, y sus propiedades elásticas efectivas se muestran en la Figura 3.3, punto A. Las componentes del tensor de elasticidad homogeneizado obtenido son: $C^h_{11} = C^h_{22} = C^h_{33} = 0.041500$, $C^h_{12} = C^h_{23} = C^h_{13} = -0.018739$ y $C^h_{44} = C^h_{55} = C^h_{66} = 0.060176$. Por tanto, el coeficiente de Poisson obtenido es de -0.82 y la fracción de volumen $f_1 = 0.3383$.

La anisotropía de las propiedades efectivas de un material con simetría cubica la cuantificamos

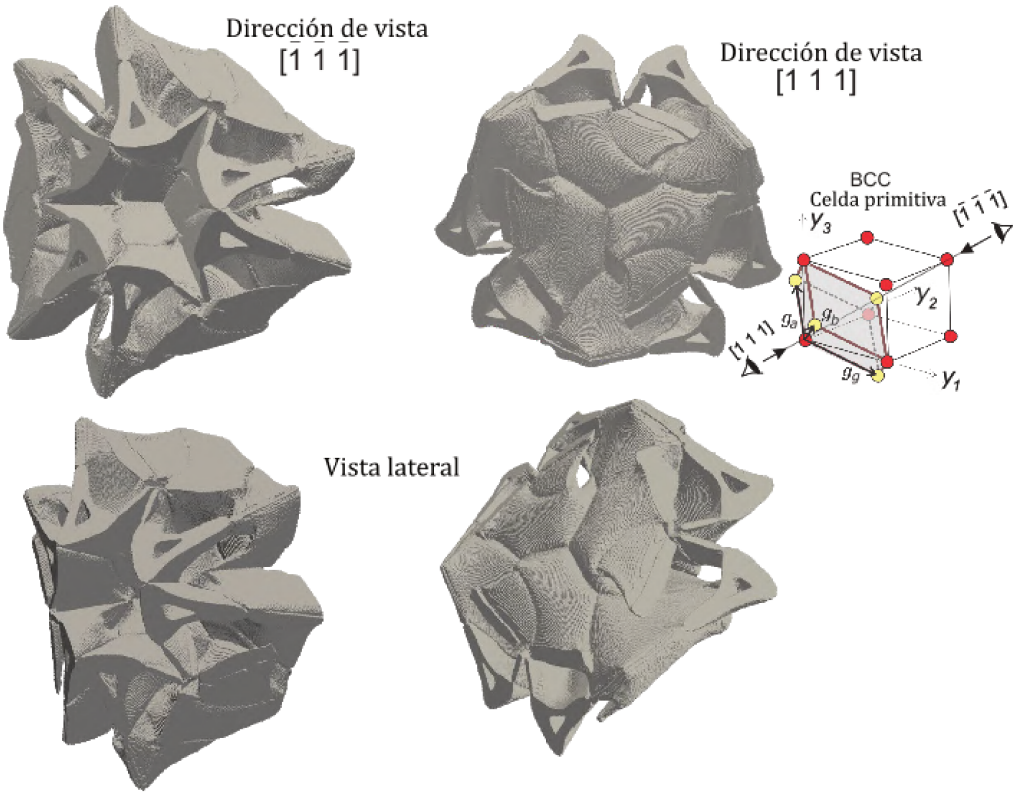

Figura 3.2: Celda primitiva del compuesto con propiedades elásticas correspondientes al punto A de la Figura 3.3. El grupo espacial impuesto es el $I23$. La celda primitiva es observada desde dos direcciones opuestas $[\bar{1}\bar{1}1]$ y $[111]$. El coeficiente de Poisson para esta microestructura es -0.82, el módulo de corte efectivo $\hat{G}^h = 0.0301$ y el módulo volumétrico efectivo $\hat{\kappa} = 0.0013405$.

mediante el coeficiente de Zener, $\xi = C^h_{44}/(C^h_{11} - C^h_{12})$, un valor de 1 indica que el $\mathbf{C}^h$ es isotrópico.

La solución presentada tiene un coeficiente de Zener, $\xi = 0.9989$, muy cercano a 1, y por tanto, la condición de isotropía se satisface casi exactamente.

3.4.2. Material con rigidez máxima

Para este caso, el objetivo es lograr un compuesto isotrópico con rigidez máxima, La formulación del problema es expresada mediante (3.6). El módulo volumétrico objetivo es $\kappa^* = 0.167$ cercano al limite superior, $\kappa^u = 0.1704$, estimado por los HS-bounds. El grupo espacial impuesto es el $Pm\bar{3}m$. El dominio de diseño es la celda primitiva de la red de Bravais cúbica simple.

Las componentes del tensor de elasticidad homogeneizado obtenido son: $C^h_{11} = C^h_{22} = C^h_{33} = 0.252523$, $C^h_{12} = C^h_{23} = C^h_{13} = 0.124672$ y $C^h_{44} = C^h_{55} = C^h_{66} = 0.127826$, con módulos volumétrico y de corte efectivos mostrados en la Figura 3.3, punto B, y un coeficiente de Zener $\xi = 0.9998$.

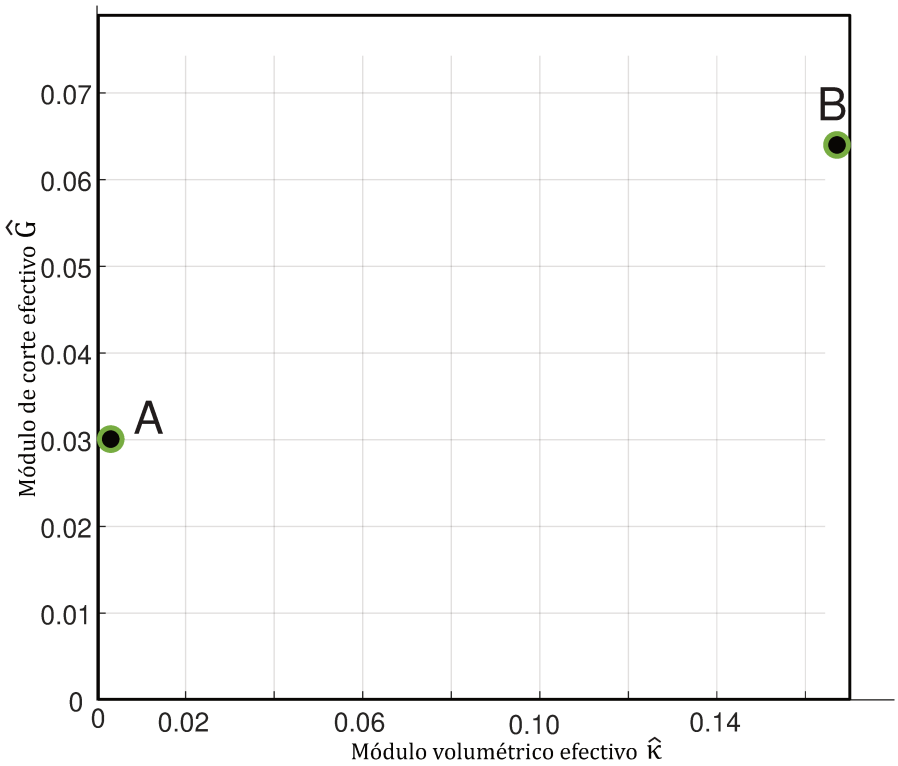

Figura 3.3: Los puntos A y B en el plano $(\hat{\kappa}, \hat{G})$ representan compuestos cuyas microarquitecturas que han sido obtenidos con una red de $256 \times 256 \times 256$ voxels. HS-bounds de las propiedades efectivas para compuestos bifásicos isotrópicos 3D (Hashin y Shtrikman, 1963).

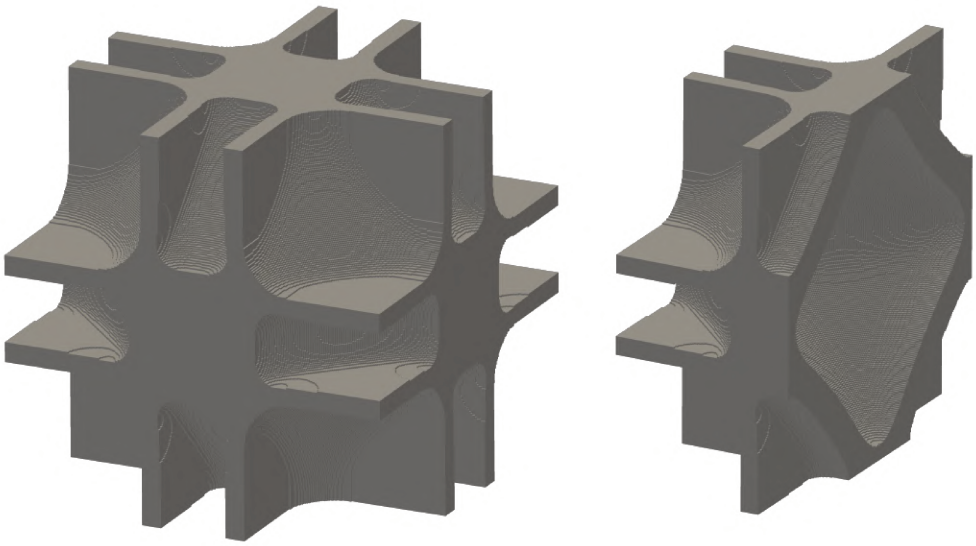

Figura 3.4: Topología del compuesto con rigidez máxima punto B de la Figura 3.3, diseñado con un grupo espacial $Pm\bar{3}m$. (a) Celda primitiva. (b) Corte medio de la microcelda.

3.5. Conclusiones

En este Capítulo se presentan dos ejemplos de diseño topológico. La metodología de optimización topológica es presentada en detalle en el anexo A. El objetivo en estos ejemplos fue obtener propiedades isotrópicas extremas, en el primer caso diseñar un material con coeficiente de Poisson negativo (ver figura 3.2) y en el segundo un material con rigidez máxima (ver Figura 3.4). Las propiedades efectivas de las topologías optimizadas muestran que las técnicas presentadas en el anexo A, combinadas con la imposición de simetrías de cristales predefinidas, concepto que ha sido especialmente utilizado y enfatizado por nuestro grupo de trabajo, conforman una metodología robusta para el diseño de metamateriales 3D con propiedades elásticas cercanas a sus límites teóricos.

En el artículo presentado en el anexo B se muestran diversos resultados, donde se exploran otros grupos espaciales de simetría cúbica y se realiza un análisis sobre la metodología de optimización topológica propuesta.

Capítulo 4

Diseño de cristales fonónicos y metamateriales acústicos

4.1. Introducción

En el presente Capítulo se presentan conceptos relacionados con el diseño de cristales fonónicos y de matemateriales acústicos. El algoritmo de optimización topológica se describe con detalle en el anexo C.

Se realiza la optimización topológica de cristales fonónicos 2D con redes cuadradas y hexagonales. Se estudia la influencia de las simetría p4mm y p6mm en el ancho máximo de los bandgaps obtenidos. Además, se realiza la optimización de metamateriales acústicos para los cuales evaluamos sus propiedades dinámicas efectivas mediante el modelo numérico presentado en el anexo D.

El objetivo es diseñar cristales fonónicos o materiales localmente resonantes en dos dimensiones maximizando el ancho absoluto del bandgap entre dos bandas de dispersión adyacentes. La relación de dispersión se calcula mediante los métodos descritos en el Capítulo 2.

4.2. Formulación del problema de optimización topológica

El objetivo es diseñar la microarquitectura de una estructura periódica, tal que, el ancho del bandgap entre dos bandas adyacentes, a priori seleccionadas, sea máximo.

Como se muestra en el Capítulo 2 la relación de dispersión $\omega(\mathbf{k})$ se obtiene resolviendo el sistema de ecuaciones discreto:

$$\left[\boldsymbol{K}(\mathbf{k}) - \omega^2 \boldsymbol{M}(\mathbf{k})\right] \boldsymbol{h}_r = \mathbf{0} \,, \tag{4.1}$$

donde $\boldsymbol{K}(\mathbf{k})$ y $\boldsymbol{M}(\mathbf{k})$ representan las respectivas matrices de rigidez y de masa luego de imponerse las condiciones de borde de Bloch (ver Capítulo 2).

Una forma de solucionar el sistema (4.1) es adoptar un valor para el vector de onda $\mathbf{k}$ y resolver

el problema de autovalores generalizados correspondiente. El número de frecuencias ω_j $(j = 1, 2, ...)$ y modos $\boldsymbol{h}_r^j$ resultado de resolver el problema (4.1) depende del número de grados de libertad.

Entonces, considerando un compuesto periódico con dos fases elásticas isotrópicas M_1 y M_2 se define la función característica:

$$\chi(\mathbf{y}) = \begin{cases} 1 & \forall \mathbf{y} \in \Omega_\mu^1 \\ 0 & \forall \mathbf{y} \in \Omega_\mu^2 \end{cases} . \tag{4.2}$$

que determina la distribución de material dentro del dominio de diseño Ω_μ.

Nuestro problema de optimización tiene como objetivo maximizar el ancho del bandgap absoluto ente dos bandas de dispersión adyacentes j y $j+1$. Este problema puede formularse como:

$$\begin{aligned} &\max_{\chi} \left(\min_{\mathbf{k}} \omega_{j+1}^2(\mathbf{k}, \chi) - \max_{\mathbf{k}} \omega_j^2(\mathbf{k}, \chi) \right); \\ &\text{tal que:} \quad \left(\boldsymbol{K} - \omega^2 \boldsymbol{M}\right) \boldsymbol{h}_r = \mathbf{0}, \quad \mathbf{k} \in L \end{aligned} \tag{4.3}$$

donde ω_{j+1} y ω_j son las frecuencias de las bandas $j+1$ y j, respectivamente, L es la frontera de la zona irreducible de Brillouin (Brillouin, 1953). La variable de diseño en (4.3) es χ.

En la figura 4.1 se muestran celdas unidad primitivas con simetría p4mm (Fig. 4.1a) y p6mm (Fig. 4.1d). Además, se muestra la primera zona de Brillouin (FBZ), la zona irreducible de Brillouin (IBZ) y el contorno de la zona irreducible de Brillouin correspondientes (Fig. 4.1b) y (Fig. 4.1e).

Para microarquitecturas con alta simetría (e.g., simetrías p4mm y p6mm) la probabilidad de que los puntos extremos de la estructura de bandas se encuentren en la frontera de la zona irreducible de Brillouin es muy alta (Maurin et al., 2018), por esta razón, durante del proceso de optimización, el analisis de la estructura de bandas puede ser restringido a vectores de onda $\mathbf{k} \in L$.

Como (4.3) es un problema de optimización maximin, donde los vectores de onda $\mathbf{k}$ para las frecuencias críticas pueden variar durante las iteraciones del algoritmo de optimización, siguiendo la denominada "extended bound formulation" (Bendsøe et al., 1983), (Olhoff, 1988), (Olhoff, 1989), (Olhoff y Du, 2013) y (Jensen y Pedersen, 2006), este problema es reformulado como:

$$\begin{aligned} &\min_{\beta_1, \beta_2, \chi} \beta_1 - \beta_2 \\ &\text{tal que:} \quad \mathfrak{f}_p := \beta_1 - \left[\omega_j^2(\mathbf{k}, \chi)\right]_p \geq 0, \quad p = 1, ..., N \\ &\qquad\quad \mathfrak{g}_q := \left[\omega_{j+1}^2(\mathbf{k}, \chi)\right]_q - \beta_2 \geq 0, \quad q = 1, ..., N \\ &\qquad\quad \left(\boldsymbol{K} - \omega^2 \boldsymbol{M}\right) \boldsymbol{h}_r = \mathbf{0}, \quad \mathbf{k} \in L_N \, , \end{aligned} \tag{4.4}$$

donde β_1 y β_2 son variables independientes adicionales que representan los límites superior e inferior del cuadrado de las frecuencias ω_j^2 y ω_{j+1}^2, respectivamente. Las variables β_1 y β_2 no son

parámetros geométricos ni de forma, por lo tanto, no dependen de la topología.

El contorno de la zona irreducible de Brillouin, definido en la red recíproca, es discretizado en N puntos, por lo tanto, para construir la relación de dispersión, $\omega(\mathbf{k})$, necesitamos resolver (4.1) N veces. Los N vectores de onda, $\mathbf{k}$, definen el conjunto L_N

La notación $\left[\omega_j^2(\mathbf{k},\chi)\right]_p$ significa que la frecuencia ω_j de la banda j es evaluada en el punto p del conjunto L_N. Análogamente, La notación $\left[\omega_{j+1}^2(\mathbf{k},\chi)\right]_q$ significa que la frecuencia ω_{j+1} de la banda $j+1$, adyacente a la banda j, es evaluada en punto q del conjunto L_N.

El problema de optimización 4.4 es resuelto mediante un algoritmo basado en los conceptos de función level-set y de derivada topológica en combinación con un método Lagrangiano aumentado. Este algoritmo es presentado en detalle en el anexo C.

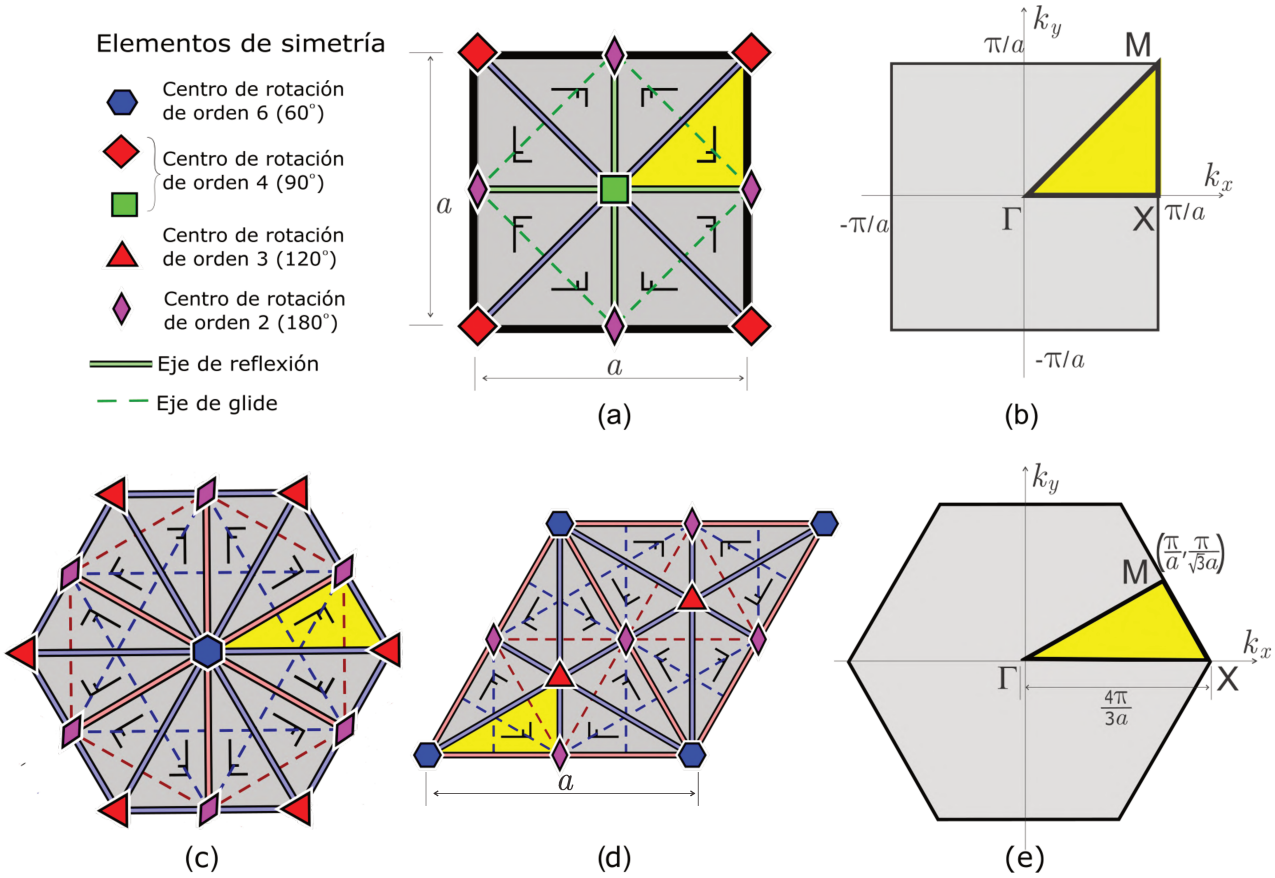

Figura 4.1: Cristales fonónicos con simetría p4mm y p6mm. ((a), (d)) Elementos de simetría y unidad asimétrica (en amarillo) de celdas unidad primitivas con simetría p4mm y p6mm.(c) Red hexagonal. ((b), (e)) Celda unidad de la red reciproca. Primera zona de Brillouin (FBZ en gris) y zona irreducible de Brillouin (IBZ en amarillo); contorno de la IBZ $[\Gamma - X - M - \Gamma]$.

4.3. Diseño de cristales fonónicos

En esta sección se presentan los resultados de la optimización topológica para cristales fonónicos compuestos por dos fases sólidas, M_1 y M_2. La optimización topológica se realiza para mi-

croestructuras con tipos de red cuadrada o hexagonal, y constante de red $a = 0.01\ m$. $E_1 = 91.15\ GPa$ y $\rho_1 = 19500\ kg/m^3$, son el módulo de Young y la densidad de la fase rígida M_1. La fase blanda M_2 es caracterizada por un módulo de Young, $E_2 = 4.9\ GPa$ y una densidad $\rho_2 = 1200\ kg/m^3$; $\nu = 0.52$ es el coeficiente de Poisson plano de ambas fases. El eje de frecuencia en los diagramas de bandas, mostrados en las figuras 4.2 y 4.3, son normalizados dividiendo por el factor $2\pi C_A/a$ que representa, multiplicada por 2π, la inversa del tiempo que tarda la onda en atravesar una celda de longitud a, donde $C_A = \sqrt{\mu_1/\rho_1}$ es la velocidad transversal de onda, con μ_1 igual al módulo de corte de la fase M_1.

Para realizar la optimización, el contorno de la zona irreducible de Brillouin se discretizó en 27 puntos, ver Figura 4.1. Las celdas unidad con red hexagonal se optimizaron con una malla de 4872 elementos finitos triangulares. Para las celdas unidad con red cuadrada se realizo un proceso de refinamiento de malla de dos etapas, se comenzó con una malla de 2048 elementos finitos triangulares y una vez alcanzada la convergencia se realiza un proceso de refinamiento de malla, para así, comenzar una segunda etapa de optimización en una malla de 8192 elementos finitos.

4.3.1. Bandgaps para ondas fuera del plano (outplane waves)

En este ejemplo, el objetivo de la optimización es encontrar el bandgap máximo para ondas fuera del plano (ver Capítulo 2). La figura 4.2 presenta la microarquitectura de los cristales fonónicos diseñados mediante optimización topológica, y sus estructuras de bandas correspondientes, para celdas unidad con simetría p4mm (Fig. 4.2a) y p6mm (Fig. 4.2b). El objetivo es maximizar los bandgaps para la 1ra (bandgap entre 1ra y 2da bandas), 2da (bandgap entre 2ra y 3ra bandas) y 3ra (bandgap entre 3ra y 4ta bandas) bandas. Las microarquitecturas de los cristales fonónicos son mostradas en un ensamble de 3x3 celdas unidad. Las celdas unidad primitiva se delimitan con un contorno de líneas rojas.

Las estructuras de bandas evidencian que se logra generar bandgaps para todos los casos analizados. El bandgap relativo, $\Delta\omega_r = 2\frac{min(\omega_{j+1}) - max(\omega_j)}{min(\omega_{j+1}) + max(\omega_j)}$, máximo de 117.43 % se generó para la 1ra banda, en la estructura con red hexagonal, mientras que el menor bandgap de 80.80 % se presenta para la 3ra banda en la estructura con red cuadrada. Comparando los bandgaps generados para cada tipo de red, la mayor diferencia se encuentra en la 3ra banda donde el bandgap generado para la estructura con red hexagonal es de 116.63 %, un 35.83 % mayor al generado para la red cuadrada, para la 1ra banda el bandgap de la red hexagonal también es mayor, en un 10.52 %, al de la red cuadrada. El caso contrario ocurre para la 2da banda donde el bandgap generado para la estructura con red cuadrada es mayor que el de la red hexagonal en un 18.72 %. Por tanto, el tipo de red más adecuado para utilizar en el diseño de cristales fonónico depende de para cuál banda queremos generar el bandgap. Estos resultados son comparables con los reportados por Li et al.

(2016) para problemas similares y muestran que el tipo de red tiene un impacto importante en la formación y tamaño del bandgap.

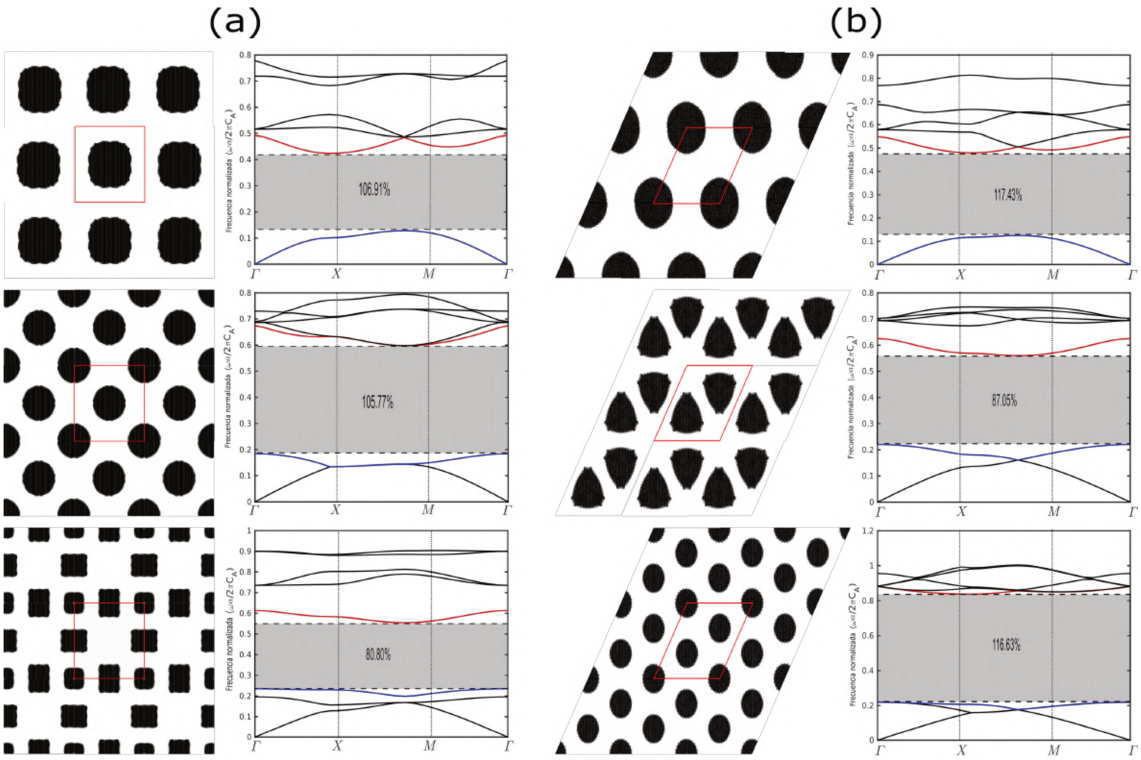

Figura 4.2: Microestructuras de cristales fonónicos diseñados y sus estructuras de banda para ondas fuera del plano (outplane waves). (a) Celda unidad (cuadrado rojo) con simetría p4mm y bandgaps entre la 1ra-2da, 2da-3ra y 3ra-4ta bandas. (b) Celda unidad (paralelogramo rojo) con simetría p6mm y bandgaps entre la 1ra-2da, 2da-3ra y 3ra-4ta bandas.

4.3.2. Bandgaps para ondas en el plano (inplane waves)

Este ejemplo tiene como objetivo optimizar los bandgaps para ondas en el plano (ver Capítulo 2), donde existe un acoplamiento entre las ondas longitudinales y transversales que se propagan en el plano.

Las microarquitecturas resultado de la optimización topológica y sus estructuras de bandas se muestran en la figura 4.3. Para este ejemplo el objetivo es maximizar los bandgaps para la 3ra (bandgap entre 3ra y 4ta bandas), 5ta (bandgap entre 5ta y 6ta bandas) y 6ta (bandgap entre 6ta y 7ma bandas) bandas.

El bandgap relativo máximo de 90.24 % se generó para la 3ra banda, en la estructura con red hexagonal, mientras que el menor bandgap de 52.38 % corresponde a la 5ta banda de la estructura con red cuadrada. Comparando los bandgaps generados para cada tipo de red, la mayor diferencia se encuentra en la 6ta banda donde el bandgap generado para la red cuadrada es de 87.47 %, un 10.21 % mayor que el generado para la red hexagonal. Sin embargo, para la 3ra y 5ta banda el bandgap obtenido para las estructuras con red hexagonal es mayor al obtenido para las estructuras

con red cuadrada, por tanto, al igual que para la ondas fuera del plano, el tipo de red más adecuado para utilizar en el diseño de cristales fonónicos depende de la banda para la que queremos generar el bandgap, lo que muestra, la importancia del tipo de red para el diseño de cristales fonónicos.

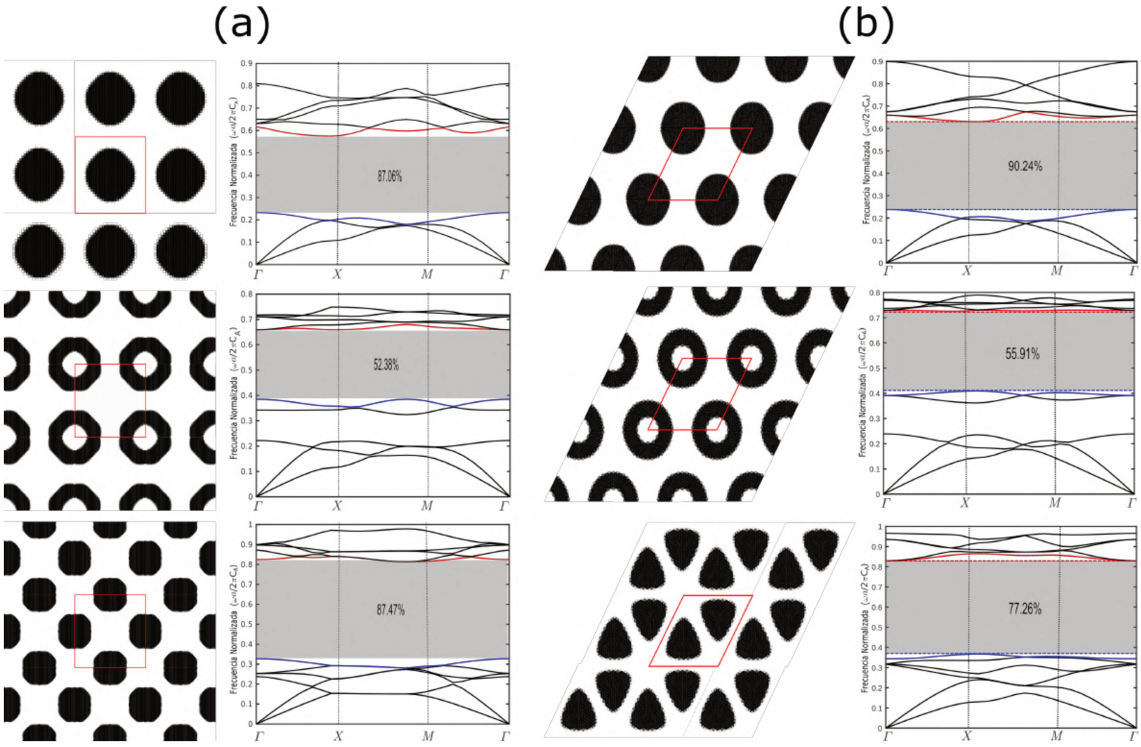

Figura 4.3: Microestructuras de cristales fonónicos diseñados y sus estructuras de banda para ondas en el plano (inplane waves). (a) Celda unidad (cuadrado rojo) con simetría p4mm y bandgaps entre la 3ra-4ta, 5ta-6ta y 6ta-7ma bandas. (b) Celda unidad (paralelogramo rojo) con simetría p6mm y bandgaps entre la 3ra-4ta, 5ta-6ta y 6ta-7ma bandas.

4.4. Diseño de metamateriales acústicos

Un metamaterial acústico es usualmente un material periódico con la particularidad de que exhibe resonancia local. A diferencia de los bandgaps generados por el fenómeno de dispersión de Bragg, donde los bandgaps solo ocurren a longitudes de onda del orden de las dimensiones de la celda unidad, para materiales localmente resonantes se genera un bandgap en el rango de frecuencias cercanas a la frecuencia de resonancia del resonador local, por lo que no depende de la longitud de onda, lo que permite abrir bandgaps a bajas frecuencias y en estructuras con celda unidad de dimensiones menores que la longitud de la onda acústica/elástica. Este mecanismo de resonancia local en estructuras sub-longitud de onda hace posible la obtención de materiales con propiedades dinámicas efectivas doble negativas (Liu et al., 2000), (Liu et al., 2005).

La propiedad de periodicidad, si bien no es requerida para materiales localmente resonantes, nos permite, mediante el modelado de la celda unidad, determinar la relación de dispersión y evaluar las propiedades dinámicas de los metamateriales acústicos.

En la presente sección se presenta el diseño de un material localmente resonante 2D, para el

cual se evaluaron las propiedades dinámicas efectivas mediante el modelo numérico presentado el anexo D. Conceptualmente, la metodología para optimizar la microesctructura de un material resonante, no difiere del caso en que las bandas se abren por efecto Bragg. Así, el método de optimización permanece esencialmente idéntico al explicado previamente y que es detallado en el Anexo C.

El metamaterial acústico diseñado consta de dos fases sólidas, M_1 y M_2, ver la Figura 4.4a. La optimización topológica se realiza para una celda unidad con simetría p4mm de dimensión $a = 0.01\ m$. Para facilitar el análisis se fijaron los grados de libertad verticales $u_y = 0$ y con el objetivo de favorecer la generación del mecanismo resonante en el contorno de la celda se fijaron franjas de material M_1 con espesor $s = 5 \cdot 10^{-4} m$, ver Figura 4.4a. $E_1 = 227.26\ GPa$ y $\rho_1 = 7780\ kg/m^3$, son el módulo de Young y la densidad de la fase rígida M_1. La fase blanda M_2 es caracterizada por un módulo de Young, $E_2 = 7.25\ GPa$ y una densidad $\rho_2 = 1180\ kg/m^3$; $\nu = 0.30$ es el coeficiente de Poisson de ambas fases.

La optimización se realizó en dos etapas, se comenzó con una malla de 2048 elementos finitos triangulares y una vez alcanzada la convergencia se realizo un proceso de refinamiento de malla, para así, comenzar una segunda etapa de optimización en una malla de 8192 elementos finitos. El contorno de la zona irreducible de Brillouin, ver Figura 4.1, se discretizó en 27 puntos. Adicionalmente, la variable β_1 se acoto superiormente con el valor de 130 kHz.

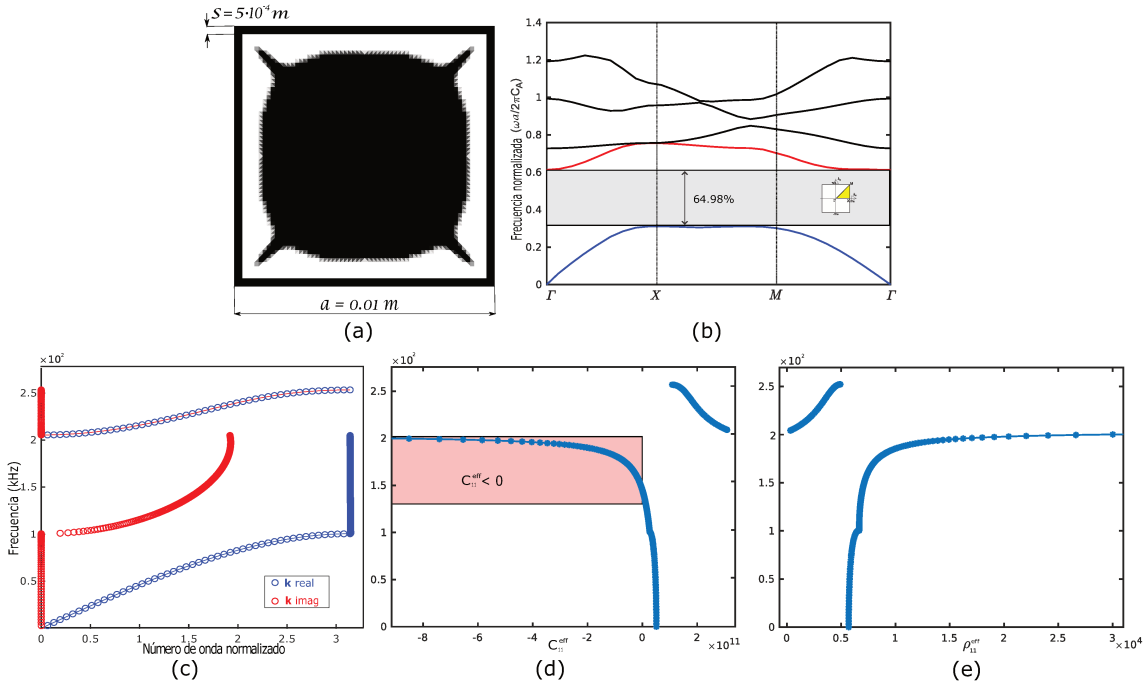

Figura 4.4: Propiedades dinámicas efectivas del material localmente resonante. (a) Microestructura optimizada de la celda unidad. (b) Estructura de bandas normalizada (c) Plot de frecuencia vs número de onda normalizado en el segmento $[\Gamma - X]$. (d) Dependencia del coeficiente de elasticidad efectivo, C_{11}^{eff}, con la frecuencia. (e) Dependencia de la densidad efectiva x-direccional, ρ_{11}^{eff}, con la frecuencia.

En la Figuras 4.4a y 4.4b se muestra la topología optimizada y la estructura de bandas computada en todo el contorno de la zona irreducible de Brillouin.

Como consecuencia de la presencia de resonancias locales la primera curva de dispersión se divide en dos ramas originando un bandgap centrado en la frecuencia de resonancia del resonador local, ver Figura 4.4c. Para calcular las bandas se tomaron 50 valores de número de onda $\mathbf{k}$ pertenecientes al segmento $[\Gamma - X]$ del contorno de la zona irreducible de Brillouin. Para estudiar la región del bandgap se utiliza el método descrito en 2.3.3 que nos permite mediante la solución del problema de autovalores (2.28) para una frecuencia ω obtener la relación $\mathbf{k}(\omega)$ correspondiente. La región del bandgap, fue discretizada en 198 puntos, $\omega \in (\omega_1^{max}), \omega_2^{min})$, donde ω_1^{max} y ω_2^{min} son los valores máximo y mínimo de frecuencias para la primera y segunda bandas respectivamente. Como se mostró en el Capítulo 2, para resolver el problema (2.28) además de la frecuencia debemos fijar la dirección de propagación de la onda $\mathbf{\Phi}$ ($\mathbf{k} = k\mathbf{\Phi}$), en particular, nuestro estudio se restringe a ondas que se propagan de forma horizontal, $k_y = 0$, por tanto, la dirección de propagación de la onda esta determinada por el vector $\mathbf{\Phi} = [1, 0]$. El bandgap determina un rango de frecuencias prohibidas para las cuales no se transmite la onda, por lo cual, los valores del número de onda $\mathbf{k}$ en la región de bandgap son complejos, ver Figura 4.4c. Para seleccionar la magnitud del número de onda, k_i, con $i \in \mathbb{Q} = \{1, 2...M\}$, donde M es el cardinal del conjunto de soluciones posibles al problema de autovalores (2.28), se sigue un criterio con el objetivo de conservar lo mejor posible su continuidad, el cual se formula como sigue:

$$i \in \mathbb{Q} : \|\{\hat{k}_i^r\} - \pi\| < \|\{\hat{k}_l^r\} - \pi\|, \ \forall l \in \mathbb{Q}, \ l \neq i. \tag{4.5}$$

donde $\hat{k}^r = a \cdot Real\,[k]$ es la parte real normalizada de la magnitud del vector de onda. En la Figura 4.4c se observa que la continuidad del vector de onda se conserva hasta la frecuencia que da inicio a la segunda banda. Las Figuras 4.4d y 4.4e muestran la dependencia con la frecuencia de las propiedades efectivas, x-direccionales, de elasticidad C_{11}^{eff} y de densidad ρ_{11}^{eff} respectivamente. Dichas propiedades fueron evaluadas mediante el modelo numérico desarrollado en el anexo D. Se puede apreciar que para gran parte de la región de bandgap, en el rango de $145\ kHz$ a $200\ kHz$ aproximadamente, el coeficiente elástico C_{11}^{eff} es negativo, mientras que la densidad efectiva ρ_{11}^{eff}, dentro o fuera del bandgap, siempre es positiva. La continuidad del vector de onda, ilustrada en al Figura 4.4c, también se observa para las propiedades efectivas. En la vecindad de la frecuencia que da origen a la segunda banda de dispersión el coeficiente de elasticidad C_{11}^{eff} y la densidad ρ_{11}^{eff} tienden asintoticamente a $-\infty$ y $+\infty$ respectivamente.

En la Figura 4.5a se muestra un segundo resultado de optimización topológica. En este caso el resonador presenta una forma cuadrada, más simple que el del resultado mostrados en la Figura 4.4a. El bandgap absoluto, $\Delta\omega_a = min(\omega_{j+1}) - max(\omega_j)$, obtenido es aproximadamente de

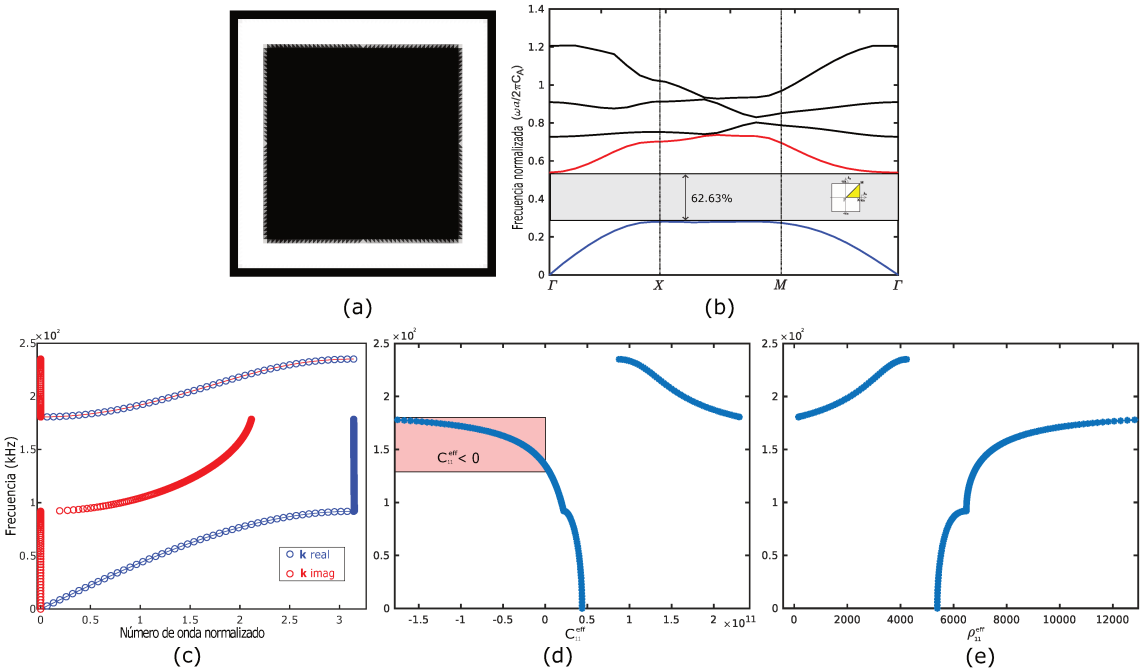

Figura 4.5: Propiedades dinámicas efectivas del material localmente resonante. (a) Microestructura optimizada de la celda unidad. (b) Estructura de bandas normalizada (c) Plot de frecuencia vs número de onda normalizado en el segmento $[\Gamma - X]$. (d) Dependencia del coeficiente de elasticidad efectivo, C_{11}^{eff}, con la frecuencia. (e) Dependencia de la densidad efectiva x-direccional, ρ_{11}^{eff}, con la frecuencia.

$861\ kHz$, inferior al generado por la microestructura mostrada en el Figura 4.4a que es de unos $1000\ kHz$. Los bandgap relativos, $\Delta\omega_r = 2\frac{min(\omega_{j+1}) - max(\omega_j)}{min(\omega_{j+1}) + max(\omega_j)}$, son del $64.98\,\%$ para el primer resultado y del $62.63\,\%$ para el segundo, ver Figuras 4.4b y 4.5b. Como era de esperar la propiedades efectivas tienen un comportamiento muy similar para ambos resultados,ver Figuras 4.4d , 4.4e, 4.5d y 4.5e, con la particularidad que para el segundo caso la frecuencia resonanante es mas baja, por lo que la región de bandgap comienza a frecuencia de aproximadamente unos $94\ kHz$ y se extiende hasta los $180\ kHz$ mientras que para el primer caso la región de bandgap se comprende en el rango de 104 a $204\ kHz$ aproximadamente.

Desafortunadamente para ninguna de las estructuras optimizadas pudimos obtener propiedades efectivas doble negativas. Finalmente, como un ejemplo adicional de validación del modelo numérico presentado en el anexo D se presenta la evaluación de las propiedades efectivas de un laminado compuesto por tres fases materiales igual al presentado por Srivastava y Nemat-Nasser (2014) para el cual los autores obtuvieron propiedades dinámicas efectiva doble negativas sobre la segunda banda de dispersión.

En la Figura 4.6a se muestra la celda unidad del compuesto trifásico de $4.3\ mm$ de espesor, diseñado para que la fase M_3 con módulo de Young, $E_3 = 300\ GPa$ y densidad, $\rho_3 = 8000\ kg/m^3$ de $0.4\ mm$ de espesor resone localmente. Las propiedades materiales y el espesor total de la fase M_1 son $E_1 = 8\ GPa$, $\rho_1 = 1180\ kg/m^3$ y $2.9\ mm$ respectivamente, mientras que los de la fase blanda M_2 son $E_1 = 0.02\ GPa$, $\rho_1 = 1100\ kg/m^3$ y $1\ mm$ respectivamente. Los des-

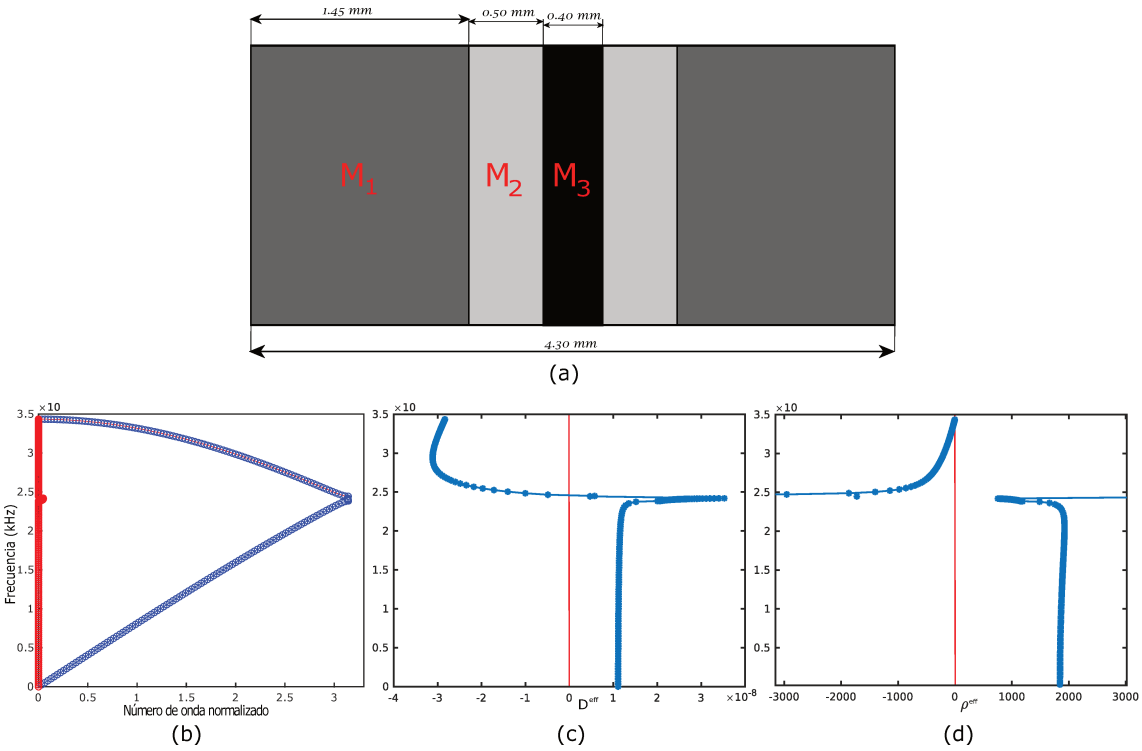

Figura 4.6: Propiedades dinámicas efectivas de un laminado compuesto por tres fases. (a) Representación de la celda unidad. (b) Plot de frecuencia vs número de onda normalizado. (c) Dependencia de la compliance efectiva, $D^{eff} = 1/E^{eff}$, con la frecuencia. (d) Dependencia de la densidad efectiva, ρ^{eff}, con la frecuencia.

plazamientos u_y se han restringido en este análisis, por lo que el problema se puede considerar 1D.

En las Figuras 4.6c y 4.6d se muestra la dependencia con la frecuencia de la compliance efectiva, D^{eff}, y de la densidad efectiva, ρ^{eff}, respectivamente. Propiedades exóticas como indice de refracción negativo se encontrarían para el rango de frecuencias que comprende a la segunda banda, donde la compliance y densidad efectivas son negativas.

Finalmente, los resultados obtenidos por nuestro modelo de homogeneización dinámica, ver anexo D, presentan una fuerte concordancia con los reportados por Srivastava y Nemat-Nasser (2014).

4.5. Conclusiones

En este Capítulo aplicamos la metodología de optimización topológica descrita en el anexo C para el diseño de cristales fonónicos y metamateriales acústicos.

Los resultados obtenidos muestran que la elección del tipo de red es fundamental para obtener estructuras con bandgaps máximos. Para futuros estudios, y siguiendo un paralelismo con el análisis efectuado en el diseño de microestructuras con propiedades elásticas extremas (anexo B), se propone explorar distintos grupos de plano de simetría (e.g p4gm, p31m, etc) para evaluar la

magnitud de su impacto en el diseño de cristales fonónicos.

Mediante el algoritmo presentado en el anexo C se diseñaron materiales localmente resonantes. El modelo de homogeneización presentado en el anexo D fue usado para determinar las propiedades dinámicas efectivas de los metamateriales acústicos diseñados. En la región de bandgap el C_{11}^{eff} se hace negativo mientras que el ρ_{11}^{eff} se mantiene positivo lo cual es coincidente con una región de prohibición de propagación de ondas. Lamentablemente, solo con el objetivo de maximizar el bandgap, no se logro obtener un material con propiedades dinámicas efectivas doble negativas. La doble negatividad solo la pudimos observar al evaluar la propiedades de un compuesto laminado propuesto por Srivastava y Nemat-Nasser (2014). Para futuros estudios se propone estudiar el acoplamiento del modelo numérico descrito en el anexo D al proceso de optimización topológica con el objetivo de diseñar materiales con propiedades exóticas como índice de refracción negativo.

Capítulo 5

Conclusiones

5.1. Contribuciones

En esta tesis se presentan dos algoritmos de optimización topológica, uno para diseñar metamateriales mecánicos y otro para el diseño de cristales fonónicos, basados en los conceptos de función level-set y de derivada topológica. El desarrollo de estos algoritmos ha insumido un esfuerzo notable, considerando ya sea la implementación de algoritmos de optimización que, aunque estándar, debieron ser adaptados al problema en cuestión y testeados debidamente; como también a la correcta implementación de las derivadas topológicas como entidad matemática adecuadas a cada problema. En particular se enfatiza el esfuerzo invertido en el desarrollo de la derivada topológica de las frecuencias propias de microceldas que se utilizan en el modelo de optimización de ancho de bandgaps. Si bien las expresiones de estas derivadas topológicas se publicaron previamente por autores como Amari y Amstutz, se debió realizar un gran esfuerzo a nivel conceptual para adaptar dichas expresiones a nuestro problema en particular. Las diferentes expresiones de las derivadas topológicas, sea para los casos con autovalor único o múltiples, se han verificado numéricamente.

Para el diseño de los metamateriales mecánicos se optimizó la topología de la microestructura con el objetivo de obtener materiales, 2D y 3D, con propiedades elásticas efectivas cercanas a los límites teóricos. Se estudió el efecto de la imposición de distintas simetrías de cristales en el diseño de los materiales donde se mostró que las propiedades máximas/mínimas obtenidas dependen fuertemente de la simetría a priori definida. Se mostró que la elección de la simetría más adecuada depende de qué punto de los límites de Cherkaev-Gibiansky, caso 2D, o de Hashin-Strikman, caso 3D, definidos en del plano $(\widehat{\kappa}, \widehat{G})$ se predefine como objetivo alcanzar. Para aproximarse al límite derecho del plano, máximo $\widehat{\kappa}$, un material con alto grado de simetría resulta el más apropiado. Al contrario, si el objetivo es aproximarse al límite izquierdo resulta mas conveniente usar otros tipos de simetrías.

Se mostró que el diseño de la micoarquitectura mediante la solución de problemas de opti-

mización topológica, combinado con la imposición de simetrías de cristales predefinidas es una metodología viable y robusta para diseñar metamateriales con propiedades elásticas efectivas cercanas a los limites teóricos.

En los problemas 3D la homogeneización se realizo con una técnica basada en FFT, la cuál fue extendida a sistemas de coordenadas no ortogonales para permitir el análisis de celdas unidad con forma de prismas no rectangulares. Además, se mostró que esta técnica en función del factor de contraste entre las fases materiales constituyentes puede ser mas eficiente que la técnica análoga basada en el método de elementos finitos.

Para el diseño de cristales fonónicos el objetivo de la optimización topológica fue obtener la microestructura del material tal que el bandgap absoluto entere dos bandas de dispersión adyacentes sea máximo. El algoritmo de optimización topológica desarrollado, acorde al mejor conocimiento del autor, es el primero basado en los conceptos de derivada topológica y función level-set propuesto para realizar el diseño de cristales fonónicos maximizando las regiones de bandgap.

Se muestra que para el cálculo de la estructura de bandas del material mediante el método de elementos finitos, cuando sea posible, la metodología preferida es usar condiciones de borde de Bloch con matrices de elemento finitos tradicionales pues este método presenta las mejores propiedades de convergencia. Además, las expresiones analíticas de la derivada topológica de la frecuencias, ω, son comprobadas numéricamente.

Finalmente, se propone un modelo de homogeneización basado en elementos finitos para evaluar las propiedades elastodinámicas efectivas de metamateriales acústicos que quizás podría ser usado como una herramienta más para realizar optimización topológica. Este modelo fue corroborado mediante una exhaustiva comparación con los resultados de modelos basados en ecuaciones integrales reportados en la literatura.

5.1.1. Resumen de contribuciones presentadas en esta Tesis

- Resolución de diseño inverso de microarquitecturas de materiales periódicos con propiedades mecánicas extremas.
- Desarrollo e implementación de un algoritmo de optimización basado en un esquema de lagrangiano aumentado con restricciones de igualdad para resolver problemas de homogeneización inversa.
- Construcción de una base de datos de microestructuras 3D con propiedades isotrópicas cercanas a los límites teóricos. http://dx.doi.org/10.17632/cc2hgr9kvh.1.
- Extensión a dominios no ortogonales de algoritmos de homogeneización basados en Transformada de Fourier.

- Evaluación de las propiedades de convergencia de los distintos métodos basados en elementos finitos para el calculo de la relación de dispersión, $\omega(\mathbf{k})$.

- Desarrollo, implementación y verificación numérica de la derivada topológica de los autovalores para el problema acústico.

- Desarrollo e implementación de un algoritmo de optimización para diseñar cristales fonónicos y materiales localmente resonantes, basado en un esquema de lagrangiano aumentado con restricciones de desigualdad, con el objetivo de maximizar los bandgaps.

- Desarrollo de un modelo de homogeneización para evaluar las propiedades dinámicas efectivas de materiales con microestructuras periódicas.

5.2. Publicaciones científicas derivadas

A continuación se listan las contribuciones científicas derivadas directa o indirectamente de los estudios y desarrollos abordados durante la presente Tesis.

5.2.1. Publicaciones en revistas

1. N. Rossi, R. Yera, C.G. Méndez, S.Toro, A.E. Huespe. *Numerical technique for the 3D microarchitecture design of elastic composites inspired by crystal symmetries*. Computer Methods in Applied Mechanics and Engineering. DOI: 10.1016/j.cma.2019.112760

2. R. Yera, N. Rossi Cabral, C.G. Méndez, A.E. Huespe. *Topology design of 2D and 3D elastic material microarchitectures with crystal symmetries displaying isotropic properties close to their theoretical limits*. Applied Materials Today. DOI: 10.1016/j.apmt.2019.100456

3. R. Yera, L. Forzani, C. G. Méndez, A. E. Huespe. *A topology optimization algorithm based on topological derivative and level set function for designing phononic crystals*. Engineering Computations. DOI: 10.1108/EC-06-2021-0352

4. R. Yera, C. G. Méndez, P.J. Sánchez, A. E. Huespe. *Effective properties of periodic media in elastodynamics problems*. Computer Methods in Materials Science. DOI: 10.7494/cmms.2021.3.0753

5.2.2. Base de Datos

Las microestructuras 3D obtenidas con propiedades efectivas cercanas a los límites teóricos fueron estandarizadas en un formato ".st" y puestas a disposición en un repositorio de acceso público.

- R. Yera, N. Rossi, C. Méndez, A.E. Huespe, Three-Dimensional Material Microstructures Dataset Displaying Extreme Isotropic Elastic Properties, Mendeley Data, v1, 2019, DOI: 10.17632/cc2hgr9kvh.1.

5.2.3. Publicaciones y presentaciones en congresos

1. R. Yera, N. Rossi, S. Toro, A.E. Huespe. *Análisis de eficiencia de técnicas tipo FEM y FFT para homogeneización de materiales.* MECOM 2018. Tucumán, Argentina.

2. N. Rossi, R. Yera, C.G. Méndez, A.E. Huespe. *Use of crystallographic symmetries for topology design of extreme isotropic elastic metamaterials.* ENIEF 2019. Santa Fe, Argentina.

3. R. Yera, C.G. Méndez, A.E. Huespe. *Phononic bandgap materials design by means of topology optimization.* ENIEF 2019. Santa Fe, Argentina.

4. R. Yera, N. Rossi, L. Forzani C.G. Méndez, A.E. Huespe. *Topological design of metamaterials with crystal symmetries for acoustic and mechanical applications.* WCCM 2020. Paris, Francia.

5. R. Yera, C.G. Méndez, A.E. Huespe. *Phononic bandgap materials design by means of topology optimization.* MECOM 2021. Resistencia, Argentina.

Bibliografía

Amigo R., Giusti S., Novotny A., Silva E., y Sokolowski J. Optimum design of flextensional piezoelectric actuators into two spatial dimensions. *SIAM Journal on Control and Optimization*, 54(2):760–789, 2016.

Amstutz S. y Andrä H. A new algorithm for topology optimization using a level-set method. *Journal of Computational Physics*, 216(2):573–588, 2006.

Amstutz S., Giusti S., Novotny A., y de Souza Neto E. Topological derivative for multi-scale linear elasticity models applied to the synthesis of microstructures. *International Journal for Numerical Methods in Engineering*, 84(6):733–756, 2010.

Amstutz S., Novotny A., y de Souza Neto E. Topological derivative-based topology optimization of structures subject to drucker–prager stress constraints. *Computer Methods in Applied Mechanics and Engineering*, 233:123–136, 2012.

Andreassen E. y Lazarov B.S.and Sigmund O. Design of manufacturable 3D extremal elastic microstructure. *Mechanics of Materials*, 69(1):1–10, 2014.

Babaee S., Shim J., Weaver J., Chen E., Patel N., y Bertoldi K. 3D soft metamaterials with negative Poisson's ratio. *Adv. Mater.*, 25(36):5044–5049, 2013.

Bendsøe M., Olhoff N., y Taylor J. A variational formulation for multicriteria structural optimization. *J Struct Mech*, 11(4):523–544, 1983.

Bendsøe M.P. y Sigmund O. *Topology optimization. Theory, methods, and applications*. Springer-Verlag, 2003.

Berryman J. y Milton G. Microgeometry of random composites and porous media. *Journal of Physics D: Applied Physics*, 21(1):87, 1988.

Bloch F. über die quantenmechanik der elektronen in kristallgittern. *Zeitschrift für Physik*, 52:555–600, 1929.

Brillouin L. *Wave propagation in periodic structures*. Dover, 1953.

Bückmann T., Schittny R., Thiel M., Kadic M., Milton G., y Wegener M. On three-dimensional dilational elastic metamaterials. *New J. Phys.*, 16:033032, 2014.

Bückmann T., Stenger N., Kadic M., Kaschke J., Frölich A., Kennerknecht T., Thiel M., y Wegener M. Tailored 3D mechanical metamaterials made by dip-in direct-laser-writing optical lithography. *Adv. Mater.*, 24(20):2710–4, 2012.

Cherkaev A. y Gibiansky L. Coupled estimates for the bulk and shear moduli of a two-dimensional isotropic elastic composite. *Journal of the Mechanics and Physics of Solids*, 41(5):937–980, 1993.

Collet M., Ouisse M., Ruzzene M., y M.N. I. Floquet-bloch decomposition for the computation

of dispersion of two-dimensional periodic, damped mechanical systems. *Int. J. Solids Struc.*, 48:2837–2848, 2011.

Croënne C., Lee E., Hu H., y Page J. Band gaps in phononic crystals: Generation mechanisms and interaction effects. *AIP Advances*, 1(4):041401, 2011.

Dong H., Zhao S., Wang Y., y Zhang C. Topology optimization of anisotropic broadband double-negative elastic metamaterials. *Journal of the Mechanics and Physics of Solids*, 105:54–80, 2017.

Eyre D. y Milton G. A fast numerical scheme for computing the response of composites using grid refinement. *The European Physical Journal-Applied Physics*, 6(1):41–47, 1999.

Gazalet J., Dupont S., Kastelik J., Rolland Q., y Djafari-Rouhani B. A tutorial survey on waves propagating in periodic media: Electronic, photonic and phononic crystals. perception of the bloch theorem in both real and fourier domains. *Wave Motion*, 50(3):619–654, 2013.

Hashin Z. y Shtrikman S. A variational approach to the theory of the elastic behaviour of multiphase materials. *Journal of the Mechanics and Physics of Solids*, 11(2):127–140, 1963.

Huang X., Radman A., y Xie Y. Topological design of microstructures of cellular materials for maximum bulk or shear modulus. *Computational Materials Science*, 50(6):1861–1870, 2011.

Hussein M., Hulbert G., y Scott R. Dispersive elastodynamics of 1D banded materials and structures. *J. Sound Vib.*, 289:779–806, 2006.

Jensen J. y Pedersen N. On maximal eigenfrequency separation in two-material structures: the 1D and 2D scalar cases. *Journal of Sound and Vibration*, 289(4-5):967–986, 2006.

John S. Strong localization of photons in certain disordered dielectric superlattices. *Rev. Lett.*, 58:2486–2489, 1987.

Kushwaha M. Classical band structure of periodic elastic composites. *International Journal of Modern Physics B*, 10(09):977–1094, 1996.

Li Y., Huang X., Meng F., y Zhou S. Evolutionary topological design for phononic band gap crystals. *Structural and Multidisciplinary Optimization*, 54:595–617, 2016.

Liu Z., Chan C., y Sheng P. Analytic model of phononic crystals with local resonances. *Phys. Rev. B*, 71, 2005.

Liu Z., Zhang X., Mao Y., Y.Y. Z., Yang Z., Chan C., y Sheng P. Locally resonant sonic materials. *Science*, 289:1734–1736, 2000.

Maurin F., Claeys C., Deckers E., y Desmet W. Probability that a band-gap extremum is located on the irreducible brillouin-zone contour for the 17 different plane crystallographic lattices. *International Journal of Solids and Structures*, 135:26–36, 2018.

Milton G. y Willis J. On modifications of newton's second law and linear continuum elastodyna-

mics. *Proceedings of the Royal Society A: Mathematical, Physical and Engineering Sciences*, 463(2079):855–880, 2007.

M.M. Sigalas E.E. Elastic and acoustic wave band structure. *J. Sound Vib.*, 158(377), 1992.

M.M. Sigalas E.E. Band structure of elastic waves in two-dimensional systems. *Solid State Commun.*, 86(141), 1993.

Moulinec H. y Suquet P. A numerical method for computing the overall response of nonlinear composites with complex microstructure. *Computer methods in applied mechanics and engineering*, 157(1-2):69–94, 1998.

Novotny A. y Sokołowski J. *Topological derivatives in shape optimization*. Springer Science & Business Media, 2012.

Nye J. *Physical Properties of Crystals: Their representation by tensors and matrices*, volumen 146. Clarendon Press-Oxford., 2006.

Olhoff N. Solution of max-min problems via bound formulation and mathematical programming. En K.B. Rozvany G.I.N., editor, *Structural Optimization*. Springer, Dordrecht, 1988.

Olhoff N. Multicriterion structural optimization via bound formulation and mathematical programming. *Structural and Multidisciplinary Optimization*, 1(1):11–17, 1989.

Olhoff N. y Du J. Structural topology optimization with respect to eigenfrequencies of vibration. En G. Rozvany y T. Lewinsky, editores, *Topology Optimization in Structural and Continuum Mechanics*. Springer-Verlag, Vienna, 2013.

Osanov M. y Guest J. Topology optimization for architected materials design. *Annual Review of Materials Science*, 46:211–233, 2016.

Policarpo H., Neves M., y Ribeiro A. Dynamical response of a multi-laminated periodic bar: Analytical, numerical and experimental study. *Shock Vib.*, 17:521–535, 2010.

Richards D. y Pines D.J. Passive reduction of gear mesh vibration using a periodic drive shaft. *J. Sound Vib.*, 264:317–342, 2003.

Sigmund O. Materials with prescribed constitutive parameters: an inverse homogenization problem. *International Journal of Solids and Structures*, 31(17):2313–2329, 1994.

Sigmund O. y Jensen J. Systematic design of phononic band-gap materials and structures by topology optimization. *Royal Society*, 361, 2003.

Srivastava A. y Nemat-Nasser S. On the limit and applicability of dynamic homogenization. *Wave Motion*, 51(7):1045–1054, 2014.

Torquato S. Optimal design of heterogeneous materials. *Annual review of materials research*, 40:101–129, 2010.

Willis J. Dynamics of composites. En *Continuum micromechanics*, páginas 265–290. Springer,

1997.

Willis J. The construction of effective relations for waves in a composite. *Comptes Rendus Mécanique*, 340(4-5):181–192, 2012.

Yablonovitch E. Inhibited spontaneous emission in solid state physics and electronics. *Rev. Lett.*, 58:2059–2062, 1987.

Zheng X., Lee H., Weisgraber T., Shusteff M., DeOtte J., Duoss E., Kuntz J., Biener M., Ge Q., Jackson J.A., Kucheyev S., Fang N., y Spadaccini C. Ultralight, ultrastiff mechanical metamaterials. *Science*, 344:1373–1377, 2014.

Anexos: Introducción

En el presente apartado se exponen los principales artículos que contienen la totalidad del trabajo desarrollado para esta Tesis. La disposición elegida no es cronológica, pero tiene como fin ordenar primero los conceptos principales, para luego presentar las aplicaciones desarrolladas.

Los artículos se listan a continuación:

Anexo A N. Rossi, R. Yera, C.G. Méndez, S.Toro, A.E. Huespe. *Numerical technique for the 3D microarchitecture design of elastic composites inspired by crystal symmetries*. Computer Methods in Applied Mechanics and Engineering, Vol 359, 2020, DOI: 10.1016/j.cma.2019.112760

Anexo B R. Yera, N. Rossi Cabral, C.G. Méndez, A.E. Huespe. *Topology design of 2D and 3D elastic material microarchitectures with crystal symmetries displaying isotropic properties close to their theoretical limits*. Applied Materials Today. Vol 18. 2020. DOI: 10.1016/j.apmt.2019.100456

Anexo C Yera, R., Forzani, L., Méndez, C.G. and Huespe, A.E., *A topology optimization algorithm based on topological derivative and level-set function for designing phononic crystals*, Engineering Computations, 39(1), 354-379. 2021. DOI: 10.1108/EC-06-2021-0352

Anexo D R. Yera, C. G. Méndez, P.J. Sánchez, A. E. Huespe. *Effective properties of periodic media in elastodynamic problems*. Computer Methods in Materials Science, 21(3), 139-148. 2021. DOI: 10.7494/cmms.2021.3.0753

El tesista declara haber participado activamente en el desarrollo de los nuevos conceptos aportados y llevado a cabo los experimentos numéricos necesarios para alcanzar los resultados que se exponen. Estas tareas fueron realizadas bajo la dirección del Dr. Alfredo Huespe y del Dr. Victor Fachinotti, y en conjunto con los co-autores de cada artículo. Las sugerencias, revisiones y comentarios de los Dres. Huespe y Fachinotti han sido una contribución invaluable para lograr la alta calidad de artículos presentados.

Los abajo firmantes avalan esta declaración.

Aval del Director de Tesis

_____

Dr. Alfredo E. Huespe

Aval del Co-Director de Tesis

_____

Dr. Victor D. Fachinotti

Anexo A

Numerical technique for the 3D microarchitecture design of elastic composites inspired by crystal symmetries, Computer Methods in Applied Mechanics and Engineering, Volume 359, 2020

El artículo presentado a continuación ha sido publicado en la revista **"Computer Methods in Applied Mechanics and Engineering"**.

N. Rossi, R. Yera, C.G. Méndez, S.Toro, A.E. Huespe. *Numerical technique for the 3D microarchitecture design of elastic composites inspired by crystal symmetries*. Computer Methods in Applied Mechanics and Engineering, Vol 359, 2020, DOI: 10.1016/j.cma.2019.112760

Numerical technique for the 3D microarchitecture design of elastic composites inspired by crystal symmetries

N. Rossi[1], R. Yera[1], C.G. Méndez[1], S.Toro[1], A.E. Huespe[1,2]
[1]CIMEC-UNL-CONICET, Predio Conicet "Dr Alberto Cassano", CP 3000 Santa Fe, Argentina
[2]E.T.S d'Enginyers de Camins, Canals i Ports, Technical University of Catalonia (Barcelona Tech)
Campus Nord UPC, Mòdul C-1, c/ Jordi Girona 1-3, 08034, Barcelona, Spain

Keywords: 3D microarchitecture synthesis; topology optimization algorithm; topology design inspired by crystal symmetries; 3D elastic metamaterials; auxetic materials; pentamode composites; stiffest composite.

Abstract

A numerical methodology developed for the microarchitecture design of 3D elastic two-phase periodic composites with effective isotropic properties close to the theoretical bounds is here presented and analyzed. This methodology is formulated as a topology optimization problem and is implemented using a level-set approach jointly with topological derivative.

The most salient characteristic of this methodology is the imposition of preestablished crystal symmetries to the designed topologies; we integrate a topological optimization formulation with crystal symmetries to design mechanical metamaterials.

The computational homogenization of the composite elastic properties is determined using a Fast Fourier Transform (FFT) technique. Due to the design domains are the primitive cells of Bravais lattices compatible with the space group imposed to the material layout, we have adapted the FFT technique to compute the effective properties in 3D parallelepiped domains.

In this work, to find the topologies satisfying the proposed targets, we test four space groups of the cubic crystal system. Thus, the achievement of composites with effective elasticity tensor having cubic symmetry is guaranteed, and the isotropic response is then enforced by adding only one scalar constraint to the topology optimization problem.

To assess the methodology, the following microarchitectures are designed and reported: two auxetic composites, three pentamode materials, and one maximum stiffness composite. With only one exception, all the remaining topologies display effective elastic properties with Zener coefficients approximating to 1.

1. Introduction

The microarchitecture synthesis of composites with unusual properties that could be manufactured using a rapid prototyping technique has recently risen an enormous interest in the community, see Kadic et al. (2019) and references cited therein. This interest is mainly due to the notorious advances observed in this type of material processing technique that opens the possibility of manufacturing complex microstructures.

Closely related to this topic, the authors of this paper, see Yera et al. (2019), have developed a topology design technique for the microarchitecture synthesis of composites where the resulting material configurations at the microscale copy the symmetry of crystals. The design goal is to attain two-phase, stiff and void, composites with periodic microstructures and isotropic effective elastic properties close to the theoretical bounds. The crucial point of this approach is the imposition of crystal symmetries to the designed microarchitectures. This criterion could be adopted as a guiding principle in the design of new microarchitectures. A discussion about the effect that different space groups have on the realization of composites with properties close to the bounds have also been addressed in the contribution of Yera et al. In this work, we study the numerical aspects related to this design methodology.

The above-mentioned topology design technique is formulated as an inverse homogenization problem which closely follows the original methodology reported by Sigmund (1994), Sigmund (2000) and clearly explained in the book by Bendsoe y Sigmund (2003). In particular, the topology optimization algorithm that we have implemented is based on a level-set-technique with a topological derivative that has been originally reported by Amstutz y Andrä (2006) and Amstutz et al. (2010). It is also worth to mention that an analogous methodology, having some elements in common with the here presented procedure, is the level-set technique reported by Allaire and co-authors, see Allaire et al. (2005). Alternative level-set-techniques for topology optimization problems can be found in the review paper by van Dijk et al. (2013).

In the present approach, the crystal symmetries are imposed to the attained topologies via a geometrical constraint on the materials configurations that are tested during the topology optimization procedure. Due to the characteristic properties of crystal symmetries, the imposition of these constraints into the topology optimization problem introduces several distinguishing fea-

tures which can be summarized as follows: i) a correct selection of the space group symmetry will automatically provide the required symmetry of the target effective physical property. ii) the geometrical symmetry constraining the admissible topologies restricts the design space, or material distribution space, determining a robust performance of the topology optimization algorithm. Furthermore, we show that by imposing suitable crystal symmetries, then, a wide range of topologies can be obtained, including the well-known pentamode diamond-like microarchitecture reported by Milton y Cherkaev (1995). This solution is analyzed in sub-Section 4.2.

Intrinsically associated to this design approach is the evaluation of the effective properties of the tested composite through a computational homogenization technique. This step is by far the most demanding computational burden of the optimization algorithm, and we adopt a Fast Fourier Transform (FFT) technique to perform it. In the case of imposing crystal symmetries, the computational homogenization may be conveniently performed in spatial domains with non-conventional shapes, such as suggested by Méndez et al. (2019) and Podestá et al. (2019). Due to the FFT technique is not well suited for solving homogenization problems in design domains with complex shapes, we have adapted it to parallelepiped domains, which is sufficient for our purposes. A validation test that we present in this paper shows the performance of the FFT technique to compute the 3D elasticity tensor homogenization of the tested composites.

The authors have analyzed in Yera et al. (2019) the use of several space groups of the cubic system to attain two-phase microstructures, one of them is void. In those cases, similar to the present work, the target has been the design of isotropic elastic composites whose effective properties are close to the theoretical bounds of Hashin-Shtrikmann. Here, we specifically present a restricted set of solutions that corresponds to three kind of composites, one auxetic, one maximum stiffness and three pentamodes, using cells with $256 \times 256 \times 256$ voxels. Therefore, these solutions display well-refined details.

A brief description of the paper is the following. First, in Section 2, we summarize the topology design approach followed in this work. We emphasize the description of the FFT technique applied to problems with non-orthogonal domains. Then, this technique is validated, and its performance is assessed and compared with the finite element method.

In Section 3, we particularize the topology design approach for solving microarchitecture design problems of isotropic composites whose effective properties are close to the theoretical bounds. In sub-Section 3.4, we address some important issues concerning the implementation of the level-set algorithm and the imposition of crystal symmetries to the tested solutions.

Section 4 presents the numerical assessments of the algorithm. The microarchitectures of some representative composites are designed using six space groups of the cubic crystal system to attain

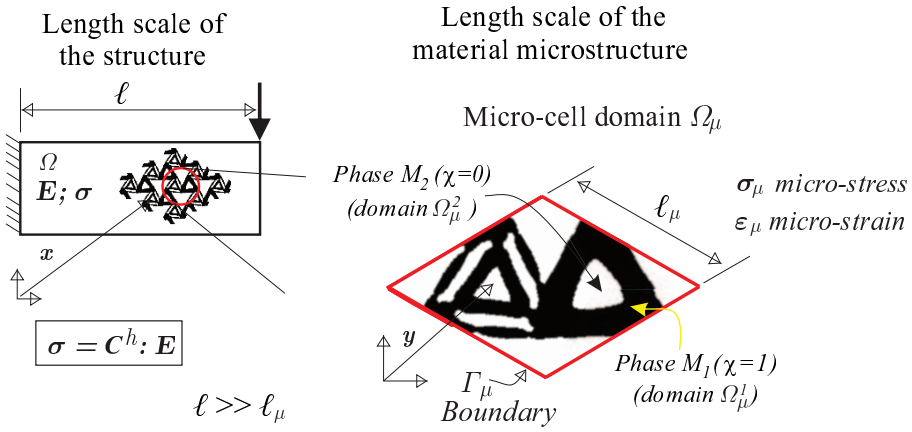

Figura A.1: Multiscale structural problem. Cell Ω_μ of the composite periodic microstructure with phases M_1 and M_2. Characteristic function χ. At the macrostructure scale, points are identified with $\mathbf{x}$ and the effective elastic properties of the composite are characterized by the homogenized constitutive elasticity tensor $\mathbf{C}^h$. At the microscale, points are identified with $\mathbf{y}$ and elasticity tensors with $\mathbf{C}$.

the isotropic response. The conclusions are presented in Section 5. Finally, some specific aspects of the topological derivative of 3D homogenization problems, which is a crucial issue of the present approach, are briefly described in Appendix I. The general algorithm is presented in Appendix II.

2. Topology design approach

Let us consider the structure sketched in Figure A.1 which displays a dominating size ℓ and is built with a material composed of two phases M_1, M_2. This composite has a periodic microstructure with a characteristic length, ℓ_μ. A very fundamental supposition in this work is that $\ell_\mu \ll \ell$. It is noteworthy to remark that all periodic microstructures have underlying Bravais lattices, whose features are widely exploited in this work. According to this observation, ℓ_μ can be associated with the size of the primitive vectors of the lattice.

At the structural length scale, the effective elastic properties of the composite can be described through the homogenized elasticity tensor $\mathbf{C}^h$, which relates the macro-strains $\boldsymbol{E}$ with the macro-stresses $\boldsymbol{\sigma}$. A representative cell Ω_μ of the microstructure is used to compute $\mathbf{C}^h$. For those composites displaying effective isotropic elastic responses, $\mathbf{C}^h$ is fully characterized by the effective bulk modulus κ^h and the effective shear modulus G^h.

Let us suppose additionally that the material configuration at the microscale can be described with a characteristic function $\chi(\mathbf{y})$ defined on Ω_μ, which is 1 in the points $\mathbf{y}$ where phase M_1 exists and is 0 where phase M_2 exists. Thus, the expressions $\mathbf{C}^h(\chi)$, $\kappa^h(\chi)$ and $G^h(\chi)$ manifest that the homogenized elastic properties depend on the spatial distribution of phases in Ω_μ.

Under these conditions, a possible topology optimization problem consists of determining the function χ satisfying the minimum of a given target function, $f(\mathbf{C}^h)$ subjected to specified constraints.

A suitable topology optimization problem for the objective pursued in this work is defined in Section 3. But before addressing this topic, we present with some detail, in the next two sub-Sections, two important aspects of the methodology. They are a procedure to select suitable spatial optimization domains, according to the target problem; as well as, an efficient technique for computing the homogenized elasticity tensor $(\mathbf{C}^h)$ in such optimization domains. More conventional issues about the formulation and evaluation of the elasticity tensor homogenization are presented in Appendix I.

2.1. Selection of the design domain Ω_μ: Bravais lattices and unit cells

The most salient feature of the present design methodology consists of imposing a predefined crystal symmetry to the designed microarchitecture with the condition that this symmetry is compatible with the target effective elastic symmetry of the problem. For a composite with periodic microstructure, the nexus between the symmetry of its microarchitecture material configuration and the symmetry displayed by its effective physical property is given by the Neumann's principle, broadly applied in crystallography, see Nye (2006).

Following this principle, Yera et al. (2019) suggest the adoption of a crystal symmetry assuring the fulfillment of the target effective elastic symmetry. Recalling that the target problem in this work aims at attaining the isotropic symmetry, then, in 2D topologies, the hexagonal crystal system guarantees the attainment of this property. Contrarily, there is not any crystal system in 3D problems guaranteeing such symmetry. According to this observation, we will be only testing space groups compatible with the Cubic crystal system because it displays the higher symmetry for 3D topologies.

The geometrical symmetry characterizing a periodic microstructure can be additionally categorized with a specific crystal space group and point group[1]. Every Bravais lattice has a point group symmetry. Therefore, there is a compatibility relationship between the symmetry of the pursued effective property and a given Bravais lattice through the associated point group. This connection has been studied in greater details by the authors in previous works, see Podestá et al. (2018a), Podestá et al. (2019) and Méndez et al. (2019).

Using these ideas, we propose a procedure which can be explained with the information described in Table A.1. In this Table, we show the compatibility relationships between the space groups, the point groups and the Bravais lattices for the Cubic crystal system.

Let us consider, for example, a target effective property with cubic symmetry. Then, five point groups and 36 space groups are compatible with this symmetry, such as shown in the third and

[1]Further details about the classification and properties of space and point groups can be found in London (2004) and Vainshtein (2013). The readers could also visit the web-page Hitzer y Perwass (2009) for visualizing the symmetry elements of different space groups.

Tabla A.1: Cubic System. Compatible point and space groups. Bravais lattices compatible with the cubic systems are: Simple Cubic (SC), Face Centered Cubic (fcc) and Body Centered Cubic (bcc). Primitive cells of the three Bravais lattices with volumes $|\Omega_\mu^{SC}| = 1.$, $|\Omega_\mu^{fcc}| = 0.25$ and $|\Omega_\mu^{bcc}| = 0.5$. The elasticity matrix with cubic symmetry in the natural basis is represented in column 1. The symbol "$* - *$" linking two coefficients means that they are equal. Only three coefficients define the elasticity matrix in natural basis. Point and spatial groups denoted in bold text are tested in this work. The number of symmetry elements in space and point groups increases toward the descending direction of rows.

Elasticity Tensor	Crystal System	Point Groups	Space Groups		
$\begin{pmatrix} * & *-* & 0 & 0 & 0 \\ & * & 0 & 0 & 0 \\ & & * & 0 & 0 \\ & & & * & 0 \\ & & & & * \end{pmatrix}$	Cubic	**23**	**P23**, P2_13	F23	**I23**, I2_13
		m3	Pm3, Pn3, Pa3	Fm3, Fd3	I3, Ia3
		432	P432, P4_232, P4_332, P4_132	F432, F4_132	I432, I4_132
		$\bar{4}$**3m**	P43m, P43n	**F$\bar{4}$3m**, F43c	**I$\bar{4}$3m**, I43d
		m$\bar{3}$m	**Pm$\bar{3}$m**, Pn$\bar{3}$n, Pm$\bar{3}$n, Pn$\bar{3}$m	Fm3m, Fm3c, Fd$\bar{3}$m, Fd$\bar{3}$c	**Im$\bar{3}$m**, Ia$\bar{3}$d
Compatible Bravais lattice			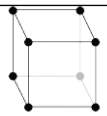 simple cubic (SC)	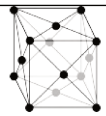 fcc	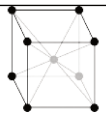 bcc
Primitive unit cells Primitive vectors are $\boldsymbol{g}_\alpha$, $\boldsymbol{g}_\beta$ and $\boldsymbol{g}_\gamma$			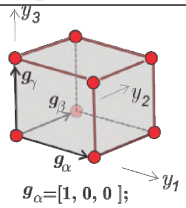 g_α=[1, 0, 0]; g_β=[0, 1, 0]; g_γ=[0, 0, 1];	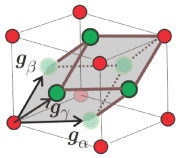 g_α=[0.5, 0.5 0.]; g_β=[0. , 0.5 0.5]; g_γ=[0.5, 0. 0.5];	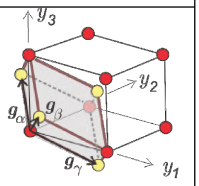 g_α=[-0.5, 0.5 0.5]; g_β=[0.5, -0.5 0.5]; g_γ=[0.5, 0.5 -0.5];

fourth columns of the Table. One of these space groups is chosen with a given criterion, for example, the $I23$. Automatically, the bcc Bravais lattice is associated with it, such as shown in the last column of the table. Finally, for solving this problem with the imposed symmetry $I23$, the primitive cell of the bcc Bravais lattice should be tentatively defined as the topology optimization domain Ω_μ. Following the same idea, if the space group $P23$ were chosen, the simple cubic Bravais lattice is compatible and the corresponding simple cubic primitive cell should be adopted.

2.2. Computational homogenization using a FFT technique in parallelepipedic domains

The FFT-based homogenization techniques have been introduced by Moulinec y Suquet (1998) for computing the tensor $\mathbf{C}^h$ of composites with rather arbitrary microstructures. Afterward, these techniques have been improved by several authors, and particularly, Eyre y Milton (1999) have introduced a specific algorithm exhibiting better convergence properties for the homogenization of composites with a large stiffness contrast between the two constituent phases. In our implementation, we follow this last approach.

Due to these techniques are now well-established, they are not shown here. Thus, the interested reader is addressed to the reference works for further details of implementations. The only issue which deserves specific attention in this work is the computation of the FFT operations in non-orthogonal domains. The effective elastic properties of the designed composites are computed with micro-cells coinciding with the spatial domains where the topology optimization problems are solved. As explained above, in general, these domains are constituted by parallelepipeds defined by the primitive vectors of Bravais lattices, and therefore, they are not rectangular prisms.

FFT in non-orthogonal coordinates

For simplicity, we describe the computation of the FFT in non-orthogonal coordinates using a two-dimensional geometry. Its generalization to 3D problems is direct.

Let us consider a periodic material whose underlying Bravais lattice has non-orthogonal primitive vectors, $\boldsymbol{g}_\alpha$ and $\boldsymbol{g}_\beta$, such as sketched in Figure A.2. We introduce the basis $\{\boldsymbol{g}_\alpha, \boldsymbol{g}_\beta\}$ to define a non-orthogonal coordinate system with an homogeneous metric tensor. A position vector $\mathbf{y}$ in this basis is expressed according to $\mathbf{y} = \theta^\alpha \boldsymbol{g}_\alpha + \theta^\beta \boldsymbol{g}_\beta$ (α and β identify different basis vectors, and therefore, the summation convention of repeated index is not applied), where $\{\theta^\alpha, \theta^\beta\}$ are the corresponding pair of coordinates, i.e., the contravariant components of $\mathbf{y}$.

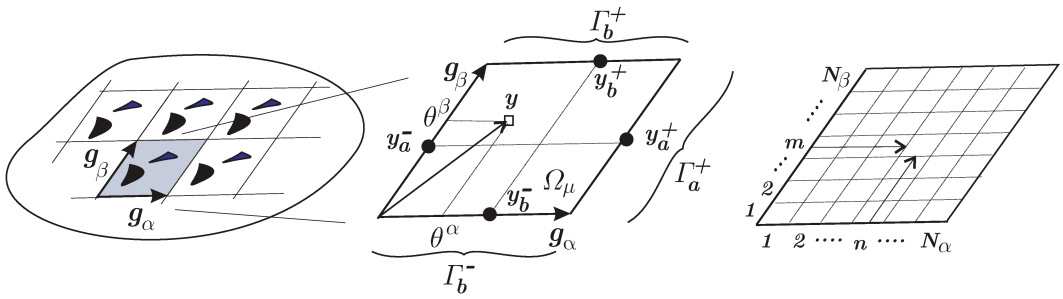

Figura A.2: Periodic microcell along non-orhogonal directions $\boldsymbol{g}_\alpha$ and $\boldsymbol{g}_\beta$. Identification of the nm-th pixel.

Let us also consider a periodic mechanical problem such that the fluctuation of the micro-displacements $\tilde{\mathbf{u}}$ and micro-tractions $\mathbf{t}$ are periodic and antiperiodic, respectively, along the directions $\boldsymbol{g}_\alpha$ and $\boldsymbol{g}_\beta$. Therefore, by defining the unit cell domain Ω_μ, the following identities are satisfied on its boundary:

$$\begin{aligned} \tilde{\mathbf{u}}(\mathbf{y}_a^+) = \tilde{\mathbf{u}}(\mathbf{y}_a^-)\ ;\ \mathbf{t}(\mathbf{y}_a^+) = -\mathbf{t}(\mathbf{y}_a^-) \quad \forall \mathbf{y}_a^+ \in \Gamma_a^+ \text{ and } \mathbf{y}_a^+ = \mathbf{y}_a^- + \boldsymbol{g}_\alpha \\ \tilde{\mathbf{u}}(\mathbf{y}_b^+) = \tilde{\mathbf{u}}(\mathbf{y}_b{}^-)\ ;\ \mathbf{t}(\mathbf{y}_b^+) = -\mathbf{t}(\mathbf{y}_b^-) \quad \forall \mathbf{y}_b{}^+ \in \Gamma_b^+ \text{ and } \mathbf{y}_b^+ = \mathbf{y}_b^- + \boldsymbol{g}_\beta \end{aligned} \tag{A.1}$$

Furthermore, we can express every component of the displacements, the strains and the stresses as fields in terms of the contravariant coordinates. Let one of these periodic function, for example a strain component, be denoted $f(\theta^\alpha, \theta^\beta)$. Then, f satisfies $f(\theta^\alpha + \Delta\theta^\alpha, \theta^\beta) = f(\theta^\alpha, \theta^\beta)$ and $f(\theta^\alpha, \theta^\beta + \Delta\theta^\beta) = f(\theta^\alpha, \theta^\beta)$ with $\Delta\theta^\alpha = 1$ and $\Delta\theta^\beta = 1$. These fields can be transformed to

the frequency domain using the Fourier Transform along the directions $\boldsymbol{g}_\alpha$ and $\boldsymbol{g}_\beta$:

$$\hat{f}(\zeta_\alpha, \zeta_\beta) = \int_0^1 \int_0^1 f(\theta^\alpha, \theta^\beta) e^{-i(\zeta_\alpha \theta^\alpha + \zeta_\beta \theta^\beta)} d\theta^\alpha d\theta^\beta \ ; \tag{A.2}$$

where the two frequencies $(\zeta_\alpha, \zeta_\beta)$ can be interpreted as the covariant components of the frequency vector $\boldsymbol{\xi} = \zeta_\alpha \mathbf{G}^\alpha + \zeta_\beta \mathbf{G}^\beta$, being $\{\mathbf{G}^\alpha, \mathbf{G}^\beta\}$ the reciprocal basis of $\{\boldsymbol{g}_\alpha, \boldsymbol{g}_\beta\}$ satisfying $\mathbf{G}^i \cdot \boldsymbol{g}_j = \delta_{ij}$ with δ_{ij} the Kronecker delta function.

By taking into account these preliminary concepts, the homogenized properties of periodic composites characterized by unit cells defined by non-orthogonal primitive vectors can be computed with the FFT algorithm. A brief summary of this algorithm implementation is next described:

1 First, the unit cell is partitioned in $(N_\alpha \times N_\beta)$ pixels[2]; N_α in the direction $\boldsymbol{g}_\alpha$ and N_β in the direction $\boldsymbol{g}_\beta$, such as shown in Figure A.2. The following set of discrete frequencies are defined:

$$\boldsymbol{\zeta}_\alpha = [\zeta_\alpha^{(1)}, \zeta_\alpha^{(2)}, ..., \zeta_\alpha^{(n)}, ..., \zeta_\alpha^{(N_\alpha)}] = \left[-\frac{N_\alpha}{2}+1, -\frac{N_\alpha}{2}+2, ..., \frac{N_\alpha}{2}\right] \ ;$$
$$\boldsymbol{\zeta}_\beta = [\zeta_\beta^{(1)}, \zeta_\beta^{(2)}, ..., \zeta_\beta^{(m)}, ..., \zeta_\beta^{(N_\beta)}] = \left[-\frac{N_\beta}{2}+1, -\frac{N_\beta}{2}+2, ..., \frac{N_\beta}{2}\right] \ ;$$
for N_α and N_β even,

(if N_α or N_β are odd, the formula in Moulinec et al. can be used). From them, we define the $(N_\alpha \times N_\beta)$ vectors of discrete frequencies transformed to the Cartesian coordinates:

$$[\boldsymbol{\xi}^{(n,m)}] = \zeta_\alpha^{(n)} \mathbf{G}^\alpha + \zeta_\beta^{(m)} \mathbf{G}^\beta \ . \tag{A.3}$$

2 The Green operator in the frequency space, $\boldsymbol{\Gamma}^0$, is evaluated for every vector $\boldsymbol{\xi}^{(n,m)}$ as follows:

$$\boldsymbol{\Gamma}^0(\boldsymbol{\xi}^{(n,m)}) = \boldsymbol{\xi}^{(n,m)} \left(\boldsymbol{\xi}^{(n,m)} \cdot \mathbf{C}^0 \cdot \boldsymbol{\xi}^{(n,m)}\right)^{-1} \boldsymbol{\xi}^{(n,m)} \ . \tag{A.4}$$

with $\mathbf{C}^0$ being a reference elasticity tensor. Note that equation (A.4), expressed in intrinsic notation, could be computed using Cartesian components, in particular $\mathbf{C}^0$ is the conventional matrix of the elastic Hooke law in Cartesian components.

3 Proceed in a standard way with the algorithm defined in Eyre et al.

Note that the stress and strain fields in both, space and frequency, domains that arise in the algorithm (10) of the reference work have the components described in Cartesian basis.

In the following, we use indices with Arabic numerals for denoting the components of tensors in Cartesian coordinates. Additionally, we use Kelvin notation for second and fourth order tensors. The stress tensor components $\{\sigma_{y_1y_1}, \sigma_{y_2y_2}, \sigma_{y_3y_3}, \sigma_{y_1y_2}, \sigma_{y_1y_3}, \sigma_{y_2y_3}\}$ are represented with

[2]The generalization to three-dimensional microcell homogenization is direct by considering $N_\alpha \times N_\beta \times N_\gamma$ voxels.

Arabic numeral indices as follows: $\{\sigma_1, \sigma_2, \sigma_3, \sigma_4, \sigma_5, \sigma_6\}$, respectively. The stress vector in Kelvin notation results $(\sigma_1, \sigma_2, \sigma_3, \sqrt{2}\sigma_4, \sqrt{2}\sigma_5, \sqrt{2}\sigma_6)$. An identical criterion is used for strains. In consequence, the corresponding elasticity matrix are denoted with two Arabic indices: C_{ij}, with $i, j = 1, ..., 6$.

Validation tests

Next, we validate the FFT technique. The effective elasticity tensor of a composite constituted of a stiff phase with an array of spherical voids geometrically placed in the positions occupying the atoms of a face-centered cubic (fcc) Bravais lattice is computed. Then, we analyze the computational cost (time) vs. accuracy that demands to solve this problem with the FFT, using different densities of grids. We also compare these results with those obtained with the Finite Element Method (FEM).

Due to the symmetry of this microarchitecture, the effective elasticity tensor displays cubic symmetry. The Young modulus of the stiff phase, M_1, is $E_1 = 1$ and the Poisson's ratio is $\nu_1 = 0.4$. The spherical voids have a radius of 0.15, wherewith the volume fraction of the composite stiff phase is $f_1 = 0.9435$. The analytic reference solution of the effective elastic moduli, reported by Cohen (2004), is given by: $(C^h_{ref})_{11} = (C^h_{ref})_{22} = (C^h_{ref})_{33} = 1.7415$, $(C^h_{ref})_{12} = (C^h_{ref})_{23} = (C^h_{ref})_{13} = 1.0982$ and $(C^h_{ref})_{44} = (C^h_{ref})_{55} = (C^h_{ref})_{66} = 0.6456$. This solution is calculated considering that the second phase is void.

In the numerical model, the void phase, M_2, is assumed to be a soft elastic material whose Young modulus is $E_2 = \gamma E_1$ with the contrast factor $\gamma = 10^{-4}$. We also show here that this factor is small enough to simulate the void. The Poisson's ratio is taken as $\nu_2 = \nu_1$.

The computational homogenization is evaluated on a primitive micro-cell Ω^p_μ of the fcc lattice, such as displayed in Figure A.3-c. Conventional and primitive cells are shown in Figure A.3-a and c. Superscript p and c indicates primitive and conventional unit cells, respectively. The conventional unit cell size is $1 \times 1 \times 1$. Note that the primitive cell has a volume $|\Omega^p_\mu| = 0.25$ compared with the volume of the conventional unit cell whose volume is $|\Omega^c_\mu| = 1$. Therefore, to attain similar accuracies, the micro-cell Ω^c_μ requires 4 times more voxels than the micro-cell Ω^p_μ. This feature of the primitive cell is remarkably most important for the design of microarchitectures. In fact, for the same composite, the primitive cell displays simpler topologies respect to those described by the conventional unit cell.

Results are plotted in Figure A.4. The curves show the computation time needed for solving every problem vs. the solution error using the primitive cell Ω^p_μ. The errors are computed as the normalized Frobenius norm of the difference between the computed elasticity tensor $\mathbf{C}^h$ and the reference one $\mathbf{C}^h_{ref}$. The numbers in the Figure indicate the grid densities and represent the number

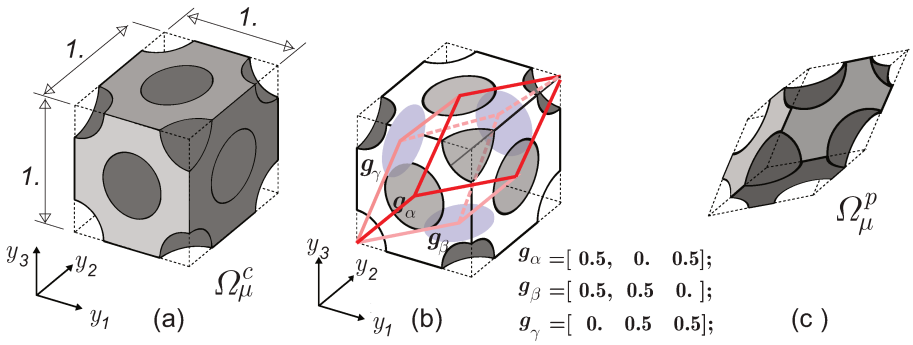

Figura A.3: Validation tests. Composite microstructure. (a) Conventional unit cell Ω^c_μ; (b-c) primitive unit cell Ω^p_μ. The primitive vectors $\boldsymbol{g}_\alpha$, $\boldsymbol{g}_\beta$ and $\boldsymbol{g}_\gamma$ also define the periodicity directions.

of voxels in each dimension. For example, the number 300 indicates that the solution is obtained with a discretization of $300 \times 300 \times 300$ voxels. The finite element mesh is built by taking the same spatial distribution of voxels and dividing each one of them into six linear tetrahedra. Solutions denoted "*without greys*" are obtained with voxels (FFT) or finite elements (FEM) having the properties of only one of the two phases. On the other hand, solutions denoted "with greys" apply the below formulas (A.20) and (A.21) to define the material properties of voxels and tetrahedra. In the case of the FFT solutions, the eight vertices of each voxel are used for this determination, but for the FEM solutions, the four nodes of every tetrahedron are used to define the property of the finite element.

As expected, the FEM and FFT methodologies tend to the correct solution by increasing the grid density. However, it is notable the effect induced by the inclusion of the grey material in both methodologies. This effect is still more remarkably in the FFT technique, there are striking differences in favor of this technique. To attain similar error levels in the computation of the effective elasticity tensor, the cost of FEM solutions is more than one order higher than that using the FFT technique. A different conclusion would be attained if grey elements were removed from the model.

The FEM uses a linear equation system iterative solver (conjugate gradient method) with incomplete Cholesky preconditioning (IChol). The error tolerances for both methodologies (FEM with iterative solver and FFT) have been fixed to 10^{-6}, and their implementations have been optimized to run in MATLAB using an Intel i9-9900K Processor with 64GB of memory ram and Intel Turbo Boost activated.

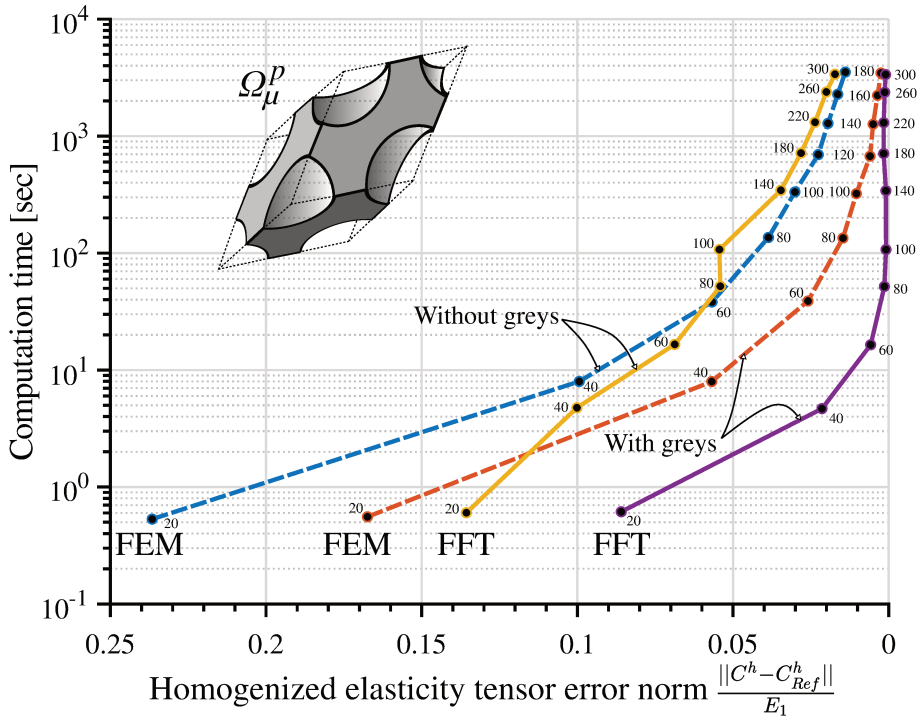

Figura A.4: Computation time vs. normalized errors to evaluate the homogenized elasticity tensors (Frobenius norm). Solutions obtained with a primitive cell (Ω_μ^p). Numbers indicate the grid density size of each solution. Comparison of FEM vs. FFT solutions.

3. Microarchitecture design of isotropic elastic composites

3.1. Bounds of the effective elastic property of two-phase well-ordered composites

Let us consider the full set of periodic composites with isotropic effective elastic properties and two isotropic elastic phases M_1 and M_2 whose bulk moduli are κ_1, κ_2, with $\kappa_2 < \kappa_1$, and shear moduli G_1, G_2, with $G_2 < G_1$, respectively, and a volume fraction of M_1 equal to f_1. Then, the effective properties of these composites, typically the bulk and shear effective moduli, $\hat{\kappa}$ and $\hat{G}$, are bounded: $\hat{\kappa}^l \leq \hat{\kappa} \leq \hat{\kappa}^u$, $\hat{G}^l \leq \hat{G} \leq \hat{G}^u$, where $\hat{\kappa}^u$ and $\hat{\kappa}^l$ are the upper and lower bounds of the effective bulk modulus, and, $\hat{G}^u$ and $\hat{G}^l$ are the upper and lower bounds of the effective shear modulus. These bounds have been theoretically estimated with the expressions derived by[3] Hashin y Shtrikman (1963) as follows:

$$\hat{\kappa}^u = \kappa_1 + \frac{1-f_1}{\frac{1}{\kappa_2-\kappa_1} + 3\frac{f_1}{3\kappa_1+4G_1}} \quad ; \quad \hat{\kappa}^l = \kappa_2 + \frac{f_1}{\frac{1}{\kappa_1-\kappa_2} + 3\frac{1-f_1}{3\kappa_2+4G_2}} \; ; \tag{A.5}$$

$$\hat{G}^u = G_1 + \frac{1-f_1}{\frac{1}{G_2-G_1} + \frac{6(\kappa_1+2G_1)f_1}{5G_1(3\kappa_1+4G_1)}} \quad ; \quad \hat{G}^l = G_2 + \frac{f_1}{\frac{1}{G_1-G_2} + \frac{6(\kappa_2+2G_2)(1-f_1)}{5G_2(3\kappa_2+4G_2)}} \; .$$

For composites constituted of two phases characterized by $\kappa_1 = 1.667$, $G_1 = 0.3571$, $\kappa_2 = \gamma\kappa_1$, $G_2 = \gamma G_1$, with the contrast factor $\gamma = 10^{-4}$, and a volume fraction $f_1 = 0.338$, these bounds

[3] Tighter bounds were reported by Berryman y Milton (1988). However, the bounds coincide with the Hashin-Shtrikmann ones when one of the phases is void.

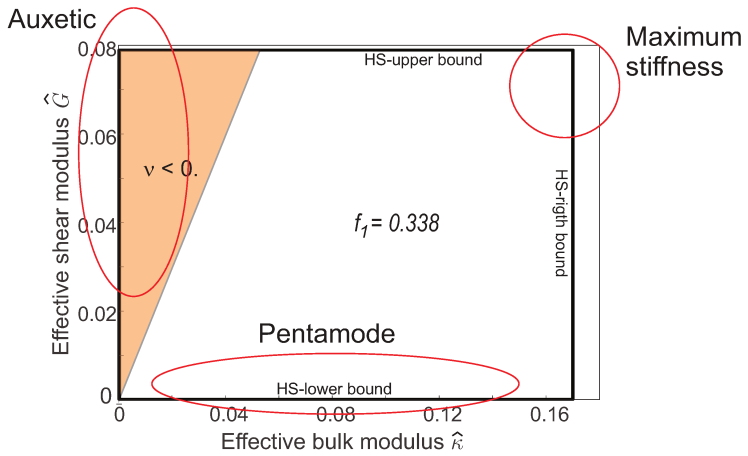

Figura A.5: Theoretical bounds of effective properties for two-phase isotropic 3D composites according to Hashin y Shtrikman (1963) (HS-bounds). Properties of phases M_1 and M_2 are $\kappa_1 = 1.667$, $G_1 = 0.3571$, $\kappa_2 = \gamma\kappa_1$, $G_2 = \gamma G_1$, contrast factor $\gamma = 10^{-4}$, volume fraction $f_1 = 0.338$.

are: $\hat{\kappa}^u = 0.170$; $\hat{\kappa}^l = 2.8 \times 10^{-4}$; $\hat{G}^u = 0.789$; $\hat{G}^l = 7.3 \times 10^{-5}$ and they are plotted in Figure A.5 and are denoted the HS-bounds.

3.2. Topology optimization problems

The goal is to design the family of two-phase composites with a predefined volume fraction, whose effective properties are isotropic and furthermore, they are the closest one to the four HS-bounds. The mathematical formulations chosen for solving this problem are the following.

Given the micro-cell Ω_μ, we define the characteristic function $\chi(\mathbf{y})$ identifying the positions where the phase M_1 is placed. It is defined by:

$$\chi(\mathbf{y}) = \begin{cases} 0 & \forall \mathbf{y} \in \Omega_\mu^2 \\ 1 & \forall \mathbf{y} \in \Omega_\mu^1 \end{cases} . \tag{A.6}$$

Then,

i) To approach the inferior HS-bound, the problem is written as:

$$\begin{aligned} &\min_{\chi} \; G^h(\chi); \\ &\text{such that:} \quad \kappa^h(\chi) - \kappa^{tg} = 0 \\ &\qquad\qquad\quad \mathbf{C}^h(\chi) \text{ is isotropic} \\ &\qquad\qquad\quad f_1^h(\chi) - {f_1}^{tg} = 0 \end{aligned} \tag{A.7}$$

where κ^{tg} is the target bulk modulus of the composite defined within the interval $\hat{\kappa}^l \leq \kappa^{tg} \leq \hat{\kappa}^u$, $f_1^h(\chi) = \int_{\Omega_\mu} \chi \; d\Omega$ is the volume fraction of phase M_1 and ${f_1}^{tg}$ is the target volume fraction. The solutions approaching the HS-lower bound can be obtained by solving a series of problems (A.7), with κ^{tg} sweeping the range of the interval $[\hat{\kappa}^l, \hat{\kappa}^u]$.

ii) An alternative problem is formulated to approach the left Hashin-Strikman bound, as follows:

$$\begin{aligned} &\min_{\chi} \kappa^h(\chi); \\ \text{such that:} \quad & G^h(\chi) - G^{tg} = 0 \\ & \mathbf{C}^h(\chi) \text{ is isotropic} \\ & {f_1}^h(\chi) - {f_1}^{tg} = 0 \end{aligned} \tag{A.8}$$

where now, the target effective shear modulus G^{tg} is chosen from the interval $\hat{G}^l \leq G^{tg} \leq \hat{G}^u$. Similarly as described above, the solutions approaching the HS-left bound can be obtained by solving a series of problems with G^{tg} sweeping the range of the interval $[\hat{G}^l, \hat{G}^u]$.

iii) In a similar way, the Hashin-Strikman superior and right bounds are approached by changing the minimization problems in (A.7) and (A.8) respectively, by one of maximization.

3.3. Rephrasing the topology optimization problems for microstructures with cubic crystal symmetries

Microstructures possessing a cubic crystal system have effective elastic responses with cubic symmetry. Thus, such as shown in Table A.1, the coefficients of their elasticity matrices satisfy the following identities: $C^h_{11} = C^h_{22} = C^h_{33}$; $C^h_{12} = C^h_{13} = C^h_{23}$; $C^h_{44} = C^h_{55} = C^h_{66}$. The remaining coefficients are strictly equal to zero.

According to this observation, as long as it can be guaranteed in advance that the microstructure will have a cubic system, the topology optimization problems (A.7)–(A.8) can be rephrased in terms of the elasticity matrix coefficients as follows:

$$\begin{aligned} &\min_{\psi \in C^0} \; C^h_{44}; \\ \text{such that:} \quad & h_1 = C^h_{11} + 2C^h_{12} - 3\kappa^{tg} = 0 \\ & h_2 = C^h_{11} - C^h_{12} - C^h_{44} = 0 \\ & h_3 = {f_1}^h(\chi) - {f_1}^{tg} = 0 \end{aligned} \tag{A.9}$$

$$\begin{aligned} &\min_{\psi \in C^0} (C^h_{12} + \frac{1}{3} C^h_{44}); \\ \text{such that:} \quad & h_1 = C^h_{11} - C^h_{12} + \frac{3}{2} C^h_{44} - 5G^{tg} = 0 \\ & h_2 = C^h_{11} - C^h_{12} - C^h_{44} = 0 \\ & h_3 = {f_1}^h(\chi) - {f_1}^{tg} = 0 \end{aligned} \tag{A.10}$$

Note that the coefficients of any isotropic elasticity tensor satisfy the following conditions: *a)*

$C^h_{44} = 2G$, *b)* $C^h_{12}+\frac{1}{3}C^h_{44} = \kappa$, *c)* $C_{11}+2C_{12} = 3\kappa$, and *d)* $C_{11}-C_{12}+3C_{44}/2 = 5G$; being κ and G the bulk and shear moduli of the material. Thus, after assuming that κ is the target bulk modulus of the problem (A.7), the objective function of this problem is replaced by the identity *a)*. The first constraint can be replaced by *c)*, which results the constraint h_1 in the rephrased formulation (A.9), while h_2 of the rephrased formulation ensures the isotropic response. An identical consideration can be applied to reformulate the problem (A.8). In this case, by assuming that G is the target shear modulus, the objective function of (A.8) is replaced by *b)*, the first constraint is replaced by *d)*, which results the constraints h_1 in the rephrased formulation (A.10) and constraint h_2 ensures the isotropic response.

3.4. Level-Set topology optimization algorithm

The topology optimization algorithm for solving the problems (A.9)–(A.10) uses the level-set method, combined with topological derivatives. The topological derivative provides the sensitivity of the target properties with changes of the characteristic function χ. The numerical technique based on these ingredients, and which is used in this paper, follows the original ideas of the algorithm presented by Amstutz y Andrä (2006) and Amstutz et al. (2010). The topological derivative concept is well described in the book by Novotny y Sokołowski (2012). Alternative formulations of topology optimizations problems using topological derivative and level-set functions have also been reported in the works of Allaire and co-authors, see Allaire et al. (2005) and references cited therein.

Let us introduce a smooth level-set function ψ defined in the microcell Ω_μ, $\psi \in C^0(\Omega_\mu)$, satisfying

$$\psi(\mathbf{y}) = \begin{cases} > 0 & \forall \mathbf{y} \in \Omega^2_\mu \\ < 0 & \forall \mathbf{y} \in \Omega^1_\mu \\ = 0 & \forall \mathbf{y} \in \partial\Omega^1_\mu \end{cases} , \tag{A.11}$$

then, the characteristic functions $\chi(\mathbf{y})$ in Ω_μ, given by expression (A.6), can be redefined as follows:

$$\chi_\psi = \begin{cases} 1 & \forall \psi \leq 0 \\ 0 & \forall \psi > 0 \end{cases} . \tag{A.12}$$

and problems (A.9)–(A.10) can be written in terms of χ_ψ:

$$\begin{aligned} &\min_{\psi \in C^0} \; C^h_{44}(\chi_\psi); \qquad\qquad (A.13)\\ &\text{such that:} \quad h_1 = C^h_{11}(\chi_\psi) + 2C^h_{12}(\chi_\psi) - 3\kappa^{tg} = 0 \\ &\qquad\qquad\; h_2 = C^h_{11}(\chi_\psi) - C^h_{12}(\chi_\psi) - C^h_{44}(\chi_\psi) = 0 \\ &\qquad\qquad\; h_3 = f^h_1(\chi_\psi) - {f_1}^{tg} = 0 \end{aligned}$$

$$\min_{\psi \in C^0} (C^h_{12}(\chi_\psi) + \frac{1}{3} C^h_{44}(\chi_\psi)); \tag{A.14}$$

$$\text{such that:} \quad h_1 = C^h_{11}(\chi_\psi) - C^h_{12}(\chi_\psi) + \frac{3}{2} C^h_{44}(\chi_\psi) - 5G^{tg} = 0$$
$$h_2 = C^h_{11}(\chi_\psi) - C^h_{12}(\chi_\psi) - C^h_{44}(\chi_\psi) = 0$$
$$h_3 = f_1^h(\chi_\psi) - {f_1}^{tg} = 0$$

By making use of an augmented Lagrangian technique, see Lopes et al. (2015), problem (A.13) (similarly for (A.14)) is reformulated as follows:

$$\max_{\lambda} \min_{\psi} \mathcal{T}(\chi_\psi, \lambda), \tag{A.15}$$

with:

$$\mathcal{T}(\chi_\psi, \lambda) = C^h_{44} + \lambda_1 h_1 + \lambda_2 h_2 + \lambda_3 h_3 + \frac{\alpha}{2} \left(h_1^2 + h_2^2 + h_3^2\right) \tag{A.16}$$

where the λ_i, with $i = 1, 2, 3$, are the Lagrange multipliers and α is the penalty parameter of the augmented term.

The solution of problem (A.15) is found by using a descent direction algorithm. Neither the Lagrangian (A.16) nor the fields involved in this expression are differentiable for changes of topologies. However, the sensitivities of the field and the Lagrangian can be obtained by applying the topological derivative concept which formally follows the rules of the differential calculus, typically, the chain rule, such as suggested by Amstutz y Andrä (2006).

Following the above-mentioned reference works on this topic, the topological derivative of $\mathcal{T}$ at point $\mathbf{y}$, denoted $D_T\mathcal{T}(\mathbf{y})$, provides the sensitivity of the functional $\mathcal{T}$ with changes of χ at the same point. Let us consider the perturbed characteristic function, χ_ϵ, of the characteristic function χ, that is defined after an interchange of phases within a ball of radius ϵ and centered at the point $\mathbf{y}$. Then the topological derivative satisfies:

$$\mathcal{T}(\chi_\epsilon, \lambda) = \mathcal{T}(\chi, \lambda) + f(\epsilon) D_T\mathcal{T}(\mathbf{y}, \lambda) + \mathcal{O}(\epsilon^3) \tag{A.17}$$

where $f(\epsilon)$ is a term proportional to the perturbed ball volume, and therefore, to ϵ^3 in 3D problems. Equation (A.17) allows to identify $D_T\mathcal{T}(\mathbf{y}, \lambda)$ as the element indicating, at every point of the domain, if a phase change would induce, or not, a decrease of the functional $\mathcal{T}$. This criteria naturally provides a descent direction for modifying the level-set function during an iterative process. This point is further developed in sub-Section 3.4.

The expression for the topological derivative of $\mathcal{T}$ can be written in terms of the topological derivative of the components of the homogenized elasticity tensor C^h_{ij}, denoted $D_T C^h_{ij}$, by simply

applying the conventional chain rule to (A.16), as follows:

$$D_T\mathcal{T}(\mathbf{y},\lambda) = D_T C^h_{44}(\mathbf{y}) + \sum_{i=1}^{3} \lambda_i \; D_T h_i(\mathbf{y}) + \alpha \sum_{i=1}^{3} \left(h_i \; D_T h_i(\mathbf{y})\right) \;, \tag{A.18}$$

and the expressions of the derivatives of the constrains $D_T h_i$ are:

$$\begin{aligned} D_T h_1 &= D_T C^h_{11} + 2 D_T C^h_{12} \\ D_T h_2 &= D_T C^h_{11} - D_T C^h_{12} - D_T C^h_{44} \\ D_T h_3 &= 1 \end{aligned} \tag{A.19}$$

Furthermore, the topological derivative terms, $D_T C^h_{ij}$, can be computed with the expression (A.35) described in Appendix I.

Analogous treatment is performed on equation (A.14), but it is not shown here.

Algorithm implementation

Next, we describe the implementation of the level-set methodology in the context of an FFT technique for computational homogenization. This implementation can be compared with alternative approaches of level-set-methodologies reported in the revision paper by van Dijk et al. (2013).

The iterative algorithm for solving the topology optimization problems (A.13) and (A.14) are described in Appendix II. In particular, two alternative schemes are defined for computing the iterative step length.

i) **Parametrization of the level-set-function (LSF)**

The FFT technique makes use of a discretization of the unit cell defined through a uniform grid of $(N_\alpha + 1) \times (N_\beta + 1) \times (N_\gamma + 1)$ points, such as schematized in Figure A.6. These points divide the volume in $N_\alpha \times N_\beta \times N_\gamma$ voxels; being N_α, N_β and N_γ the number of voxels along the coordinate directions $\boldsymbol{g}_\alpha$, $\boldsymbol{g}_\beta$ and $\boldsymbol{g}_\gamma$, respectively. The vertices of these voxels are the grid points.

The level-set-function $\psi(\mathbf{y})$ is defined in the grid points and is identified by $\hat{\psi}_p = \psi(\mathbf{y}_p)$, where $\mathbf{y}_p$ is the spatial position of the $p-$th grid point. The set $\{\hat{\psi}_p\}$, for: $p = 1, ..., (N_\alpha + 1)(N_\beta + 1)(N_\gamma + 1)$ are the level-set-function parameters.

ii) **Geometry mapping from the LSF parametrization**

The elastic property of the $v-$th voxel represented in Figure A.6, is characterized with the elasticity tensor $\hat{\mathbf{C}}^v$ that is computed with the convex combination of the elasticity tensors

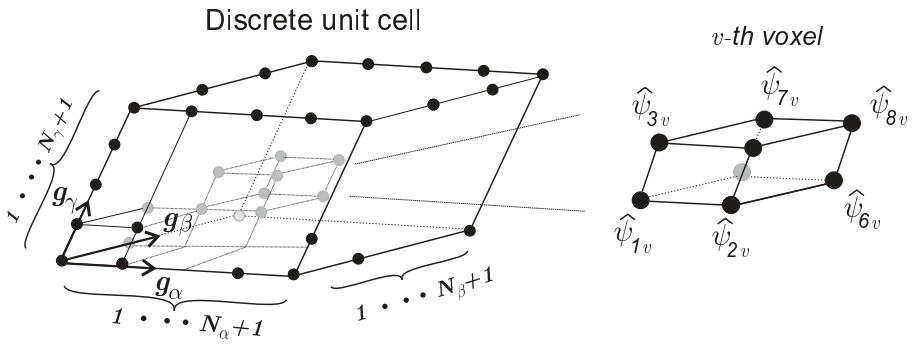

Figura A.6: Discrete unit cell. Parameters of the level-set-function associated with the $v-$th voxel.

$\mathbf{C}_{M_1}$ and $\mathbf{C}_{M_2}$, of phases M_1 and M_2 respectively, as follows:

$$\hat{\mathbf{C}}^v = \hat{\omega}^v \mathbf{C}_{M_1} + (1 - \hat{\omega}^v)\mathbf{C}_{M_2} \tag{A.20}$$

where the coefficient $\hat{\omega}^v$, of the $v-$th voxel, is evaluated with the eight level-set function parameters, $\hat{\psi}_{p_v}$ for: $p_v = 1, ..., 8$, that correspond to the $v-$th voxel vertices, as follows

$$\hat{\omega}^v = \frac{\sum_{p_v=1}^{8} |\hat{\psi}_{p_v}^-|}{\sum_{p_v=1}^{8} |\hat{\psi}_{p_v}|} \quad ; \quad \hat{\psi}_{p_v}^- = \begin{cases} \hat{\psi}_{p_v} & \text{if: } \hat{\psi}_{p_v} < 0; \\ 0 & \text{otherwise} \end{cases} \tag{A.21}$$

with $\hat{\omega}^v \in [0, 1]$. The numerator of this expression is the addition of the absolute values of the level-set function parameters with negative values.

The term $\hat{\omega}^v$ plays the role of a smoothed characteristic function, similar to χ defined in equation (A.6). According to equations (A.20) and (A.21), if the eight level-set-function parameters of a voxel are negative (positive), the elasticity tensor coincides with the elasticity tensor of phase M_1 (M_2). Alternatively, if the level-set function parameters are positive and negative, the material elastic stiffness can be interpreted as a mixture with proportional stiffness to $\hat{\omega}^v$. The salient feature of equation (A.21) is that a smooth transition from $\mathbf{C}_{M_1}$ to $\mathbf{C}_{M_2}$ is induced by a continuous movement of the interface, i.e., the zero iso-surface level-set function, across the voxel.

iii) **Updating the LSF parameters**

Once the topological derivative of $\mathcal{T}$ is known, the level-set-function is updated, at iteration $k + 1$, as follows:

$$\psi^{k+1} = \psi^k + \tau g, \tag{A.22}$$

where $g(\mathbf{y})$ is defined by:

$$g(\mathbf{y}) = \begin{cases} -(D_T\mathcal{T}) & if : \psi < 0 \\ +(D_T\mathcal{T}) & if : \psi > 0 \end{cases}, \tag{A.23}$$

and can be interpreted as a descent direction of $\mathcal{T}$, and τ is a step length. Additional discussions for determining the value of the τ are presented in Appendix II.

For the problem (A.13), the topological derivative of $\mathcal{T}$ is initially computed in the $N_\alpha \times N_\beta \times N_\gamma$ voxels according to equations (A.18), (A.19) and (A.35). Then, they are mapped to the grid points by averaging the values of the neighboring voxels. The resulting nodal derivative at the generic grid point p is denoted $\hat{g}_p$. Finally, the level-set function parameters in the grid points are updated with equation (A.22).

The iterative updating of the Lagrange multipliers λ_i of the Lagrangian function $\mathcal{T}$ are further discussed in the Appendix II.

iv) **Regularization and filtering of the LSF parameters**

The level-set function parameters are filtered through a discrete convolution product

$$\psi^f(\mathbf{y}_p) = (\psi * K)(\mathbf{y}_p) \; ; \tag{A.24}$$

where ψ^f are the level-set function parameters after the filtering and the discrete convolution product is defined as

$$\psi^f(\mathbf{y}_p) = (\psi * K)(\mathbf{y}_p) = \sum_{k=1}^{(N_\alpha+1)\times(N_\beta+1)\times(N_\gamma+1)} \hat{\psi}_k K(\mathbf{y}_k - \mathbf{y}_p) \; ; \tag{A.25}$$

and the Kernel K is

$$K(\mathbf{x}) = \begin{cases} \beta - \frac{\|\mathbf{x}\|}{\ell_f} & if : \|\mathbf{x}\| < \ell_f \\ 0 & if : \|\mathbf{x}\| > \ell_f \end{cases} \; ; \tag{A.26}$$

with the coefficient β being taken such that $\sum_k K(\mathbf{y}_k - \mathbf{y}_p) = 1$, for all p. The filter radius ℓ_f determines the minimum allowed length scale of the designed topology. The topological derivative is also filtered with a similar expression.

v) **Convergence criterion**

Convergence is achieved when the following two criteria are accomplished:

a) Following to Amstutz (2011), a local optimality criterion of problem (A.15) is given by the condition

$$D_T\mathcal{T} > 0 \quad ; \quad \forall \mathbf{y} \in \Omega_\mu$$

which can be implemented by verifying the inequality

$$\frac{\hat{\boldsymbol{g}} \cdot \hat{\boldsymbol{\psi}}}{\|\hat{\boldsymbol{g}}\|\|\hat{\boldsymbol{\psi}}\|} > (1 - tol_\psi) \; ; \tag{A.27}$$

where the vectors $\hat{\boldsymbol{g}}$ and $\hat{\boldsymbol{\psi}}$ collect the values of $\hat{g}$ and $\hat{\psi}$, respectively, of the grid points ($\hat{\boldsymbol{g}} = \{\hat{g}_p\}$ and $\hat{\boldsymbol{\psi}} = \{\hat{\psi}_p\}$, with $p = 1, ..., (N_\alpha + 1) \times (N_\beta + 1) \times (N_\gamma + 1)$).

b) All constraints must be satisfied with given prescribed tolerances:

$$|h_i| < tol_{h_i} \quad ; \quad \text{with } i = 1, 2, 3 \tag{A.28}$$

vi) **Nested grid refinements**

The optimization problems are solved using a grid refinement scheme. Initially, they are solved with a rather coarse grid of points. Once their solutions attain the convergence criteria in this coarse grid, the solutions are projected onto a finer grid, and the iterative scheme is restarted.

Each refinement step consists of exactly doubling the number of voxels per cell side, and therefore, from one step to the next, the number of voxels increases with a factor 8. Using this approach, the level-set function parameters of the coarser grid are projected onto the finer one. The projection procedure is the following: i) For coincident points of both grids, the parameters are identically copied. ii) For those points of the finer grid not coinciding with the points of the coarser grid, the parameters are the average values of the parameters defined in the closest points of the coarser grid, such as it is sketched for a 2D problem in Figure A.7.

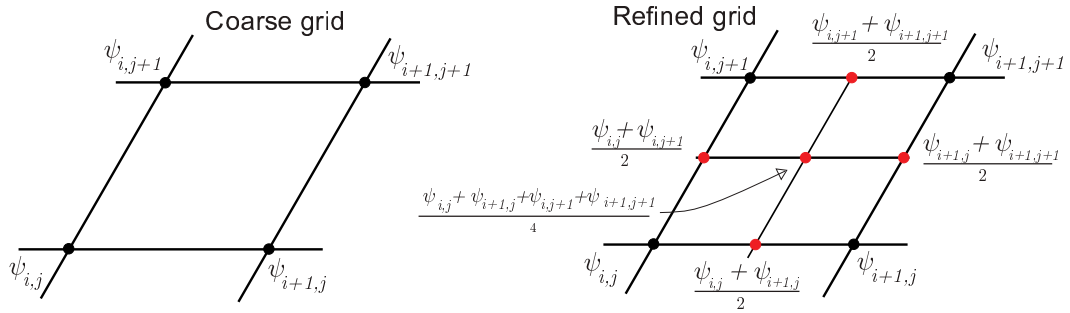

Figura A.7: Nested grid refinement procedure. Mapping of the level-set function parameters, from the coarser grid onto the finer one.

3.5. Strategy for imposing the space group symmetry

The topology computed at each iteration of the optimization algorithm is forced to exhibit the crystal symmetry defined by a preestablished space group. To get this objective, we adopt the following strategy.

a) First, the set of points belonging to the asymmetric unit[4] of the design domain is identified.

[4]The asymmetric unit and the corresponding image points are defined for all the space groups in the International Tables of Crystallography (London (2004)).

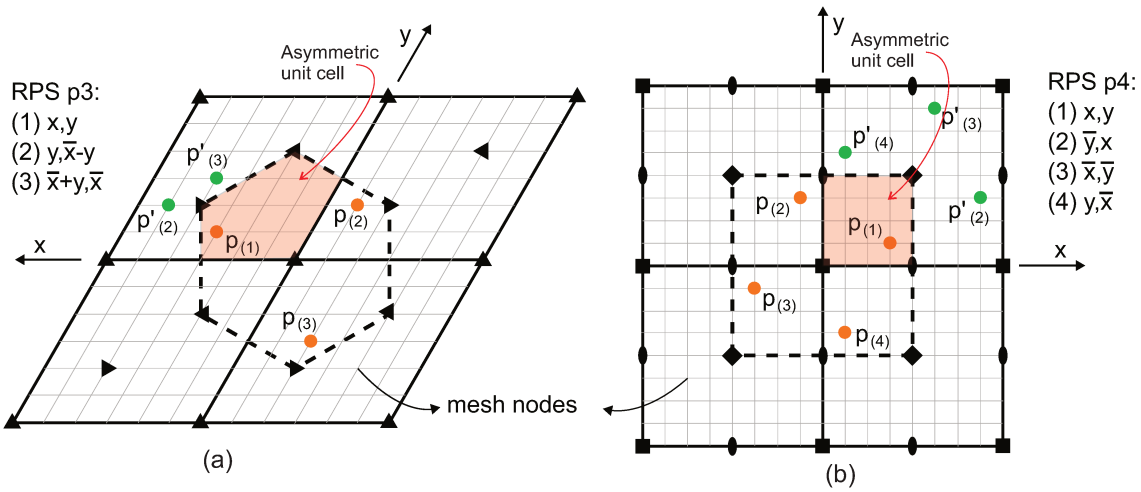

Figura A.8: Procedure to impose the 2D crystal symmetry. Plane groups (a) $p3$ and (b) $p4$. Primitive cells are depicted with solid lines and Wigner-Seitz (Voronoi) cells with dotted lines. Orange dots are image points which are located using the RPS information for every point in the asymmetric unit cell. Green dots are the result of the symmetry translations of orange points that lay outside the parallelepiped cell.

b) The image points, related to the asymmetric unit points through the symmetry operations of the space group, are next identified. Both set of points depend on the crystal space group.

c) In each iteration of the optimization algorithm, the average values of the level-set function parameters and topological derivatives of the asymmetric unit point and its image points are computed. These average values are assigned to all of them.

For regular grids of points, such as those used in the FFT scheme, the identification of the image points associated with every point in the asymmetric unit is achieved by using the regular point system (RPS)[5], see Vainshtein (2013). Examples of RPS and the mechanism of locating the image points in the grid are shown in Figure A.8 for two 2D cases. Information about the adopted origin of the coordinate system and the RPS for plane and space groups are specified in the International Tables for Crystallography London (2004). In the case of the plane group $p3$, the coordinates taken as examples of generic coordinates are $x = 3/6$ and $y = 1/6$, while for the plane group $p4$, these coordinates are $x = 3/8$ and $y = 1/8$. [6]

4. Numerical assessments

Microarchitecture design problems to attain composites with isotropic elastic properties close to the theoretical estimated bounds are next solved. Main results of this task have been presented by

[5] An RPS is the set of points that are associated with one generic point, occupying an arbitrary spatial position, through the symmetry group operations. The coordinates of these points are expressed as a function of the generic point coordinates.

[6] To be consistent with the notation used in the International Tables of Crystallography (London (2004)), the coordinates in Figure A.8 are denoted (x, y) instead of the usual notation for the contravariant coordinates that we have adopted in this work.

the authors elsewhere, see Yera et al. (2019), where the influence of imposing crystal symmetries to attain the desired objective has been evaluated by testing four space groups of the cubic crystal systems for 3D problems. Additional results of similar problems have been reported by Andreassen y Lazarov (2014).

The numerical performance of the topology optimization algorithms is analyzed in three specific design cases. They aim at attaining microstructures whose effective properties display: a) one of the most negative Poisson's ratios (auxetic composite); b) the stiffest response and c) pentamodal features. The effective elastic properties of these composites in the space $(\hat{\kappa}, \hat{G})$ occupy the locations displayed in Figure A.5. The composites with negative Poisson's ratios have their properties on the left region of the HS-bound. They are composites demanding high shear modulus and small bulk modulus. The stiffest composite is positioned at the upper right bound in the $(\hat{\kappa}, \hat{G})$ space, demanding high $\hat{\kappa}$ and $\hat{G}$ moduli, and pentamode composites are characterized by small shear modulus and are positioned at the lower HS-bound in the same space. Three instances of pentamode composites are solved.

The attained optimal solutions depend on the crystal symmetry adopted for solving the topology optimization problem. Yera et al. have shown that closer solutions to the theoretical bounds can be found by choosing suitable crystal space groups for each case. For example, the space groups $I23$ and $P23$ are appropriate to attain maximal properties in the region close to the HS-left bound, coincident with the response of auxetic materials. Furthermore, the proper selection of the optimization domain, Ω_μ, has also a notable influence. In the same paper, Yera et al. also show that topologies with bcc primitive cell provide topologies with closer properties to the HS upper bound than those provided by a simple cubic cell.

4.1. Specific technique for solving the present numerical assessments

The topology optimization algorithm described in Appendix II, with scheme 2, has been used for solving the auxetic composite. The remaining microarchitectures reported in this Section have been obtained with the same algorithm but using scheme 1.

The optimization process starts by taking a grid with $32 \times 32 \times 32$ voxels. It is followed by posterior refinements till reaching grids of $256 \times 256 \times 256$ voxels[7]. The initial topology configurations in all cases are a random distribution satisfying the target volume fraction of the stiff phase.

The solutions of the problems reported in this work are obtained with the filter radius fixed to zero. However, as it can be observed in the attained topologies of Figures A.10 to A.14, they do not display a finer sub-scale. This outcome may be due to the adopted grid refinement strategy. The

[7]The sequence of grid refinements consists of taking $32, 64, 128$ and 256 voxels per spatial dimension.

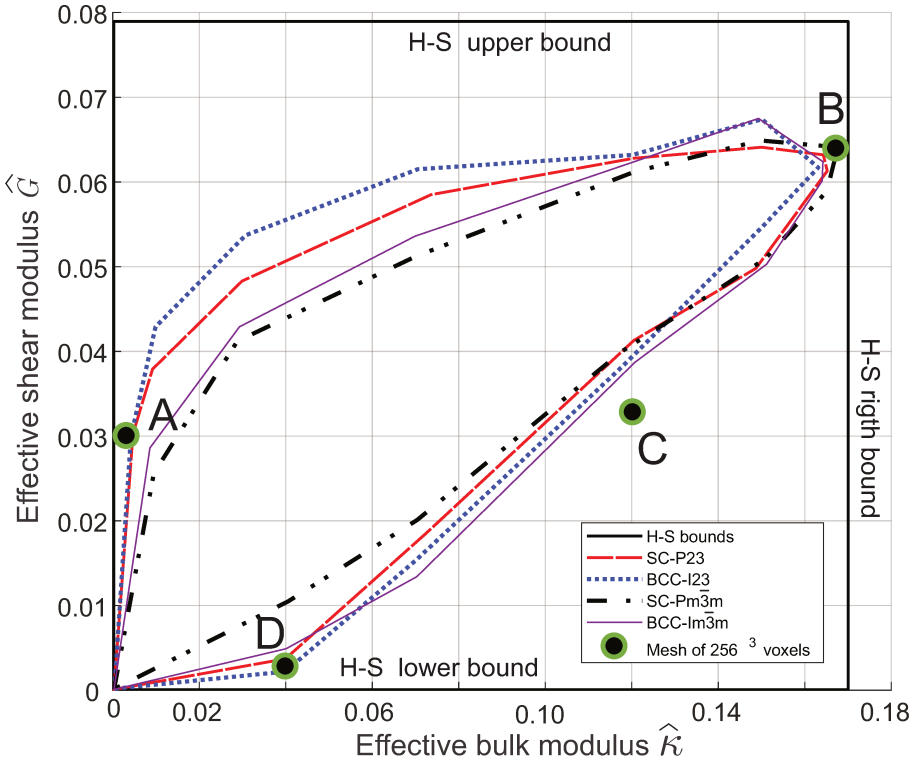

Figura A.9: The points A, B, C and D in the plane $(\hat{\kappa}, \hat{G})$ have been obtained with the present methodology and grids of $256 \times 256 \times 256$ voxels. The curves have been taken from Yera et al. (2019) with the space groups and unit cells of the cubic crystal system: P23 with a primitive cubic cell (SC-P23), I23 with a bcc primitive cell (BCC-I23), $Pm\bar{3}m$ with primitive cubic cell (SC-$Pm\bar{3}m$) and $Im\bar{3}m$ with bcc primitive cell (BCC-$Im\bar{3}m$). HS-bounds of effective properties for two-phase isotropic 3D composites according to Hashin y Shtrikman (1963) (HS-bounds).

coarse grid taken for starting the optimization process precludes the generation of a fine topology structure. We have observed that in the posterior grid refinement steps, the algorithm does not longer introduce a sub-scale.

4.2. 3D topology design problems

The designed composites have the same elastic properties, for both phases, defined in the previous sub-Section 3.1. Therefore, the Figure A.9 copies the HS-bounds in the space $(\hat{\kappa}, \hat{G})$ depicted in Figure A.5. In the same Figure A.9, we also show four solutions A; B, C, and D that have been obtained with the present methodology. They are discussed in sub-Sections 4.2, 4.2, 4.2:case-a and 4.2:case-b, respectively. Following the suggestions raised by Yera et al., different space groups have been imposed on the topology optimization problems to get these solutions. The results reported by these authors using grids of 100 voxels are also shown in the Figure.

Finally, the last example in sub-Section 4.2:case-c, describes a particular solution of a penta-mode composite with a smaller volume fraction $f_1 = 0.1$.

Auxetic materials

The synthesis of auxetics materials has recently raised an enormous interest in the community due to the unusual properties that they display, such as increased resistance to indentation, synclasticity, improvement of fracture toughness, etc. (Saxena et al. (2016) and Cabras y Brun (2014)). For example, Podestá et al. (2018b) have shown that optimal design of elastic structures demands the use of auxetics materials.

In this test, the objective is to attain an isotropic composite with minimum Poisson's ratio for a relatively high target shear modulus. The problem formulation (A.14) is used in this case with a target shear modulus[8] $G^{tg} = 0.03$.

The designed microarchitecture has been solved with an imposed space group $I23$ of the cubic crystal system. Figure A.10 displays the resulting topology, and their effective elastic properties are plotted in Figure A.9, point A. The components of the attained homogenized elasticity tensor are: $C^h_{11} = C^h_{22} = C^h_{33} = 0.041500$, $C^h_{12} = C^h_{23} = C^h_{13} = -0.018739$ and $C^h_{44} = C^h_{55} = C^h_{66} = 0.060176$. Thus, the attained Poisson's ratio is -0.82 and the volume fraction is $f_1 = 0.3383$.

We use the Zener ratio to quantify the anisotropy of the effective material properties having cubic symmetry. The Zener ratio is computed with the formula: $\xi = C^h_{44}/(C^h_{11} - C^h_{12})$. A value 1 for this ratio indicates that $\mathbf{C}^h$ is isotropic.

The present solution has a Zener ratio of value $\xi = 0.9989$, very close to 1, and therefore, it satisfies almost exact isotropic response. It is important to remark that several auxetic composites reported in the literature are strongly anisotropic.

Deformation mechanism of the designed auxetic material

Additional insight respect to the deformation mechanism characterizing the microarchitecture of Figure A.10 can be conceived by analyzing an alternative, but equivalent, solution. First, notice that the topology depicted in Figure A.10, obtained with the space group $I23$, tends to show a higher symmetry than the enforced one. According to this observation, we achieve a simpler microstructure, though slightly less efficient, by imposing the space group $I\bar{4}3m$. The so-attained microstructure is described in Figure A.11 and its effective Poisson's ratio is -0.74. Notice that the main difference between the solutions of Figures A.10 and A.11 lies on the thin sub-structures that are commonly attained when extreme materials are designed.

The deformation mechanism of the simpler microstructure in Figure A.11 is next explained. Figures A.11 (a) and (b) show the primitive and conventional cells. Figures A.11 (d) and (e) present

[8] It is worth to mention that solutions reported by Yera et al. (2019) and Andreassen y Lazarov (2014) show that it is possible to attain more negative Poisson's ratios using smaller target values of the shear modulus G^{tg}.

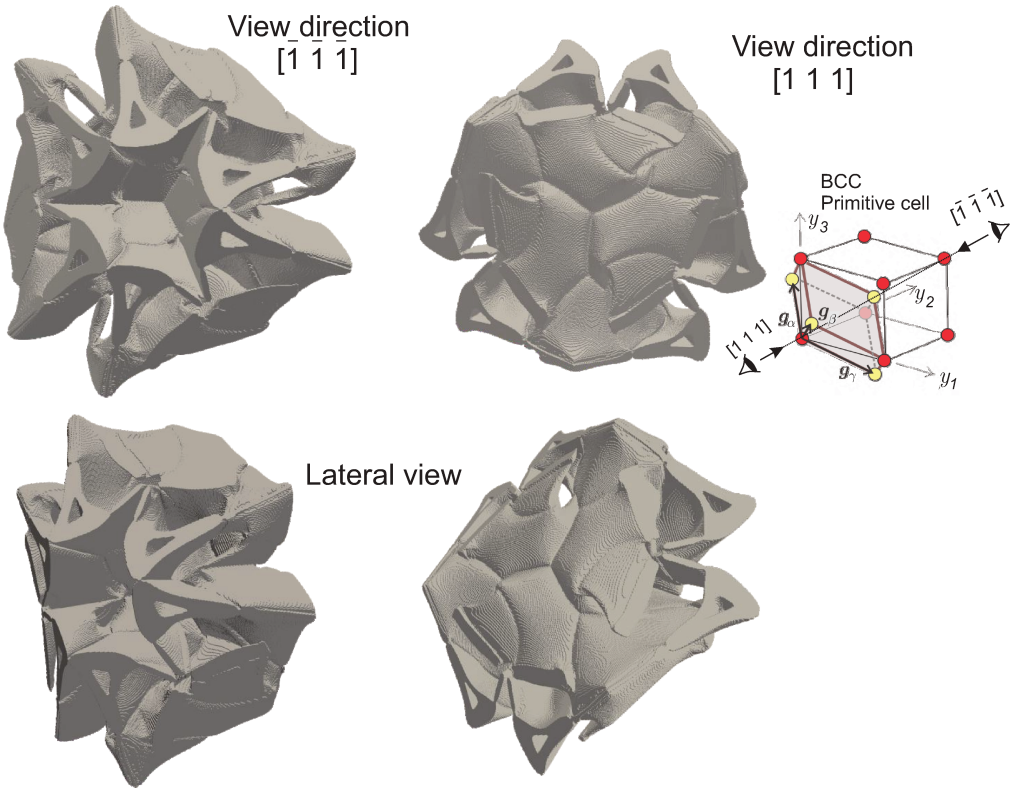

Figura A.10: Primitive cell of the composite with elastic properties corresponding to Point A in Fig A.9. Imposed space group $I23$. Primitive cell observed from two opposite viewpoints: $[\bar{1}\bar{1}\bar{1}]$ and $[111]$. The Poisson's ratio of this microstructure is -0.82, the effective shear modulus $\hat{G} = 0.0301$ and the effective bulk modulus $\hat{\kappa} = 0.0013405$.

the details of the interior region of the conventional cell and the external faces of the conventional cell, respectively. Also, they sketch the deformation mechanism when the microstructure is subjected to a macroscopic strain.

Three cell configurations are presented in Figures A.11 (d) and (e). The central pictures display the original configurations of the cell. The pictures on the right side display the deformed cell when it is stretched in the direction $[1\,0\,0]$. The pictures on the left side display the deformed cell when it is compressed in the same direction. Notice the original and deformed positions of the points 1, 2 and 3 in the three configurations of Figure A.11 (d). It can be seen the microstructure unfolding mechanism that is activated when it is stretched; the points are moving away and the dihedral angle α increases. Alternatively, in the reverse direction, in a compressive regime, the microstructure folding mechanism is activated; the points are approaching and the dihedral angle α decreases. The points 1, 2 in the three configurations of the Figure A.11 (e) display a similar folding/unfolding mechanism.

We point out that the deformation mechanism of the microstructure could be envisaged through the simpler deformation mechanism displayed by the origami in Figure (c). Both structures deform following a similar pattern.

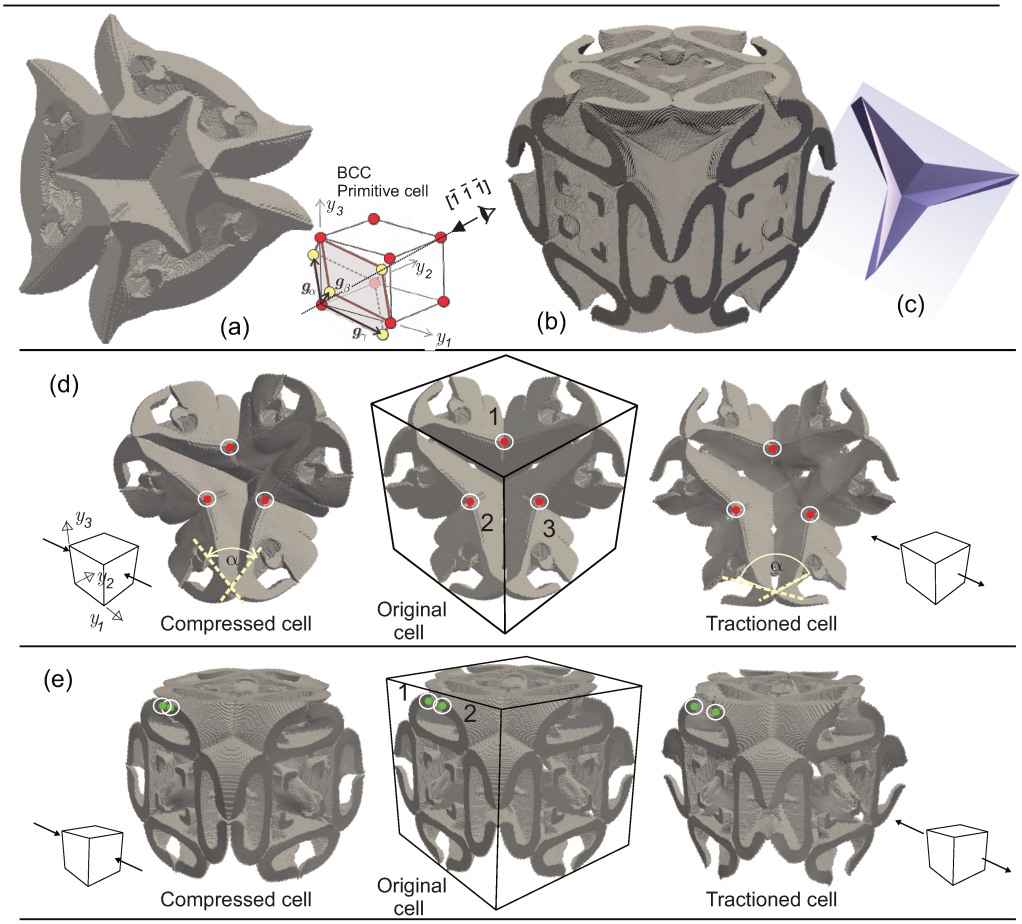

Figura A.11: Auxetic composite with space group $I\bar{4}3m$ and Poisson's ratio -0.74. (a) Primitive cell observed from viewpoint $[\bar{1}\,\bar{1}\,\bar{1}]$. (b) Conventional cell. (c) Origami displaying a similar deformation mechanism to the auxetic composite. (d) Half of the conventional cell constituted by the contribution of four primitive cells. Internal region views. (e) External views of the conventional cell.

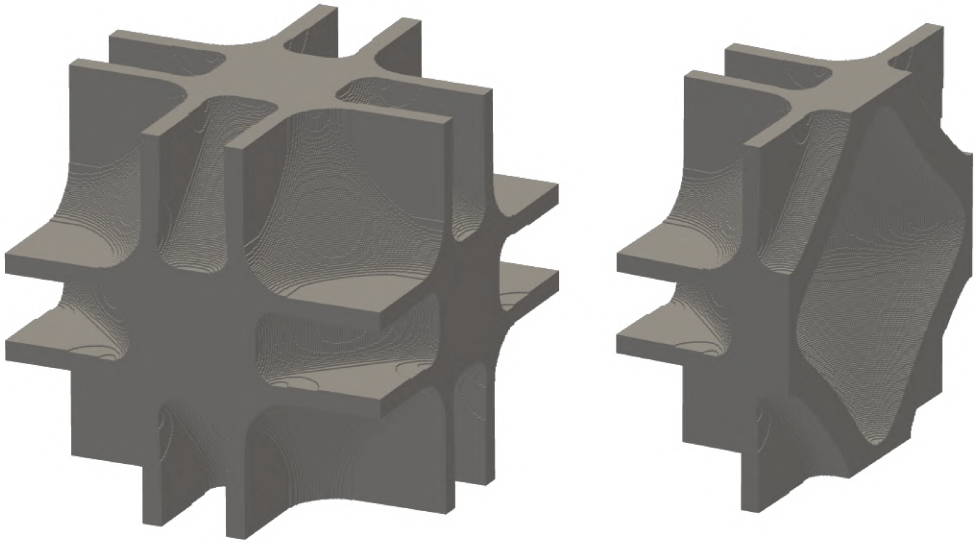

Figura A.12: Topology of the maximum stiffness composite, point B in Figure A.9, designed with a $Pm\bar{3}m$ space group. (a) Primitive cell. (b) Trimmed microcell showing the interior void.

Maximum stiffness materials

With the present approach, we have noted that the topology optimization algorithm finds solutions close to the HS-right bound more easily than solutions close to the HS-upper bound. According to this observation, in this problem, we find the topology by solving a maximization problem with the formulation (A.13). The target bulk modulus is $\kappa^{tg} = 0.167$ close to the upper bulk modulus, $\kappa^{u} = 0.1704$, estimated by the HS-bounds. The enforced space group is $Pm\bar{3}m$. The design domain is the primitive cell of the simple cubic Bravais lattice.

Figure A.12 displays the attained topology. It is constituted of a void volume covered with a layered structure in three orthogonal directions that contributes to increasing the shear stiffness. This topology can be compared with the microstructure of Figure A.14 obtained for high bulk modulus and low shear stiffness.

The homogenized elasticity tensor components of the microarchitecture displayed in Figure A.12 is: $C^h_{11} = C^h_{22} = C^h_{33} = 0.252523$, $C^h_{12} = C^h_{23} = C^h_{13} = 0.124672$ and $C^h_{44} = C^h_{55} = C^h_{66} = 0.127826$, with effective bulk and shear moduli plotted in Figure A.9, point B. The Zener ratio is $\xi = 0.9998$.

Pentamode materials

The name of pentamode materials has been coined by Milton y Cherkaev (1995)[9] to designate the class of composites displaying a stiff response for one characteristic strain mode while displa-

[9] At the same time, Sigmund (1995) has independently introduced this kind of composites in the context of inverse homogenization problems.

ying easy modes of deformations for the remaining five characteristic strain modes. We consider that the characteristic strain modes are assumed to be the six eigenvectors of the elasticity tensor. Thus, for a typical isotropic material, the stiff deformation mode can be associated with the eigenvalue coinciding with the bulk modulus, while the compliant response is associated with the shear modulus. It means that a pentamode material displays an almost null shear modulus jointly with a non-null bulk modulus. Pentamode materials have an interest because any achievable effective elastic material can be generated using an assemblage of pentamode materials, such as mentioned in the paper by Milton y Cherkaev (1995). In this reference work, the authors also propose a natural candidate for the pentamode materials, being a diamond-type structure in which four linkages meet at a point.

Case a: microstructure of a pentamode composite attained with $P23$ space group (point D in Figure A.9)

We solve the problem (A.13) with $\kappa^{tg} = 0.04$ and the imposed space group $P23$. The solved microstructure is displayed in Figure A.13, and it has effective properties which correspond to the point D in Figure A.9. The components of its homogenized elasticity tensor are: $C^h_{11} = C^h_{22} = C^h_{33} = 0.04363$, $C^h_{12} = C^h_{13} = C^h_{23} = 0.03817$ and $C^h_{44} = C^h_{55} = C^h_{66} = 0.00630$. Thus, the Zener coefficient is $\xi = 1.1538$, with a ratio: $\kappa^h/G^h \approx 13$. The six eigenvalues of the elasticity tensor are 0.1997, 0.0630, 0.0630, 0.0630, 0.0547 and 0.00547, respectively, Then, the ratios between the maximum λ_{max}, the medium λ_{med} or the minimum λ_{min} eigenvalues are: $\lambda_{max}/\lambda_{med} = 19$ and $\lambda_{max}\lambda_{min} = 22$,

The topology is constituted of four interconnected helix-like sub-structures. Each sub-structure is formed by three linked bulky elements. Details of the links are displayed in Figure A.13-b. Unlike the Milton microstructure that is analyzed in the following case-c, in this topology, the linkage of the three bulky elements is not reduced to a point. Additionally, as it can be observed in Figure A.13-a, the internal region of the cell displays the four helix-like sub-structures which are interconnected through a small microstructure constituted by four bars.

From this result, we can conclude that the deformation mechanisms generated by the four helix-like linked substructures are responsible for providing an almost isotropic effective elastic response of the composite, while their linkage would probably need the introduction of a sub-topology, with a smaller length scale to further decrease the effective shear modulus.

Case b: Microstructure of a pentamode composite attained with the $Im\bar{3}m$ space group (point C in Figure A.9)

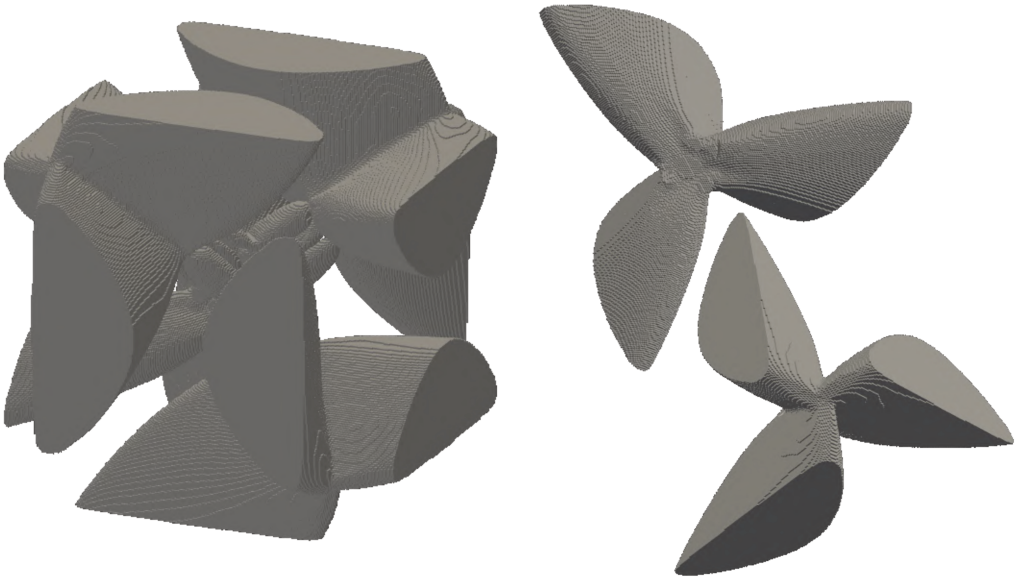

Figura A.13: Pentamode material attained with the space group $P23$. Effective properties corresponds to point D of Figure A.9. (a) Primitive cell; (b) detail of the joints of the substructures.

Although the microstructure of Figure A.13 displays a high bulk to shear moduli ratio, it is attained by imposing a low target bulk modulus $\kappa^{tg} < \kappa^{u}/4$. With higher values of κ^{tg}, the ratio κ^{h}/G^{h} of the attained composites decreases and their material properties tend to move away from the lower theoretical HS-bound.

A typical case is the topology shown in Figure A.14, which corresponds to Point C in Figure A.9, obtained with the formulation (A.13), with $\kappa^{tg} = 0.12$ and imposing a space group symmetry $Im\bar{3}m$. This result shows two well-recognized sub-structures which are linked through a bar-like system of elements. The components of the homogenized elasticity tensor of this microstructure are: $C^{h}_{11} = C^{h}_{22} = C^{h}_{33} = 0.16458$, $C^{h}_{12} = C^{h}_{13} = C^{h}_{23} = 0.09815$ and $C^{h}_{44} = C^{h}_{55} = C^{h}_{66} = 0.06500$. Thus, the Zener coefficient is $\xi = 0.9785$,

The attained shear modulus of this microstructure is far from the lower HS-bound. However it is interesting to note certain similitude with the topologies reported by Sigmund (2000) for the equivalent problem, identified as the Walpole point problem in 2D. Both 2D and 3D structures have the maximum possible symmetry, i.e. $p6mm$ with a hexagonal lattice in the 2D case, and $Im\bar{3}m$ with a bcc lattice in the 3D case. Another remarkable aspect is that both topologies tend to include additional sub-structures displaying a smaller length scale. Compare Point 9 of Figure 7 in Sigmund's work and the details in Figure A.14-(b). In the 2D case, the lower length scale structure is a laminated material.

In the 3D case reported here, two independent saddle-shaped sub-structures conform, after cell assembly, a system of hollow "tubes" which are interconnected by parallel bars/cylinders in three directions, such as observed in the details depicted in Figure A.14. Remarkably, Milton y

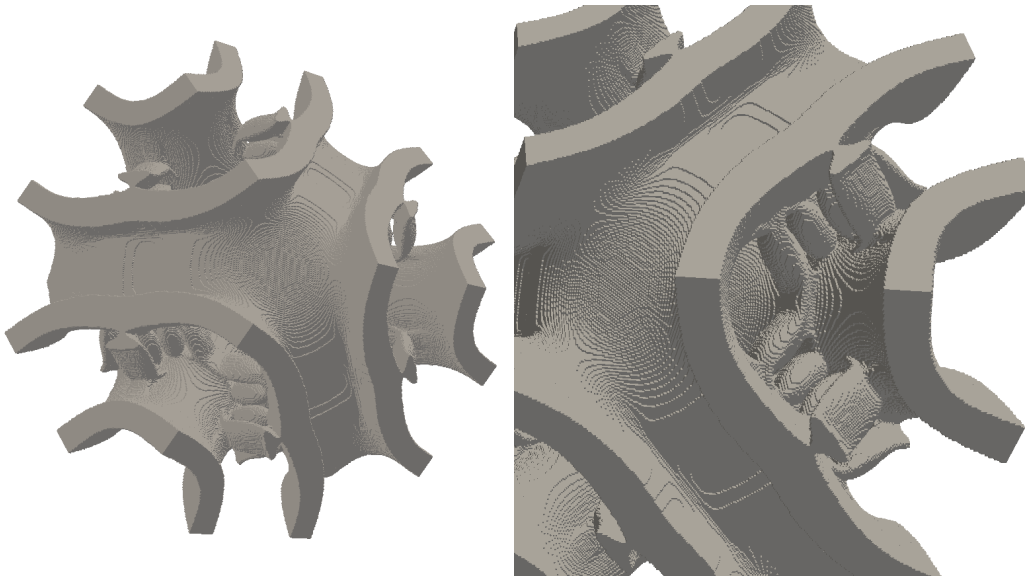

Figura A.14: Topology obtained with the $Im\bar{3}m$. Effective properties corresponds to Point C in Fig A.9. Primitive cell and details of links between the two sub-structures constituting the composite.

Camar-Eddine (2018) have recently discussed similar kinds of microstructures in the context of isotropic pentamode material. The microstructures proposed by these authors have almost zero shear modulus and can be realized with a system of parallel cylinders, having characteristic sizes much lower than the microarchitecture size, which are inserted into structures having maximum bulk and shear moduli. These cylinders are placed in a sufficient number of orientations to ensure the isotropy of the composite. Additionally, in the discussion presented by Milton et al. (2017), it has been pointed out that multiscale substructures are necessary to achieve simple topologies with properties close to the theoretical bounds. According to these comments and due to the design constraints that we adopt in this work, the bar system observed in Figure A.14 does not constitute a true lower scale length of the microstructure, and therefore, they could be the reason for preventing an additional decrement of the shear modulus.

Case c: microstructure of a pentamode composite attained with $F\bar{4}3m$ space group and smaller volume fraction

The diamond's cubic structure depicted in Figure A.15, with the internal atoms *i* equal to the face atoms *f* of the conventional cell, has a crystal symmetry with the $Fd\bar{3}m$ space group and fcc Bravais lattice. When the atoms *i* are different to atoms *f*, the crystal symmetry is lowered to the space group $F\bar{4}3m$.

An interesting point demonstrating the potentiality of the present methodology lies in the fact that by imposing a space group $F\bar{4}3m$, with fcc Bravais lattice, we attain a microarchitecture similar to that proposed by Milton et al., displaying the higher symmetry $Fd\bar{3}m$ of the diamond-

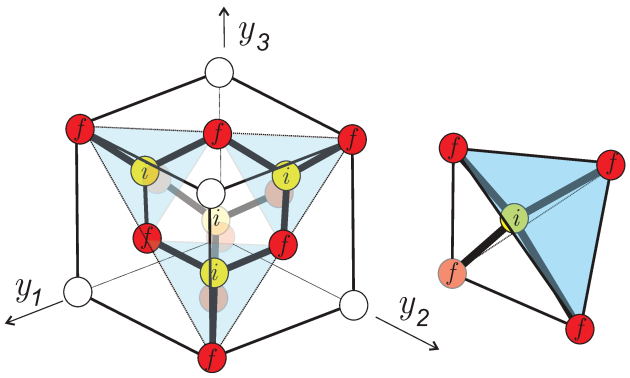

Figura A.15: Diamond's crystal structure. Atoms f are on the unit cell faces and atoms i are on the interior of the cell.

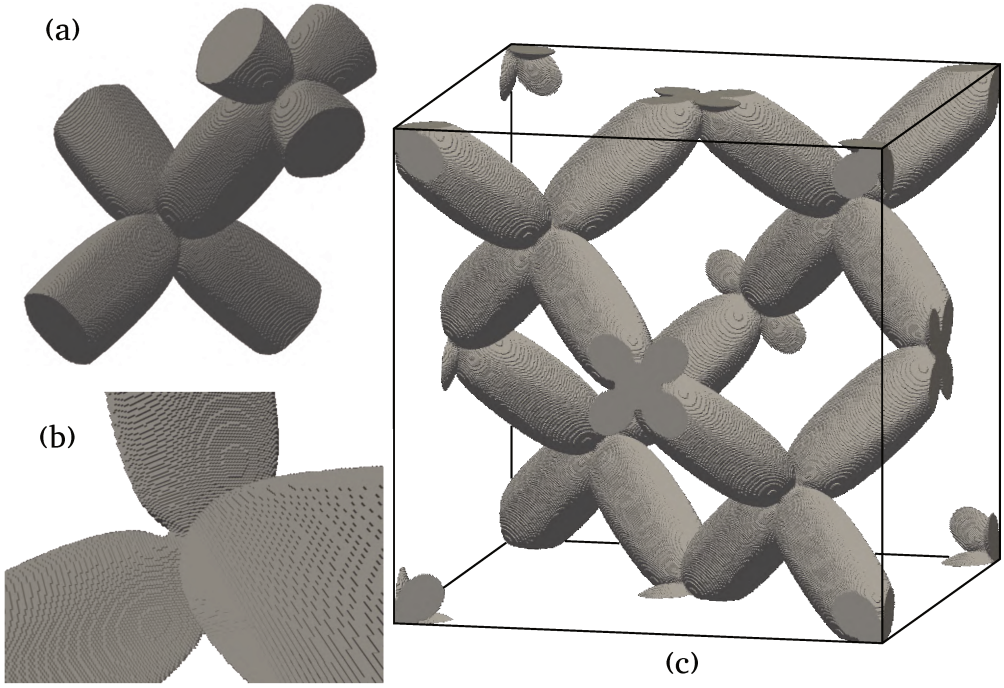

Figura A.16: Topology obtained with space group $F\bar{4}3m$. (a) Primitive parallelepiped cell; (b) Detail of the joints shape; (c) Conventional cell.

like structure. This solution is shown in Figure A.16 and has been obtained for a stiff volume fraction of 0.1. This microstructure is slightly different from that reported by Kadic et al. (2012). In the present case, the optimal bars conforming the diamond-like microstructure are similar to ellipsoids, with the section of the bars not being exactly circular but similar to hexagons with rounded vertices, as can be noted in the Figure.

A detail of the geometry of the bar joints are shown in Figure A.16-(b).

The homogenized elasticity tensor is $C_{11} = 0.00994$, $C_{12} = 0.00936$ and $C_{44} = 0.00157$. The six eigenvalues of this tensor are: 0.02866, 0.00157, 0.00157, 0.00157, 0.00057, and 0.00057. Thus, the six eigenvalues of the elasticity tensor are 0.02866, 0.00157, 0.00157, 0.00157, 0.00057, and 0.00057, respectively. And the ratios between the maximum, λ_{max}, the medium, λ_{med} or the minimum, λ_{min}, eigenvalues are: $\lambda_{max}/\lambda_{med} = 18$ and $\lambda_{max}/\lambda_{min} = 50$. The Zener coefficient

is $\xi > 2$ resulting a composite whose properties are far from being isotropic. In this case, the specific tolerance of the algorithm corresponding to the isotropy constraint has been handled to force the convergence conditions.

The ratio $\kappa^h/G^h = 16$ is low if compared with the results reported by Kadic et al. However, note that the solution of Kadic et al. corresponds to a volume fraction less than 0.05.

4.3. Computational burden for solving the topology optimization problems

Several additional tests have been performed to assess the computational burden demanded by the present methodology. The four topology optimization problems denoted A, B, C and D in Figure A.9 have been solved with:

i) two space groups: $P23$ and $I23$, and

ii) using the iterative schemes 1 and 2 described in Appendix II.

Ten instances of each problem have been tested. For each instance, the iterative process is initiated with a random distribution of the stiff phase and a grid of $32 \times 32 \times 32$ voxels. After convergence, a new iterative process is started with a grid of $64 \times 64 \times 64$ voxels. In this case, the initial material configuration is the projection of the coarse grid solution onto the fine grid.

The results, in terms of computational burden, are reported in Table **??**. This table compares the number of tests that have converged, the total number of iterations required to converge, the number of homogenization evaluations that have been performed and the attained best objective function value of each problem.

The Table rows denoted: *C/T* report the ratio between the number of converged tests divided by the total numbers of tested instances, which is 10 in all cases; *MNI* report the number of iterations needed to converge (the mean value of the converged instances); *MNH* report the number of times (average) that the homogenization elasticity tensor has been computed; and *BOf* report the attained optimum value of the objective function.

The Table columns $P23$ and $I23$ report the results of the five problems with topologies satisfying the crystal symmetries with either the $P23$ or $I23$ space groups; *Grid* 32^3 and *Grid* 64^3 identify the results obtained with either $32 \times 32 \times 32$ or $64 \times 64 \times 64$ voxels; and *Sch 1* and *Sch 2* identify the iterative scheme, described in Appendix II, adopted to solve the problem. The scheme using a predefined step length (parameter τ in equation (A.22)) is denoted with *Sch 1*. The line search scheme is denoted with *Sch 2*.

Tabla A.2: Computational burden for solving the topology design problems A, B, C and D of Figure **??**. First column identifies the problem.

		P23				I23			
		Grid 32^3		Grid 64^3		Grid 32^3		Grid 64^3	
		Sch 1	Sch 2	Sch 1	Sch 2	Sch 1	Sch 2	Sch 1	Sch 2
A	C/T	6/10	10/10	5/6	10/10	10/10	10/10	10/10	10/10
	MNI	843	366	193	114	816	264	94	87
	MNH	845	1120	194	447	818	872	95	305
	BOf	5.94e-3	6.67e-3	3.67e-3	3.74e-3	4.98e-3	5.30e-3	3.18e-3	2.44e-3
B	C/T	9/10	10/10	9/9	10/10	5/10	9/10	4/8	8/9
	MNI	409	607	68	78	702	906	127	198
	MNH	411	2162	69	221	704	2752	128	457
	BOf	6.67e-2	6.58e-2	6.69e-2	6.79e-2	6.66e-2	6.39e-2	6.66e-2	6.54e-2
C	C/T	10/10	10/10	10/10	8/10	9/10	6/10	9/9	6/6
	MNI	973	629	166	118	875	309	88	58
	MNH	975	1522	167	385	877	915	89	167
	BOf	3.51e-2	3.72e-2	3.40e-2	3.50e-2	3.91e-2	3.97e-2	3.75e-2	3.83e-2
D	C/T	5/10	8/10	4/5	8/8	7/10	8/10	7/7	7/8
	MNH	859	736	23	36	929	630	228	107
	MNH	861	2060	24	116	931	1754	229	317
	BOf	3.62e-3	3.34e-3	2.92e-3	2.50e-3	5.58e-3	3.14e-3	3.99e-3	2.61e-3

According to the data reported in Table **??**, we observe that the number of iteration required for convergence notably changes according to the problem. Additionally, we can estimate the robustness performance of the algorithm by analyzing the number of converged solutions respect to the total number of performed tests.

In most tested cases, scheme 2 demands more homogenization evaluations than scheme 1 to achieve the solution, resulting in a more costly procedure. However, scheme 2 does not need to guess the step length for generic cases, which yields a more reliable procedure.

5. Conclusions

In this paper, we have shown that the microarchitecture design of elastic materials attained through the solution of topology optimization problems, combined with the imposition of pre-defined crystal symmetries, is a viable and robust methodology for designing 3D metamaterials with effective elastic properties close to the theoretical bounds.

To reach this objective, we have adopted two similar topology optimization problems that are formulated as inverse homogenization techniques. The implementation details of the algorithm for solving these formulations have also been presented. The algorithm is based on a level-set function technique with the sensitivities, for the iterative correction of the level-set function, evaluated through the topology derivative of the problem.

We have used an FFT technique reported in the literature to compute efficiently the homogenized elastic properties of 3D composites. The contrast factor for modeling the void phase has been taken small enough to provide accurate solutions without substantially penalizing the computational cost required by the FFT technique. A good performance of the FFT technique has been attained after introducing grey voxels in the interfaces which simulate materials with intermediate properties of the constituent phases.

To confirm the computational efficiency of this homogenization technique, we have presented a detailed numerical assessment consisting of computing the homogenized elasticity tensor of a periodic microstructure with an fcc Bravais lattice. Results, in terms of computational time vs. accuracy, have been compared with solutions obtained using the FEM. Under these circumstances and including the grey material in the model, the FFT technique has a favorable performance if compared with the FEM.

The design technique, as well as the computation of the homogenized elastic properties of composites with arbitrary crystal symmetries and periodic topologies, requires the use of primitive cells of Bravais lattices that are associated with the pre-defined space group imposed to the topology. One of the most salient features of these cells is that they are not necessarily rectangular prisms. Therefore, the use of the FFT technique reported in the literature has to be adapted to these situations where the cell faces are non-orthogonal. This issue has specifically been addressed in this work.

To attain the microarchitectures with effective properties close to the theoretical bounds, we have imposed crystal symmetries with different space groups which have been adopted in concordance with the conclusions of a previous paper of the authors (Yera et al. (2019)). The imposed space groups are compatible with the cubic crystal system. Therefore, the obtained topologies have effective elastic properties with cubic symmetry. Based on this evidence, the isotropy of these microstructures can be measured with the Zener coefficient who is reported for all cases discussed in the paper. Excluding the pentamode material of case c in sub-Section 4.2, in all the remaining cases, the Zener coefficients are close to 1. Therefore, we conclude that the isotropic response is fulfilled in almost the complete set of designed topologies.

In sub-Section 4.3, we have evaluated the computational burden required for solving several topology design cases. An important conclusion can be drawn from the data reported in Table **??**. It refers to the relatively high number of tests that have reached convergence. We conclude that the methodology with the crystal symmetry ingredients displays good and robust performances.

An interesting final remark about the integrated design strategy, here discussed, is its suitability for imposing different space group symmetries due to the regular grids used for solving the FFT

scheme.

Acknowledgments

The authors acknowledge the financial support from CONICET and ANPCyT (grants PIP 2013-2015 631 and PICT 2014-3372 and 2016-2673).

We thank Dr. Ricardo Lebensohn, from Los Alamos National Laboratory, for the discussion hold about some topics related to the FFT homogenization technique in parallelepiped domains addressed in this work.

APPENDIX I: Homogenized elasticity tensor and its topological Derivative

Let us consider the problem sketched in Figure A.1. The macro-stress $\boldsymbol{\sigma}$ and macro-strain $\boldsymbol{E}$ are the volumetric average, in the micro-cell Ω_μ, of the corresponding micro-stress $\boldsymbol{\sigma}_\mu$ and micro-strain $\boldsymbol{\varepsilon}_\mu$ observed at the micro-scale: $\boldsymbol{\sigma} = \langle \boldsymbol{\sigma}_\mu \rangle$ and $\boldsymbol{E} = \langle \boldsymbol{\varepsilon}_\mu \rangle$. Also, $\boldsymbol{\varepsilon}_\mu(\mathbf{y})$ can be split into the average strain $\boldsymbol{E}$ plus a fluctuation term $\tilde{\boldsymbol{\varepsilon}}_\mu(\mathbf{y})$ with zero average value in Ω_μ:

$$\boldsymbol{\varepsilon}_\mu(\mathbf{y}) = \boldsymbol{E} + \tilde{\boldsymbol{\varepsilon}}_\mu(\mathbf{y}) \; . \tag{A.29}$$

The fluctuation micro-strain is the symmetric gradient of a fluctuation displacement field, $\tilde{\mathbf{u}}$ which is periodic on the boundary Γ_μ of Ω_μ. The displacement fluctuations $\tilde{\mathbf{u}}$ are periodic along the directions defined by the primitive vectors of the Bravais lattice.

Stresses and strains at the macro-scale are related through the homogenized elasticity tensor $\mathbf{C}^h$:

$$\boldsymbol{\sigma} = \mathbf{C}^h \boldsymbol{E} \; , \tag{A.30}$$

and stresses and strains at the micro-scale are related through the constitutive law:

$$\boldsymbol{\sigma}_\mu(\mathbf{y}) = \mathbf{C}(\mathbf{y}) \boldsymbol{\varepsilon}_\mu(\mathbf{y}) \, . \tag{A.31}$$

where $\mathbf{C}(\mathbf{y})$ is the elasticity tensor of phase at the point $\mathbf{y}$. Additionally, $\boldsymbol{\sigma}_\mu$ is a self-equilibrated stress field: $\nabla \cdot \boldsymbol{\sigma}_\mu = \mathbf{0}$ in Ω_μ.

By following to Moulinec et al, the micro-scale field equations with the corresponding boundary conditions can be rewritten as an auxiliary problem and reduced to the Lippmann-Schwinger integral equation for $\tilde{\boldsymbol{\varepsilon}}_\mu(\tilde{\mathbf{u}})$, which, finally, can be iteratively solved in the frequency space, using a fixed-point algorithm.

Homogenized elasticity tensor

Let us define the canonical base of the macro-strain tensors $\mathcal{E} := \{\boldsymbol{E}^{I_1}, ..., \boldsymbol{E}^{I_6}\}$, where the indices $I_1, I_2, ..., I_6$ identify every one of the six strain bases $\boldsymbol{E}^{I_m}$. The six components of each strain base is written in the conventional way, $E_{ij}^{I_n}$, with $i, j = 1, 2, 3$. Then, the components of the canonical strain bases are defined by

$$\boldsymbol{E}_{ij}^{I_n} = \begin{cases} 1 & \text{if } (i,j) \in I_n \\ 0 & \text{if } (i,j) \notin I_n \end{cases} \tag{A.32}$$

where the following association between component indices, i, j, and strain base indices, I_n, is defined: $(1,1) \in I_1$; $(2,2) \in I_2$; $(3,3) \in I_3$; $\{(1,2),(2,1)\} \in I_4$; $\{(2,3),(3,2)\} \in I_5$; $\{(1,3),(3,1)\} \in I_6$.

The components of the homogenized elasticity matrix[10] is computed with the expression:

$$\mathbf{C}_{mn}^{h} = \boldsymbol{\sigma}(\boldsymbol{E}^{I_m}) : \boldsymbol{E}^{I_n} \qquad ; \qquad m, n = 1, 2, ..., 6 \; ; \tag{A.33}$$

where $\boldsymbol{\sigma}(\boldsymbol{E}^{I_m})$ is the homogenized macro-stress satisfying the multiscale equations, defined above, for the given macro-strain $\boldsymbol{E}^{I_m}$.

Thus, six problems $\boldsymbol{\sigma}(\boldsymbol{E}^{I_m})$, with $m = 1, ...6$, are solved. Associated to each one of them, the micro-strain $\varepsilon_{\mu}^{I_m}$ and the micro-stress $\boldsymbol{\sigma}_{\mu}^{I_m}$ are also computed in the micro-cell. According to equation (A.29), the micro-strain $\boldsymbol{\varepsilon}_{\mu}^{I_m}$ is split as follows:

$$\boldsymbol{\varepsilon}_{\mu}^{I_m}(\mathbf{y}) = \boldsymbol{E}^{I_m} + \tilde{\boldsymbol{\varepsilon}}_{\mu}^{I_m}(\mathbf{y}), \tag{A.34}$$

where $\tilde{\boldsymbol{\varepsilon}}_{\mu}^{I_m}$ is a fluctuation term with zero average value on the micro-cell.

Topological derivative of the homogenized elasticity tensor

The book by Novotny y Sokołowski (2012) describes the topological derivative of the energy function associated with an elastic boundary value problem defined in a given spatial domain. Following this approach, Giusti (2009) develops the topological derivative of the effective elasticity tensor obtained using a computational homogenization procedure for 2D problems. This term has subsequently been used by Amstutz et al. (2010) for solving a topology optimization algorithm. Here, we only present a summary of these concepts and the expression used for the topology derivative in 3D problems, see Giusti (2019) and Lopes et al. (2015).

The topological derivative of the homogenized elasticity tensor represents the sensitivity of this tensor to infinitesimal spherical perturbation in the homogenization domain, such as sketched in Figure A.17. Let us consider that, at the point $\hat{\mathbf{y}}$ of the microcell, it exists the base elastic material with the Lamè parameters $(\lambda; \mu)$ and Poisson's ratio ν. This material is substituted by an infinitesimal spherical perturbation with another elastic material with parameters $(\lambda_0; \mu_0)$. Then,

[10] At this point, we are implicitly introducing the Kelvin notation for tensors.

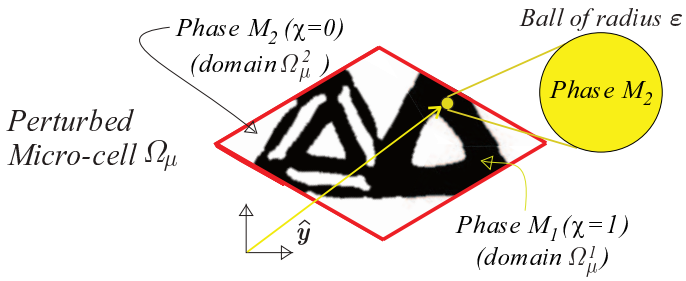

Figura A.17: Perturbed micro-cell domain.

the topological derivative of the homogenized elasticity tensor can be computed with the expression:

$$D_T \mathbf{C}^h_{mn}\left(\chi(\hat{\mathbf{y}})\right) = \boldsymbol{\varepsilon}^{I_m}_\mu(\hat{\mathbf{y}}) : \mathbb{P} : \boldsymbol{\varepsilon}^{I_n}_\mu(\hat{\mathbf{y}}) \qquad ; \qquad m,n = 1,...,6 \tag{A.35}$$

where $\mathbb{P}$ is the polarization tensor[11].

$$\mathbb{P} = \alpha_1 \left(\alpha_2(\mathbf{1}\otimes\mathbf{1}) + 2\mathbb{I}\right) \; ; \tag{A.36}$$

the symbols $\mathbf{1}$ and $\mathbb{I}$ represent the second and fourth order unit tensor, respectively, and the coefficient α_1 and α_2 are:

$$\begin{aligned} \alpha_1 &= \left(\frac{15\mu\delta_\mu(\nu-1)}{15\mu(1-\nu)+2\delta_\mu(5\nu-4)}\right); \\ \alpha_2 &= \frac{\delta_\lambda\left[15\mu\lambda(1-\nu)+2\lambda\delta_\mu(5\nu-4)\right]-2\delta_\mu(\lambda\delta_\mu-5\mu\nu\delta_\lambda)}{5\delta_\mu\left[3\mu\lambda(1-\nu)-3\mu\nu\delta_\lambda-\lambda\delta_\mu(1-2\nu)\right]}; \end{aligned} \tag{A.37}$$

with $\delta_\lambda = \lambda - \lambda_0$; $\delta_\mu = \mu - \mu_0$.

The strains $\boldsymbol{\varepsilon}^{I_m}_\mu$ and $\boldsymbol{\varepsilon}^{I_n}_\mu$ in equation (A.35) are the solutions of the FFT technique to each one of the six problems ($m,n = 1,2,...,6$) and are given by equation (A.34). Note from (A.35) that the topological derivative of $\mathbf{C}^h$ is defined in each point of the micro-cell ($\hat{\mathbf{y}} \in \Omega_\mu$).

APPENDIX II: Iterative schemes for solving the optimization algorithms

We have implemented two alternative iterative schemes for solving the equations governing the optimization algorithm which are described in sub-Section 3.4. In this Appendix, we describe both implementations.

Both implementations are inspired by the Augmented Lagrangian technique and adopt a fixed penalty parameter. The first scheme uses a pre-defined linearly decreasing step size, τ. This parameter determine the size the level-set function update equation (A.22). The second scheme

[11] Additional description and properties of the polarization tensor for 3D problems can be found in Ammari et al. (2008), where it is called the Elastic Moment Tensor (EMT)

determines the step size, τ, using a linear search technique. The step size of the first scheme and how it is decreased is defined through a previous adjust procedure.

Both schemes are summarized in the following Box.

General Algorithm

Initialization: Level-set function ψ^0; Lagrange multipliers λ_i^0; penalty parameter α; Amstutz criteria tolerance tol_ψ; constraints tolerances tol_{h_i}.

Iteration $k+1$:

1. Build the characteristic function $\chi(\psi^k)$ defined in equation (A.12).
2. Perform the homogenization.
3. Evaluate the augmented Lagrangian $\mathcal{T}(\psi^k, \lambda^k)$ defined in equation (A.16)
4. Compute the topological derivative $D_\psi \mathbf{C}^h_{mn}\left(\chi(\hat{\mathbf{y}})\right)$ using equation (A.35); apply the filter; impose the symmetries.
5. Compute the search direction of the augmented Lagrangian problem, g^k, with equation (A.23), and using $D_\psi \mathcal{T}(\psi^k, \lambda^k)$ from equation (A.18).
6. Determine the steep size parameter τ.
   - **scheme 1:** *Linearly decreased with k.*
   - **scheme 2:** $\begin{cases} Choose\ a\ safewarded\ minimum\ step\ size\ \tau_{min}. \\ Perform\ a\ linear\ search:\ \tau \in [\tau_{min}, 1]. \end{cases}$
7. Update the level-set function ψ^{k+1} with equation (A.22); apply the filter; impose the symmetries.
8. Update the Lagrange multipliers: $\lambda_i^{k+1} = \lambda_i^k + \alpha h_i$.
9. Convergence test using equations (A.27) and (A.28)

The line search procedure for determining the step size, scheme 2, is based on the Moré and Thuente Moré y Thuente (1994) algorithm. We use the topological derivative in the sense of the usual derivative.

Bibliografía

Allaire G., De Gournay F., Jouve F., y Toader A. Structural optimization using topological and shape sensitivity via a level set method. *Control and cybernetics*, 34(1):59, 2005.

Ammari H., Calmon P., y Iakovleva E. Direct elastic imaging of a small inclusion. *SIAM Journal on Imaging Sciences*, 1(2):169–187, 2008.

Amstutz S. Analysis of a level set method for topology optimization. *Optimization Methods and Software*, 26(4-5):555–573, 2011.

Amstutz S. y Andrä H. A new algorithm for topology optimization using a level-set method. *Journal of Computational Physics*, 216(2):573–588, 2006.

Amstutz S., Giusti S., Novotny A., y de Souza Neto E. Topological derivative for multi-scale linear elasticity models applied to the synthesis of microstructures. *International Journal for Numerical Methods in Engineering*, 84(6):733–756, 2010.

Andreassen E. y Lazarov B.S.and Sigmund O. Design of manufacturable 3D extremal elastic microstructure. *Mechanics of Materials*, 69(1):1–10, 2014.

Bendsoe M. y Sigmund O. *Topology optimization: theory, methods, and applications*. Springer Science & Business Media, 2003.

Berryman J. y Milton G. Microgeometry of random composites and porous media. *Journal of Physics D: Applied Physics*, 21(1):87, 1988.

Cabras L. y Brun M. Auxetic two-dimensional lattices with poisson's ratio arbitrarily close to-1. En *Proceedings of the Royal Society of London A: Mathematical, Physical and Engineering Sciences*, volumen 470, páginas 1–23. 2014.

Cohen I. Simple algebraic approximations for the effective elastic moduli of cubic arrays of spheres. *Journal of the Mechanics and Physics of Solids*, 52(9):2167–2183, 2004.

Eyre D. y Milton G. A fast numerical scheme for computing the response of composites using grid refinement. *The European Physical Journal-Applied Physics*, 6(1):41–47, 1999.

Giusti S. *Análise de sensibilidade topológica em modelos constitutivos multiescalas*. Tesis de Doctorado, Laboratório Nacional de Computa cão Científica, LNCC, Brazil, 2009.

Giusti S. Personal communication. 2019.

Hashin Z. y Shtrikman S. A variational approach to the theory of the elastic behaviour of multiphase materials. *Journal of the Mechanics and Physics of Solids*, 11(2):127–140, 1963.

Hitzer E. y Perwass C. Visualization of fundamental symmetries in nature. En *Proceedings of Fuzzy System Symposium (FSS 2009), Tsukuba, Japan, 14-16 Jul.* 2009. Http://spacegroup.info/.

Kadic M., Bückmann T., Stenger N., Thiel M., y Wegener M. On the practicability of pentamode mechanical metamaterials. *Applied Physics Letters*, 100(19):191901, 2012.

Kadic M., Milton G., van Hecke M., y Wegener M. 3D metamaterials. *Nature Reviews Physics*, 1:198–210, 2019.

London E.P.B.., editor. *International Tables for Crystallography. Volume C, Mathematical, Physical and Chemical Tables. Dordrecht*. Published for the International Union of Crystallography by Kluwer Academic Publishers, 2004.

Lopes C., Santos R.d., y Novotny A. Topological derivative-based topology optimization of

structures subject to multiple load-cases. *Latin American Journal of Solids and Structures*, 12(5):834–860, 2015.

Méndez C., Podestá J., Toro S., Huespe A., y Oliver J. Making use of symmetries in the three-dimensional elastic inverse homogenization problem. *Journal for Multiscale Computational Engineering*, 17:261–280, 2019.

Milton G., Briane M., y Harutyunyan D. On the possible effective elasticity tensors of 2-dimensional and 3-dimensional printed materials. *Mathematics and Mechanics of Complex Systems*, 5(1):41–94, 2017.

Milton G. y Camar-Eddine M. Near optimal pentamodes as a tool for guiding stress while minimizing compliance in 3d-printed materials: A complete solution to the weak g-closure problem for 3d-printed materials. *Journal of the Mechanics and Physics of Solids*, 114:194–208, 2018.

Milton G. y Cherkaev A. Which elasticity tensors are realizable? *Journal of engineering materials and technology*, 117(4):483–493, 1995.

Moré J. y Thuente D. Line search algorithms with guaranteed sufficient decrease. *ACM Transactions on Mathematical Software*, 20:286–307, 1994.

Moulinec H. y Suquet P. A numerical method for computing the overall response of nonlinear composites with complex microstructure. *Computer methods in applied mechanics and engineering*, 157(1-2):69–94, 1998.

Novotny A. y Sokołowski J. *Topological derivatives in shape optimization*. Springer Science & Business Media, 2012.

Nye J. *Physical Properties of Crystals: Their representation by tensors and matrices*, volumen 146. Clarendon Press-Oxford., 2006.

Podestá J., Méndez C., Toro S., y Huespe A. Symmetry considerations for topology design in the elastic inverse homogenization problem. *Journal of the Mechanics and Physics of Solids*, 128:54–78, 2019.

Podestá J., Méndez C., Toro S., Huespe A., y Oliver J. Material design of elastic structures using voronoi cells. *International Journal for Numerical Methods in Engineering*, 115(3):269–292, 2018a.

Podestá J., Méndez C., Toro S., Huespe A., y Oliver J. Material design of elastic structures using voronoi cells. *International Journal for Numerical Methods in Engineering*, 2018b.

Saxena K.K., Das R., y Calius E. Three decades of auxetics research- materials with negative poisson's ratio: a review. *Advanced Engineering Materials*, 18(11):1847–1870, 2016.

Sigmund O. Materials with prescribed constitutive parameters: an inverse homogenization problem. *International Journal of Solids and Structures*, 31(17):2313–2329, 1994.

Sigmund O. Tailoring materials with prescribed elastic properties. *Mechanics of Materials*, 20(4):351–368, 1995.

Sigmund O. A new class of extremal composites. *Journal of the Mechanics and Physics of Solids*, 48(2):397–428, 2000.

Vainshtein B. *Fundamentals of crystals: Symmetry, and methods of structural crystallography*, volumen 1. Springer Science & Business Media, 2013.

van Dijk N., Maute K., Langelaar M., y Van Keulen F. Level-set methods for structural topology optimization: a review. *Structural and Multidisciplinary Optimization*, 48(3):437–472, 2013.

Yera R., Rossi Cabral N., Méndez G., y Huespe A. Topology design of 2D and 3D elastic material microarchitectures with crystal symmetries displaying isotropic properties close to their theoretical limits. *In press: Applied Materials Today*, 2019. DOI: 10.1016/j.apmt.2019.100456.

Anexo B

Topology design of 2D and 3D elastic material microarchitectures with crystal symmetries displaying isotropic properties close to their theoretical limits, Applied Materials Today, Volume 18, 2020

El artículo presentado a continuación ha sido publicado en la revista **"Applied Materials Today"**.

R. Yera, N. Rossi Cabral, C.G. Méndez, A.E. Huespe. *Topology design of 2D and 3D elastic material microarchitectures with crystal symmetries displaying isotropic properties close to their theoretical limits*. Applied Materials Today. Vol 18. 2020. DOI: 10.1016/j.apmt.2019.100456

Topology design of 2D and 3D elastic material microarchitectures with crystal symmetries displaying isotropic properties close to their theoretical limits

R. Yera[1], N. Rossi Cabral[1], C.G. Méndez[1], A.E. Huespe[1,2]
[1]CIMEC-UNL-CONICET, Predio Conicet Dr Alberto Cassano, CP 3000 Santa Fe, Argentina
[2]E.T.S dEnginyers de Camins, Canals i Ports, Technical University of Catalonia (Barcelona Tech)
Campus Nord UPC, Mòdul C-1, c/ Jordi Girona 1-3, 08034, Barcelona, Spain

Keywords: Three and two-dimensional (3D and 2D) microarchitecture designs; extreme isotropic elastic properties; crystal symmetries; topology optimization; inverse homogenization technique.

Abstract

This paper evaluates the effect that different imposed crystal symmetries have on the topology design of two-phase isotropic elastic composites ruled by the target of attaining extreme theoretical properties. Extreme properties are defined by the Cherkaev-Gibiansky bounds, for 2D cases, or the Hashin-Shtrikman bounds, for 3D cases.

The topology design methodology used in this study is an inverse homogenization technique which is mathematically formulated as a topology optimization problem. The crystal symmetry is imposed on the material configuration within a predefined design domain, which is taken as the primitive cell of the underlying Bravais lattice of the crystal system studied in each case.

The influence of imposing crystal symmetries to the microstructure topologies is evaluated by testing five plane groups of the hexagonal crystal system for 2D problems and four space groups of the cubic crystal systems for 3D problems.

A discussion about the adequacy of the tested plane or space groups to attain elastic properties close to the theoretical bounds are presented. The extracted conclusions could be meaningful for more general classes of topology design problems in the thermal, phononic or photonic fields.

1. Introduction

The notable increase in the use of additive manufacturing techniques for processing complex material microstructures opens the possibility of realizing materials designed for given targets (Kadic et al. (2019)). In line with this problem, we present a topology design methodology for two and three-dimensional (2D and 3D) two-phase periodic microarchitectures ruled by the objective of attaining extreme isotropic elastic properties[1]. The crucial point in this contribution is the imposition of crystal symmetries to the designed topologies, which has to be considered as a guiding principle in the context of the adopted methodology.

The design methodology that we follow is based on a well-established mathematical tool, an inverse homogenization technique formulated as a topology optimization problem, supplemented with the necessary geometrical constraints to get the required symmetries copying that of a predefined crystal. Then, using this approach, we study the effects induced by the imposition of different space groups onto the accomplishment of the problem targets.

The study of crystal symmetries and the related mathematical method, i.e., the group theory, is one of the most fundamental topics in crystallography, particularly in crystal physics. Thus, the general concepts associated with the crystal symmetry properties, the notions of point, plane and space groups, as well as the symmetry classification which are necessary to develop this work, are taken from the International Tables for Crystallography, see London (2004). Additional references are the books by Vainshtein (2013) and Sólyom (2007).

The space groups of 3D periodic arrangements of crystals characterize their symmetry properties. Symmetry elements of these space groups are constituted by rotation axes, mirror-reflection planes, inversion-rotation axes, glide-reflection planes, and screw axes. The point groups are the nexus, via the Neuman's theorem, between the symmetry of the microstructure topology, defined by the crystal space group, and the symmetry of the macroscopic effective physical properties, see Nye (2006). This concept is the cornerstone of the present approach.

Inverse homogenization techniques for topology designs are well-established in the literature. In this sense, the work pioneered by Sigmund (1994), the numerous posterior contributions of this author and coworkers, as well as the huge number of papers addressed to this topic (see for example Torquato (2010) and Osanov y Guest (2016)), are a clear indication of the power of this technique to obtain new microarchitecture topologies which are hard to be imagined if using ad-hoc design methodologies, see, in particular, the brief discussion by Milton (2018). Inverse homogenization

[1] The concept of extreme material has been coined by Milton y Cherkaev (1995). They give this name to materials which elasticity tensors have some eigenvalues very large and the remaining ones are very small. Here, following to Sigmund (2000), we use this concept in a slightly broader sense, including all those isotropic composites whose effective properties attain extreme bulk and shear modulus.

techniques can be formulated as a mathematical topology optimization problem posed in a spatial domain Ω_μ. Their solutions provide the optimal topologies, or spatial material layouts, satisfying the proposed targets. An overview of these techniques for different problems can be found in the book by Bendsoe y Sigmund (2003).

We closely follow the works of Sigmund (2000) and Andreassen y Lazarov (2014), where, 3D (2D) microarchitecture design problems aiming at obtaining extreme composites using inverse homogenization techniques have been reported. Here, we solve the topology optimization algorithm with the necessary geometrical constraints to impose a space (plane) group to the obtained material layout. The space (plane) group is defined apriori according to the symmetry of the target effective elastic response.

The implementation of this approach has required the development of a particular numerical treatment for handling the high computational cost demanded by 3D microstructure designs. Nevertheless, we leave for a forthcoming paper a detailed description of the numerical aspects of the methodology. It is notably to remark here that the topology optimization algorithm is solved with a spatial filter to avoid the occurrence of thin microstructures. Therefore, the attained topologies have only one length scale. The authors have previously reported some studies performed with this methodology for 2D problems in Podestá et al. (2018) and Podestá et al. (2019) and 3D problems in Méndez et al. (2019).

In this paper, initially and after a summary of the concepts on which this work is based on, we evaluate in Section 3 several plane groups to design 2D microarchitectures aiming at obtaining extreme elastic properties. The material isotropy is guaranteed by taking plane groups of the hexagonal crystal system. Subsequently, in Section 4, we perform a similar analysis for 3D problems. In these cases, the isotropic elastic response cannot be guaranteed by any space group[2]. Thus, we test four space groups with the highest and the lowest symmetries of the cubic crystal system, adding one isotropy constraint to the topology optimization problem. The 2D and 3D material configurations obtained with different plane and space groups are compared and discussed. Finally, the conclusions are presented.

Some representative 3D microstructures designed with this methodology are available as supplementary material in the dataset Yera et al. (2019). These microarchitectures are stored in .stl format and are ready for 3D printing.

[2]It is worth to remark that, when topologies with multiple length scales are allowed, the crystal symmetry does not matter for attaining isotropic effective responses, such as happens in randomly textured polycrystals with isotropic macroscopic response. However, the important point here is that topologies implying multiple length scales are not so practical and their consideration enlarges the design space which makes the optimization more difficult.

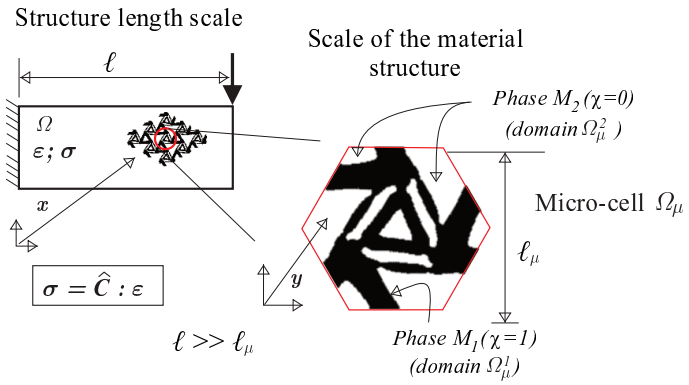

Figura B.1: Topology optimization problem. Cell Ω_μ of the microstructured composite with phases M_1 and M_2 and the characteristic function χ. At the macrostructural scale, the effective elastic properties of the composite are represented by the homogenized constitutive elasticity tensor $\hat{\mathbf{C}}$.

2. Inverse material design problem

We design microstructures of periodic composites constituted by two isotropic phases, M_1 and M_2, and a given volume fraction f_1 of M_1. Two well-separated scales of lengths are assumed, see Figure B.1; the structure length scale, ℓ, and the microstructural length scale ℓ_μ in where the geometrical configuration of the phase distribution is defined. Thus, it is satisfied that $\ell \gg \ell_\mu$. The effective material properties are evaluated at the structural scale.

The composite has to display the closest effective isotropic elastic properties to its theoretically estimated bounds. In particular, for the here studied cases in 2D problems, these bound have been reported by Cherkaev y Gibiansky (1993), and for 3D problems, they have been reported by Hashin y Shtrikman (1963). The elastic properties of the component phases are chosen to allow for effective properties with negative Poissons ratios. Thus, the design of isotropic auxetic materials is an additional challenge addressed for some extreme target conditions.

In this Section, and after defining the theoretical bounds reported in the literature, we describe the optimization problems that are formulated to attain the closest properties to these bounds.

2.1. Analytical bounds of two-phase composites with effective isotropic elasticity

The bounds described in this Section for the effective bulk and shear moduli, $\hat{\kappa}$ and $\hat{G}$, respectively[3], of isotropic two-phase composites, are valid for well-ordered composites, i.e. $\kappa_2 < \kappa_1$ and $G_2 < G_1$, where κ_1 and G_1 are the bulk and shear moduli of the stiff phase, M_1, and κ_2 and G_2 are the bulk and shear moduli of the soft phase, M_2. These bounds are next defined in the space $(\hat{K}, \hat{G})$ for 2D problems[4] and $(\hat{\kappa}, \hat{G})$ for 3D problems.

[3]The symbol $\hat{(\cdot)}$ denotes an effective value of the elastic property.

[4]The plane strain modulus K is given by $K = \kappa + G/3$, where κ and G are the conventional bulk and shear moduli of the three-dimensional theory. The elastic constant in the plane strain $\nu_p = \nu/(1-\nu)$, where ν is the conventional 3D Poisson's ratio and $-1 \leq \nu_p \leq 1$, is here taken as the plane strain Poisson's ratio. The parameter K is known as the Kolosov constant. For additional details about the connection between the 2D and 3D elastic constants we reference

Plane strain problems. According to the analysis of Cherkaev et al., the effective moduli of an isotropic composite constituted by the phase M_1, with bulk modulus[5] $K_1 = 5/7$, shear modulus $G_1 = 5/13$ and volume fraction $f_1 = 0.5$, and the phase M_2, with bulk modulus $K_2 = K_1/200$ and shear modulus $G_2 = G_1/200$; can be bounded in the space $(\hat{K}, \hat{G})$ with an upper coupled bound defined by the curve:

$$\hat{G}^u(\hat{K}) = \frac{\omega^u(f_1G_1 + f_2G_2) + G_1G_2}{G_2f_1 + G_1f_2 + \omega^u} \quad ; \quad \omega^u = -G_1 + \frac{\alpha^u y_K}{\beta^u y_K - \gamma^u}; \tag{B.1}$$

and a lower coupled bound, defined by the curve:

$$\hat{G}^l(\hat{K}) = \frac{\omega^l(f_1G_1 + f_2G_2) + G_1G_2}{f_1G_2 + f_2G_1 + \omega^l} \quad ; \quad \omega^l = -G_1 + \frac{\alpha^l(\frac{1}{y_K} + \frac{1}{K_1})}{\beta^l(\frac{1}{y_K} + \frac{1}{K_1}) - \gamma^l}; \tag{B.2}$$

where

$$y_K = -K_1K_2\frac{\hat{K} - \frac{1}{(\frac{f_1}{K_1} + \frac{f_2}{K_2})}}{\hat{K} - (f_1K_1 + f_2K_2)}\left(\frac{f_1}{K_1} + \frac{f_2}{K_2}\right); \tag{B.3}$$

The coefficient in (B.1)–(B.2) are: $\alpha^l = 0.4107$, $\beta^l = 1.0653$, $\gamma^l = 0.0110$, $\alpha^u = -0.1256$, $\beta^u = -0.2200$ and $\gamma^u = 2.0 \times 10^{-4}$.

The curves $(\hat{K}, \hat{G}^u)$ and $(\hat{K}, \hat{G}^l)$ are plotted in Figure B.2-a and, in the following, are denoted CG-bounds.

Three-dimensional problems. The best known bounds at the present time for 3D composites, when one phase is void, are the Hashin-Shtrikman bounds (denoted HS-bounds in the following) which are given by the expressions:

$$\begin{aligned} \hat{\kappa}^u &= \kappa_1 + \frac{1 - f_1}{\frac{1}{\kappa_2 - \kappa_1} + 3\frac{f_1}{3\kappa_1 + 4G_1}} \quad ; \quad \hat{\kappa}^l = \kappa_2 + \frac{f_1}{\frac{1}{\kappa_1 - \kappa_2} + 3\frac{1-f_1}{3\kappa_2 + 4G_2}} \; ; \\ \hat{G}^u &= G_1 + \frac{1 - f_1}{\frac{1}{G_2 - G_1} + \frac{6(\kappa_1 + 2G_1)f_1}{5G_1(3\kappa_1 + 4G_1)}} \quad ; \quad \hat{G}^l = G_2 + \frac{f_1}{\frac{1}{G_1 - G_2} + \frac{6(\kappa_2 + 2G_2)(1-f_1)}{5G_2(3\kappa_2 + 4G_2)}} \; . \end{aligned} \tag{B.4}$$

By following to Andreassen y Lazarov (2014), we adopt $\kappa_1 = 1.667$, $G_1 = 0.3571$, $\kappa_2 = \gamma\kappa_1$, $G_2 = \gamma G_1$, with the contrast factor $\gamma = 10^{-4}$, and the volume fraction $f_1 = 0.338$. For these composites, the HS-bounds are: $\hat{\kappa}^u = 0.170$; $\hat{\kappa}^l = 2.8 \times 10^{-4}$; $\hat{G}^u = 0.789$; $\hat{G}^l = 7.3 \times 10^{-5}$ and are plotted in Figure B.2-b, in the space $(\hat{\kappa}, \hat{G})$.

Remark: in two-dimensions the Cherkaev-Gibiansky bounds degenerate to the Hashin-Shtrikman bounds in the limit in which one phase is void. This is similar to the way the Berryman-Milton-Phan-Thien bounds degenerate in three dimensions to the Hashin-Shtrikman bounds, see Berryman y Milton (1988) and references cited therein.

the work by Thorpe y Jasiuk (1992).

[5] Stifnesses and lengths are defined in arbitrary units.

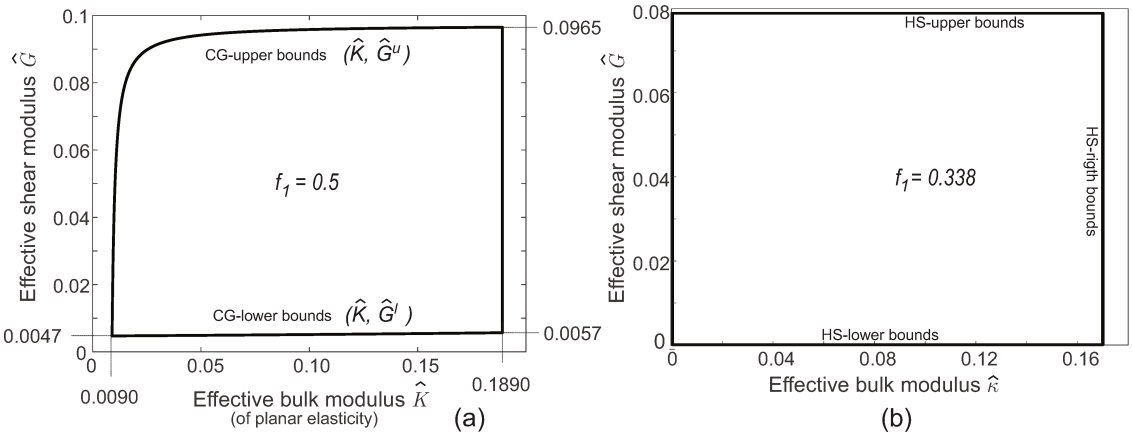

Figura B.2: Analytic bounds of effective properties for two-phase isotropic composites. a) Plane elasticity. Bounds according to Cherkaev y Gibiansky (1993) (CG-bounds). Properties of phases M_1 and M_2 are $K_1 = 5/7$; $K_2 = K_1/200$; $G_1 = 5/13$; $G_2 = G_1/200$. Volume fraction of phase M_1 is $f_1 = 0.5$. b) 3D elasticity bounds according to Hashin y Shtrikman (1963) (HS-bounds). Properties of phases M_1 and M_2 are $\kappa_1 = 1.667$, $G_1 = 0.3571$, $\kappa_2 = \gamma\kappa_1$, $G_2 = \gamma G_1$, contrast factor $\gamma = 10^{-4}$, volume fraction $f_1 = 0.338$.

2.2. Topology optimization problem

Let us consider a basic micro-cell, identified by Ω_μ, of the two-phase composite. The phases M_1 and M_2 occupy the domains Ω_μ^1 and Ω_μ^2, respectively, see Figure B.1.

In Ω_μ, we define a characteristic function $\chi(\mathbf{y})$ identifying the positions where the phase M_1 is placed. It is defined by:

$$\chi(\mathbf{y}) = \begin{cases} 0 & \forall \mathbf{y} \in \Omega_\mu^2 \\ 1 & \forall \mathbf{y} \in \Omega_\mu^1 \end{cases} . \tag{B.5}$$

The homogenized elasticity tensor of the composite, $\hat{\mathbf{C}}$, depends on the geometrical configuration of the phases M_1 and M_2 in Ω_μ. We make explicit this dependence by introducing the notation $\hat{\mathbf{C}}(\chi)$. If the effective properties of the composite are isotropic, then, $\hat{\mathbf{C}}$ can be determined accordingly with the effective bulk and shear moduli, denoted $\hat{\kappa}(\chi)$ and $\hat{G}(\chi)$, respectively.

Three-dimensional topology optimization problems

The optimal design of microarchitecture topologies whose target effective properties are the points on the lower Hashin-Shtrikman bounds are obtained by solving a set of n discrete topology optimization problems formulated as follows:

$$\begin{aligned} &\min_{\chi} \ \hat{G}(\chi); \\ &\text{such that:} \quad \hat{\kappa}(\chi) - \kappa_j^* = 0 \\ &\qquad\qquad\ \ \hat{\mathbf{C}}(\chi) \text{ is isotropic} \\ &\qquad\qquad\ \ f_1(\chi) - f_1^* = 0 \end{aligned} \tag{B.6}$$

where κ_j^* (with $1 \leq j \leq n$) is the $j-$th target bulk modulus of the composite defined whitin the interval $\hat{\kappa}^l \leq \kappa_j^* \leq \hat{\kappa}^u$ and f_1^* is the target volume fraction of phase M_1. The problem (B.6) expres-

ses that the minimum of the effective shear modulus, $\hat{G}$, is searched by varying the characteristic function χ within Ω_μ.

Similarly, the Hashin-Strikman upper bound is approached by solving the maximum $\hat{G}(\chi)$, with identical constraints of problem (B.6).

Alternatively, the topologies approaching the left Hashin-Strikman bound are sought by solving the problems:

$$\begin{aligned} &\min_{\chi} \hat{\kappa}(\chi); \\ \text{such that:} \quad &\hat{G}(\chi) - G_j^* = 0 \\ &\hat{\mathbf{C}}(\chi) \text{ is isotropic} \\ &f_1(\chi) - f_1^* = 0 \end{aligned} \tag{B.7}$$

where now, the target effective shear modulus G_j^* of the $j-$th optimization problem is chosen from the the interval $\hat{G}^l \leq G_j^* \leq \hat{G}^u$. The extreme composites on the right H-S bound are approached by changing the minimum problem in (B.7) by one of maximizing the effective bulk modulus.

In the case that the effective elastic properties have cubic symmetry, situation that is guaranteed by taking a material configuration having a space group consistent with the cubic crystal system, the coefficients $\hat{C}_{ij}$, with $i, j = 1, ..., 6$, of the elasticity matrix[6] $\hat{\mathbf{C}}$ satisfy the general identities displayed in Table **??**, resulting: $\hat{C}_{11} = \hat{C}_{22} = \hat{C}_{33}$; $\hat{C}_{12} = \hat{C}_{13} = \hat{C}_{23}$; $\hat{C}_{44} = \hat{C}_{55} = \hat{C}_{66}$. The remaining coefficients of the elasticity matrix are zero. Any tensor $\hat{\mathbf{C}}$ with cubic symmetry is isotropic if additionally its coefficients satisfies:

$$\hat{C}_{11} - \hat{C}_{12} - \hat{C}_{44} = 0 \,, \tag{B.8}$$

resulting:

$$\hat{G}^{iso} = \frac{\hat{C}_{44}}{2} \,, \tag{B.9}$$

$$\hat{\kappa}^{iso} = \frac{1}{3}(\hat{C}_{11} + 2\hat{C}_{12}) \,, \tag{B.10}$$

where $\hat{\kappa}^{iso}$ and $\hat{G}^{iso}$ are the bulk and shear moduli of the effective elastic isotropic response. In the problems (B.6) and (B.7), the elastic isotropy is imposed by the equation (B.8).

Based on these identities we reformulate the problem (B.6) in terms of the components of $\hat{\mathbf{C}}$

[6] We use Kelvin's notation.

as follows:

$$\begin{aligned} &\min_{\chi} \ \hat{C}_{44}, \\ &\text{such that:} \quad \hat{C}_{11} + 2\hat{C}_{12} - 3\kappa_j^* = 0 \ , \\ &\qquad\qquad \hat{C}_{11} - \hat{C}_{12} - \hat{C}_{44} = 0 \ , \\ &\qquad\qquad f_1(\chi) - f_1^* = 0 \ , \end{aligned} \tag{B.11}$$

and problem (B.7) as follows:

$$\begin{aligned} &\min_{\chi}(\hat{C}_{12} + \frac{1}{3}\hat{C}_{44}), \\ &\text{such that:} \quad (\hat{C}_{11} - \hat{C}_{12} + \frac{3}{2}\hat{C}_{44}) - 5G_j^* = 0 \ , \\ &\qquad\qquad \hat{C}_{11} - \hat{C}_{12} - \hat{C}_{44} = 0 \ , \\ &\qquad\qquad f_1(\chi) - f_1^* = 0 \ . \end{aligned} \tag{B.12}$$

The objective function in problem (B.12) results from replacing the isotropy constraint (B.8) in equation (B.10).

Two-dimensional (plane strain) topology optimization problems

The optimal design of 2D microstructures whose target is to attain an extreme isotropic material is also performed using a topology optimization algorithm with a slightly different formulation to those stated in (B.6) or (B.7). In this case, those problems are formulated without specifically imposing the isotropic elasticity constraint, because this property is guaranteed by enforcing topologies with hexagonal symmetry.

Topology optimization algorithm

The algorithm used for solving the problems (B.11)–(B.12) is based on a level-set method jointly with topological derivative evaluating the sensitivity of response with changes of the characteristic function χ defined in (B.5). The numerical technique follows the original proposal of Amstutz y Andrä (2006) and Amstutz et al. (2010). The topological derivative has been studied by Novotny y Sokołowski (2012). Additional details of this algorithm for solving 3D problems can be found in Méndez et al. (2019).

In all cases, the configurations for the algorithm onset are random distributions of the stiff phase in Ω_μ.

Tabla B.1: Hexagonal (2D) Crystal System. Compatible point and plane groups. The elasticity matrix is isotropic and is represented in column 1, with the coefficient C_{11} and C_{12} characterizing the elastic properties.

Elasticity Matrix	Crystal system	Point group	Plane group	Compatible Bravais lattice	Wigner-Seitz and primitive unit cell
$\begin{bmatrix} C_{11} & C_{12} & 0 \\ C_{12} & C_{11} & 0 \\ 0 & 0 & C_{11}-C_{12} \end{bmatrix}$	hexagonal	3	p3	hexagonal	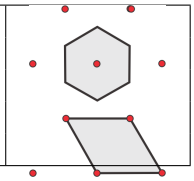
		3m	p3m1		
			p31m		
		6	p6		
		6mm	p6mm		

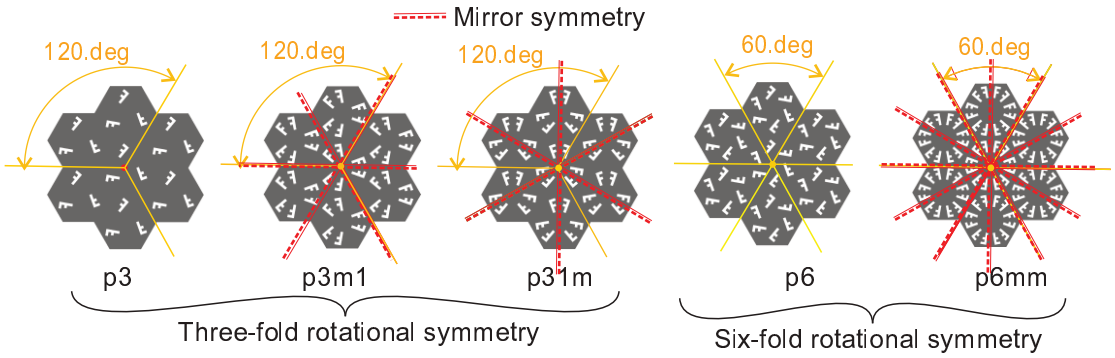

Figura B.3: Symmetry elements of plane groups $p3$, $p3m1$, $p31m$, $p6$, $p6mm$. Note that the mirror planes of the $p3m1$ plane group intersect the Voronoi cell differently to that of the $p31m$ plane group.

2.3. Use of specific plane group and space group symmetries

We focus only on particular cases of space group symmetries for designing composites with isotropic effective elastic responses.

Hexagonal crystal system for 2D isotropic material design

The isotropy of 2D elastic properties is guaranteed if the periodic material configuration is compatible with the *hexagonal crystal system* whose main properties are summarized in Table **??**. Thus, the plane groups $p3$, $p3m1$, $p31m$, $p6$, and $p6mm$[7] guarantee the obtention of isotropic effective elastic properties, and therefore, they are the ones tested in this work.

The symmetry elements of these plane groups are depicted in Figure B.3. The underlying Bravais lattice compatible with these plane groups is hexagonal.

Cubic crystal system for 3D isotropic material design

There are 230 space groups characterizing periodic microstructures in 3D. None of them guarantee an isotropic effective elastic response. Under this circumstance, we study the cubic space groups, which have the highest possible crystal symmetries in 3D. We only focus on the *cubic*

[7] We use the Herrman-Maugin notation to identify point, plane and space groups, see International Tables of Crystallography London (2004).

Tabla B.2: Cubic System. Compatible point and space groups. Two Bravais lattices compatible with the cubic systems are sc and bcc. Conventional (or Centered) and Wigner-Seitz cells of the two Bravais lattices. The elasticity matrix in the natural bais is represented in column 1. The symbol "$*-*$" linking two coefficients means that they are equal. Thus, only three coefficients define the elasticity matrix in natural basis. The evaluated point and space groups are denoted in bold.

Elasticity Tensor	Crystal System	Point Groups	Space Groups	
$\begin{pmatrix} * & *-* & 0 & 0 & 0 \\ & * & 0 & 0 & 0 \\ & & * & 0 & 0 & 0 \\ & & & * & 0 & 0 \\ & & & & * & 0 \\ & & & & & * \end{pmatrix}$	Cubic	**23**	**P23**, P2_13	**I23,** $I2_13$
		m3	Pm3, Pn3, Pa3	Im3, Ia3
		432	P432, P4_232, P4_332, P4_132	I432, I4_132
		43m	P43m, P43n	I43m, I43d
		m$\bar{3}$m	**Pm$\bar{3}$m**, Pn3n, Pm$\bar{3}$n, Pn$\bar{3}$m	**Im$\bar{3}$m**, Ia$\bar{3}$d
Compatible Bravais lattice (Conventional cells)			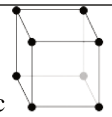 sc	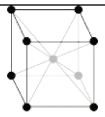 bcc
Wigner-Seitz cell			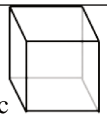 sc	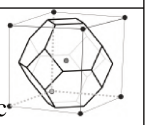 bcc

crystal system whose Bravais lattices are sc (primitive simple cubic) or bcc (body-centered cubic). A further analysis would include the fcc lattice.

Additional details about the *cubic crystal system* are presented in Table **??**. Column 4 of this Table displays all the space groups that are compatible with the sc and bcc lattices. Point and space groups being compatible are described in identical lines of columns 3 and 4. It can be guaranteed that the effective elasticity properties of any composite whose material layout has a symmetry compatible with a point group listed in column 3 satisfy cubic symmetry, and therefore, the corresponding elastic matrix coefficients, expressed in natural basis, should satisfy the identities shown in column 1. In the last two rows of Table **??**, we show the Conventional and Wigner-Seitz (Voronoi) cells of both lattices which are here studied[8]. Primitive cells of this lattice are shown in Figure B.4. The primitive and the conventional unit cells are identical for the sc lattice and different for the bcc lattice.

We only analyze the design of topologies with space groups $P23$, $I23$, $Pm\bar{3}m$ and $Im\bar{3}m$. Some of the symmetry elements of these space groups are shown in Figure B.5.

The space groups $P23$ and $I23$ have fewer symmetry elements than the $Pm\bar{3}m$ and $Im\bar{3}m$ cases. The first ones can be considered as the space groups with the lowest symmetries and the

[8]In this work, three types of unit cells are mentioned and used: *i)* Wigner-Seitz (or Voronoi) unit cells; *ii)* primitive unit cells defined by the primitive vectors of the lattice and *iii)* the conventional cells whose faces are planes parallel to the coordinate planes. Voronoi and primitive cells have minimum volume, while conventional cells, in general, do not have minimum volume

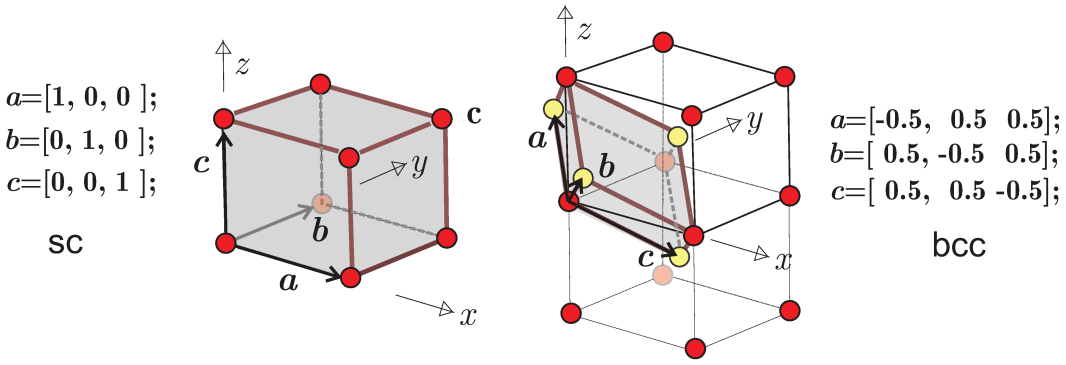

Figura B.4: Primitive cells of cubic Bravais Lattices of sc and bcc lattices are defined by the primitive vectors $\mathbf{a}$, $\boldsymbol{b}$, $\boldsymbol{c}$. The volumes of the primitive unit cells are $V_{sc} = 1$, $V_{bcc} = 0.5$. Conventional cells are defined in both cases by the vectors $(1, 0, 0)$, $(0, 1, 0)$ and $(0, 0, 1)$.

second ones with the highest of the *cubic crystal system*. Also, the space groups $P23$ and $Pm3m$ are compatible with an sc Bravais lattice, while the $I23$ and $Im\bar{3}m$ are compatible with a bcc Bravais lattice. Note further that the space group $I23$ has two-fold screw axes which provide higher symmetry properties than that of the space group $P23$. As will be observed in the following, this higher symmetry of the $I23$ space group affects the capacity for obtaining some minimal/maximal properties close to the extreme materials.

The objective here is to make a comparative analysis of the topologies obtained using both extreme cases of symmetries, with point groups 23 and $m\bar{3}m$, and two different Bravais lattices, sc and bcc.

2.4. Technique for solving the inverse design problem

Significant issues for solving the topology optimization algorithm summarized in sub-Section 2.2 are next remarked.

i) **Selection of the design domain Ω_μ:** following to Podestá et al. (2019), Ω_μ is taken as the primitive cell of a Bravais lattice having a point group symmetry compatible with the target elastic properties. This lattice is identified as the underlying Bravais lattice of the composite. For 2D problems, the hexagonal Bravais lattice is taken, and the corresponding primitive cell is the parallelogram depicted in Figure B.6. In 3D problems, the domain Ω_μ coincides with the primitive cell of the underlying Bravais lattice[9]. The primitive cells of SP and bcc lattices are shown in Figure B.4.

ii) **Computational homogenization:** the effective properties of the composite are evaluated using a base cell coinciding with Ω_μ. Periodic conditions of the material layout, by repea-

[9]Selecting the primitive unit cell of the Bravais lattice instead of the conventional cell means that the design domain would represent the minimum possible volume of the composite which tesselation reproduce the periodic microstructure. Then, for identical microstructures, the minimum volume of Ω_μ, instead of using a conventional cell, implies to search for a simpler material configuration.

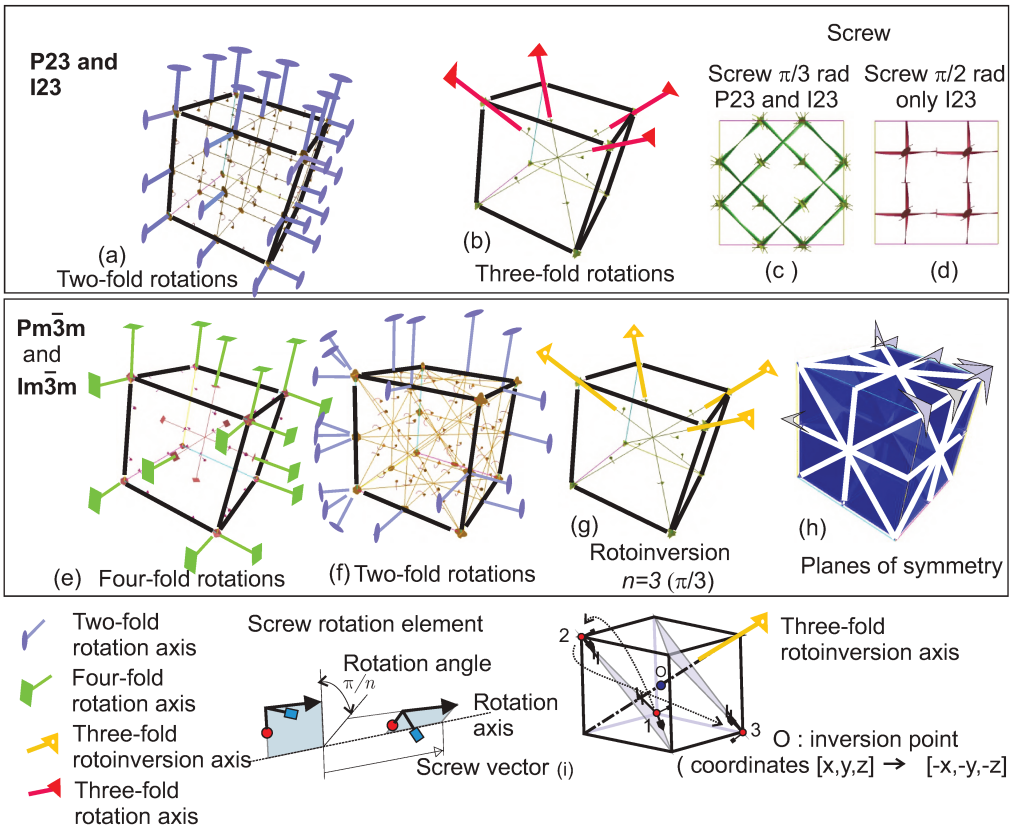

Figura B.5: (a) to (h) Symmetry elements in conventional sc and bcc cells, of the space groups $P23$, $I23$, $Pm\bar{3}m$ and $Im\bar{3}m3$. Glide and screw elements of space groups $Pm\bar{3}m$ and $Im\bar{3}m3$ are not shown. c) and d) orthogarphic view of screw elements of space groups $P23$ and $I23$. i) representation of the screw rotation and rotoinversion symmetry elements. The symmetry elements of space groups can be interactively visualized with the software *"Space Group Visualizer"* described in Hitzer y Perwass (2009).

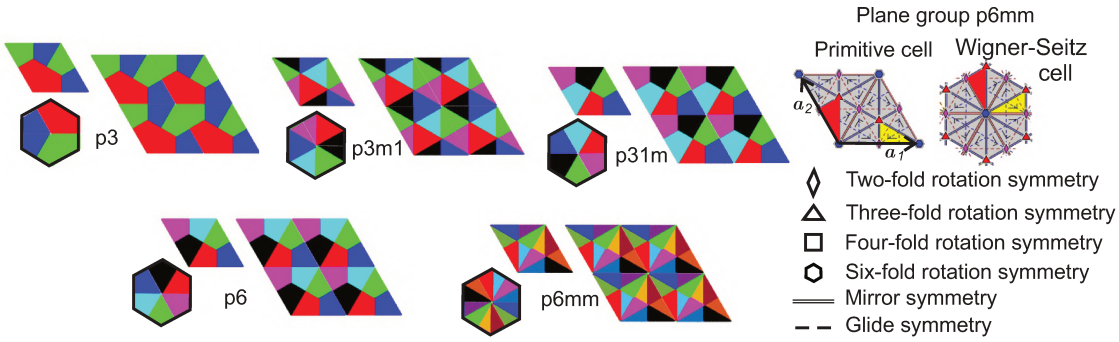

Figura B.6: Five plane groups of the *hexagonal crystal system*. Asymmetric units in red and their image points. The asymmetric unit domain is easily distinguished in the Wigner-Seitz cell but hardly recognized in primitive cells. Symbols used for identifying the symmetry elements in plane groups.

ting the pattern defined by this base cell, are coincident with the primitive directions of the underlying Bravais lattice. Thus, periodic boundary conditions of the displacement fluctuations compatible with this criterion are imposed on the base cell.

In 3D problems, the homogenization of the effective properties is computed with an FFT (Fast Fourier Transform) technique[10].

iii) **Implementation of the space group symmetry:** the symmetry of the microarchitecture topology agreeing with a pre-established space group is imposed in two steps. The first step consists of defining a set of points in the primitive cell, known as the asymmetric unit domain[11], and then to find their image points. The asymmetric domain is the reduced volume of the primitive cell which can be replicated by applying the symmetry operations of the space group to obtain the full primitive cell configuration. Therefore, the asymmetric unit contains the complete information necessary for the description of the crystal structure. In Figure B.6, we depict the plane group consistent with the *hexagonal crystal system* and the asymmetric unit domains in red. In different colors are depicted the image points. The asymmetric unit domains, as well as the image points of the conventional cells for all plane and space groups, are defined in the International Tables for Crystallography (London (2004)).

3. Design of 2-D isotropic materials

The attainment of a 2D microstructure with isotropic effective elastic response is strictly guaranteed[12] by imposing the following plane groups $p3$, $p3m1$, $p31m$, $p6$ and $p6mm$ which are

[10]The FFT technique for homogenization implemented in this work has been taken from Eyre y Milton (1999). In 2D, this step of the inverse homogenization problem is computed with a Finite Element technique. Additional details of the numerical aspects of this technique are addressed in Rossi Cabral et al. (2019).

[11]See point 2.1.3.8 inLondon (2004)

[12]The effective elasticity tensor of all the 2D microarchitectures displayed in this Section are exactly isotropic until the machine precision.

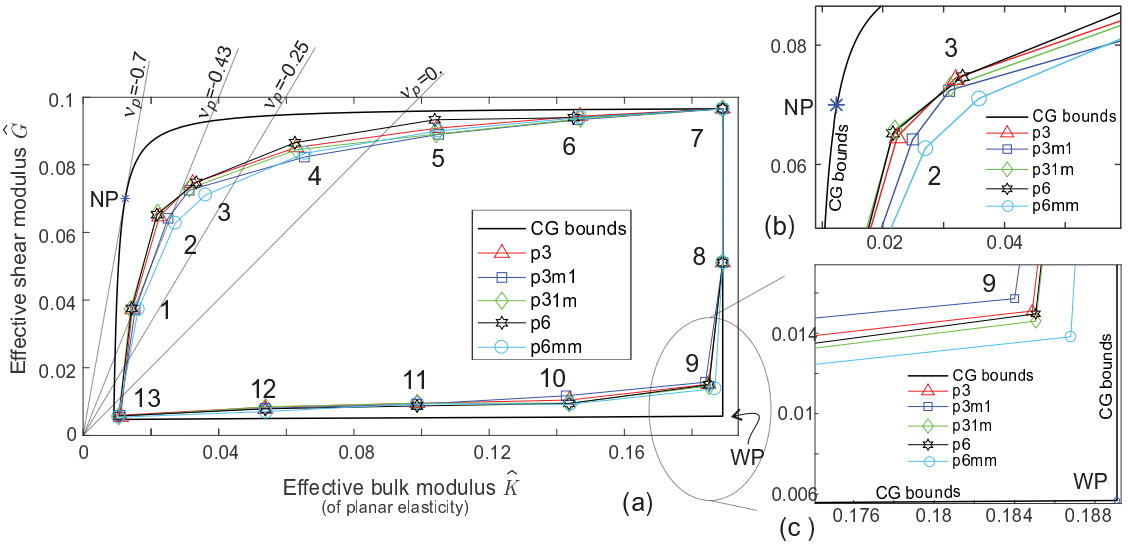

Figura B.7: Two-dimensional design of extreme isotropic microstructures: a) Cherkaev y Gibiansky (1993) bounds (CG-bounds)) and best solutions obtained with plane groups $p3$, $p3m1$, $p31m$, $p6$ and $p6mm$; b) zoom of the region near to the most negative Poisson's ratio (Point NP) of the CG-bounds: c) zoom of the region near to the Walpole Point (Point WP).

ordered from the lowest to the highest symmetries. We take a primitive unit cell of the hexagonal Bravais lattice to solve the topology optimization algorithm.

The designs of materials whose properties are close to the bounds, for two-phase composites defined in Section 2.1, are studied for 13 different target conditions identified by the corresponding points in the space ($\hat{K}$,$\hat{G}$) depicted in Figure B.7-a. The bounds reported by Cherkaev et al. are displayed again in the Figure, as well as some isolines of negative Poisson's ratios. The Point NP marks the elastic properties with the most negative Poisson's ratio estimated with the CG-bounds.

3.1. Discussion of results

After evaluating these solutions, the following discussion can be addressed.

1) The enforcement of a plane group with the highest symmetry ($p6mm$) is the most adequate to attain microarchitectures with elastic properties close to the region with low shear and high bulk moduli, i.e., near the Walpole Point (Point WP in Figure B.7-a and c);

2) The enforcement of a plane groups with a hexagonal Bravais lattice and only few symmetry elements guaranteeing isotropy ($p3$, $p31m$ and $p6$) are useful to attain elastic properties close to the bounds in the region with high shear and low bulk moduli, near the points with negative Poisson ratios denoted NP in Figure B.7-a and b;

3) There are no substantial differences by using plane groups with high or low symmetries for capturing extreme materials close to the other two vertices defined by the CG-bounds.

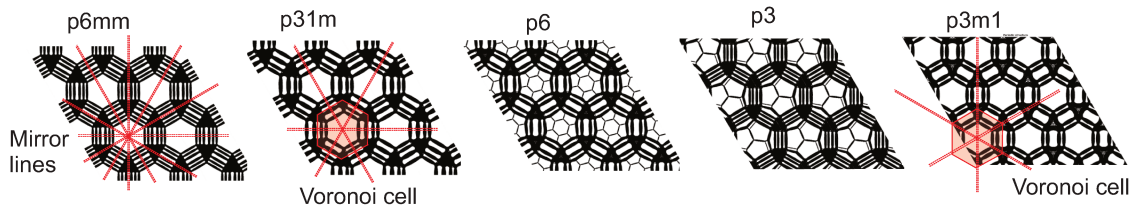

Figura B.8: Two-dimensional design of extreme isotropic microstructures: Walpole Point WP in Figure B.7-a and c. Topologies obtained with plane groups $p6mm$, $p31m$, $p6$, $p3$, $p3m1$. Mirror lines and Voronoi cells.

Problem target: Walpole Point (Problem 9 in Figure B.7-a)

The material layouts obtained with different plane groups for the WP point (of Figure B.7-a and c) are depicted in Figure B.8. These solutions confirm the conclusions reported by Sigmund (2000). The most extreme properties are attained with the symmetry $p6mm$ and the topology agrees with that reported by Sigmund in the same paper. Notably in this case, the microstructure is constituted by laminated bars and rigid joints. Sigmund has proven that parameterizing this topology and performing an optimization of the geometry configuration through these parameters, the material almost reaches the Walpole Point. It is evident that the additional symmetry lines of the $p6mm$ plane group guide the algorithm to attain a more adequate limit condition.

The same Figure B.8 shows that when a lower symmetry is imposed, for example $p3$, the algorithm searches for a solution tending to capture similar symmetry elements to those shown by the $p6mm$ plane group.

It is remarked that the Walpole point is asymptotically attained when one phase is void, both in two and three dimensions, such as mentioned in the introduction of the paper by Milton y Camar-Eddine (2018).

Problem target: minimum Poisson's ratio (Problem 2 in Figure B.7-a)

The resulting topologies for the problem identified with number 2 in Figure B.7-a, whose target is to attain the bound for the composite with the most negative Poisson's ratio (Point NP in the CG-bounds), are shown in Figure B.9. In general, these topologies agree with the ones reported in the paper by Podestá et al. (2019). We note in Figure B.7-a and b that the effective response is rather sensitive to the imposed plane group. The microarchitectures giving a good tendency are either chiral (obtained with the plane groups $p6$ and $p3$ without mirror symmetry lines) as well as not chiral (obtained with the plane group $p31m$ with one system of mirror symmetry line). Again, we note that $p31m$, $p6$ and $p3$ plane groups try to attain microstructures constituted by laminate bars. Note the similarity of the configuration attained with $p6$ symmetry and the parameterized microstructure studied in Ostanin et al. (2018).

The solutions with the plane groups $p3m1$ and $p6mm$ are clearly inefficient if compared with

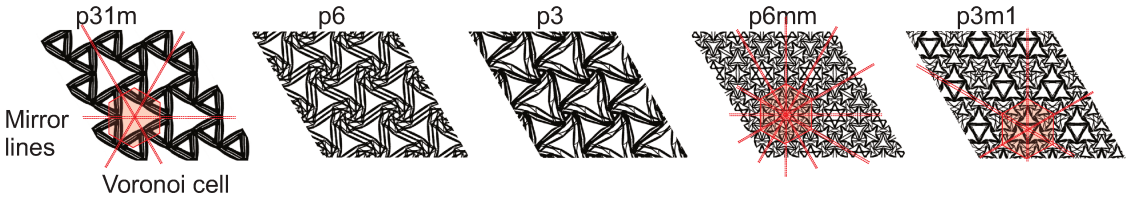

Figura B.9: Two-dimensional design of isotropic microstructures: most negative Poisson's ratio (Point NP in Figure B.7-a and b). Topologies obtained with plane groups $p31m$, $p6$, $p3$, $p6mm$, and $p3m1$. Mirror lines and Voronoi cells.

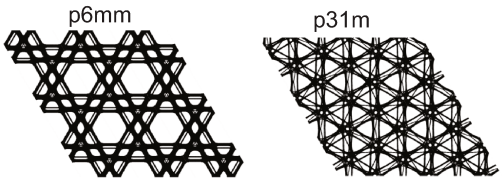

Figura B.10: Two-dimensional design of extreme isotropic microstructures: maximum shear and bulk moduli (Problem 7 in Figure B.7-a). Topologies obtained with plane groups $p6mm$ and $p3m1$.

the $p6$ and $p3$ solutions. This response can be explained by the mirror lines of the plane group $p6mm$ yielding an inadequate topology for emulating the deformation mechanisms typical of auxetic materials. The inefficiency of the solutions for both plane groups $p3m1$ and $p6mm$ are additionally confirmed by observing the intricate resolved microarchitectures displayed in Figure B.9.

The above discussed conclusions are valid for designing extreme composites whose target properties lay on a larger part of the left and upper CG-bounds, for example, for the problems denoted with the numbers 1 to 5 in Figure B.7-a.

Problem target: maximum shear and bulk moduli (Problem 7 in Figure B.7-a)

Similar microstructures are obtained with the five plane groups when searching for the stiffer microstructure at the upper right vertex of the CG-bounds, maximum shear and bulk moduli.

Figure B.10 depicts the solutions attained with the plane groups $p6mm$ and $p31m$. They are similar microstructures to those reported by Sigmund (2000).

Smooth transition of topologies along the CG-bounds

Figure B.11 displays a sequence of the microarchitectures attained in problems 1 to 4 (with plane group $p31m$), as well as, 8 to 11 (with plane group $p6mm$). There can be seen a smooth and continuous transition of topologies for the problems along the CG-boundary. These results open the possibility to define families of microarchitectures, via parametrization of their geometrical configuration, which could be used as a tool, by appealing to parameter optimization, for attaining topologies with properties even closer to the limits.

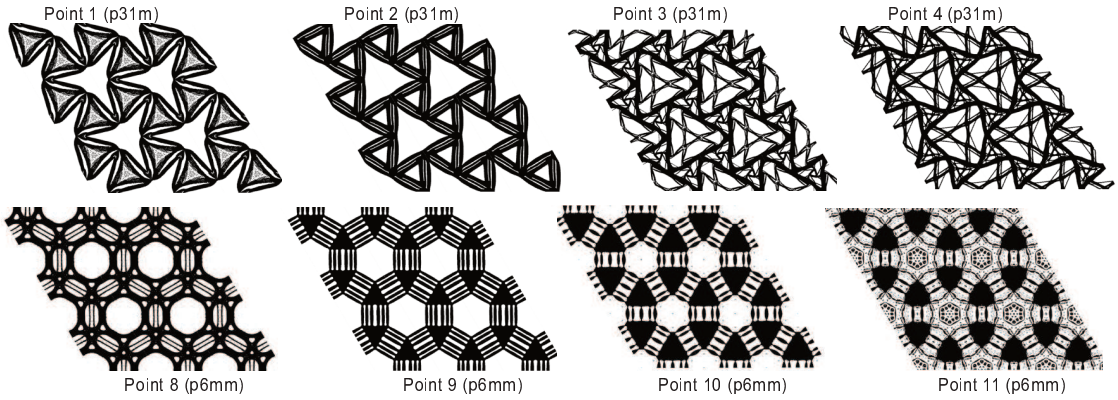

Figura B.11: Transitions of topologies (Points 1 to 4 with $p31m$ plane group (above) and 8 to 11 with $p6mm$ plane group (below)). The problem numbers are identified in Figure B.7-a.

4. Design of 3-D isotropic materials

Four different space groups $P23$, $Pm\bar{3}m$ (with sc Bravais lattices) and $I23$, $Im\bar{3}m$ (with bcc Bravais lattices) are adopted for designing the 3D topologies. All the solutions have been got with a Fast Fourier Transform procedure to compute the homogenized elastic properties. The cells have $100 \times 100 \times 100$ voxels in all cases.

Figure B.12 plots the results in the space $(\hat{\kappa}, \hat{G})$. The HS-upper and lower bounds and some isolines of properties with negative Poisson's ratios are depicted, as well as 13 sets of solutions obtained with the four mentioned space groups. Each set of solutions are denoted with the numbers 1 to 13. Several instances have been run for every set of Problems 1 to 13 and for every space group. The solutions depicted in Figure B.12 correspond to the best obtained case of all the runs for each space group.

Isotropy analysis

With the coefficients of the homogenized elasticity tensor $\hat{C}$, we compute the Zener ratios[13] of some representative microarchitectures as follows:

$$\xi = \frac{\hat{C}_{44}}{\hat{C}_{11} - \hat{C}_{12}} \tag{B.13}$$

A value 1 for this ratio indicates that $\hat{C}$ is isotropic[14]. Contrarily, a large value of ξ indicates that $\hat{C}$ is far from being isotropic. Some Zener ratios are reported in Table B.3. In general, they are close to 1, meaning that the effective response almost satisfies the isotropy constraint imposed on the topology optimization algorithm.

[13]The Zener ratio quantifies the anisotropy of the effective material properties having cubic symmetry.

[14]For the subsequent analysis, the elasticity tensors whose Zener ratios are different from 1 are projected to the space of isotropic tensors using the technique reported by Meille y Garboczi (2001).

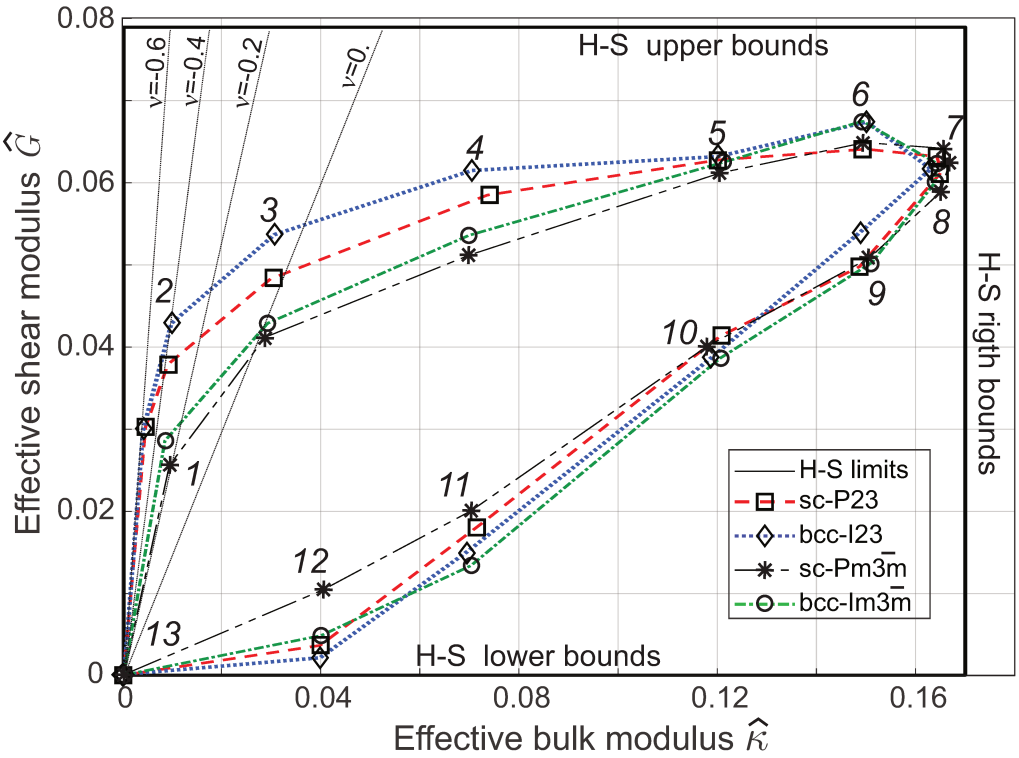

Figura B.12: Three-Dimensional design of composites whose properties are close to the theoretical bounds. Hashin-Shtrikman bounds in the space $(\hat{\kappa}, \hat{G})$. Solutions for 13 different sets of problems using four space groups $P23$, $Pm\bar{3}m$ (with sc Bravais lattice) and $I23$, $Im\bar{3}m$ (with bcc Bravais lattice). Isolines of properties with negative Posson's ratios are shown.

Tabla B.3: Zener ratio ξ quantifying the anisotropy of 3-D microarchitecture design solutions with space groups $P23$, $I23$, $Pm\bar{3}m$ and $Im\bar{3}m$. The number of the problem in column 1 coincides with the problem number identified in Figure B.12.

Problem	$P23$	$I23$	$Pm\bar{3}m$	$Im\bar{3}m$
1	1.009	1.012	0.943	0.995
2	0.978	1.014	1.047	1.005
7	1.035	1.010	1.004	0.987
12	1.455	1.539	1.140	0.995

4.1. Discussion of results

After evaluating the results plotted in Figure B.12 and Table B.3, the following conclusions can be drawn:

1) In the region of the space $(\hat{\kappa}, \hat{G})$ corresponding to small $\hat{\kappa}$ and large $\hat{G}$, i.e., negative or small Poisson's ratios, the point group (either 23 or $m\bar{3}m$) have a higher influence than the Bravais lattice (sc or bcc) to achieve properties close to the bounds. The closest solutions are attained with the point group 23, which has fewer symmetry elements than the $m\bar{3}m$ point group.

2) In the region of the space $(\hat{\kappa}, \hat{G})$ corresponding to high bulk and shear moduli, problems 6 and 7, the solutions are similar for identical lattices, independently of the point group. The reason for this response is that topologies with the highest symmetries display properties closer to the limit values in this specific region of the space $(\hat{\kappa}, \hat{G})$. Thus, when a space group with lower symmetry is imposed in the algorithm, it seeks for solutions with higher symmetry than the enforced one.

According to this conclusion, which is similar to that presented at the end of sub-Section 3.1, there would be a tendency to think that, in all cases, the imposition of the lowest symmetries is preferable to the highest ones and leaving to the algorithm, the search for higher symmetries, if it were the case. However, this conclusion is not correct in general. We have discussed in sub-Section 3.1 that the enforcement of appropriate symmetries has been beneficial for obtaining a marginally closer solution to the theoretical limits, as well as, to achieve notably more stable, robust and repetitive responses of the topology optimization algorithm.

3) The following tendency has been observed in general for attaining the points on the HS-upper and right bounds. The bcc lattice provides solutions with larger values of $\hat{G}$, while the sc lattice provides solutions with slightly larger values of $\hat{\kappa}$.

4) In the HS-lower bound region, problem 12, where the HS-bound estimates the occurrence of pentamode materials, the solutions with space groups $P23$, $I23$ and $Im\bar{3}m$ give lower shear stiffnesses. However, according to the results in Table B.3, the $P23$ and $I23$ solutions cannot be considered as isotropic. Alternatively, the $Im\bar{3}m$ solution attains a low shear modulus with a closely isotropic response.

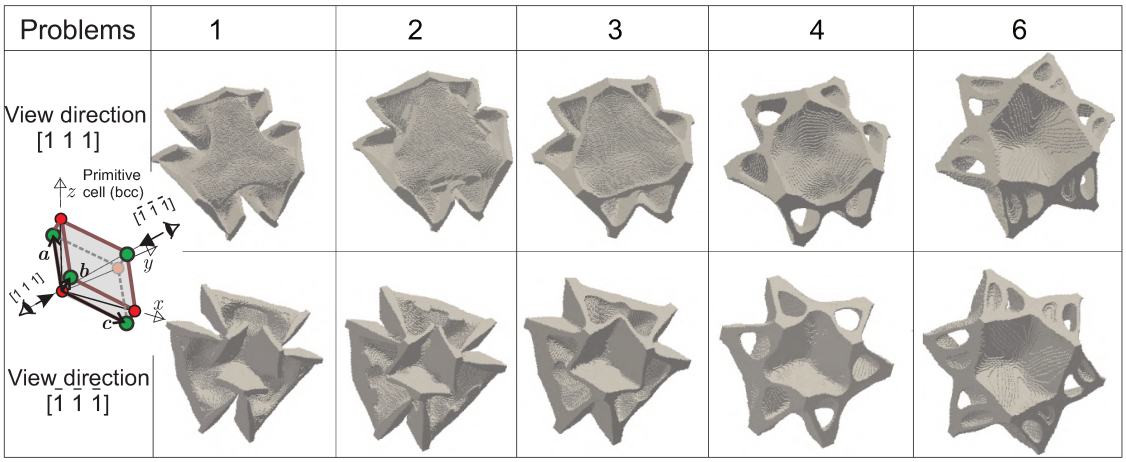

Figura B.13: Microarchitecture transitions with maximal shear stiffness and target points along the HS-upper bound. Space group $I23$. Problems 1, 2, 3 , 4 and 6 are in correspondence with those in Figure B.12. Topologies of the bcc primitive cell observed from two points of view: [1 1 1] and [$\bar{1}$ $\bar{1}$ $\bar{1}$].

Microarchitecture transition along the upper bound

An almost continuous transition of topologies with the imposed space group $I23$ is attained when designing microstructures with maximum shear modulus close to the HS-upper bound. These microarchitectures are depicted in Figure B.13 and correspond to solutions of Problems 1, 2, 3, 4, and 6 of Figure B.12. The attained microarchitectures are displayed from two opposite points of view, according to the directions [1 1 1] and [$\bar{1}$ $\bar{1}$ $\bar{1}$], respectively[15].

Due to the characteristic symmetries of space group $Im\bar{3}m$, the topologies with this space group display an identical appearance when viewed from both directions [1 1 1] and [$\bar{1}$ $\bar{1}$ $\bar{1}$] because in this point group $m\bar{3}m$, both directions belongs to the same family $\langle 111 \rangle$. Such property is not satisfied, in general, by topologies with $I23$ space group, property which is confirmed in Figure B.13. However, the similar appearance observed from both points of view is noted in the solution of Problem 6, Figure B.13.

The above observation confirms once again the previously discussed concept about that the imposition of a low symmetry condition, such as the $I23$, does not inhibit the attainment of topologies with higher symmetries, copying that of the space group $Im\bar{3}m$. This observation is additionally supported by the fact that solutions obtained with space groups $I23$ and $Im\bar{3}m$ have almost the same elastic properties stated in Figure B.12,

[15] We use Miller indices to identify crystallographic directions and planes. A family of planes is denoted between braces "{...}" and collect all the planes which are related through the symmetry operations of the point group. Therefore, two families of planes with identical Miller indices but different point groups may indicate different sets of planes. The same observation is done for the family of directions denoted between angle brackets "⟨...⟩".

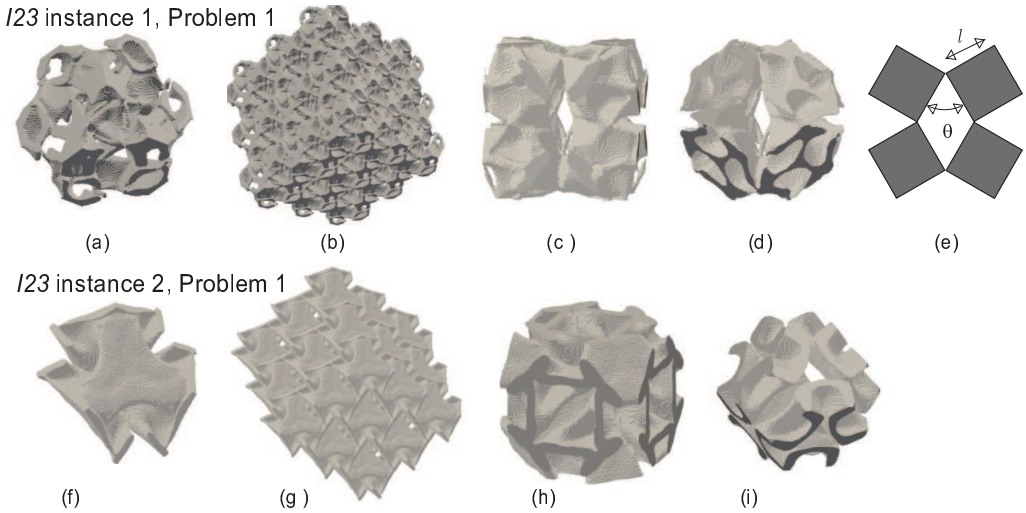

Figura B.14: Two instances of composites with minimum Poisson's ratio attained with Problem 1 in Figure B.12, space group $I23$. **Instance 1**: a) primitive cell; b) assembled microstructure; c) conventional cell; d) Voronoi cell; e) 2D rotating polygonal models described in Ren et al. (2018). **Instance 2**: f) primitive cell; g) assembled microstructure; h) conventional cell; i) Voronoi cell.

Microarchitecture of auxetic materials

Several designed 3D microarchitectures with auxetic properties show topologies characterized by similar deformation mechanisms to those reported in the literature for 2D problems. A typical case is a microstructure designed to have minimum Poisson's ratio (Problem 1 in Figure B.12) using the spatial group $I23$. Two different solutions are depicted in Figure B.14 called Instances 1 and 2. It can be noted that the conventional cell of *Instance 1*, Figure B.14-c, consists of eight blocks, similar to rigid cubes, connected at their edges with joints. These rigid cubes are allowed to have a relative rotation between them. Thus, the deformation mechanism to get the required auxetic behavior is similar to the 2D microstructure reported in the literature and called *rotating polygonal models*, see Ren et al. (2018) and Attard y Grima (2012). For comparison, the rotating polygonal microstructure is reproduced in Figure B.14-e. Some other three-dimensional microarchitectures having a Poisson's ratio approaching -1 are reported in Milton (2015).

One additional attained microstructure with similar elastic properties is denoted *Instance 2*. It is displayed in Figure B.14 f-i. The Voronoi cell of this microstructure shows four identical independent substructures which stay interconnected after the cell assembling. At the best of our knowledge, this microstructure has not been previously reported in the literature.

Configurations resulting from the auxetic 3D microstructures projected onto cutting planes

An additional aspect which shed some light on the understanding of the attained 3D microstructures comes from the analysis of the resulting projected topologies by cutting the designed microarchitectures with specific families of planes. Of particular interest are those projected topologies onto planes containing symmetry elements.

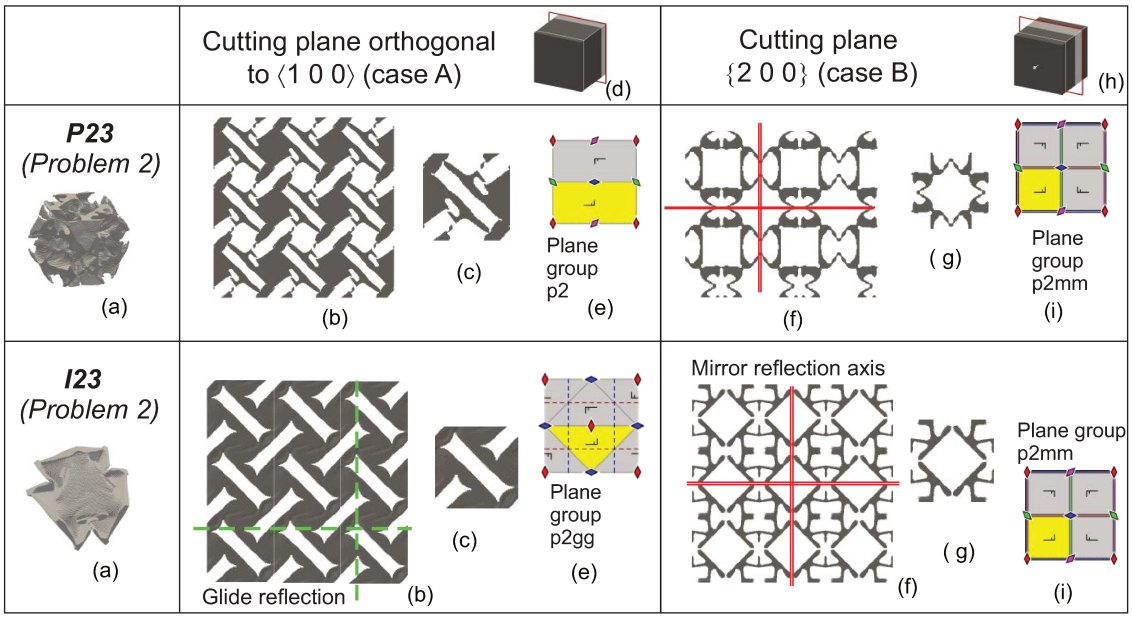

Figura B.15: Projected microstructures attained of problem 2 in Figure B.12. Space groups $P23$ and $I23$. Two projected configurations according to two different cut plane positions (cases A and B). a) primitive cells; b) and f) projected topologies of the assembled composites; c) and g) projected topologies of the conventional unit cells; d) positions in the conventional cell of the cutting planes; e) and i) plane groups and symmetry elements. The symbols representing the plane group symmetry elements are described in Figure B.6.

We analyze the projected configuration onto planes orthogonal to three families of directions: $\langle 1\,0\,0\rangle$, $\langle 1\,1\,0\rangle$ and $\langle 1\,1\,1\rangle$.

This analysis is restricted to the solutions of problems 1 and 2 of Figure B.12 displaying the most negative Poissson's ratios.

a) Cutting planes orthogonal to $\langle 1\,0\,0\rangle$

a.1) Space groups $P23$ and $I23$

The projected configurations onto generic planes orthogonal to $\langle 1\,0\,0\rangle$ of topologies with point groups 23 display a plane group $p2$ with a square lattice. However, there are some specific positions of these cutting planes in where the projected topology may displays additional symmetry elements.

Particularly, when the position of the cutting plane is at the middle distance between two consecutive planes of the family $\{2\,0\,0\}$, the space group $I23$ projects as a plane group $p2gg$. This result is a consequence of the additional two-fold screw axes existing in the $I23$ space group exhibited in Figure B.5-d. Therefore, the space group $P23$ does not possess this symmetry. Figure B.15, case A, display the projected configuration of both space groups onto this particular plane. Although both configurations display analogous patterns, as a consequence of the additional glide reflection elements in the space group $I23$, this microstructure presents a better resolution and, according to Figure B.12, shows closer elastic properties to the bounds.

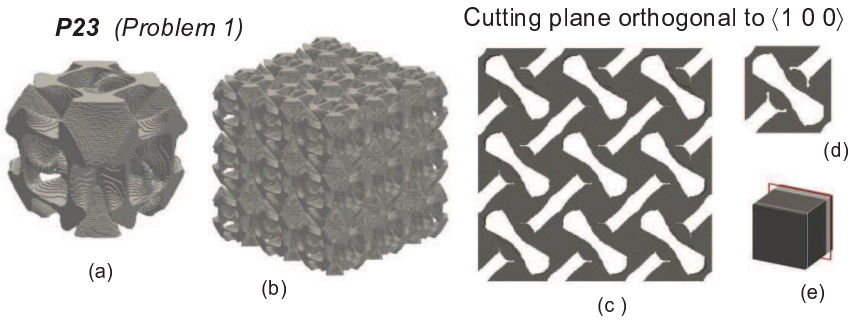

Figura B.16: Microstructure attained with Problem 1 in Figure B.12. Space group $P23$. a) primitive cell; b) assembled microstructure; c) projected topology of the assembled composite onto the plane orthogonal to $\langle 1\,0\,0\rangle$ situated between two consecutive planes of the family $\{2\,0\,0\}$; d) projected topology of the primitive unit cell onto the same plane; e) Position of the cutting plane relative to the primitive cell.

It is interesting to compare the similitude between the configuration displayed in Figure B.15-b of space group $I23$, and the layout reported as antitetrachiral by Alderson et al. (2010). We observe that the here obtained projected topology is an anti-tetrachiral configuration. Notably, the anti-tetrachiral configuration is a $p4gm$ plane group. Such as mentioned by Alderson et al. (2010), in 2D cases, the anti-tetrachiral configuration, if compared with alternative chiral configurations, is the most performer one for attaining Poisson's ratios close to -1, see Chen et al. (2013).

Additionally, the topologies projected onto planes belonging to the family $\{2\,0\,0\}$, which contains two-fold rotation axes, have mirror lines resulting with a plane group $p2mm$, such as shown in Figure B.15-f. This plane group penalizes the realization of auxetic materials. However, apparently, the arising of this detrimental configuration in a small number of planes is not sufficient to generate an inadequate response of the full microarchitecture.

Next, based on the results obtained in Problems 1 and 2 of Figure B.12 with the spaces groups $P23$ and $I23$, we re-examine an issue already discussed above. We note that the imposition of a space group, $P23$, with a less number of symmetry elements on the topology optimization algorithm, leaving it to attain the adequate configuration symmetry, does not work correctly in Problem 2. In this case, the solution with the $I23$ space group is notably better than the solution obtained with the $P23$ space group. However, this conjecture does work when analyzing the results of Problem 1. Examining the projected configuration of the $P23$ solution of Problem 1, depicted in Figure B.16, we note that it tends to capture a higher symmetry, with mirror symmetry lines, and which additionally is similar to the topologies $I23$ displayed in Figures B.15-b.

At this point, it is necessary to distinguish between the point groups $p2mg$ and $p2mm$ and their capacity to achieve auxetics 2D composites. The glide symmetry element of the $p2mg$ plane group is not necessarily so prejudicial as the mirror symmetry element is in the $p2mm$ case. There are several topologies in 2D having plane group $p2mg$ with isotropic elastic properties and negative Poisson's ratio, see the discussion in Section 5.1.5 of the paper by Podestá et al. (2019).

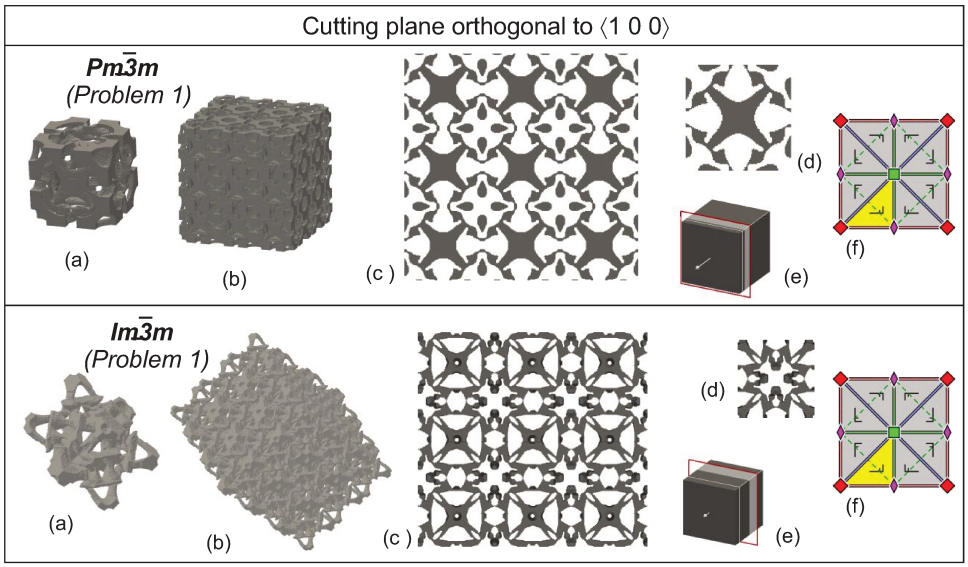

Figura B.17: Microstructure attained with Problem 1 in Figure B.12. Space groups $Pm\bar{3}m$ and $Im\bar{3}m$. a) primitive cells; b) assembled microstructures; c) projected topologies of the assembled composites onto a generic plane orthogonal to $\langle 1\,0\,0\rangle$; d) projected topologies of the conventional unit cells onto the same plane; e) Positions of the cutting planes relative to the conventional cells; f) symmetry elements of $Pm\bar{3}m$ and $Im\bar{3}m$ configurations projected onto the generic plane. The symbols representing the plane group symmetry elements are described in Figure B.6.

a.2) Space groups $Pm\bar{3}m$ and $Im\bar{3}m$

The $Pm\bar{3}m$ and $Im\bar{3}m$ space groups project onto a plane group $p4mm$ when the cutting plane is a generic plane orthogonal to $\langle 1\,0\,0\rangle$. Figure B.17-f shows the symmetry elements of this plane group, and Figures B.17-c and d display the material configurations of the designed microstructures of Problem 1 in Figure B.12 projected onto this plane. Observe the complex topology shown by both microstructures.

According to the conclusions achieved for 2D topologies, the plane group $p4mm$ involves a large number of mirror symmetry elements, which is very detrimental to obtain large negative Poisson's ratios. The same conclusion can be generalized to be applied to the results obtained in 3D designs with both spaces groups $Pm\bar{3}m$ and $Im\bar{3}m$. The bad performances displayed in Figure B.12, Problems 1 and 2 , by the elastic properties of these space groups, can then be associated with this feature.

b) Cutting planes orthogonal to $\langle 1\,1\,0\rangle$

b.1) Space groups $P23$ and $I23$

The projected lattice onto the cutting planes orthogonal to $\langle 1\,1\,0\rangle$ generate a Rectangular Primitive lattice for the three-dimensional sc lattice and a Rectangular Centered one for the bcc lattice. In both cases, the aspect ratios of the conventional plane cells are $\sqrt{2}$.

The projections of the spaces groups $P23$ and $I23$ onto generic planes orthogonal to $\langle 1\,1\,0\rangle$ do not generate any symmetry element. Therefore, the plane group is $p1$. However, in the particular

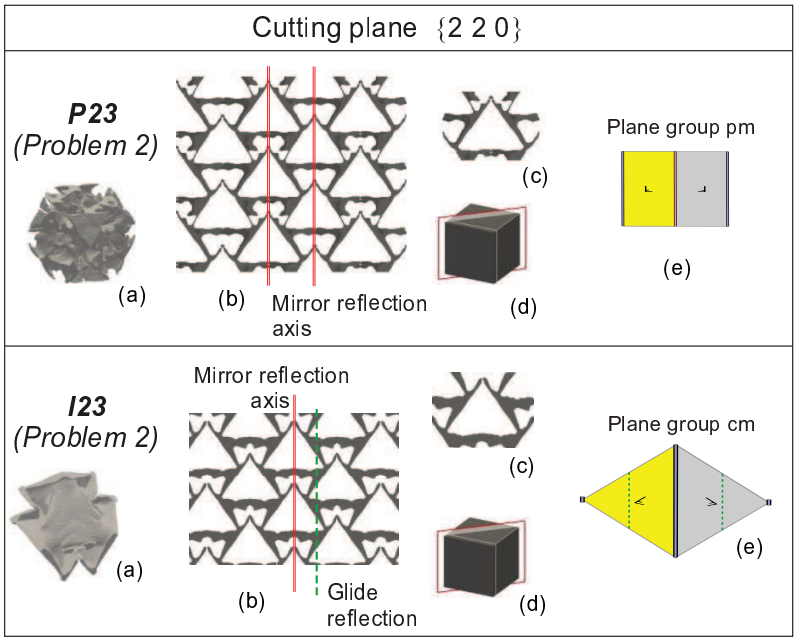

Figura B.18: Projected microstructures attained with Problem 2 in Figure B.12. Space groups $P23$ and $I23$. Cutting plane $\{2\,2\,0\}$. a) primitive cells; b) projected topologies of the assembled composites; c) projected topologies of the conventional unit cells; d) Positions of the cutting planes relative to the conventional cells; e) plane groups and symmetry elements. The symbols representing the plane group symmetry elements are described in Figure B.6.

case of the plane family $\{2\,2\,0\}$, which contains the two-fold rotation axes, the plane group projected by the space groups $P23$ and $I23$ change to pm and cm, respectively. Thus, the topologies obtained with $P23$ and $I23$ for the Problem 2 projected onto that specific plane family are shown in Figure B.18. Also, Figure B.18-c identifies the symmetry lines of the projected configurations. Note that the plane group pm has two parallel symmetry mirror lines, while the cm has only one mirror line and one glide reflection line, such as exhibited in Figure B.18-e. A consequence of these attributes is that the space group $P23$ displays a projected topology with two different types of triangles, while the $I23$ displays only one type of triangle. It is interesting to compare the resemblance between these topologies with the 2D configuration depicted in Figure B.9, $p31m$ plane group, which is one of the best plane groups to attain negative Poisson's ratio.

b.2) Plane groups $Pm\bar{3}m$ and $Im\bar{3}m$

The space group $Pm\bar{3}m$ projects onto the generic planes orthogonal to $\langle 1\,1\,0\rangle$ as a plane group $p2mm$ and the $Im\bar{3}m$ as a plane group $c2mm$. Again, and such as observed for 2D problems, for both space groups, the enforced symmetry onto these planes are not convenient for attaining negative Poisson's ratios.

c) Cutting planes orthogonal to $\langle 1\,1\,1\rangle$

c.1) Plane groups $P23$ and $I23$

The projected configurations onto generic planes orthogonal to $\langle 1\,1\,1\rangle$ of the space groups

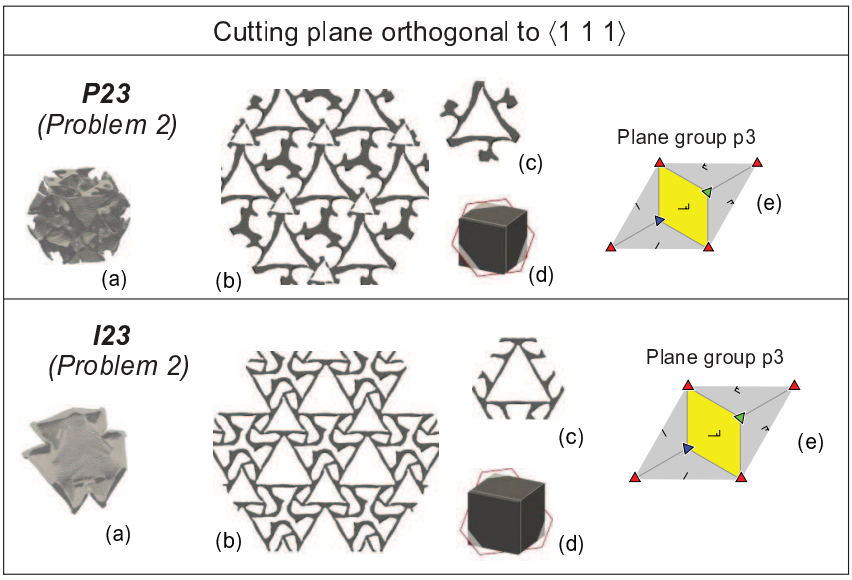

Figura B.19: Projected microstructures attained with Problem 2 in Figure B.19. Space groups $P23$ and $I23$. Column 1: Cutting planes orthogonal to $\langle 1\,1\,1\rangle$. a) primitive cells; b) projected topologies of the assemble composites; c) projected topologies of the conventional unit cells; d) Positions of the cutting planes relative to the conventional cells; e) plane groups and symmetry elements. The symbols representing the plane group symmetry elements are described in Figure B.6.

$P23$ and $I23$ display a configuration with a hexagonal Bravais lattice and plane group $p3$. The symmetry elements of the plane group $p3$ are shown in Figure B.19-e. The topologies of the obtained microarchitectures with these space groups ($P23$ and $I23$) are displayed in Figure B.19-b. These topologies have a tendency to attain a higher symmetry than the $p3$ enforced by the space groups.

The topologies attained in Problem 1 of Figure B.12 projected onto planes orthogonal to $\{1\,1\,1\}$ almost copy, even with more confidence than in projections onto generic planes $\langle 1\,1\,1\rangle$, a plane group $p3m1$. They are shown in Figure B.20-c and d.It is notable that the algorithm searches for configurations with higher symmetries than the imposed ones also on planes orthogonal to $\langle 1\,0\,0\rangle$ and $\langle 1\,1\,0\rangle$.

Analyzing the attained symmetries in these cases, we observe that they are compatible with space group configurations $P\bar{4}3m$ and $I\bar{4}3m$ projected onto the same family of planes. This conclusion may be a symptom that these space groups are better than the imposed ones for reaching the problem target.

c.2) Plane groups $Pm\bar{3}m$ and $Im\bar{3}m$

Figure B.21 shows the topologies attained with $Pm\bar{3}m$ space group and projected onto cutting planes orthogonal to $\langle 1\,1\,1\rangle$. In this generic plane, the projected topology has $p3m1$ plane group. Particularly, if the cutting plane belongs to the family $\{2\,2\,2\}$, which contains the inversion center of the point group element $\bar{3}$, the plane group is a $p6mm$. Identical symmetry properties are valid

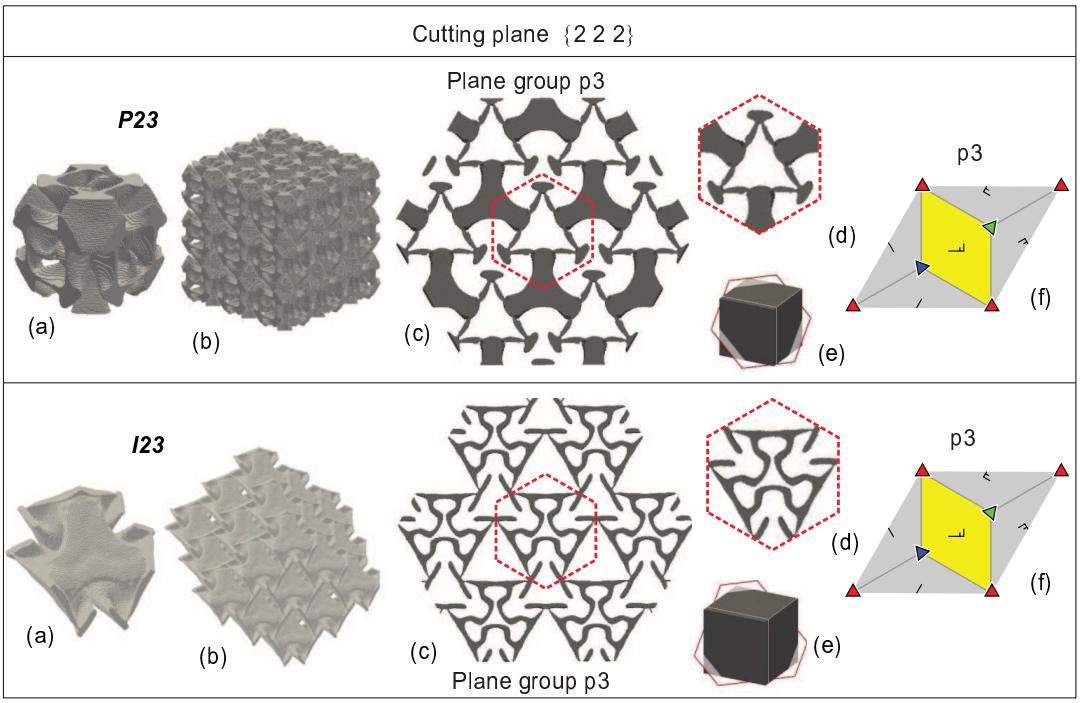

Figura B.20: Microstructure attained with Problem 1 in Figure B.12. Space groups $P23$ and $I23$. a) primitive cells; b) assembled microstructure; c) projected topologies of the assembled composite onto the family of planes $\{2\,2\,2\}$; d) Voronoi unit cell of the projected topologies; e) Positions of the cutting planes relative to the conventional cells; f) Projected symmetry elements onto a generic plane orthogonal to $\langle 1\,1\,1\rangle$ of space groups $P23$ and $I23$. The symbols representing the plane group symmetry elements are described in Figure B.6.

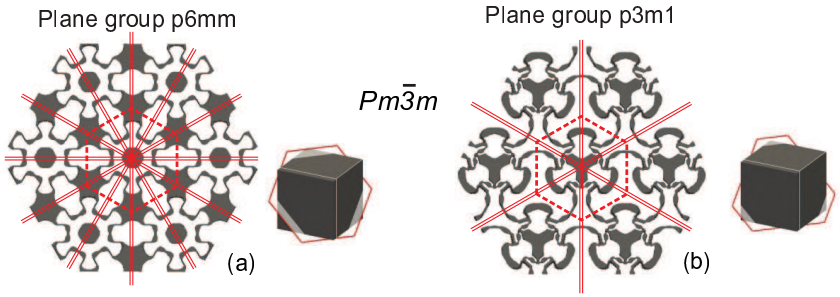

Figura B.21: Projected topologies onto planes orthogonal to $\langle 1\,1\,1\rangle$ of the microarchitectures at Problem 1 in Figure B.12, space group $Pm\bar{3}m$. a) cutting plane belongs to the family $\{2\,2\,2\}$; b) generic cutting plane orthogonal to $\langle 1\,1\,1\rangle$.

for topologies with $Im\bar{3}m$ space groups, except that the family of planes containing the inversion centers is the $\{4\,4\,4\}$.

Again in this case, the results obtained with the space group $Pm\bar{3}m$ and $Im\bar{3}m$ confirm the comment mentioned in sub-Section 3.1 about that the plane group $p6mm$ penalizes severely the capturing of auxetic materials.

Microarchitectures for pentamode materials

The lower estimation of the HS-bounds corresponds to isotropic materials with close to zero shear modulus. Therefore, according to the denomination of Milton y Cherkaev (1995), they are

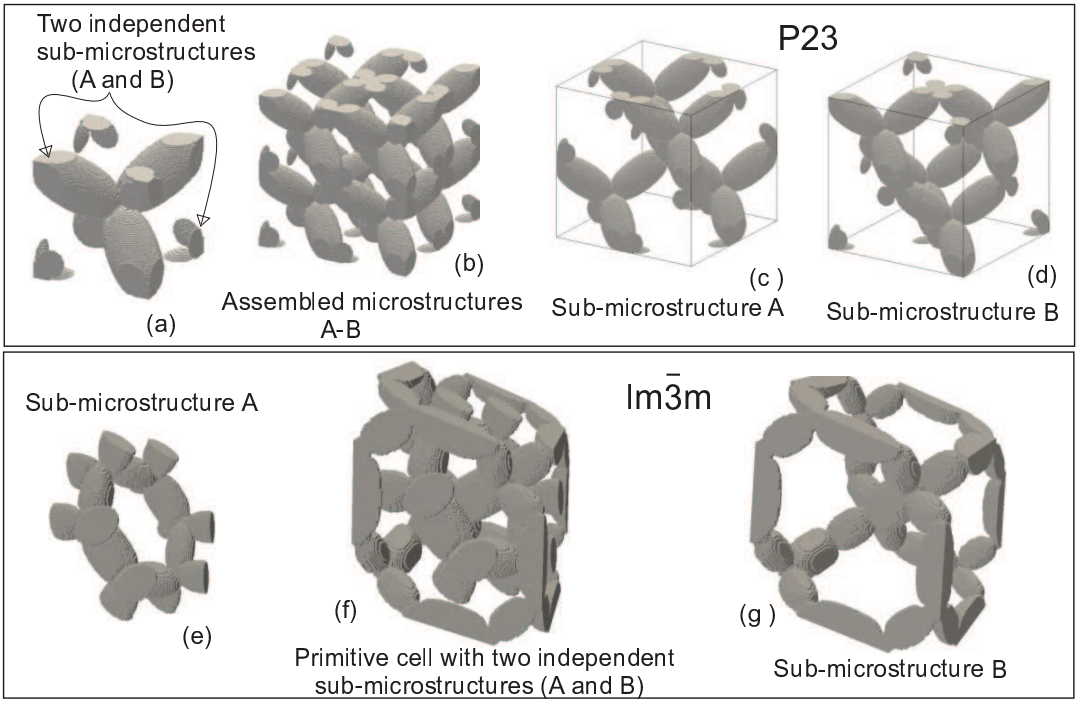

Figura B.22: Topologies attained with Problem 12 in Figure B.12 by enforcing a space group $P23$ (a to d) and $Im\hat{3}m$ (e to g). a) and f) are the primitive unit cells; b) assembled microstructures; c, d e and g) sub-microstructures.

pentamode materials[16].

By solving the isotropic problem of minimum shear modulus for the bulk modulus $\hat{\kappa} = 0.04$ (Problem 12 in Figure B.12), we obtain a similar microstructure to that reported in the literature for this family of metamaterials, see Milton y Cherkaev (1995), Kadic et al. (2012) and Kadic et al. (2014). As can be observed in Figure B.22, the microstructures obtained using the present methodology with space groups $P23$ and $Im\bar{3}m$ are constituted by two independent sub-microarchitectures in the cubic cell, respectively. Each sub-microstructure is approximately similar to the ones reported by Kadic et al. (2012) in Figure 1-b and are, typically, constituted by rigid elements connected through flexible joints.

The homogenized elasticity tensors of the microstructure obtained with the $P23$ space group has the following six eigenvalues: 0.1196; 0.0098; 0.0098; 0.0084 ; 0.0084 ; 0.0084, and the ratio between the maximum and minimum is approximately 14.

The homogenized elasticity tensors of the microstructure obtained with the $Im\bar{3}m$ space group has the following six eigenvalues: 0.1204, 0.0098 ; 0.0098 ; 0.0098; 0.0098; 0.0098. The ratio between the maximum and minimum is approximately 12.

The $I23$ solution, which gives the lowest shear modulus, display eight sub-microstructures,

[16] A Pentamode material is a class of extremal material having five easy (compliant) modes of deformation in a three-dimensional space, and having only one non-easy (stiff) mode of deformation. The elasticity tensor of this material has one non-null eigenvalue and five null eigenvalues (hence the name of pentamode given to this class of materials). In 1995, Milton y Cherkaev (1995) have coined the name of pentamode materials in the context of linear elasticity. In the same year, Sigmund (1995) has independently introduced it in the context of inverse homogenization problems.

and a second instance of the $P23$ solution, not shown here, displays four sub-microstructures. Thus, according to the present results, we perceive that an increase in the number of sub-microstructures entails a decrease of the shear modulus.

5. Conclusions

In this paper, we have analyzed the role that the symmetries of crystals play in the topology design of isotropic elastic materials when the design target is to attain properties close to the theoretical bounds, and the optimum design methodology is based on an inverse homogenization technique. The summary of the attained results are depicted in Figures B.7 and B.12. They are a demonstration that the maximal/minimal achievable properties strongly depend on the crystal symmetries imposed on the mathematical technique. And most important, the adequate crystal symmetries to reach these maximal/minimal properties change with the limit target point, or sector, on the CG and HS-bounds in the plane $(\hat{\kappa}, \hat{G})$. In both cases, 2D and 3D, we have found that the bounds on the right part of the plane, with maximum $\hat{\kappa}$, can be approximated with the higher crystal symmetries. Contrarily, to approach the left bound, it is better to explore other types of symmetries.

In 2D problems, the isotropy of the composite is guaranteed by adopting plane group symmetries consistent with the *hexagonal crystal system*. However, not all these plane groups have identical effects. For example, to attain auxetic composites, it is convenient to explore the $p3$, $p31m$ and $p6$ plane groups, while the $p6mm$ and $p3m1$ are unsuitable in these cases. Notably, the plane groups $p6$ and $p3$ allow for the development of chiral configurations. Conclusions are different if the extreme target properties are the maximal bulk and minimal shear moduli (the Walpole Point). In this case, the plane group $p6mm$ is the most effective one. For this particular problem, we have also shown that the imposition of a plane group with low symmetry, such as $p3$, does not provide as good solutions as those attained by imposing the $p6mm$ plane group. This result proves that a procedure which takes a plane group with low symmetry ($p3$) and leaving the algorithm for searching the higher symmetry ($p6mm$) does not work, in general, with the best performance.

In 3D problems, we have only analyzed symmetries of the *cubic crystal system*. In this case, the dependence on the space group for attaining maximal/minimal properties is still more pronounced than in 2D cases. The space groups $I23$ and $P23$ are notably more suitable to attain maximal properties in the region close to the HS-left-upper bound, coincident with the response of auxetic materials. A similar conclusion about the proper selection of the cell defining the optimization domain Ω_μ can be drawn. The bcc primitive cell has turned out to be notably more advantageous than the simple cubic (sc) cell to get maximal properties in some sectors of the plane $(\hat{\kappa}, \hat{G})$, along

the HS-upper bound.

Even when we have not specifically analyzed the numerical response of the topology optimization algorithm, we envisage that the additional crystal symmetry constraints notably increase the robustness and stability of the algorithm, by limiting the search space of the geometrical variables defining the topology.

Finally, we remark that the use of crystal symmetries for topology design can be easily extended to other more general thermal, photonic, acoustic microarchitecture design problems, anticipating similar potential benefits to those here explored.

Acknowledgments

The authors acknowledge the financial support from CONICET and ANPCyT (grants PICT 2014-3372 and 2016-2673).

Bibliografía

Alderson A., Alderson K., Attard D., Evans K., Gatt R., Grima J., Miller W., Ravirala N., Smith C., y Zied K. Elastic constants of 3-, 4-and 6-connected chiral and anti-chiral honeycombs subject to uniaxial in-plane loading. *Composites Science and Technology*, 70(7):1042–1048, 2010.

Amstutz S. y Andrä H. A new algorithm for topology optimization using a level-set method. *Journal of Computational Physics*, 216(2):573–588, 2006.

Amstutz S., Giusti S., Novotny A., y de Souza Neto E. Topological derivative for multi-scale linear elasticity models applied to the synthesis of microstructures. *International Journal for Numerical Methods in Engineering*, 84(6):733–756, 2010.

Andreassen E. y Lazarov B.S.and Sigmund O. Design of manufacturable 3D extremal elastic microstructure. *Mechanics of Materials*, 69(1):1–10, 2014.

Attard D. y Grima J. A three-dimensional rotating rigid units network exhibiting negative poisson's ratios. *Physica Status Solidi (b)*, 249(7):1330–1338, 2012.

Bendsoe M. y Sigmund O. *Topology Optimization: Theory, Methods, and Applications*. Springer Science & Business Media, 2003.

Berryman J. y Milton G. Microgeometry of random composites and porous media. *Journal of Physics D: Applied Physics*, 21(1):87, 1988.

Chen Y., Scarpa F., Liu Y., y Leng J. Elasticity of anti-tetrachiral anisotropic lattices. *International Journal of Solids and Structures*, 50(6):996–1004, 2013.

Cherkaev A. y Gibiansky L. Coupled estimates for the bulk and shear moduli of a two-dimensional

isotropic elastic composite. *Journal of the Mechanics and Physics of Solids*, 41(5):937–980, 1993.

Eyre D. y Milton G. A fast numerical scheme for computing the response of composites using grid refinement. *The European Physical Journal-Applied Physics*, 6(1):41–47, 1999.

Hashin Z. y Shtrikman S. A variational approach to the theory of the elastic behaviour of multiphase materials. *Journal of the Mechanics and Physics of Solids*, 11(2):127–140, 1963.

Hitzer E. y Perwass C. Visualization of fundamental symmetries in nature. En *Proceedings of Fuzzy System Symposium (FSS 2009), Tsukuba, Japan, 14-16 Jul.* 2009. Http://spacegroup.info/.

Kadic M., Bückmann T., Schittny R., Gumbsch P., y Wegener M. Pentamode metamaterials with independently tailored bulk modulus and mass density. *Physical Review Applied*, 2(5):054007, 2014.

Kadic M., Bückmann T., Stenger N., Thiel M., y Wegener M. On the practicability of pentamode mechanical metamaterials. *Applied Physics Letters*, 100(19):191901, 2012.

Kadic M., Milton G., van Hecke M., y Wegener M. 3D metamaterials. *Nature Reviews Physics*, 1:198–210, 2019.

London E.P.B.., editor. *International Tables for Crystallography. Volume C, Mathematical, Physical and Chemical Tables. Dordrecht*. Published for the International Union of Crystallography by Kluwer Academic Publishers, 2004.

Meille S. y Garboczi E. Linear elastic properties of 2d and 3d models of porous materials made from elongated objects. *Modelling and Simulation in Materials Science and Engineering*, 9(5):371, 2001.

Méndez C., Podestá J., Toro S., Huespe A., y Oliver J. Making use of symmetries in the three-dimensional elastic inverse homogenization problem. *Journal for Multiscale Computational Engineering*, 17:261–280, 2019.

Milton G. New examples of three-dimensional dilational materials. *physica status solidi (b)*, 252(7):1426–1430, 2015.

Milton G. Stiff competition. *Nature*, 564(7734):E1, 2018.

Milton G. y Camar-Eddine M. Near optimal pentamodes as a tool for guiding stress while minimizing compliance in 3d-printed materials: A complete solution to the weak g-closure problem for 3d-printed materials. *Journal of the Mechanics and Physics of Solids*, 114:194–208, 2018.

Milton G. y Cherkaev A. Which elasticity tensors are realizable? *Journal of Engineering Materials and Technology*, 117(4):483–493, 1995.

Novotny A. y Sokołowski J. *Topological derivatives in shape optimization*. Springer Science &

Business Media, 2012.

Nye J. *Physical Properties of Crystals: Their Representation by Tensors and Matrices*, volumen 146. Clarendon Press-Oxford., 2006.

Osanov M. y Guest J. Topology optimization for architected materials design. *Annual Review of Materials Science*, 46:211–233, 2016.

Ostanin I., Ovchinnikov G., Tozoni D., y Zorin D. A parametric class of composites with a large achievable range of effective elastic properties. *Journal of the Mechanics and Physics of Solids*, 118:204–217, 2018.

Podestá J., Méndez C., Toro S., y Huespe A. Symmetry considerations for topology design in the elastic inverse homogenization problem. *Journal of the Mechanics and Physics of Solids*, 128:54–78, 2019.

Podestá J., Méndez C., Toro S., Huespe A., y Oliver J. Material design of elastic structures using voronoi cells. *International Journal for Numerical Methods in Engineering*, 115(3):269–292, 2018.

Ren X., Das R., Tran P., Ngo T., y Xie Y. Auxetic metamaterials and structures: A review. *Smart Materials and Structures*, 2018.

Rossi Cabral N., Yera R., Méndez C., y Huespe A. Numerical technique for the 3d microarchitecture topology design of elastic composites inspired on crystal symmetries. *submitted to: Computer methods in applied mechanics and engineering*, 2019.

Sigmund O. Materials with prescribed constitutive parameters: an inverse homogenization problem. *International Journal of Solids and Structures*, 31(17):2313–2329, 1994.

Sigmund O. Tailoring materials with prescribed elastic properties. *Mechanics of Materials*, 20(4):351–368, 1995.

Sigmund O. A new class of extremal composites. *Journal of the Mechanics and Physics of Solids*, 48(2):397–428, 2000.

Sólyom J. *Fundamentals of the Physics of Solids: Volume 1: Structure and Dynamics*. Springer Science & Business Media, 2007.

Thorpe M. y Jasiuk I. New results in the theory of elasticity for two-dimensional composites. *Proceedings of the Royal Society of London. Series A: Mathematical and Physical Sciences*, 438(1904):531–544, 1992.

Torquato S. Optimal design of heterogeneous materials. *Annual Review of Materials Rresearch*, 40:101–129, 2010.

Vainshtein B. *Fundamentals of crystals: Symmetry, and methods of structural crystallography*, volumen 1. Springer Science & Business Media, 2013.

Yera R., Rossi N., Méndez C., y Huespe A. *Three-dimensional material microstructures dataset displaying extreme isotropic elastic properties*. 2019. Mendeley Data, v1 http://dx.doi.org/10.17632/cc2hgr9kvh.2.

Anexo C

A topology optimization algorithm based on topological derivative and level set function for designing phononic crystals, Engineering Computations, Volume 39, 2021

El artículo presentado a continuación ha sido publicado en la revista **"Engineering Computations"**.

Yera, R., Forzani, L., Mndez, C.G. and Huespe, A.E., *A topology optimization algorithm based on topological derivative and level-set function for designing phononic crystals*, Engineering Computations, 39(1), 354-379. 2021. DOI: 10.1108/EC-06-2021-0352

A topology optimization algorithm based on topological derivative and level set function for designing phononic crystals

Rolando Yera[1], Luisina Forzani[1], Carlos G. Méndez[1], Alfredo E. Huespe[1,2]
[1]CIMEC-UNL-CONICET, Predio Conicet Dr Alberto Cassano, CP 3000 Santa Fe, Argentina
[2]E.T.S dEnginyers de Camins, Canals i Ports, Technical University of Catalonia (Barcelona Tech)
Campus Nord UPC, Mòdul C-1, c/ Jordi Girona 1-3, 08034, Barcelona, Spain

Abstract

Purpose: This work presents a topology optimization method for designing microarchitectures of phononic crystals. The objective is to get microstructures having, as a consequence of wave propagation phenomena in these media, bandgaps between two specified bands. An additional target is to enlarge the range of frequencies of these bandgaps.
Design/methodology/approach: The resulting optimization problem is solved employing an augmented Lagrangian technique based on the proximal point methods. The main primal variable of the Lagrangian function is the characteristic function determining the spatial geometrical arrangement of different phases within the unit cell of the phononic crystal. This characteristic function is defined in terms of a level-set function. Descent directions of the Lagrangian function are evaluated by using the topological derivatives of the eigenvalues obtained through the dispersion relation of the phononic crystal.
Findings: The description of the optimization algorithm is emphasized and its intrinsic properties to attain adequate phononic crystal topologies are discussed. Particular attention is addressed to validate the analytical expressions of the topological derivative. Application examples for several cases are presented, and the numerical performance of the optimization algorithm for attaining the corresponding solutions is discussed.
Originality: the original contribution results in the description and numerical assessment of a topology optimization algorithm using the joint concepts of the level-set function and topological derivative to design phononic crystals.

1. Introduction

The speed of elastic waves traveling in a periodic medium depends on the wave vector. This phenomenon induces a wave dispersion effect which makes possible the appearance of forbidden frequency bands, or bandgaps, in the spectrum of this medium (Kushwaha (1996)). At such frequencies, the waves cannot propagate.

Specifically designed periodic microstructures which are built to promote the generation, widening, or handling of bandgaps are called phononic crystals as well as metamaterials. The usual distinction between phononic crystals and metamaterials is enlightened by Croënne et al. (2011), who also describes three mechanisms, namely Bragg, hybridization, and weak elastic coupling

effects, inducing the occurrence of bandgaps. Also, bandgap formation at low frequencies and long-wavelength in metamaterials can be artificially opened through a locally resonant mechanism.

The properties displayed by the band spectra, specifically the bandgaps, are notably dependent on the medium microarchitecture. This microarchitecture governs the frequency and the width of the bandgaps. Considering that several applications in a wide range of technologies depend on the existence of large bandgaps, a suitable design criterion of phononic crystals consists of enlarging the bandgap width generated between two bands. The objective is to attain the opening of artificial bandgaps placed in the desired frequency range.

Several contributions have been published in the '90s to understand the effect that microarchitectures have on this phenomenon. Pioneers' works were reported by Sigalas y Economou (1992) and Kushwaha et al. (1993). In both cases, these authors have studied elastic waves in composites constituted by identical spheres (Sigalas et al.) or cylinders (Kushwaha et al.), of radius R, placed periodically within a host homogeneous material. Geometrical variables, such as the volume fraction of spheres or cylinders, lattice constant, symmetry of the sphere configurations; and material variables, such as densities and stiffness contrasts have been considered to determine the band structure features.

A more systematic microarchitecture design of phononic crystals to widening bandgaps can be carried out through topology optimization techniques. Only to cite a few of them, we mention the work of Sigmund's and coauthors, see Jensen y Sigmund (2004) using the so-called solid isotropic material penalization (SIMP) jointly with the method of moving asymptotes; the techniques based on genetic algorithm (GA), Dong et al. (2014); or the technique named bi-directional evolutionary structural optimization (BESO) adopted by Li et al. (2018) as well as by Zhang et al. (2017) to particularly explore hexagonal lattices. An extensive review on different methodologies that can be used to solve this microarchitecture design problem can be found in the paper by Yi y Youn (2016), see also Li et al. (2019)

Following the concept established by topology optimization techniques as a means to design optimal phononic crystals, we would like to highlight a comment taken from Yi y Youn (2016). According to these authors, *"... there exists a great promise for other alternative techniques such as the level set method, the Heaviside projection method, and the phase-field method, to be used in this topic in the future"*. A recent paper following a methodology based on level-set method has been reported by Noguchi et al. (2018). Also, aligned with this comment, in this work, we report a microarchitecture design methodology which is formulated as a topology optimization problem. The optimization problem is solved through an augmented Lagrangian technique, based on a pro-

ximal point method (Nocedal y Wright (2006)), that employs a level-set function to define the spatial configurations of the crystal phases. Sensitivities of the Lagrangian function are evaluated with topological derivatives.

Our interest points toward the microarchitecture design of phononic crystals stressing the numerical aspect of the reported methodology. Even when the reported algorithm is thought for the handling of phonic crystal bandgaps, we emphasize that it can be slightly modified to design metamaterials where the objective is the opening of bandgaps through locally resonant mechanisms. We leave for future works the specific study of optimal microarchitectures of phononic crystals exploring different kinds of material configurations; typically, different types of crystal symmetries, contrasts of elastic properties between the host material and the scatterers, volume fraction of scatterers, etc.

The paper is organized as follows: Section 2 presents a summarized description of the elastic wave propagation equation in periodic media and the numerical methodology to perform the band structure analysis. In Section 3, we formulate the material design problem. Section 4 describes the adopted optimization algorithm for solving this problem. This section corresponds to the chief contribution of the paper. Details of the numerical implementation of the algorithm are given in Section 5. The last part of the paper is devoted to the numerical verification of the topological derivative expressions presented at the end of Section 3. An example to define the microstructure of a phononic crystal with the widest bandgaps is also presented in this part of the paper. Finally, we discuss some conclusions.

2. Bandgaps in phononic crystals

2.1. Plane waves in a periodic medium

The Navier's equation of motion in the intrinsic form for an isotropic solid medium is given by the expression:

$$\nabla\left[(\lambda+2\mu)\nabla\cdot\mathbf{u}\right]-\nabla\wedge(\mu\nabla\wedge\mathbf{u})=\rho\ddot{\mathbf{u}}\ , \tag{C.1}$$

where λ, μ and ρ are the Lame's parameters and density of the medium, respectively; and $\mathbf{u}$ is the displacement vector. Due to the character assumed for the medium, λ, μ and ρ are spatially varying terms. Body forces are neglected in equation C.1.

Considering now the canonical basis in $\mathbb{R}^3$, $\{\mathbf{e}_x;\mathbf{e}_y;\mathbf{e}_z\}$, and the material position vector $\mathbf{x}$, expressed as $\mathbf{x}=x\mathbf{e}_x+y\mathbf{e}_y+z\mathbf{e}_z$, we assume a plane motion defined in $(\mathbf{e}_x;\mathbf{e}_y)$, such that the three components of the vector $\mathbf{u}$, $\mathbf{u}=u_x\mathbf{e}_x+u_y\mathbf{e}_y+u_z\mathbf{e}_z$, are functions only of the coordinates x and y. Additionally, we also assume that $\lambda(x,y)$, $\mu(x,y)$ and $\rho(x,y)$ are periodic properties in the plane $(\mathbf{e}_x;\mathbf{e}_y)$ with translation invariance in the direction $\mathbf{e}_z$. Under these conditions, the

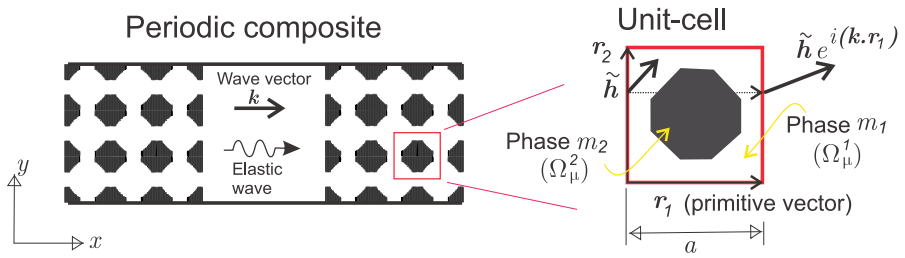

Figura C.1: Elastic wave traveling in a periodic medium. Unit-cell with Bloch boundary conditions.

Navier's equation in the canonical basis can be written as two uncoupled equations in the plane $(\mathbf{e}_x, \mathbf{e}_y)$; one is a vectorial equation written in terms of the vector $\mathbf{u}_{ip}$, comprising two components of the displacement vector $\mathbf{u}$: $\mathbf{u}_{ip} = u_x\mathbf{e}_x + u_y\mathbf{e}_y$, and the other is a scalar equation in terms of the component u_z, denoted $u_{op} = u_z(x, y)$. Both equations are given as follows:

$$\nabla_p \left[(\lambda + 2\mu)\nabla_p \cdot \mathbf{u}_{ip}\right] - \nabla_p \wedge (\mu \nabla_p \wedge \mathbf{u}_{ip}) = \rho \ddot{\mathbf{u}}_{ip} \quad ; \tag{C.2}$$

$$\nabla_p \cdot (\mu \nabla_p u_{op}) = \rho \ddot{u}_{op} \quad ; \tag{C.3}$$

where the two-dimensional gradient operator ∇_p is defined by $\nabla_p = (\partial/\partial x)\,\mathbf{e}_x + (\partial/\partial y)\,\mathbf{e}_y$ and the outer product $\nabla_p \wedge \mathbf{u}_{ip}$ results a vector with z-component.

Particularly, in periodic media, both equations C.2 and C.3 have Bloch wave-type solutions, see Gazalet et al. (2013), expressed as follows:

$$\mathbf{u}_{ip} = \hat{\mathbf{u}}(x, y)e^{i(\mathbf{k}_{ip}\cdot\mathbf{x} - \omega_{ip}t)} = \left[\hat{\mathbf{u}}(x, y)e^{i(\mathbf{k}_{ip}\cdot\mathbf{x})}\right] e^{-i\omega_{ip}t} \quad , \tag{C.4}$$

$$u_{op} = \hat{u}(x, y)e^{i(\mathbf{k}_{op}\cdot\mathbf{x} - \omega_{op}t)} = \left[\hat{u}(x, y)e^{i(\mathbf{k}_{op}\cdot\mathbf{x})}\right] e^{-i\omega_{op}t} \quad , \tag{C.5}$$

with $\mathbf{u}_{ip}$ and u_{op} being called the *in-plane* and the *out-of-plane* waves, respectively. Time is denoted by t, $\mathbf{k}_{ip}$ and $\mathbf{k}_{op}$ are the wave vectors, and ω_{ip} and ω_{op} are the angular frequencies of both waves, respectively. To make the notation more compact from now on, we remove the subindices ip and op from the physical magnitudes of both waves. Thus, it can be understood from each particular context to which wave these magnitudes refer.

The particular characteristics of Bloch waves is that the terms $\hat{\mathbf{u}}(x, y)$ and $\hat{u}(x, y)$, in equations (C.4) and (C.5), are periodic functions reproducing the same translation symmetry of the medium.

2.2. Bandgap structure analysis

Waves propagating in periodic media are dispersive, which means that the frequency ω and the wave speed depend on the wave vector $\mathbf{k}$. The evaluation of the pair $(\mathbf{k}, \omega)$ for different waves, whose propagation is admitted in the periodic medium, is summarily described next.

Solutions (C.4), with the unkowns: $\hat{\mathbf{u}}$, $\mathbf{k}$ and ω, are introduced in the weak conventional variational formulation of the harmonic (spectral) motion equations related to (C.2) (a similar treatment

is given to (C.5) with equation (C.3)). The variational formulation is solved in a unit cell, Ω_μ, of the periodic material with boundary conditions satisfying the Bloch condition for the periodic medium, see Figure C.1. We mention two strategies to perform this step.

i) In the first strategy, the assumed unknown is the function $\hat{\mathbf{u}}$ in equation (C.4). Then, the explicit function $\tilde{\boldsymbol{h}}(\mathbf{x}) = \hat{\mathbf{u}}(\mathbf{x})e^{i(\mathbf{k}\cdot\mathbf{x})}$ and the virtual displacement field $\delta\tilde{\boldsymbol{h}}(\mathbf{x}) = \delta\hat{\mathbf{u}}(\mathbf{x})e^{i(\mathbf{k}\cdot\mathbf{x})}$ are introduced into the variational formulation jointly with periodic boundary conditions on $\hat{\mathbf{u}}$ and $\delta\hat{\mathbf{u}}$. By adopting this strategy, the gradient operator could be generalized by including a $\mathbf{k}$ dependent term, which comes from the definition taken for the $\tilde{\boldsymbol{h}}$ function. The strain-displacement equation has to be modified accordingly, see for example the formulation in Yera et al. (2021).

ii) In the second strategy, the assumed unknown is the function $\tilde{\boldsymbol{h}}(\mathbf{x})$, which are introduced into the variational formulation. Admissible variations are $\delta\tilde{\boldsymbol{h}}(\mathbf{x})$. The boundary conditions for $\tilde{\boldsymbol{h}}(\mathbf{x})$ should satisfy: $\tilde{\boldsymbol{h}}(\mathbf{x}+\boldsymbol{r}) = \tilde{\boldsymbol{h}}(\mathbf{x})e^{i(\mathbf{k}\cdot\boldsymbol{r})}$, where $\boldsymbol{r}$ is a primitive vector of the underlying Bravais lattice of the periodic material, see Figure C.1. Similar boundary conditions are imposed to $\delta\tilde{\boldsymbol{h}}(\mathbf{x})$. Using this strategy, the conventional strain-displacement operator is preserved. This formulation has been discussed by Krattiger y Hussein (2018). In this work, we follow this strategy.

The resulting variational formulation derived from the second strategy is solved using the Finite Element Methods. Considering this technique, the obtained discrete equation system is:

$$\bar{\mathbb{P}}(\mathbf{k})\left[\mathbb{K}-\omega^2\mathbb{M}\right]\mathbb{P}(\mathbf{k})\boldsymbol{h}_r = \left[\boldsymbol{K}(\mathbf{k})-\omega^2\boldsymbol{M}(\mathbf{k})\right]\boldsymbol{h}_r = \mathbf{0}\ , \tag{C.6}$$

where $\mathbb{K}$ and $\mathbb{M}$ are the unconstrained stiffness and mass matrices. The matrix $\mathbb{P}$ imposes the Bloch conditions on the boundary d.o.f's. This matrix connects the vector $\boldsymbol{h}_r$, which gathers the (reduced) unconstrained nodal parameters of the interpolated function $\tilde{\boldsymbol{h}}(x,y)$, with the vector $\boldsymbol{h}$, that collects the full set of the nodal parameters of the same interpolated function:

$$\boldsymbol{h} = \mathbb{P}\boldsymbol{h}_r\ . \tag{C.7}$$

By considering the unit-cell finite element mesh sketched in Figure C.2, expression (C.7) is im-

plemented with the following terms:

$$\boldsymbol{h} = \begin{bmatrix} \boldsymbol{h}_I \\ \boldsymbol{h}_L \\ \boldsymbol{h}_R \\ \boldsymbol{h}_B \\ \boldsymbol{h}_T \\ \boldsymbol{h}_{BL} \\ \boldsymbol{h}_{BR} \\ \boldsymbol{h}_{TR} \\ \boldsymbol{h}_{TL} \end{bmatrix} \quad ; \quad \mathbb{P} \begin{bmatrix} \mathbf{I}_I & \mathbf{0} & \mathbf{0} & \mathbf{0} \\ \mathbf{0} & \mathbf{I}_L & \mathbf{0} & \mathbf{0} \\ \mathbf{0} & \xi_1\mathbf{I}_L & \mathbf{0} & \mathbf{0} \\ \mathbf{0} & \mathbf{0} & \mathbf{I}_B & \mathbf{0} \\ \mathbf{0} & \mathbf{0} & \xi_2\mathbf{I}_B & \mathbf{0} \\ \mathbf{0} & \mathbf{0} & \mathbf{0} & \mathbf{I}_{BL} \\ \mathbf{0} & \mathbf{0} & \mathbf{0} & \xi_1\mathbf{I}_{BL} \\ \mathbf{0} & \mathbf{0} & \mathbf{0} & \xi_1\xi_2\mathbf{I}_{BL} \\ \mathbf{0} & \mathbf{0} & \mathbf{0} & \xi_2\mathbf{I}_{BL} \end{bmatrix} \quad ; \quad \boldsymbol{h}_r = \begin{bmatrix} \boldsymbol{h}_I \\ \boldsymbol{h}_L \\ \boldsymbol{h}_B \\ \boldsymbol{h}_B L \end{bmatrix} . \tag{C.8}$$

where the subindices I, L, R, B, T, BL, BR, TR and TL in (C.8) identify the d.o.f. sets of the nodes indicated in the Figure. $\mathbf{I}_I$, $\mathbf{I}_L$, $\mathbf{I}_B$ and $\mathbf{I}_{BL}$ are identity matrices whose dimensions are given by the number of d.o.f.'s of the vectors $\boldsymbol{h}_I$, $\boldsymbol{h}_L$, $\boldsymbol{h}_B$ and $\boldsymbol{h}_{BL}$, respectively. The coefficients ξ_1 and ξ_2 are: $\xi_1 = e^{i(\mathbf{k}\cdot\boldsymbol{r}_1)}$ and $\xi_2 = e^{i(\mathbf{k}\cdot\boldsymbol{r}_2)}$, $\boldsymbol{r}_1$ and $\boldsymbol{r}_2$ are the primitive translation vectors of the lattice.

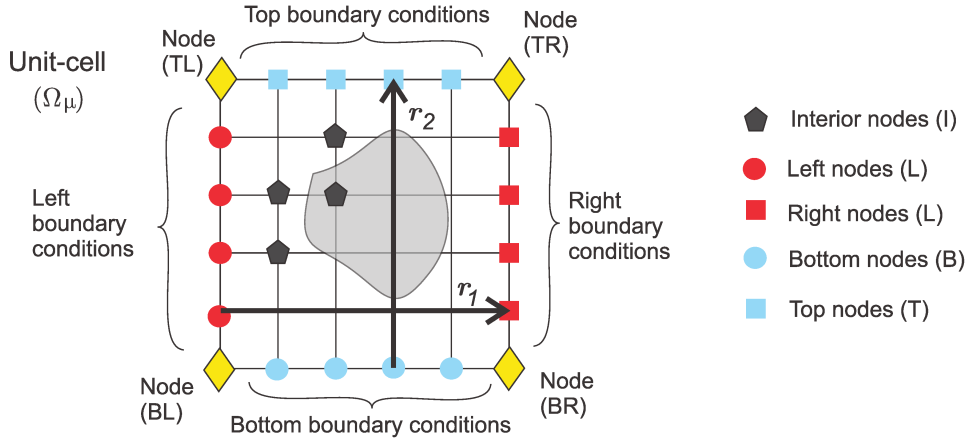

Figura C.2: Finite element mesh of the unit-cell Ω_μ. Denomination of different sets of nodes.

The reader can find further details about the imposition of boundary conditions using the matrix $\mathbb{P}(\mathbf{k})$ in the paper by Krattiger y Hussein (2018). In equation (C.6), $\bar{\mathbb{P}}$ is the conjugate transpose of $\mathbb{P}$.

Additionally to $\boldsymbol{h}_r$, the equation system (C.6) has two unknowns: $\mathbf{k}$ and ω, which can be determined in different ways. The one which we follow in this work consists on adopting a specific value of $\mathbf{k}$, then, considering a non-trivial solution $\boldsymbol{h}_r$, we solve the associated eigenvalue problem (C.6). The number of frequencies ω_j ($j = 1, 2, ...$) and modes $\boldsymbol{h}_j$ depends on the number of the problem d.o.f's. We only consider the lower frequencies.

This procedure establishes a functional dependency of every mode ω_j with $\mathbf{k}$, known as the dispersion relation: $\omega_j(\mathbf{k})$. Therefore, diagrams for every ω_j may be plotted in terms of the wave vectors in the irreducible Brillouin zone. The band structure obtained from these diagrams describes the range of allowed frequencies for the transmitted waves, as well as, the range of forbidden frequencies or bandgaps.

3. Microarchitecture design methodology

Considering a two-phase periodic composite with phases denoted m_1 and m_2, as shown in Figure C.1, our objective consists of designing the geometrical configuration of the microstructure, i.e. the distribution of phases m_1 and m_2 in Ω_μ, to provide the maximum band-gap between two adjacent bands j and $j+1$.

The adopted methodology for solving this problem is a material design technique based on topology optimization. The topology optimization strategy is a gradient-based technique that uses the topological derivative to compute the sensitivities and the level-set function. Next, we describe the mathematical formulation of this methodology.

3.1. Formulation of the topology optimization problem

Following the design methodology presented in Podestá et al. (2019), we select beforehand the symmetry of the material configuration to be attained after solving the problem. This symmetry also stipulates the shape of the design domain Ω_μ. The characteristic size of Ω_μ is arbitrarily taken as $a = 1$, where a is the lattice constant of the composite lattice system associated with the chosen configuration symmetry. In consequence, the frequencies are normalized to provide a band structure representation independent of the unit-cell size a.

By splitting Ω_μ into two disjoint subdomains, Ω_μ^1 constituted by phase m_1 and Ω_μ^2 constituted by phase m_2, we define the characteristic function $\chi(\mathbf{x})$ as follows:

$$\chi(\mathbf{x}) = \begin{cases} 0 & \forall \mathbf{x} \in \Omega_\mu^2 \\ 1 & \forall \mathbf{x} \in \Omega_\mu^1 \end{cases} \tag{C.9}$$

The optimization problem consists on maximizing the absolute bandgap width which is formulated as follows:

$$\begin{aligned} &\max_{\chi} \left(\min_{\mathbf{k}} \omega_{j+1}^2(\mathbf{k}, \chi) - \max_{\mathbf{k}} \omega_j^2(\mathbf{k}, \chi) \right); \\ &\text{such that:} \quad \left(\boldsymbol{K} - \omega^2 \boldsymbol{M} \right) \boldsymbol{h}_r = \mathbf{0}, \quad \mathbf{k} \in L \end{aligned} \tag{C.10}$$

where ω_{j+1} and ω_j are the frequencies of bands $j+1$ and j, respectively, and L is the boundary of the irreducible Brillouin zone (see Brillouin (1953)). The design variable in (C.10) is χ. Thus, the full space of phase configurations is tested to find the optimal solution.

Figure C.3 shows the unit-cell symmetry elements of a phononic crystal with p4mm space group symmetry. Also, the first Brillouin zone (FBZ), the irreducible Brillouin zone (IBZ) and the irreducible Brillouin zone boundary are depicted. For highly symmetric microarchitectures (e.g., with p4mm and p6mm space group symmetries) the probability that the extreme points of the band structure occur on the boundary of the irreducible Brillouin zone is very high (see Maurin et al.

(2018)). For this reason, during the optimization process, the analysis of the band structure can be restricted only to wave vectors $\mathbf{k} \in L$. Checking the bandgap structures for wave vectors $\mathbf{k}$ in the interior of the irreducible Brillouin zone may be a possibility for topologies with low symmetries.

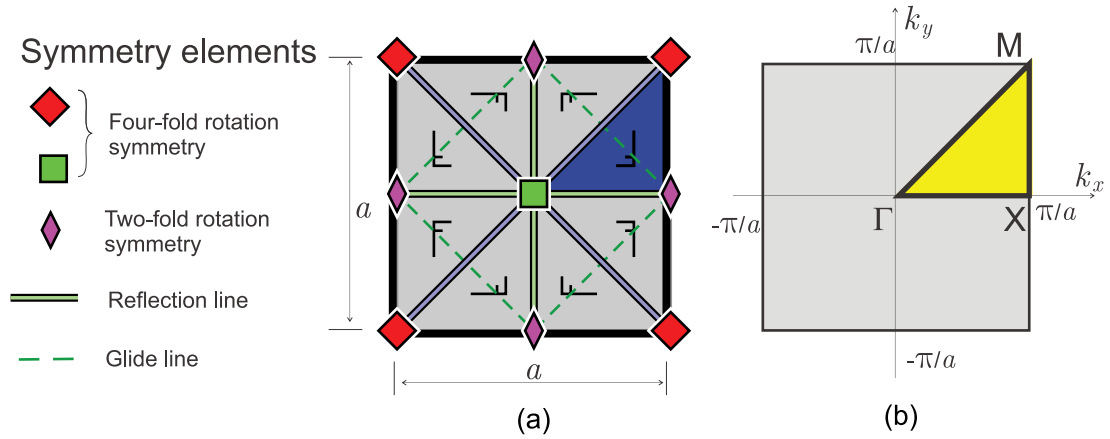

Figura C.3: Phononic crystal with p4mm symmetry. (a) Unit cell symmetry elements and asymmetric unit (in blue). (b) Unit cell of the reciprocal lattice. First Brillouin zone (FBZ in gray) and irreducible Brillouin zone (IBZ in yellow); boundary of the IBZ $[\Gamma - X - M - \Gamma]$.

The problem (C.10) is a maximin optimization problem where the wave vectors $\mathbf{k}$ for the critical frequencies may change during the optimization algorithm iterations. Such as mentioned by Sigmund y Jensen (2003), this is a dirty objective function. Therefore, and following the extended bound formulation due to Bendsøe et al. (1983), Olhoff (1988), Olhoff (1989), Olhoff y Du (2013) and Jensen y Pedersen (2006), this maximin problem is rephrased as the following nonlinear programming problem

$$\begin{aligned} &\min_{\beta_1,\beta_2,\chi} \ \beta_1 - \beta_2 \\ &\text{such that:} \quad \mathfrak{f}_p := \beta_1 - \left[\omega_j^2(\mathbf{k},\chi)\right]_p \geq 0, \quad p = 1,...,N \\ &\qquad\qquad \mathfrak{g}_q := \left[\omega_{j+1}^2(\mathbf{k},\chi)\right]_q - \beta_2 \geq 0, \quad q = 1,...,N \\ &\qquad\qquad \left(\boldsymbol{K} - \omega^2 \boldsymbol{M}\right) \boldsymbol{h}_r = \mathbf{0}, \quad \mathbf{k} \in L_N \ , \end{aligned} \tag{C.11}$$

where β_1 and β_2 are additional variables representing the upper and lower bounds of the square frequencies ω_j^2 and ω_{j+1}^2, respectively, such as expressed in the constraints equations $\mathfrak{f}_p$ and $\mathfrak{g}_q$. Variables β_1 and β_2 are neither geometrical nor shape parameters, therefore, they do not depend on the topology.

A discrete number of points N are chosen on the boundary of the irreducible Brillouin zone to scan the frequencies. The wave vectors $\mathbf{k}$ of these N points define the set L_N. The notation $\left[\omega_j^2(\mathbf{k},\chi)\right]_p$ means that the frequency ω_j of band j is evaluated at the discrete point p on the Brillouin zone boundary. Similarly, the notation $\left[\omega_{j+1}^2(\mathbf{k},\chi)\right]_q$ means that the frequency ω_{j+1} of the band $j+1$, adjacent to the band j, is evaluated at the discrete point q on the Brillouin zone

boundary.

The first $2N$ constraints in the problem (C.11) involving the frequencies ω_j and ω_{j+1} can be summed up into two vectorial constraints:

$$\mathfrak{F} \geq \mathbf{0} \ , \tag{C.12}$$

$$\mathfrak{G} \geq \mathbf{0} \ , \tag{C.13}$$

where the vector $\mathfrak{F} \in \mathbb{R}^N$ gathers the components $\mathfrak{F} = \{\mathfrak{f}_1, ..., \mathfrak{f}_p, .., \mathfrak{f}_N\}$ and the vector $\mathfrak{G} \in \mathbb{R}^N$ gathers the components $\mathfrak{G} = \{\mathfrak{g}_1, ..., \mathfrak{g}_q, .., \mathfrak{g}_N\}$, therefore, these vectorial inequalities are interpreted component by component.

4. Optimization algorithm

The level-set function to handle the material configuration in Ω_μ is subsequently introduced, and then, the optimization problems (C.11) is rephrased in terms of this level-set-function. The resulting formulation is solved with an optimization algorithm based on an augmented Lagrangian technique. The evaluation of the sensitivities defining the gradient of the augmented Lagrangian technique is computed through the topological derivative which is a key point to define a descent direction of the Lagrangian functional. Particularly, the eigenvalue topological derivative represents the sensitivity of every eigenvalue of the problem (C.6) to infinitesimal domain perturbation (topological changes) in Ω_μ.

The combined use of the level-set function and the topological derivative, which is adopted in this work, follows closely the approach formerly presented by Amstutz y Andrä (2006) and Amstutz et al. (2010) in topology design of mechanical structures. Concerning the topological derivative for eigenvalue problems, the reader can get further details in the book by Novotny y Sokołowski (2013).

The level-set function is introduced in the following sub-Section. After that, in the same sub-Section, the augmented Lagrangian technique is described jointly with additional details that have been used for solving the present problem. The description of the topological derivative is left for sub-Section 4.3.

4.1. Level-set function.

The level-set function ψ is a scalar function arbitrarily defined in Ω_μ but satisfying $\psi \in C^0(\Omega_\mu)$ and:

$$\psi(\mathbf{x}) = \begin{cases} > 0 & \forall\, \mathbf{x} \in \Omega_\mu^2 \\ < 0 & \forall\, \mathbf{x} \in \Omega_\mu^1 \\ = 0 & \forall\, \mathbf{x} \in \partial\Omega_\mu^{1-2} \end{cases} \ , \tag{C.14}$$

where $\partial\Omega_{\mu}^{1-2}$ is the interface between material m_1 and m_2. Once ψ is defined, the characteristic function $\chi(\mathbf{x})$, in (C.9), can be rephrased as:

$$\chi_{\psi} = \begin{cases} 1 & \forall\ \psi \leq 0 \\ 0 & \forall\ \psi > 0 \end{cases} \quad , \tag{C.15}$$

and the problem (C.11) can be reformulated in terms of χ_{ψ}, resulting:

$$\begin{aligned} &\min_{\beta_1,\beta_2,\psi} \beta_1 - \beta_2 \\ &\text{such that:} \quad \mathfrak{f}_p := \beta_1 - \left[\omega_j^2(\mathbf{k},\chi_{\psi})\right]_p \geq 0, \ \ p = 1,...,N \\ &\qquad\qquad \mathfrak{g}_q := \left[\omega_{j+1}^2(\mathbf{k},\chi_{\psi})\right]_q - \beta_2 \geq 0, \ \ q = 1,...,N \\ &\qquad\qquad \left(\boldsymbol{K} - \omega^2\boldsymbol{M}\right)\boldsymbol{h}_r = \mathbf{0}, \ \ \mathbf{k} \in L_N \ . \end{aligned} \tag{C.16}$$

4.2. Augmented Lagrangian Technique

The problem (C.16) is solved through an augmented Lagrangian technique. Specifically, we use an unconstrained formulation of the the augmented Lagrangian subproblem (Nocedal y Wright (2006)) described in the Appendix I, see also Lopes et al. (2015). According to this formulation, the generalized Lagrangian $\mathcal{L}$, see equation (C.54) in Appendix I, is given by:

$$\begin{aligned} \mathcal{L}(\beta_1,\beta_2,\chi_{\psi},\tilde{\lambda},\tilde{\gamma}) = \beta_1 - \beta_2 - \sum_{p\in\Lambda}\tilde{\lambda}_p\mathfrak{f}_p - \sum_{q\in\Pi}\tilde{\gamma}_q\mathfrak{g}_q + \frac{\alpha}{2}\left(\sum_{p\in\Lambda}\mathfrak{f}_p^2 + \sum_{q\in\Pi}\mathfrak{g}_q^2\right) - \\ -\frac{1}{2\alpha}\left(\sum_{p\in\widehat{\Lambda}}(\tilde{\lambda}_p)^2 + \sum_{q\in\widehat{\Pi}}(\tilde{\gamma}_q)^2\right) \ , \end{aligned} \tag{C.17}$$

where $\tilde{\lambda}_p$ and $\tilde{\gamma}_q$ are Lagrange multipliers and α is a penalty parameter. Also, defining the sets $\mathcal{P} = \{1,...,N\}$ and $\mathcal{Q} = \{1,...,N\}$, then, the sets Λ, Π, $\widehat{\Lambda}$ and $\widehat{\Pi}$ in (C.17) are:

$$\begin{aligned} \Lambda &= \left\{p \mid p \in \mathcal{P} \wedge \mathfrak{f}_p - \tilde{\lambda}_p/\alpha < 0\right\}, \\ \Pi &= \left\{q \mid q \in \mathcal{Q} \wedge \mathfrak{g}_q - \tilde{\gamma}_q/\alpha < 0\right\}, \\ \widehat{\Lambda} &= \mathcal{P} \setminus \Lambda, \\ \widehat{\Pi} &= \mathcal{Q} \setminus \Pi \ . \end{aligned} \tag{C.18}$$

Consequently, the equivalent unconstrained form of (C.16), can be written as:

$$\min_{\beta_1,\beta_2,\chi_{\psi}} \max_{\tilde{\boldsymbol{\lambda}},\tilde{\boldsymbol{\gamma}}} \mathcal{L}(\beta_1,\beta_2,\chi_{\psi},\tilde{\boldsymbol{\lambda}},\tilde{\boldsymbol{\gamma}}) \ . \tag{C.19}$$

The inner maximization problem is solved in closed form as shown in the Appendix I. The outer minimization problem in (C.19) is solved by using a descent direction algorithm.

The main ingredient to define a descent direction of $\mathcal{L}$ respect to the the design variable χ_{ψ}

is to introduce its topological derivative[1]. Following the above-mentioned reference works on this topic, the topological derivative of $\mathcal{L}$ at point $\mathbf{x} \in \Omega_\mu$, denoted $D_T\mathcal{L}(\mathbf{x})$, provides the sensitivity of the functional $\mathcal{L}$ with changes of χ at the same point. In the books by Novotny y Sokołowski (2013) and Novotny et al. (2019), the authors defines the generic concept of topological derivative. Particularly, these authors analyze the topological derivative of the energy function associated with an elastic boundary value problem posed in a given spatial domain.

First, we obtain the generic expression of the topological derivative of the function $\mathcal{L}$ which depends on the topological derivative of the eigenvalues related to problem (C.6). We left for the next subsection the explicit description of the topological derivative of the eigenvalues.

Let us consider a perturbed characteristic function, χ_ϵ, that is similar to χ everywhere in Ω_μ, except within an infinitesimal ball of radius ϵ and centered at $\mathbf{x}$. The topological derivative in 2D problems satisfies:

$$\mathcal{L}(\beta_1, \beta_2, \chi_\epsilon, \tilde{\lambda}, \tilde{\gamma}) = \mathcal{L}(\beta_1, \beta_2, \chi, \tilde{\lambda}, \tilde{\gamma}) + f(\epsilon) D_T\mathcal{L}(\beta_1, \beta_2, \mathbf{x}, \tilde{\lambda}, \tilde{\gamma}) + o(f(\epsilon)) \tag{C.20}$$

where $f(\epsilon)$ is proportional to the perturbed ball area. From equation (C.20), $D_T\mathcal{L}(\beta_1, \beta_2, \mathbf{x}, \tilde{\lambda}, \tilde{\gamma})$ is the term of minimum order in ϵ indicating at $\mathbf{x}$, if a phase change would induce a decrease of the functional $\mathcal{L}$. This criteria naturally provides a descent direction of the Lagrangian $\mathcal{L}$.

The chain rule, which applies to the conventional differential calculus, can be generalized to the operator $D_T(\cdot)$, see references cited above. Then, by applying this rule to the expression (C.17), the topological derivative of the Lagrangian is:

$$D_T\mathcal{L}(\beta_1, \beta_2, \mathbf{x}, \tilde{\lambda}, \tilde{\gamma}) = -\sum_{p\in\Lambda} \tilde{\lambda}_p D_T\mathfrak{f}_p - \sum_{q\in\Pi} \tilde{\gamma}_q D_T\mathfrak{g}_q + \alpha \left(\sum_{p\in\Lambda} \mathfrak{f}_p D_T\mathfrak{f}_p + \sum_{q\in\Pi} \mathfrak{g}_q D_T\mathfrak{g}_q \right) \tag{C.21}$$

where $D_T\mathfrak{f}_p$ and $D_T\mathfrak{g}_q$ are the topological derivatives of the components $p \in \Lambda$ and $q \in \Pi$ of the vectors $\mathfrak{F}$ and $\mathfrak{G}$, respectively. These expressions are:

$$\begin{aligned} D_T\mathfrak{f}_p &= -D_T[\omega_j^2]_p \ , \\ D_T\mathfrak{g}_q &= D_T[\omega_{j+1}^2]_q \ . \end{aligned} \tag{C.22}$$

which are the topological derivatives of the eigenvalues $[\omega_j^2]$ and $[\omega_{j+1}^2]$ at points p and q, respectively.

[1] Neither the Lagrangian (C.54) nor the fields involved in it are differentiable for changes of topologies. However, the sensitivities of the field and the Lagrangian can be obtained by applying the topological derivative concept which formally follows the rules of the differential calculus, typically, the chain rule, such as suggested by Amstutz y Andrä (2006).

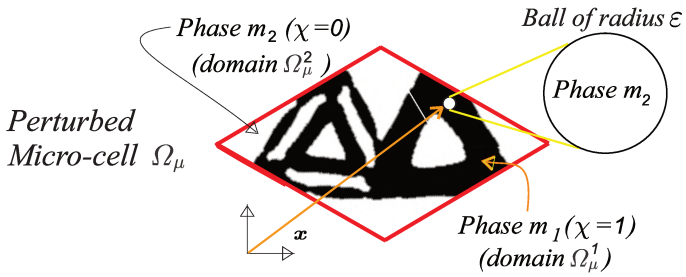

Figura C.4: Perturbed micro-cell domain.

4.3. Topological Derivative of eigenvalues

The topological derivative of the eigenvalues resulting from problem (C.6) has been analytically obtained and reported in the work by Ammari et al. (2008). Alternatively, it can be numerically estimated through the sensitivity (or change) of the eigenvalues to infinitesimal circular perturbation in the domain, by introducing an interchange of phases in the circular hole centered at $\mathbf{x}$ with radius ϵ, as sketched in Figure C.4. Then, the perturbed eigenvalues are evaluated in the new configuration. The topological derivative can be estimated with both, the original and the perturbed, eigenvalues. This procedure is numerically assessed and compared with the analytical expression in Section 6.

The expression of the topological derivative of the eigenvalue described next has been taken from the paper by Amstutz (2011b). Let us consider that a background elastic material with Lamè parameters λ_1 ; μ_1 and density ρ_1 exists at the point $\mathbf{x}$ in Ω_μ. Within an infinitesimal circular hole, this material is substituted by other elastic material whose parameters: $\lambda_2; \mu_2; \rho_2$ are proportional to those of the background material via two contrast factors: ϑ_s for the Lamè parameters and ϑ_d for density, resulting: $\lambda_2 = \vartheta_s \lambda_1$; $\mu_2 = \vartheta_s \mu_1$ and $\rho_2 = \vartheta_d \rho_1$. We denote η_ℓ the ℓ-th eigenvalue of problem (C.6), and $\boldsymbol{h}_\ell$ the eigenvector, or displacement mode, associated to it. Observe that the full d.o.fs of $\boldsymbol{h}_\ell$ are implicitly defined through the relation (C.7). We also assume that the set of eigenvectors are orthonormalized, i.e.:

$$\int_{\Omega_\mu} \rho_1 (\boldsymbol{h}_o \cdot \boldsymbol{h}_s)\, dV = \delta_{os} \quad ; \quad \forall \text{ indices } o, s\,. \tag{C.23}$$

Then, the topological derivative of η_ℓ, denoted $D_T \eta_\ell$, is given by:

$$D_T \eta_\ell(\mathbf{x}) = D_T C_\ell(\mathbf{x}) - \eta_\ell \rho_1 (1 - \vartheta_d)(\boldsymbol{h}_\ell \cdot \boldsymbol{h}_\ell) \tag{C.24}$$

where $D_T C_\ell(\mathbf{x})$ results :

$$D_T C_\ell(\mathbf{x}) = \zeta_a \left[2\boldsymbol{\sigma}_\ell : \boldsymbol{\varepsilon}_\ell + \zeta_b tr(\boldsymbol{\sigma}_\ell) tr(\boldsymbol{\varepsilon}_\ell) \right] \tag{C.25}$$

being $\boldsymbol{\varepsilon}_\ell$ the strain compatible with $\boldsymbol{h}_\ell$ and $\boldsymbol{\sigma}_\ell$ the stress related to $\boldsymbol{\varepsilon}_\ell$ through the linear elastic

constitutive law. All these terms correspond to the elastodynamic solutions of the unperturbed problem. In expressions (C.24) and (C.25), all terms are evaluated at $\mathbf{x}$. The coefficients ζ_a and ζ_b are defined by the expressions:

$$\zeta_a = \frac{(1-\vartheta_s)(\kappa_1+1)}{2(\kappa_1\vartheta_s+1)} \quad ; \quad \zeta_b = \frac{(\vartheta_s-1)(\kappa_1-2)}{\kappa_1+2\vartheta_s-1} \quad ; \quad .$$

with κ_1 being the bulk modulus of the background material: $\kappa_1 = (\lambda_1+3\mu_1)/(\lambda_1+\mu_1)$.

There exist some specific cases for evaluating the topological derivative of eigenvalues that must be particularly contemplated. These cases arise very often during the iterative process of the optimization algorithm and are described in the following two items:

i) The topology optimization algorithms for attaining the wider bandgaps in composites with high symmetry must check the simultaneous phase changes in all the symmetry points of the design domain. This procedure requires the evaluation of a topological derivative of eigenvalues when simultaneous multiple perturbations are admitted in the design domain. Thus, let us assume that there exist multiple simultaneous perturbations situated in positions $\mathbf{x}^{(j)}$ of Ω_μ with: $j = 1, ..., np$, where np is the number of simultaneous perturbations. The topological derivative is given by (see Novotny y Sokołowski (2013)) :

$$D_T\eta_\ell = \sum_{j=1}^{np}\left[D_TC_\ell^{(j)} - \eta\rho_1(1-\vartheta_d)(\boldsymbol{h}_\ell^{(j)}\cdot\boldsymbol{h}_\ell^{(j)})\right] \tag{C.26}$$

where:

$$D_TC_\ell^{(j)} = \zeta_a\left[2\boldsymbol{\sigma}_\ell^{(j)} : \boldsymbol{\varepsilon}_\ell^{(j)} + \zeta_b\, tr(\boldsymbol{\sigma}_\ell^{(j)})tr(\boldsymbol{\varepsilon}_\ell^{(j)})\right] \tag{C.27}$$

Accordingly with (C.25), the terms $\boldsymbol{\sigma}_\ell^{(j)}$ and $\boldsymbol{\varepsilon}_\ell^{(j)}$ are the stress and strain unperturbed solution evaluated in the points $\mathbf{x}^{(j)}$.

ii) An additional specific case that must be considered refers to the evaluation of the topological derivative when multiple eigenvalues exist (ver Nazarov y Sokolowski (2008)). Let us consider the eigenvalue η_p with multiplicity δ_p, $(... < \eta_{p-1} < \eta_p = ... = \eta_{p+\delta_p-1} < \eta_{p+\delta_p} < ...)$. There are δ_p related eigenmodes denoted: $\boldsymbol{h}_p; ....; \boldsymbol{h}_{p+\delta_p}$. The topological derivative of η_p is determined by the eigenvalues $\beta_p^{(1)}, ..., \beta_p^{(\delta_p)}$ of the symmetric matrix $\boldsymbol{Q}$ with components k, m:

$$Q_{km} = D_TC_{km} - \eta\rho_1(1-\vartheta_d)\left(\boldsymbol{h}_{p+k-1}\cdot\boldsymbol{h}_{p+m-1}\right) \;;\; k,m = 1, ..., \delta_p \tag{C.28}$$

where:

$$D_TC_{km} = \zeta_a\left[2\boldsymbol{\sigma}_{p+k-1} : \boldsymbol{\varepsilon}_{p+m-1} + \zeta_b\, tr(\boldsymbol{\sigma}_{p+k-1})tr(\boldsymbol{\varepsilon}_{p+m-1})\right] \tag{C.29}$$

5. Implementation of the numerical procedure

Some issues deserving specific attention for implementing the level-set methodology in the optimization algorithm are presented in the following. It is remarked that alternative implementations of level-set-methodologies have been reported in the review paper of van Dijk et al. (2013).

i) **Interpolation of the level-set-function**

It has been mentioned above that the Finite Element Method is used to determine the band structure. Specifically, linear triangle finite element meshes with one quadrature point (at the centroid of the finite element) are here adopted. The level-set function is interpolated on the same mesh using the conventional finite element technique: $\psi(\mathbf{x}) = N_i(\mathbf{x})\psi_i$ where N_i are the shape functions and ψ_i are the nodal interpolation parameters of the level-set-function ($i = 1, 2, ..., N_p$, with N_p being the number of the mesh nodes). Thus, the interpolation parameters (nodal values) of ψ are collected in the vector $\boldsymbol{\psi} \in \mathbb{R}^{N_p}$.

ii) **Evaluation of the characteristic function**

The function χ_ψ is calculated in every v-th finite element, see Figure C.5. We take the three nodal parameters of the level-set-function that correspond to this element: ψ_i^v (with: $i = 1, 2, 3$), and the nodal coordinates $\mathbf{x}_i^v$ of the nodes and determine χ_ψ at the centroid, which is denoted χ_ψ^v, as follows:

a) $\chi_\psi^v = 1, \quad \text{if } \psi_i^v \leq 0; \quad \forall\, i \in \{1, 2, 3\}.$

b) $\chi_\psi^v = 0, \quad \text{if } \psi_i^v > 0; \quad \forall\, i \in \{1, 2, 3\}.$

c) alternatively, if the zero-level-set of the interpolated function $\psi(\mathbf{x})$ (i.e., the segment given by $\psi(\mathbf{x}) = 0$) intersect the element, then, compute:

c.1) the finite element area, A^v,

c.2) the area A^- of the triangle (or quadrilateral) in where $\psi(\mathbf{x}) < 0$

Finally, compute: $\chi_\psi^v = \dfrac{A^-}{A^v}$

iii) **Geometry and material mapping from the level-set-function parametrization**

The elastic properties of the $v-$th finite element, that are characterized with the elasticity tensor $\mathbf{C}^v$ and the density ρ^v, are computed with the convex combination of the elasticity tensors $\mathbf{C}_1$ and $\mathbf{C}_2$ of phases m_1 and m_2, respectively, as follows:

$$\mathbf{C}^v = \chi_\psi^v \mathbf{C}_1 + (1 - \chi_\psi^v)\mathbf{C}_2 \tag{C.30}$$

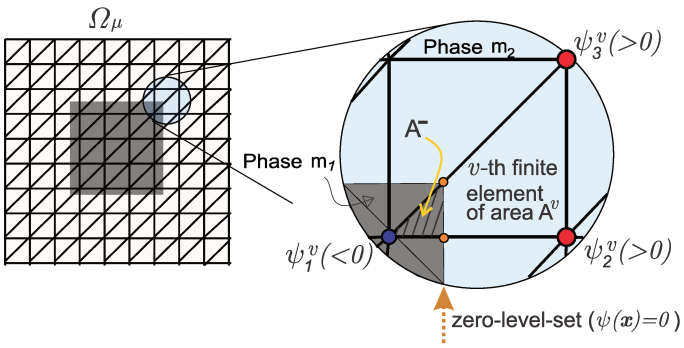

Figura C.5: Determination of the characteristic function χ_ψ^v at the $v-$th finite element.

$$\rho^v = \chi_\psi^v \rho_1 + (1 - \chi_\psi^v)\rho_2 \tag{C.31}$$

According to equations (C.30) and (C.31), if, for a given finite element, the three nodal parameters of the level-set-function are negative (positive), the elasticity tensor (density) coincides with the elasticity tensor (density) of phase m_1 (m_2). Alternatively, if the level-set function parameters are positive and negative, the material elastic stiffness (density) can be interpreted as a mixture of the stiffness (densities) of both phases. The salient feature of this procedure is that a smooth transition from $\mathbf{C}_1$ to $\mathbf{C}_2$ is induced by a continuous movement of the interface across the element.

iii) **Update of the level-set-function, the variables β_1, β_2 and the Lagrange multipliers**

Once the characteristic function χ_ψ^v and the topological derivatives of the Lagrangian function, $D_T\mathcal{L}$, are computed with equation (C.21) at the centroid of the v-th finite element, we determine g_ψ^v as follows:

$$g_\psi^v = (1 - 2\chi_\psi^v) D_T^v \mathcal{L}\,, \tag{C.32}$$

which can be interpreted as a descent direction of the Lagrangian function. By interpolating the corresponding field $g_\psi(\mathbf{x})$ with the standard finite element expression: $g_\psi(\mathbf{x}) = N_i(\mathbf{x})(g_\psi)_i$, the vector $\boldsymbol{g}_\psi \in \mathbb{R}^{N_p}$, gathering the nodal parameters, are obtained using a projection of g_ψ^v to the nodes via a conventional least square technique. Finally, $\boldsymbol{g}_\psi$ is normalized :

$$\hat{\boldsymbol{g}}_\psi = \frac{\boldsymbol{g}_\psi}{\|g_\psi\|_{L^2}}\,. \tag{C.33}$$

where the notation $\|\cdot\|_{L^2}$ means the conventional L^2 norm in (Ω_μ).

With $\hat{\boldsymbol{g}}_\psi$, the vector of nodal level-set-function at iteration k, $\boldsymbol{\psi}^k$, is updated at $k+1$, as follows:

$$\boldsymbol{\psi}^{k+1} = \hat{\boldsymbol{\psi}}^k + \tau \hat{\boldsymbol{g}}_\psi^k, \tag{C.34}$$

where τ is an adequate step length that should provide a decrease in the cost function. Since the topology defined by $\boldsymbol{\psi}$ and $c\boldsymbol{\psi}$ is the same where $c > 0$ is a scalar constant, we can normalize $\boldsymbol{\psi}$. We denote $\hat{\boldsymbol{\psi}}^k$ the normalized vector of $\boldsymbol{\psi}^k$:

$$\hat{\boldsymbol{\psi}}^k = \frac{\boldsymbol{\psi}^k}{\|\psi\|_{L^2}} \tag{C.35}$$

The descent direction of the augmented Lagrangian problem for the variables β_1 and β_2, denoted $g^k_{\beta_1}$ and $g^k_{\beta_2}$, are

$$g^k_{\beta_1} = -\frac{\partial \mathcal{L}}{\partial \beta_1} = -1 + \sum_{p\in\Lambda} \tilde{\lambda}_p \frac{\partial \mathfrak{f}_p}{\partial \beta_1} - \alpha \sum_{p\in\Lambda} \mathfrak{f}_p \frac{\partial \mathfrak{f}_p}{\partial \beta_1} \ , \tag{C.36}$$

$$g^k_{\beta_2} = -\frac{\partial \mathcal{L}}{\partial \beta_2} = 1 + \sum_{q\in\Pi} \tilde{\gamma}_q \frac{\partial \mathfrak{g}_q}{\partial \beta_2} - \alpha \sum_{q\in\Pi} \mathfrak{g}_q \frac{\partial \mathfrak{g}_q}{\partial \beta_2} \ . \tag{C.37}$$

Then, the update scheme for β_1 and β_2 are:

$$\beta_1^{k+1} = \beta_1^k + \tau g^k_{\beta_1} \ , \tag{C.38}$$

$$\beta_2^{k+1} = \beta_2^k + \tau g^k_{\beta_2} \tag{C.39}$$

and every component of the Lagrange multiplier vector $\tilde{\boldsymbol{\lambda}}$ are updated using the following expressions:

$$\tilde{\lambda}_p^{k+1} = \begin{cases} \tilde{\lambda}_p^k - \alpha \mathfrak{f}_p, & \text{if} \quad \mathfrak{f}_p - \tilde{\lambda}_p^k/\alpha \leq 0 \\ 0, & \text{otherwise} \end{cases} \ ; \tag{C.40}$$

and the components of $\tilde{\boldsymbol{\gamma}}$ are updated according to:

$$\tilde{\gamma}_q^{k+1} = \begin{cases} \tilde{\gamma}_q^k - \alpha \mathfrak{g}_q, & \text{if} \quad \mathfrak{g}_q - \tilde{\lambda}_q/\alpha \leq 0 \\ 0, & \text{otherwise} \end{cases} \ . \tag{C.41}$$

iv) **Convergence criterion**

Convergence is achieved when the following two criteria are accomplished:

a) The derivatives $\partial\mathcal{L}/\partial\beta_1$, $\partial\mathcal{L}/\partial\beta_2$ are sufficiently small:

$$\sqrt{\left(\frac{\partial \mathcal{L}}{\partial \beta_1}\right)^2 + \left(\frac{\partial \mathcal{L}}{\partial \beta_2}\right)^2} < tol_\beta \tag{C.42}$$

where tol_β is a given tolerance. Furthermore, following Amstutz's work (Amstutz (2011a)), an additional local optimality criterion of problem (C.19) is given by the condition:

$$D_T\mathcal{L} > 0 \quad , \quad \forall\, \mathbf{x} \in \Omega_\mu \, ,$$

which can be implemented by verifying the inequality

$$\hat{\boldsymbol{g}} \cdot \hat{\boldsymbol{\psi}} \; > (1 - tol_{\psi}) \; ; \tag{C.43}$$

where tol_{ψ} is a given tolerance.

b) All constraints must be satisfied:

$$\begin{array}{l} \mathfrak{f}_p \geq 0 \quad ; \quad \forall p \in \{1, 2, ..., N\} \\ \mathfrak{g}_q \geq 0 \quad ; \quad \forall q \in \{1, 2, ..., N\} \end{array} \tag{C.44}$$

v) **Iterative scheme**

The implemented iterative scheme inspired by the Augmented Lagrangian technique is summarized in the following Box.

Box 1: General Algorithm

Initialize: Level-set function $\boldsymbol{\psi}^0$; β_1^0 and β_2^0; Lagrange multipliers $\tilde{\boldsymbol{\lambda}}^0$, $\tilde{\boldsymbol{\gamma}}^0$; penalty parameter α^0; tolerances tol_β and tol_ψ.

Iteration k:

1. Construct the characteristic function $\chi^v(\boldsymbol{\psi}^k)$.
2. Compute the elastic properties and density (equations (C.30) and (C.31)) in every finite element.
3. Compute the band structure (solve (C.6) $\forall\, \mathbf{k} \in L_N$).
4. Evaluate the augmented Lagrangian $\mathcal{L}(\beta_1^k, \beta_2^k, \boldsymbol{\psi}^k, \tilde{\boldsymbol{\lambda}}^k, \tilde{\boldsymbol{\gamma}}^k)$ defined by equation (C.17)
5. Compute the topological derivative of eigenvalues: $D_T\omega_j^2\left(\chi(\hat{\mathbf{x}})\right)$ and $D_T\omega_{j+1}^2\left(\chi(\hat{\mathbf{x}})\right)$ using equation (C.26), or, in the case of multiple eigenvalues (C.28).
6. Compute the search directions $g_{\beta_1}^k$, $g_{\beta_2}^k$ and $\hat{\boldsymbol{g}}_\psi^k$, with equations (C.34) (C.36) (C.37).
7. Determine the steep size parameter $\tau \in [\tau_{min}, \tau_{max}]$, by means of a linear search procedure, where τ_{min} and τ_{max} are the safewarded minimum and maximum step sizes
8. Update β_1^{k+1}, β_2^{k+1} and $\boldsymbol{\psi}^{k+1}$ with equations (C.38), (C.39) and (C.34), respectively. Normalize $\boldsymbol{\psi}^{k+1}$ by computing $\hat{\boldsymbol{\psi}}^{k+1}$. Impose symmetries constraints.
9. If the convergence conditions (equations (C.42), (C.43) and (C.44)) are fulfilled then **stop**.
10. If condition (C.43) is fulfilled and (C.44) is violated, then: $\alpha \leftarrow \text{mín}(\alpha + \Delta\alpha; \alpha_{max})$
11. If conditions (C.42) and (C.43) are fulfilled or $\tau == \tau_{min}$ then update the Lagrange multipliers: $\tilde{\boldsymbol{\lambda}}^{k+1}$ and $\tilde{\boldsymbol{\gamma}}^{k+1}$ with equations (C.40), (C.41), respectively. **Return to 1.**

vi) **Nested grid refinements**

The optimization problem is solved using a sequential finite element mesh refinement procedure. Initially, the problem is solved with a coarse grid. After attaining the algorithm convergence, according to Box 1, the level-set function is projected onto a finer finite element mesh, and the iterative process is restarted on the new mesh. This procedure may be continued in subsequent refinement steps.

A refinement step consists of splitting every triangular finite element of the structured mesh into four elements. Thus, the number of elements increases with a factor 4 from one step to

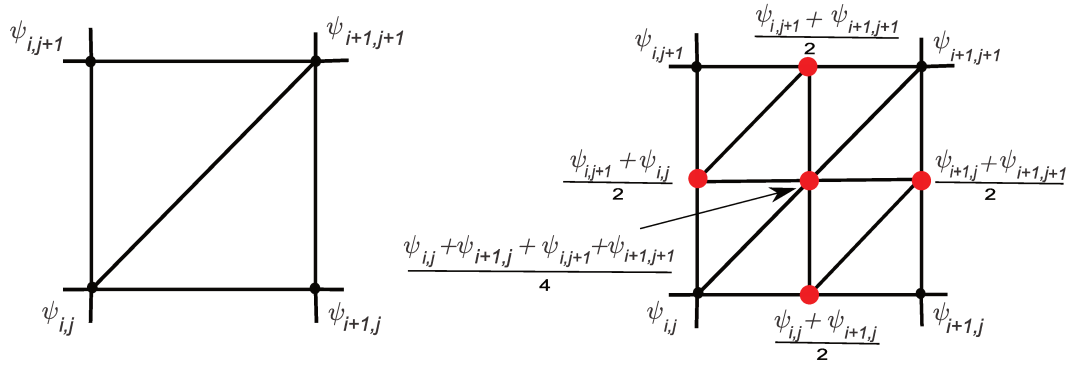

Figura C.6: Nested finite element mesh refinement procedure. Mapping of the level-set function parameters, from the coarser grid (left) onto the finer mesh (right).

the next. The level-set function parameters of the coarser grid are projected onto the finer one. The projection procedure, which is sketched in Figure C.6, is determined as follows: i) the parameters of the fine grid are copied from the coarse one in the coincident nodes. ii) In those nodes of the finer grid which do not coincide with the coarser grid nodes, the parameters are the average values of those defined in the closest nodes of the coarser grid.

5.1. Symmetry imposition

The material configuration computed at each iteration of the optimization algorithm is forced to exhibit the crystal symmetry defined by a pre-established space group. To attain this objective, we adopt the following strategy, similar to that describe by Rossi Cabral et al. (2020).

a) A finite element mesh preserving the space group symmetry is built, and the set of points (nodes) belonging to the asymmetric unit[2] are identified.

b) The image points related to every point of the asymmetric unit through the symmetry operations are next identified. Both sets of points (those belonging to the image and the asymmetric unit) depend on the crystal space group.

c) At the iteration $k+1$, the topological derivatives of the eigenvalues $D_T[\omega_j^2]_p$, $p \in \Lambda$ and $D_T[\omega_{j+1}^2]_q$, $q \in \Pi$ are computed according to (C.26) or (C.28) depending if the eigenvalue is simple or multiple respectively. These values are copied to the symmetrical points of the mesh. Note that the additive property of the topological derivatives for multiple simultaneous perturbations is implicitly assumed in (C.26). This procedure is numerically validated in the next Section.

Then the topological derivative of the Lagrangian function, $D_T\mathcal{L}$ is computed according to equation (C.21). Finally, the updating of $\boldsymbol{\psi}^{k+1}$ (equation (C.34)) is performed.

[2]The asymmetric unit and the corresponding image points are defined for all the space groups in the International Tables of Crystallography (London (2004)). See also Vainshtein (2013) for further description about this topic.

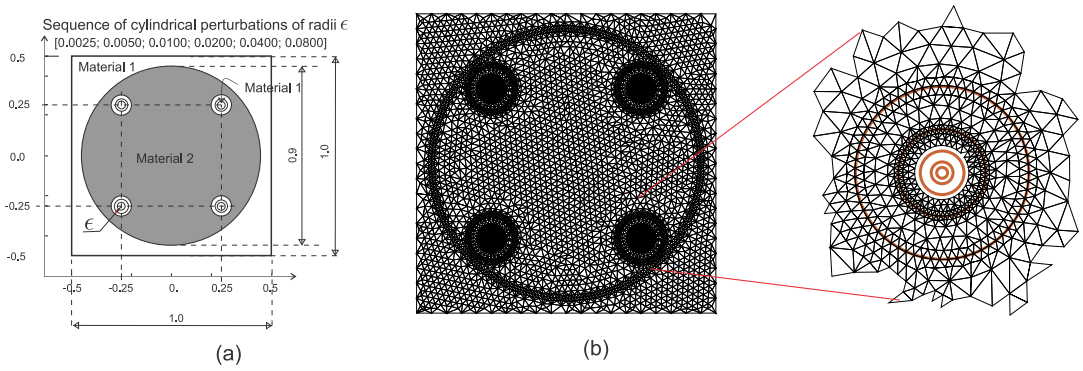

Figura C.7: Validation of the topological derivative of the eigenvalues. a) Unit cell of the periodic composite. The configuration of Material 2, in gray, is perturbed by introducing a sequence of cylindrical holes with radii $\epsilon \to 0$ of Material 1; b) finite element mesh of the unit cell and detail of the regions where phase m_2 is perturbed.

6. Numerical verification of the topological derivative formulas

Numerical experiments are carried out to verify the analytical expressions of the topological derivatives described in sub-Section 4.3. These experiments are performed by taking a unit cell of the composite, with size 1×1, which has a configuration with a $p4mm$ symmetry. The host media corresponds to phase m_1 and the cylindrical inclusions are constituted by phase m_2. This unit cell is shown in Figure C.7-a.

A sequence of problems (C.6) is solved. Each problem results from substituting a cylindrical hole at a point of the inclusion with phase m_2 by the host material with phase m_1. The successive instances of this sequence consist of decreasing the hole radius ϵ toward zero. Simultaneously, and considering the symmetry imposed to the material configuration, three identical holes are introduced at the image points of the domain. In this experiment, the holes are assumed as topology perturbations.

Let us consider the $j-$th eigenvalue of the original problem (C.6) and the $j-$th eigenvalue of the perturbed problem which are denoted ω_0^2 and ω_ϵ^2, respectively. The following sequence of numbers is computed:

$$\Delta_{\omega,\epsilon} = \frac{\omega_\epsilon^2 - \omega_0^2}{\pi \epsilon^2} \ , \tag{C.45}$$

where the hole radius ϵ corresponds to one element of the set:

$$\{0.08;\ 0.04;\ 0.03;\ 0.01;\ 0.005;\ 0.0025\}.$$

Considering that four simultaneous cylindrical perturbations are introduced at points z_1, z_2, z_3, z_4, we assume that the following additive asymptotic expansion hold, see Amstutz (2011b) and Novotny y Sokołowski (2013):

$$\omega_\epsilon^2 - \omega_0^2 = \sum_{k=1}^{4} f(\epsilon_k) \widehat{D_T}(\omega_0^2)(z_k) + o(f(\epsilon_1), ..., f(\epsilon_4)) \tag{C.46}$$

where $f(\epsilon_k) = \pi\epsilon_k^2$ is the area (volume per unit thickness) of the k-th perturbation and the term $\widehat{D_T}(\omega^2)$ is given by equation (C.24) after replacing η_ℓ by ω_0^2. Even when expression (C.24) is derived from the asymptotic expansion of ω_ϵ^2 for a single perturbation (Amstutz (2011b)), the additive behavior expressed in (C.46) can be naturally assumed; Sokołowski y Żochowski (2003) prove the additive property of asymptotic expansions for some cases (see also Amstutz y Ciligot-Travain (2010)). In our experiment, the four perturbations have the same radius ϵ, then, we have

$$\lim_{\epsilon\to 0} \Delta_{\omega,\epsilon} = \sum_{k=1}^{4} \widehat{D_T}(\omega_0^2)(z_k) = D_T(\omega_0^2)$$

The experimental test is performed with the following material parameters: Young moduli $E_1 = 49.01\ GPa$, $E_2 = 91.15\ GPa$, Poisson's ratio $\nu = 0.52$, $\rho_1 = 1200\ kg/m^3$, $\rho_2 = 19500\ kg/m^3$. The finite element mesh shown in Figure C.7-b with a detail of the perturbed zones (having 17844 triangular elements) is identical for all the problems in the proposed ϵ-sequence. The mesh becomes increasingly refined when approaching the hole center.

Figure C.8 shows the results obtained with the present analysis for the third (left column) and fourth (right column) eigenvalues and three wave vectors $\mathbf{k} = (0,0); (\pi,0)$ and (π,π). The straight horizontal red solid-line is the analytical expression of the eigenvalue topological derivatives, $D_T(\omega_0^2)$. The dashed blue lines with dots show the numerical assessments of the expressions (C.45) in terms of $1/\epsilon$. Figure C.9 display similar results for the fifth and sixth frequency bands.

All cases of the numerical assessments display the correct trend toward the analytical expression of the topological derivatives when $\epsilon \to 0$.

7. Examples of phononic crystal designs

We perform the microstructure designs of phononic crystal with p4mm symmetry. Three different cases, (a), (b) and (c), are assessed. In each case, the objective is to attain the wider absolute bandgaps for in-plane waves between:

case a): the third and fourth bands,

case b): the fifth and sixth bands,

case c): the eight and ninth bands,

respectively. The initial configurations are built by applying a Heaviside projection filter to a randomly generated topology. We emphasize that the filter is used only to obtain the initial configurations.

The material properties of the constituent phases are the following. Host material: $E_1 = 91.15 \times 10^7\ kg/(cm\,s^2)$, $\nu_1 = 0.52$ (Young modulus and Poisson ratio of plane elasticity),

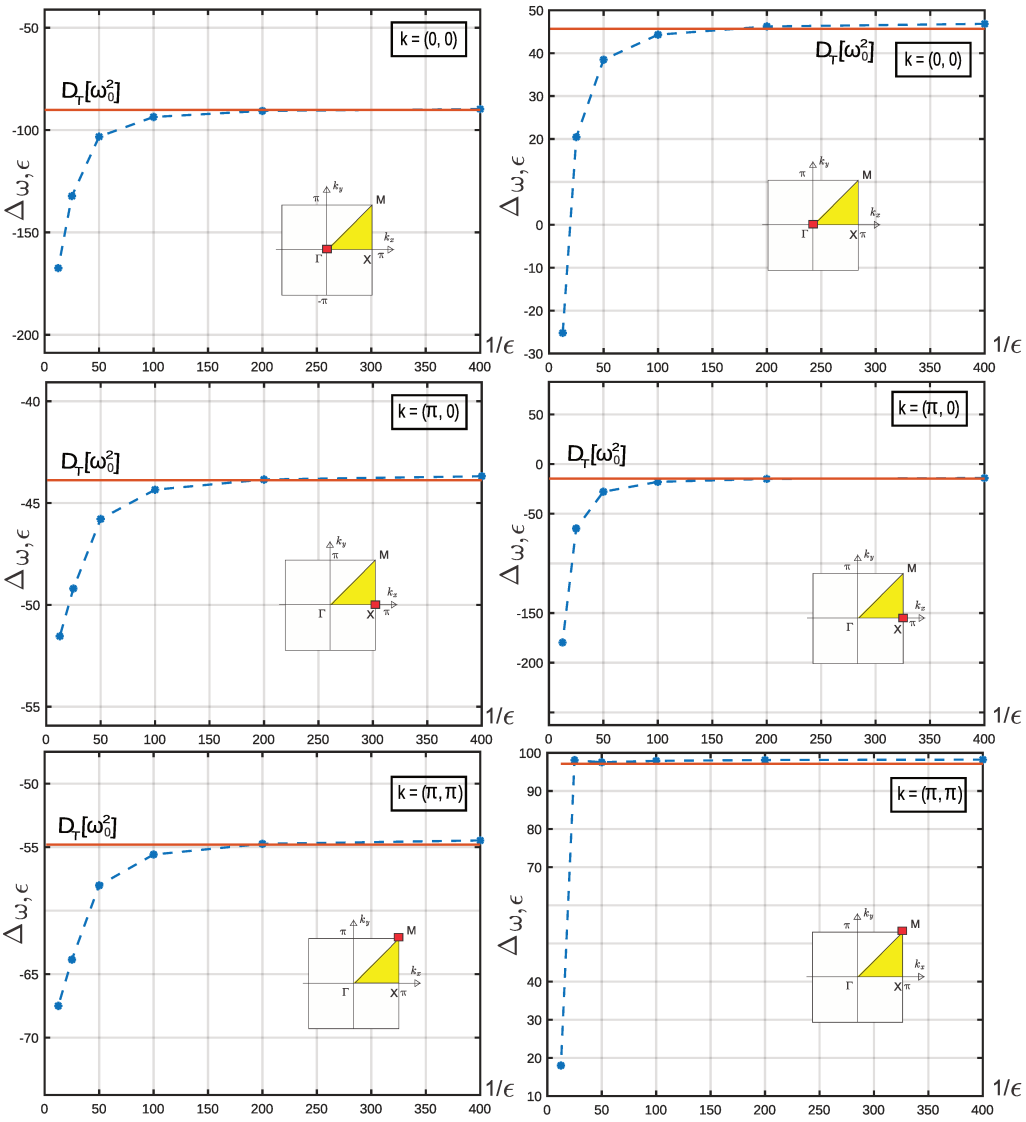

Figura C.8: Analytical expression of the eigenvalue topological derivatives (red lines) compared with their numerical assessments (dashed blue lines with dots) for the third (left column) and fourth (right column) eigenvalues. Eigenvalues are the square of the angular frequencies. Wave vectors $\mathbf{k} = (0, 0)$ (row 1), $\mathbf{k} = (\pi, 0)$ (row 2) and $\mathbf{k} = (\pi, \pi)$ (row 3) corresponding to Γ, X and M points, respectively.

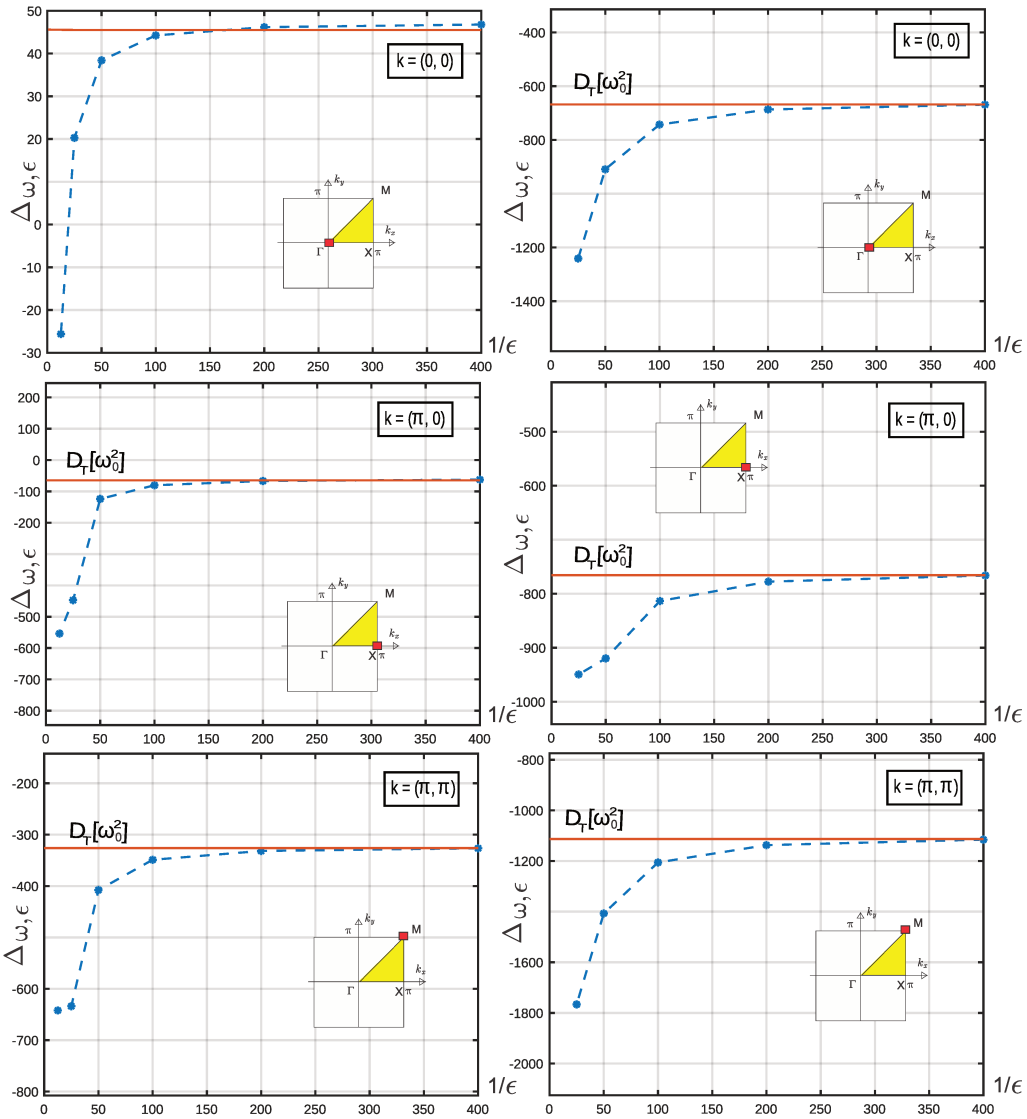

Figura C.9: Analytical expression of the eigenvalue topological derivatives (red lines) compared with their numerical assessments (dashed blue lines with dots) for the fifth (left column) and sixth (right column) eigenvalues. Eigenvalues are the square of the angular frequencies. Wave vectors $\mathbf{k} = (0, 0)$ (row 1), $\mathbf{k} = (\pi, 0)$ (row 2) and $\mathbf{k} = (\pi, \pi)$ (row 3) corresponding to Γ, X and M points, respectively.

$\rho_1 = 1.95 \times 10^{-2}\ kg/cm^3$. Inclusions: $E_2 = 49.01 \times 10^6\ kg/(cm\, s^2)$, $\nu_2 = 0.52$, and $\rho_2 = 1.20 \times 10^{-3}\ kg/cm^3$. The unit cell size is $a = 1\ cm$. The initial penalty parameter of the optimization algorithm is $\alpha^0 = 1$, the penalty parameter increment is $\Delta\alpha = 0.1$, and $\alpha_{max} = 10$. The convergence tolerances are $tol_\beta = 10^{-3}$ and $tol_\psi = 0.005$.

The dispersion branches of the band structure are computed with $N = 27$ discrete points on the boundary of the IBZ zone. Therefore, the optimization problem results with $2N = 54$ constraints.

The algorithm for solving these examples uses a two-stage nested grid refinement procedure. The first stage is solved with a mesh having 4096 triangular finite elements and the second stage with a mesh having 16384 finite elements.

7.1. Discussion of results

The results obtained for the three cases a), b) and c) are summarized and depicted in Figures C.10, C.11 and C.12, respectively.

Figures C.10-a, C.11-a and C.12-a show the microarchitectures (unit cells and assembled phononic crystals) that have been obtained with the topology optimization algorithm. Observe the well-defined interfaces of the final geometrical configurations attained with this technique. We also note that the bandgaps at higher frequencies demand more complex microstructures.

The microstructure acoustic properties of the three cases are analyzed with the band structure diagrams plotted in Figures C.10-b, C.11-b and C.12-b. In these Figures, we also shown the bandgaps generated by each microstructure. The frequencies axes in the plots are normalized with the unit cell size a and a characteristic wave velocity $C_A = \sqrt{\mu_1/\rho_1}$, where μ_1 is the shear modulus of the phase m_1. Curves in red and blue identify the upper and lower bands where the objective bandgaps come up. The relative bandgap widths are also depicted in these figures.

The numerical behaviour of the algorithm in terms of the iteration numbers required to get the convergence are summarized in Figures C.10-c-f, C.11-c-f and C.12-c-f. Next, we discuss these results.

- Figures C.10-c, C.11-c and C.12-c are plots of the product $\hat{\boldsymbol{g}} \cdot \hat{\boldsymbol{\psi}}$, as well as, the horizontal red line corresponding to the value $1 - tol_\psi = 0.995$. The criterion (C.43) is satisfied when the dashed blue lines with dots is closer to 1 than the horizontal red line. In the three cases, we note that this criterion is reached in a few number of iterations.

- Figures C.10-d, C.11-d and C.12-d plot the left term ($\sqrt{(\partial\mathcal{L}/\partial\beta_1)^2 + (\partial\mathcal{L}/\partial\beta_2)^2}$) of the criterion (C.42). They are plotted with dashed blue lines. The dashed red straight-line plot the $\min(\mathfrak{f}_p, \mathfrak{g}_q)\ \forall\, p, q$, defined in the criteria (C.44), in terms of the iteration numbers. The response of these plots show notable jumps after the mesh refinement.

- Dotted blue curves in Figures C.10-e, C.11-e and C.12-e are plots of the maximum component of the vector $\bar{\boldsymbol{\lambda}}$ of Lagrange multipliers introduced in the function (C.17). The dotted red curves are plots of the maximum component of the vector $\bar{\gamma}$ of Lagrange multipliers also introduced in the same function.

- Figures C.10-f, C.11-f and C.12-f are plots of the maximum absolute bandgap in terms of the iteration number.

The topologies and bandgaps (frequency ranges) attained with the present technique compare very well with those reported by Li et al. (2016) for similar problems. Note, however, that we search for the maximum absolute bandgap, while the mentioned reference work searches for the maximum relative bandgap.

8. Conclusions

In this paper, we have described a new topology optimization algorithm for the design of phononic crystal microarchitectures. After assessing the number of iterations required to converge and the quality of the optimized topology, we conclude that the algorithm shows an adequate performance.

The well-defined interfaces generated by this topology optimization algorithm is a remarked feature.

One of the central issues to reach a good performance of the algorithm based on the present methodology is to account for the analytical expressions of the topological derivative. In the phononic crystal design problem, the relevant derivatives are the topological derivatives of the frequencies associated with the wave propagation phenomena. The paper presents analytical expressions of these derivatives, which, in the particular case of multiple and simultaneous perturbations, have been validated through numerical experiments.

The examples presented in the paper compare well with solutions reported in the literature for similar problems.

Finally, we mention that we have tested the algorithm with different starting material configurations. The conclusion is that the attained microarchitecture for a specific topology optimization problem depends on this condition. Therefore, in practical cases, it is suggested to test several initial configurations before choosing the final topology. This characteristic is typical of problem with multiple local minimum, such as happens in the material design problem addressed in this paper.

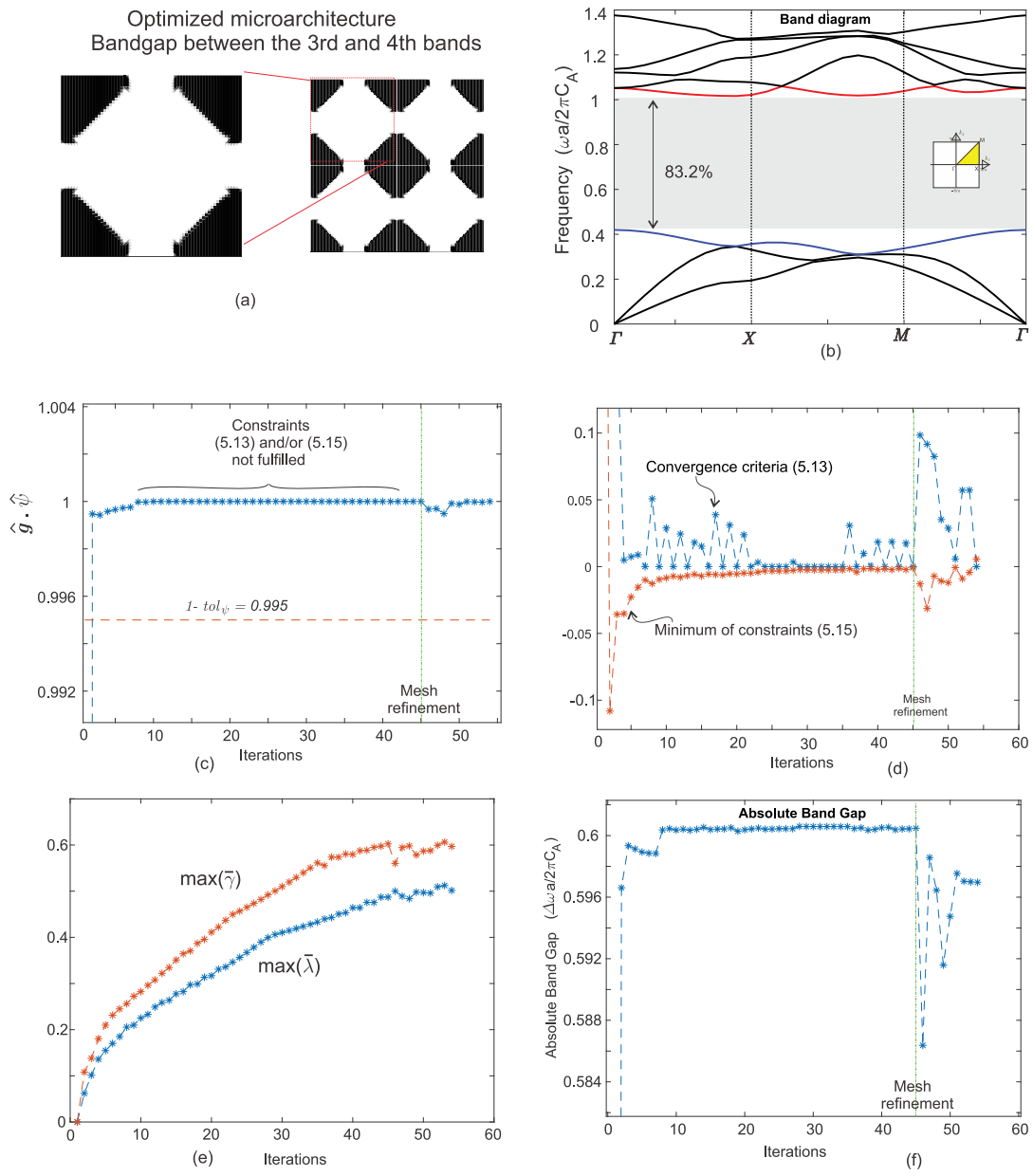

Figura C.10: Case a - bandgap between the third and fourth bands. a) Microarchitecture topology, b) band structure diagram and relative bandgap width; c) criterion (C.43) versus iteration number; d) convergence criterion (C.42) and minimum value of the constraints (C.44) versus iteration number; e) maximum component of the Lagrange multiplier vectors versus iteration number; f) absolute band gap versus iteration number.

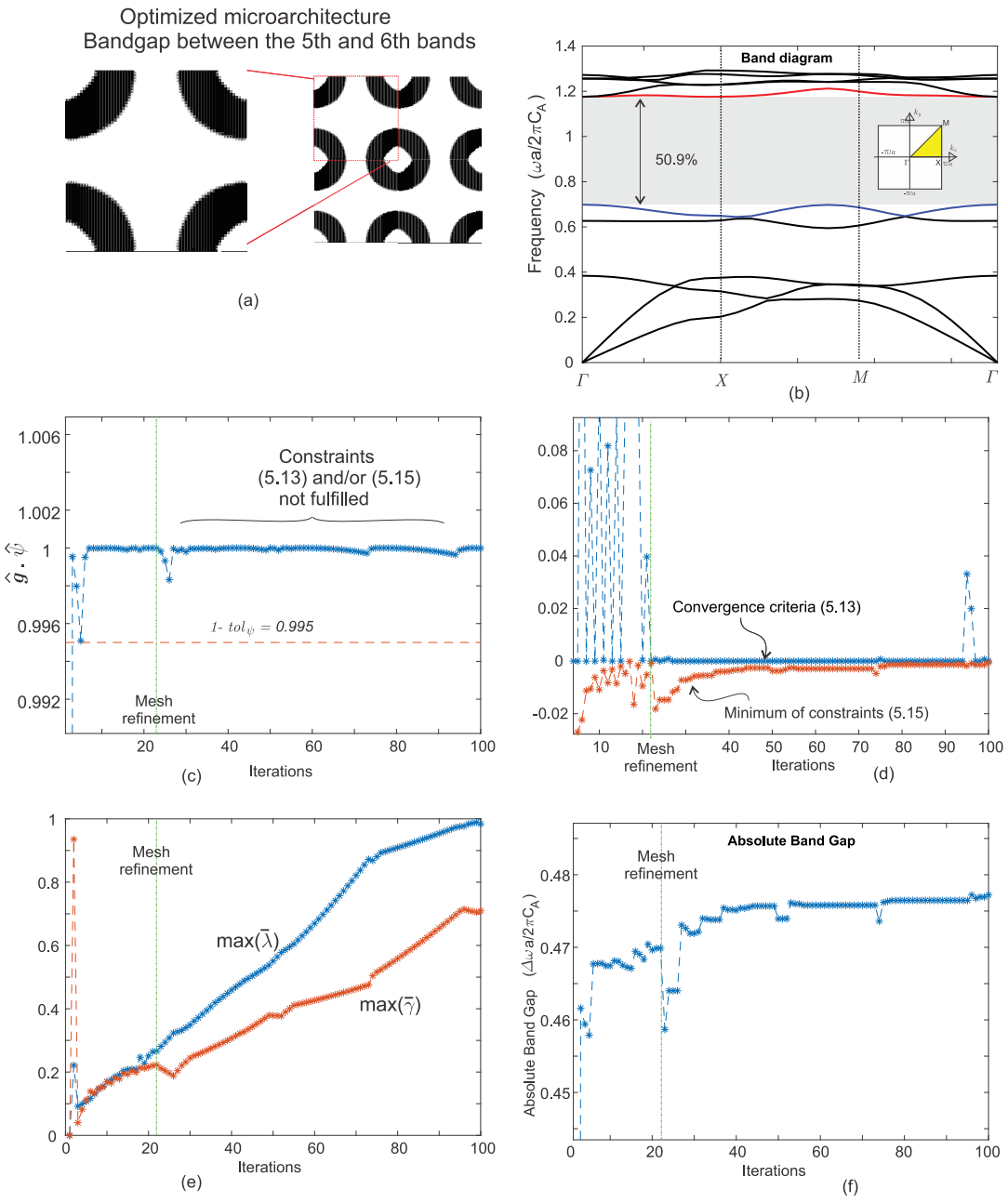

Figura C.11: Case b - bandgap between the fifth and sixth bands. a) Microarchitecture topology, b) band structure diagram and relative bandgap width; c) criteria (C.43) versus iteration number; d) convergence criteria (C.42) and minimum value of the constraints (C.44) versus iteration number; e) maximum component of the Lagrange multiplier vectors versus iteration number; f) absolute band gap versus iteration number.

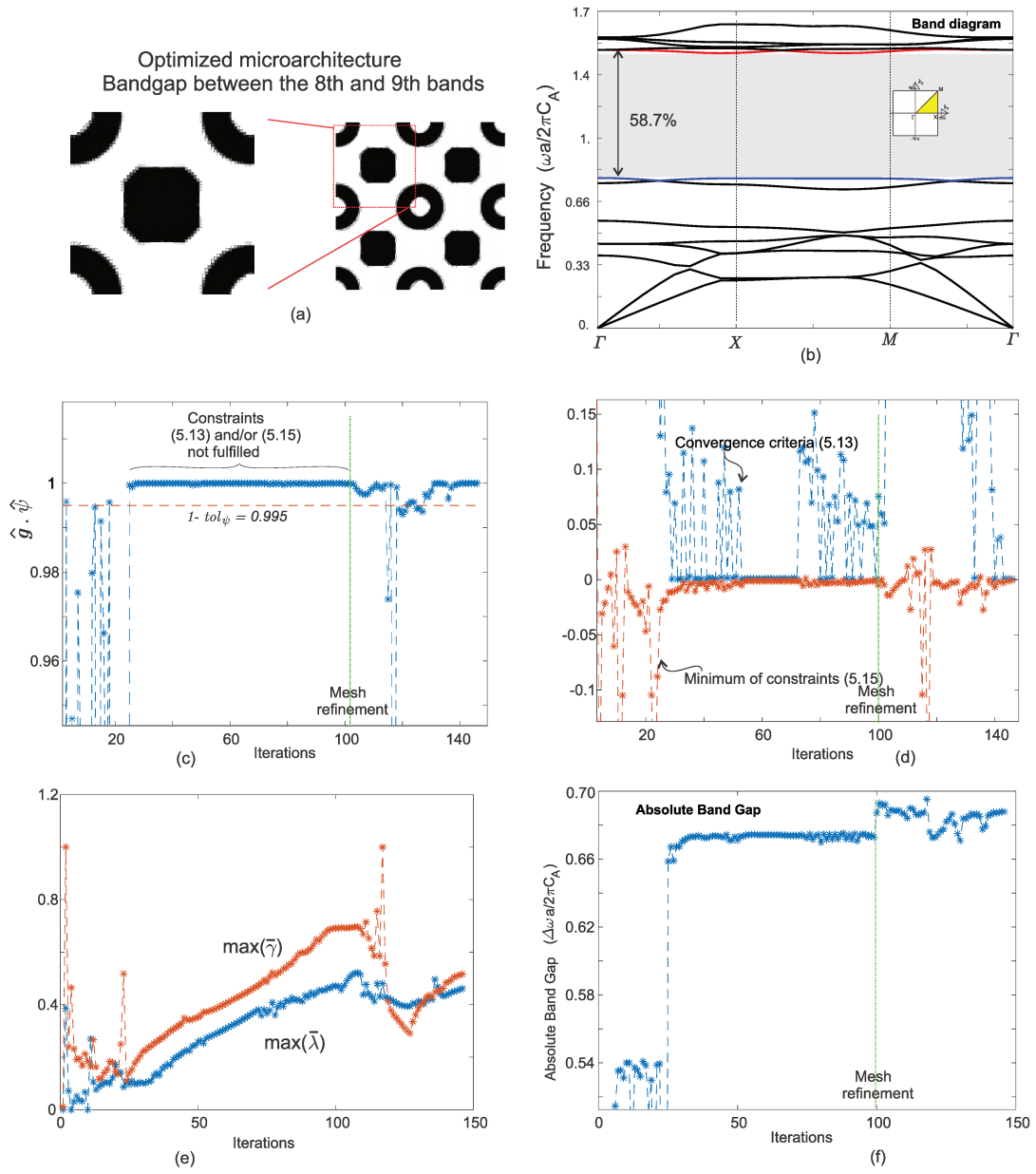

Figura C.12: Case c - bandgap between the eighth and ninth bands. a) Microarchitecture topology, b) band structure diagram and relative bandgap width; c) criteria (C.43) versus iteration number; d) convergence criteria (C.42) and minimum value of the constraints (C.44) versus iteration number; e) maximum component of the Lagrange multiplier vectors versus iteration number; f) absolute band gap versus iteration number.

Appendix I: Augmented Lagrangian Formulation

An specific augmented Lagrangian formulation of the inequality-constrained problems (C.11) used in this work can be derived through a technique based on the proximal point method, see Nocedal y Wright (2006). Proximal point method replaces the original problem by a sequence of more regular sub-problems and is equivalent to an augmented Lagrangian problem applied to the dual variables.

For simplicity, let us suppose that a given optimization problem only has inequality constraints:

$$\min_{x} f(x) \quad \text{subject to} \;\; c_i(x) \geq 0, \;\; i \in I. \tag{C.47}$$

This problem can be equivalently written in a Lagrangian formalism:

$$\min_{x \epsilon R^n} F(x) = \min_{x \text{ feasible}} f(x) \tag{C.48}$$

where

$$F(x) = \max_{\tilde{\lambda} \geq 0} \left\{ f(x) - \sum_{i \epsilon I} \tilde{\lambda}_i c_i(x) \right\} = \begin{cases} f(x) & \text{if } x \text{ is feasible} \\ \infty & \text{otherwise} \end{cases} \tag{C.49}$$

In this format, F is evidently non-smooth. Alternatively, we could replace F by a smooth approximation $\hat{F}(x; \tilde{\lambda}^k, \alpha_k)$ as follows:

$$\hat{F}(x; \tilde{\lambda}^k, \alpha_k) = \max_{\tilde{\lambda} \geq 0} \left\{ f(x) - \sum_{i \epsilon I} \tilde{\lambda}_i c_i(x) - \frac{1}{2\alpha_k} \sum_{i \epsilon I} (\tilde{\lambda}_i - \tilde{\lambda}_i^k)^2 \right\}, \tag{C.50}$$

where α_k is a penalty parameter which, in general, can be modified through the iterations and $\tilde{\lambda}^k$ is an estimation of the Lagrange multiplier. The final term in C.50 penalizes the values of $\tilde{\lambda}$ which are away from a previous estimation $\tilde{\lambda}^k$.

Finally, the original problem (C.47) is reformulated as:

$$\min_{x \in R^n} \max_{\tilde{\lambda} \geq 0} \left\{ f(x) - \sum_{i \epsilon I} \tilde{\lambda}_i c_i(x) - \frac{1}{2\alpha_k} \sum_{i \epsilon I} (\tilde{\lambda}_i - \tilde{\lambda}_i^k)^2 \right\}, \tag{C.51}$$

where the expression in brackets can be seen as a generalized Lagrangian function. The inner maximization problem in (C.51) can be explicitly solved as follows:

$$\tilde{\lambda}_i = \begin{cases} 0 & \text{if } \; -c_i(x) + \tilde{\lambda}_i^k / \alpha_k \leq 0 \\ \tilde{\lambda}_i^k - \alpha_k c_i(x) & \text{otherwise} \end{cases} \tag{C.52}$$

Substituting the values of (C.52) in (C.50) we have :

$$\hat{F}(x; \tilde{\lambda}^k, \alpha_k) = \begin{cases} f(x) - \sum_{i \epsilon I} \tilde{\lambda}_i^k c_i(x) + \frac{\alpha_k}{2} \sum_{i \epsilon I} c_i(x)^2 & \text{if } \; c_i(x) - \tilde{\lambda}_i^k / \alpha_k < 0 \\ f(x) - \frac{1}{2\alpha_k} \sum_{i \epsilon I} (\tilde{\lambda}_i^k)^2 & \text{otherwise} \end{cases} \tag{C.53}$$

which is smooth. Expression (C.53) can be cast as follows:

$$\hat{F}(x;\tilde{\lambda}^k,\alpha_k) = f(x) - \sum_{i\epsilon I_\Lambda} \tilde{\lambda}_i^k c_i(x) + \frac{\alpha_k}{2}\sum_{i\epsilon I_\Lambda} c_i(x)^2 - \frac{1}{2\alpha_k}\sum_{i\epsilon I_{\widehat{\Lambda}}} (\tilde{\lambda}_i^k)^2 \tag{C.54}$$

where

$$\begin{aligned} I_\Lambda &= \left\{ i \mid i \in I \ \wedge \ c_i(x) - \tilde{\lambda}_i^k/\alpha_k < 0 \right\}, \\ I_{\widehat{\Lambda}} &= I \setminus I_\Lambda, \end{aligned} \tag{C.55}$$

Thus, we can obtain a new iterate x_k by solving:

$$\min_x \hat{F}(x;\tilde{\lambda}^k,\alpha_k) \ , \tag{C.56}$$

and using (C.52), we get the estimated Lagrange multiplier at iteration $k+1$: $\tilde{\lambda}^{k+1}$.

According to Nocedal y Wright (2006), the numerical performances of this unconstrained formulation have not been widely reported in the literature because it is not the basis of any major software package.

We chose this formulation, instead of a more conventional one such as the bound-constrained formulation with slack variables, see Nocedal y Wright (2006), because we need to compute only the topological derivatives of those constraints with indices $i \in I_\Lambda$. Instead, the introduction of the slack variable requires the computation of the topological derivatives of the complete set of constraints ($2N$ derivatives).

Bibliografía

Ammari H., Calmon P., y Iakovleva E. Direct elastic imaging of a small inclusion. *SIAM Journal on Imaging Sciences*, 1(2):169–187, 2008.

Amstutz S. Analysis of a level set method for topology optimization. *Optimization Methods and Software*, 26(4-5):555–573, 2011a.

Amstutz S. Augmented lagrangian for cone constrained topology optimization. *Computational Optimization and Applications*, 49(1):101–122, 2011b.

Amstutz S. y Andrä H. A new algorithm for topology optimization using a level-set method. *Journal of Computational Physics*, 216(2):573–588, 2006.

Amstutz S. y Ciligot-Travain M. Optimality conditions for shape and topology optimization subject to a cone constraint. *SIAM J. Control Optim.*, 48(6):40564077, 2010. ISSN 0363-0129.

Amstutz S., Giusti S., Novotny A., y de Souza Neto E. Topological derivative for multi-scale linear elasticity models applied to the synthesis of microstructures. *International Journal for Numerical Methods in Engineering*, 84(6):733–756, 2010.

Bendsøe M., Olhoff N., y Taylor J. A variational formulation for multicriteria structural optimization. *J Struct Mech*, 11(4):523–544, 1983.

Brillouin L. *Wave propagation in periodic structures*. Dover, 1953.

Croënne C., Lee E., Hu H., y Page J. Band gaps in phononic crystals: Generation mechanisms and interaction effects. *AIP Advances*, 1(4):041401, 2011.

Dong H., Su X., Wang Y., y Zhang C. Topological optimization of two-dimensional phononic crystals based on the finite element method and genetic algorithm. *Structural and Multidisciplinary Optimization*, 50(4):593–604, 2014.

Gazalet J., Dupont S., Kastelik J., Rolland Q., y Djafari-Rouhani B. A tutorial survey on waves propagating in periodic media: Electronic, photonic and phononic crystals. perception of the bloch theorem in both real and fourier domains. *Wave Motion*, 50(3):619–654, 2013.

Jensen J. y Pedersen N. On maximal eigenfrequency separation in two-material structures: the 1D and 2D scalar cases. *Journal of Sound and Vibration*, 289(4-5):967–986, 2006.

Jensen J. y Sigmund O. Systematic design of photonic crystal structures using topology optimization: low-loss waveguide bends. *Appl. Phys. Lett.*, 84:2022, 2004.

Krattiger D. y Hussein M.I. Generalized bloch mode synthesis for accelerated calculation of elastic band structures. *Journal of Computational Physics*, 357:183–205, 2018.

Kushwaha M. Classical band structure of periodic elastic composites. *International Journal of Modern Physics B*, 10(09):977–1094, 1996.

Kushwaha M., Halevi P., Dobrzynski L., y B. D.R. Acoustic band structure of periodic elastic composites. *Phys. Rev. Lett.*, 71(2022), 1993.

Li W., Meng F., Chen Y., Li Y., y Huang X. Topology optimization of photonic and phononic crystals and metamaterials: a review. *Advanced Theory and Simulations*, 2(7):1900017, 2019.

Li Y., Huang X., Meng F., y Zhou S. Evolutionary topological design for phononic band gap crystals. *Structural and Multidisciplinary Optimization*, 54:595–617, 2016.

Li Y., Meng F., Li S., Jia B., Zhou S., y Huang X. Designing broad phononic band gaps for in-plane modes. *Physics Letters A*, 382(10):679–684, 2018.

London E.P.B.., editor. *International Tables for Crystallography. Volume C, Mathematical, Physical and Chemical Tables. Dordrecht*. Published for the International Union of Crystallography by Kluwer Academic Publishers, 2004.

Lopes C., Santos R.d., y Novotny A. Topological derivative-based topology optimization of structures subject to multiple load-cases. *Latin American Journal of Solids and Structures*, 12(5):834–860, 2015.

Maurin F., Claeys C., Deckers E., y Desmet W. Probability that a band-gap extremum is located on the irreducible brillouin-zone contour for the 17 different plane crystallographic lattices. *International Journal of Solids and Structures*, 135:26–36, 2018.

Nazarov S. y Sokolowski J. Shape sensitivity analysis of eigenvalues revisited. *Control and Cybernetics*, 37, 2008.

Nocedal J. y Wright S. *Numerical Optimization*. Springer, 2006.

Noguchi Y., Yamada T., Izui K., y Nishiwaki S. Topology optimization for hyperbolic acoustic metamaterials using a high-frequency homogenization method. *Computer Methods in Applied Mechanics and Engineering*, 335:419–471, 2018.

Novotny A. y Sokołowski J. *Topological Derivatives in Shape Optimization. Interaction of Mechanics and Mathematics Series.* Springer-Verlag, Berlin, Heidelberg, 2013.

Novotny A., Sokołowski J., y Żochowski A. *Applications of the topological derivative method*. Springer, 2019.

Olhoff N. Solution of max-min problems via bound formulation and mathematical programming. En K.B. Rozvany G.I.N., editor, *Structural Optimization*. Springer, Dordrecht, 1988.

Olhoff N. Multicriterion structural optimization via bound formulation and mathematical programming. *Structural and Multidisciplinary Optimization*, 1(1):11–17, 1989.

Olhoff N. y Du J. Structural topology optimization with respect to eigenfrequencies of vibration. En G. Rozvany y T. Lewinsky, editores, *Topology Optimization in Structural and Continuum Mechanics*. Springer-Verlag, Vienna, 2013.

Podestá J., Méndez C., Toro S., y Huespe A. Symmetry considerations for topology design in the elastic inverse homogenization problem. *Journal of the Mechanics and Physics of Solids*, 128, 2019.

Rossi Cabral N., Yera R., Méndez C.G. T.S., y Huespe A. Numerical technique for the 3D microarchitecture design of elastic composites inspired by crystal symmetries. *Comput. Meth. App. Mech. Eng.*, 359, 2020.

Sigalas M. y Economou E. Elastic and acoustic wave band structure. *Journal of sound and vibration*, 158(2):377–382, 1992.

Sigmund O. y Jensen J. Systematic design of phononic band-gap materials and structures by topology optimization. *Royal Society*, 361, 2003.

Sokołowski J. y Żochowski A. Optimality conditions for simultaneous topology and shape optimization. *SIAM Journal on Control and Optimization*, 42(4):1198–1221, 2003.

Vainshtein B. *Fundamentals of crystals: Symmetry, and methods of structural crystallography*, volumen 1. Springer Science & Business Media, 2013.

van Dijk N., Maute K., Langelaar M., y Van Keulen F. Level-set methods for structural topology optimization: a review. *Structural and Multidisciplinary Optimization*, 48(3):437–472, 2013.

Yera R., Mndez C., Snchez P., y Huespe A. Effective properties in elastodynamics problems with

periodic materials. *submitted to: Computer Methods in Materials Science*, 2021.

Yi G. y Youn B. A comprehensive survey on topology optimization of phononic crystals. *Structural and Multidisciplinary Optimization*, 54(5):1315–1344, 2016.

Zhang Z., Li Y., Meng F., y Huang X. Topological design of phononic band gap crystals with sixfold symmetric hexagonal lattice. *Computational Materials Science*, 139:97–105, 2017.

Anexo D

Effective properties of periodic media in elastodynamic problems, Computer Methods in Materials Science, Volume 21, 2021

El artículo presentado a continuación ha sido publicado en la revista **"Computer Methods in Materials Science"**.

R. Yera, C. G. Méndez, P.J. Sánchez, A. E. Huespe. *Effective properties of periodic media in elastodynamic problems*. Computer Methods in Materials Science, 21(3), 139-148. 2021. DOI: 10.7494/cmms.2021.3.0753

Effective properties of periodic media in elastodynamics problems

R. Yera[1], C. G. Méndez[1], P.J. Sánchez[1,2], A. E. Huespe[1,3]
[1]CIMEC-UNL-CONICET, Predio Conicet Dr Alberto Cassano, CP 3000 Santa Fe, Argentina
[2]Gimni UTN-FRSF, Lavaise 610, CP 3000 Santa Fe, Argentina.
[3]FIQ-UNL, Santiago del Estero 2800, Santa Fe, CP, 3000, Argentina

The authors of this paper would like to express
their appreciation and honour to Prof. Maciej Pietrzyk.
This paper is dedicated to him.

Abstract

This paper describes a homogenization model for evaluating the effective elastodynamic properties of acoustic metamaterials in problems involving wave propagation.

The methodology is based on determining the constitutive equations in terms of averaged quantities observed at the macroscale. In this sense, the approach follows very closely the pioneering ideas introduced by Willis, and afterwards, followed by several authors in the last ten years. The distinctive characteristic of our approach is that we write the microscale equation in the spatial domain.

The model is validated with previous results published in the literature, and our results copy them almost exactly.

The resulting homogenization model could be used as an additional tool for the topology design of acoustic metamaterials.

Keywords: effective properties of acoustic metamaterials; wave propagation in periodic media; Bloch waves; phononic crystals.

1. Introduction

The construction of dispersion curves characterizing the response of acoustic metamaterials, or phononic crystals, displaying periodic microarchitectures subjected to wave propagation pro-

blems, is nowadays rather standard. There exist consensus about how these curves have to be evaluated. Particularly, in layered composites, there are exact procedures and solutions available in the literature. Hussein and co-authors have studied this problem in several works and they have reported efficient numerical techniques to compute these dispersion curves (see the revision work Hussein et al. (2014) and references cited therein, see also D. Krattiger (2018)).

Alternatively, there is not a general agreement about how to evaluate the effective properties, observed at the macroescale level, of such acoustic metamaterials. This problem has been reported by several researchers and much of the described models were derived from previous analyses coming from photonic crystals. We remark that the evaluation of the effective elasticity and density properties in an elastodynamic problem is the most typical case in metamaterials where non-conventional situations can arise, as shown in the paper Dong et al. (2017). For example, an interesting discussion about the attainment of non-conventional effective properties in heterogeneous materials with microstructure is reported in the work Milton y Willis (2007). These authors discuss the consequences that such effective properties impose on the very fundamental responses of accelerating bodies in classical mechanics, in particular, the impact that they have on the second Newton's law. A tensorial non-isotropic effective density, negative densities, or stiffnesses are typical results that can be obtained in these cases (double negative materials).

In this paper, we propose a numerical model to evaluate the effective properties of an acoustic metamaterial. These effective properties are obtained through an averaging procedure involving the constitutive response connecting the mechanical magnitudes observed at the macroscale as averaged quantities: stresses ($\boldsymbol{\Sigma}$), momentum density vector ($\boldsymbol{P}$), strains ($\boldsymbol{E}$), displacements ($\boldsymbol{U}$) and velocities ($\dot{\boldsymbol{U}}$), with those observed at the microscale: stresses ($\boldsymbol{\sigma}$), momentum density vector ($\boldsymbol{p}$), displacements ($\mathbf{u}$) and velocities ($\dot{\mathbf{u}}$). Our procedure follows closely the pioneering works of Willis Willis (1997)-Willis (2012) to find the general form of constitutive relations in dynamic media with microstructure.

The original ideas of Willis were based on the ensemble averaging concept of a non-periodic composite, and then, these ideas have been particularized for periodic materials. Nemat Nasser and co-authors have followed this line in several works, only to cite a few, we mention Nemat-Nasser y Srivastava (2011) and Nemat-Nasser et al. (2011), and a good review is presented in the paper Srivastava (2015). Nassar et al. also have followed the original ideas of Willis to implement a homogenization model in dynamic problems, see Nassar et al. (2016). Particularly relevant for the development of our present proposal is the paper Nassar et al. (2015). The works of Willis, Nemat Nasser et al., and Nassar et al. use the Green's function technique to solve the microscale problem arising from the mechanical formulation. They need to transform the mechanical variables

to the Fourier or Laplace space. In our case, however, and as a distinctive characteristic, we formulate the microscale equations in the spatial domain that allows resolving pointwise eigenfields (displacements, stresses, etc.) with the conventional finite element method.

The effective properties obtained with the approach developed by Willis shown a cross-coupling effect between the averaged stresses and momentums with the averaged strains and velocities. This result is also replicated by our model. Nevertheless, considering that these couplings have been widely studied in the literature, see the review of Willis (Willis (1997)), we will not give any further details about this issue.

In our approach, we assume that the solutions of the elastodynamic wave propagation problem in periodic media are Bloch waves. An interesting description of Bloch waves in periodic media is found in the paper by Gazelet et al. Gazalet et al. (2013).

Several limitations of the Willis'approach have been previously reported. Non-uniqueness of the solution has been originally mentioned in the works of Willis. This author suggests to include an additional eigenstrain in the constitutive equation of the average stress to recover uniqueness (see Nassar et al. (2015)). Also, limitations of the model at high frequencies have been reported in Srivastava y Nemat-Nasser (2014). However, our primary interest in this work is to avoid the analysis of these issues. Such analysis is left for a future work.

In the next Section, we introduce a very short summary of the Bloch wave solutions for an elastodynamic problem in periodic media. We introduce the average field of a Bloch wave within a periodic micro-architecture. In Section 3, the homogenization model is introduced. The bridging scale equations, connecting both scales of analysis, are developed using a generalized version of the Hill-Mandel lemma. Section 4 presents the numerical treatment given to the microscale equation. We use a Lagrange Multiplier technique to relax the field constraint required by the homogenization model at the microscale. In Section 5 we describe some details of the numerical implementation of the homogenization algorithm. In Section 6, the methodology is numerically validated by comparing the results of the present model with those reported in the literature. Finally, the conclusions of this work are presented.

2. Theory

Let us consider the Bloch solution (Bloch type solutions are denoted by a superimposed hat) of a propagating wave in a periodic media with unit cell Ω_μ, $\hat{\varphi}(\mathbf{x})$, with (possible) complex wave-number vector $\mathbf{k}$, which is also harmonic in time with frequency ω, whose expression is:

$$\hat{\varphi}(\mathbf{x}) = \varphi(\mathbf{x}) e^{i(\mathbf{k}\cdot\mathbf{x}-\omega t)}. \tag{D.1}$$

This is typically a periodic function in space, $\varphi(\mathbf{x})$, modulated by a plane wave function $e^{i\mathbf{k}\cdot\mathbf{x}}$ and by the harmonic time function $e^{-i\omega t}$. The periodicity of $\varphi(\mathbf{x})$ is related to the unit cell of the periodic material Ω_μ. The function $\varphi(\mathbf{x})$ is identically repeated for every unit cell, and therefore, it satisfies the following identity: $\varphi(\mathbf{x}) = \varphi(\mathbf{x} + n_1\mathbf{a}_1 + n_2\mathbf{a}_2)$ where $\mathbf{a}_1$ and $\mathbf{a}_2$ are the primitive vectors of the Bravais lattice underlying of the periodic material (see Figure D.2), and n_1 and n_2 are arbitrary integer numbers.

Following the conventional treatment of harmonic problems in time, we replace the time derivative by the factor $-i\omega$ and remove the explicit time dependence $e^{-i\omega t}$ from the momentum balance equation, while only the spatial dependence is held explicit.

According to the ideas introduced originally by Willis, and particularly following the work Nassar et al. (2015), we define the effective value of the mechanical terms.

Let us consider a particular term of the momentum balance equation, the divergence of the stress field. Using the Bloch wave expression for the stress:

$$\nabla_x \cdot \hat{\boldsymbol{\sigma}}(\mathbf{x}) = \nabla_x \cdot \boldsymbol{\sigma}(\mathbf{x}) e^{i\mathbf{k}\cdot\mathbf{x}}\,, \tag{D.2}$$

we multiply this expression by $e^{-i\mathbf{k}\cdot\mathbf{y}}$ (see Figure D.1) and replace the variable $\mathbf{X} = \mathbf{x} - \mathbf{y}$:

$$\nabla_x \cdot \boldsymbol{\sigma}(\mathbf{x}) e^{i\mathbf{k}\cdot(\mathbf{x}-\mathbf{y})} = \nabla_X \cdot \boldsymbol{\sigma}(\mathbf{X}+\mathbf{y}) e^{i\mathbf{k}\cdot\mathbf{X}}\,. \tag{D.3}$$

Finally, we average this expression in the microcell Ω_μ, such as proposed in Nemat-Nasser y Srivastava (2011), to get:

$$\left\langle \nabla_X \cdot \boldsymbol{\sigma}(\mathbf{X}+\mathbf{y}) e^{i\mathbf{k}\cdot\mathbf{X}} \right\rangle_{\mathbf{y}\in\Omega_\mu} = \nabla_X \cdot \langle \boldsymbol{\sigma}(\mathbf{X}+\mathbf{y}) \rangle_{\mathbf{y}\in\Omega_\mu} e^{i\mathbf{k}\cdot\mathbf{X}} \tag{D.4}$$

where the notation $\langle(\cdot)\rangle$ means the average operator in Ω_μ. Following this concept, we define the average value of the generic field $\varphi(\mathbf{x})$ as follows:

$$\hat{\Phi}(\mathbf{X}) = \Phi(\mathbf{X}) e^{i\mathbf{k}\cdot\mathbf{X}} \quad ; \tag{D.5}$$

where:

$$\Phi(\mathbf{X}) = \langle \varphi(\mathbf{X}+\mathbf{y}) \rangle_{\mathbf{y}\in\Omega_\mu} = \frac{1}{|\Omega_\mu|} \int_{\Omega_\mu} \varphi(\mathbf{X}+\mathbf{y}) d\mathbf{y} \tag{D.6}$$

There are three important issues which are remarked in the following items:

i) due to the periodicity of $\varphi(\mathbf{x})$, its averaged valued $\langle \varphi(\mathbf{X}+\mathbf{y}) \rangle_{\mathbf{y}}$ denoted $\Phi(\mathbf{X})$, is identical for every micro-cell Ω_μ at different positions $\mathbf{X}$. The macroscale coordinate $\mathbf{X}$ identifies the position of Ω_μ. Therefore, the effective value Φ does not depend on $\mathbf{X}$;

ii) the averaging procedure applied to all mechanical fields, preserves the form of the balance equation at the macroscale. These equations are derived below;

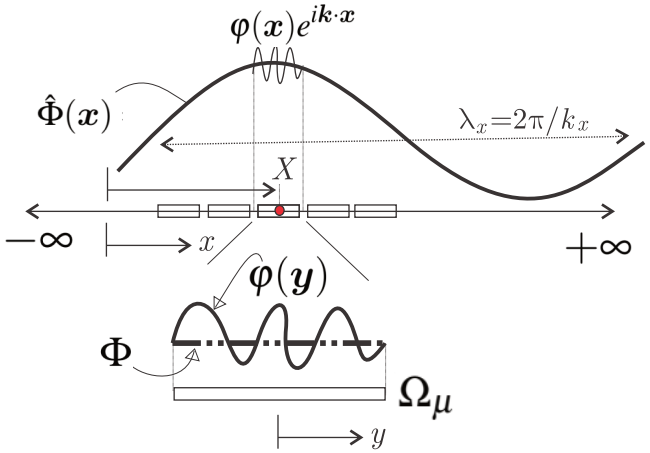

Figura D.1: Schematic description of the Bloch wave solution $\hat{\varphi}(\mathbf{x})$ for a periodic material and its average field $\hat{\Phi}(\mathbf{x})$.

iii) in the following, we will not make a further distinction between the two variables $\mathbf{x}$ and $\mathbf{X}$. Additionally, it is understood that the domain where the average operation is performed is the microcell Ω_μ. In consequence, we remove the sub-index in the notation: $\langle\cdot\rangle_{\mathbf{y}\in\Omega_\mu}$.

The following identities hold for the symmetric gradient of a vectorial field $\hat{\varphi}$ and the corresponding average field $\hat{\Phi}(\mathbf{x})$:

$$\nabla_{\mathbf{x}}\hat{\varphi}(\mathbf{x}) = \nabla_k(\varphi(\mathbf{x}))e^{i\mathbf{k}\cdot\mathbf{x}} \quad ; \quad \nabla_k(\cdot) = \nabla_{\mathbf{x}}(\cdot) + i\mathbf{k}\otimes^s(\cdot) \tag{D.7}$$

$$\nabla_{\mathbf{x}}\hat{\Phi}(\mathbf{x}) = \nabla_k\langle\varphi(\mathbf{x})\rangle e^{i\mathbf{k}\cdot\mathbf{x}} = i\mathbf{k}\otimes^s(\Phi) \tag{D.8}$$

$$\tag{D.9}$$

where $\nabla_{\mathbf{x}}$ is the symmetric gradient and $(\cdot\otimes^s\cdot)$ is the symmetric tensorial product. The complex conjugate of the gradient is:

$$\overline{\nabla_k}(\cdot) = \overline{\nabla_{\mathbf{x}}}(\cdot) - i\bar{\mathbf{k}}\otimes^s(\cdot) \tag{D.10}$$

3. Homogenization model

Let us consider the displacement and velocity fields as Bloch waves:

$$\hat{\mathbf{u}}(\mathbf{x}) = \mathbf{u}(\mathbf{x})e^{i\mathbf{k}\cdot\mathbf{x}} \quad ; \quad \hat{\dot{\mathbf{u}}}(\mathbf{x}) = \dot{\mathbf{u}}(\mathbf{x})e^{i\mathbf{k}\cdot\mathbf{x}} \tag{D.11}$$

where the periodic functions $\mathbf{u}(\mathbf{x})$ and $\dot{\mathbf{u}}(\mathbf{x})$, in Ω_μ, are approached as follows:

$$\mathbf{u}(\mathbf{y}) = \boldsymbol{U} + \tilde{\mathbf{u}}(\mathbf{y}) \quad ; \quad \langle\mathbf{u}\rangle = \boldsymbol{U} \quad ; \quad \langle\tilde{\mathbf{u}}\rangle = \mathbf{0}; \tag{D.12}$$

$$\dot{\mathbf{u}}(\mathbf{y}) = \dot{\boldsymbol{U}} + \dot{\tilde{\mathbf{u}}}(\mathbf{y}) \quad ; \quad \langle\dot{\mathbf{u}}\rangle = \dot{\boldsymbol{U}} \quad ; \quad \left\langle\dot{\tilde{\mathbf{u}}}\right\rangle = \mathbf{0}; \tag{D.13}$$

Considering the item *i)* of the previous Section, we note that $\boldsymbol{U}$ does not depend on $\mathbf{X}$, and the macroscale displacement results: $\hat{\boldsymbol{U}}(\mathbf{X}) = \boldsymbol{U}e^{i\mathbf{k}\cdot\mathbf{X}}$.

The strain field in Ω_μ is:

$$\hat{\boldsymbol{\varepsilon}}(\mathbf{x}) = \boldsymbol{\varepsilon}(\mathbf{x}) e^{i\mathbf{k}\cdot\mathbf{x}} \ , \tag{D.14}$$

$$\boldsymbol{\varepsilon}(\mathbf{x}) = \nabla_k(\boldsymbol{U} + \tilde{\mathbf{u}}) = \underbrace{i\mathbf{k} \otimes^s \boldsymbol{U}}_{\boldsymbol{E}} + \nabla_k \tilde{\mathbf{u}} = \boldsymbol{E} + \nabla_k \, . \tilde{\mathbf{u}} \tag{D.15}$$

Note that $\tilde{\mathbf{u}}$ is a periodic function with a null average value (see equation (D.12)). Therefore, $\langle \nabla_k \tilde{\mathbf{u}} \rangle = \langle \nabla_{\mathbf{x}} \tilde{\mathbf{u}} \rangle + i\mathbf{k} \otimes^s \langle \tilde{\mathbf{u}} \rangle = \mathbf{0}$, resulting:

$$\langle \boldsymbol{\varepsilon}(\mathbf{x}) \rangle = \boldsymbol{E} \ . \tag{D.16}$$

3.1. A generalized version of the Hill-Mandel homogenization lemma

We assume that $\boldsymbol{U}$ and $\tilde{\mathbf{u}}$ can be arbitrarily defined with the condition that $\tilde{\mathbf{u}}$ is periodic and $\langle \tilde{\mathbf{u}} \rangle = \mathbf{0}$. Then, admissible variations of the average displacement $\boldsymbol{U}$ and displacement fluctuations $\tilde{\mathbf{u}}$ are defined as follows: $\delta\boldsymbol{U}$ is an arbitrary vector in $\mathbb{R}^{ndim}$, and $\delta\tilde{\mathbf{u}} \in \mathcal{V}_u$, where the vectorial space $\mathcal{V}_u$ is defined as follows:

$$\mathcal{V}_u = \{ \delta\tilde{\mathbf{u}} \ \mid \ \ \delta\tilde{\mathbf{u}} \text{ is periodic} \ \ ; \ \text{ and } \ \langle \delta\tilde{\mathbf{u}} \rangle = \mathbf{0} \} \tag{D.17}$$

Admissible variations of the average strain are $\delta\boldsymbol{E} = i\mathbf{k} \otimes^s \delta\boldsymbol{U}$ and admissible strains in Ω_μ are: $\delta\boldsymbol{\varepsilon} = i\mathbf{k} \otimes^s \delta\boldsymbol{U} + \nabla_k(\delta\tilde{\mathbf{u}})$.

The Hill-Mandel homogenization principle is presented as follows:

$$\begin{aligned} &\boldsymbol{\Sigma} : \overline{\delta\boldsymbol{E}} - i\omega \boldsymbol{P} \cdot \overline{\delta\boldsymbol{U}} = \left\langle \boldsymbol{\sigma} : \overline{\delta\boldsymbol{\varepsilon}} - i\omega \boldsymbol{p} \cdot \overline{\delta\tilde{\mathbf{u}}} \right\rangle \quad ; \\ &\forall \ \overline{\delta\boldsymbol{U}} \in \mathbb{R}^{ndim} \qquad ; \qquad \forall \ \overline{\delta\tilde{\mathbf{u}}} \in \mathcal{V}_u \end{aligned} \tag{D.18}$$

the symbols $(:)$ and $(\cdot)$ denotes internal products of second order tensors and vectors, respectively. Also, the symbol $\overline{(\cdot)}$ represents the complex conjugate term [1].

In equation (D.18), the expressions $\boldsymbol{\Sigma}$ and $\boldsymbol{P}$ are averaged variables conjugate to $\boldsymbol{E}$ and $\dot{\boldsymbol{U}}$, respectively. Arbitrary variations of $\boldsymbol{U}$ and $\tilde{\mathbf{u}}$ defines the connection of $\boldsymbol{\Sigma}$ and $\boldsymbol{P}$ with the microscale (non-averaged) variables, as shown in the following.

i) Performing arbitrary variations of $\delta\boldsymbol{U}$, expression (D.18) gives:

$$i\mathbf{k}\boldsymbol{\Sigma} + i\omega\boldsymbol{P} = \langle i\mathbf{k}\boldsymbol{\sigma} + i\omega\boldsymbol{p} \rangle \tag{D.19}$$

[1] Note that by adopting admissible displacement variations, $\delta\hat{\mathbf{u}}$, which have a Bloch-wave form with conjugate admissible displacements given by $\overline{\delta\hat{\mathbf{u}}} = \delta\mathbf{u} e^{-i\mathbf{k}\cdot\mathbf{x}}$, then, the virtual internal work results: $\hat{\boldsymbol{\sigma}} : \nabla_{\mathbf{x}} \overline{\delta\hat{\mathbf{u}}} = \tilde{\boldsymbol{\sigma}} : \overline{\nabla_k \delta\tilde{\mathbf{u}}}$. Thus, this internal product can be written only in terms of the periodic parts of $\hat{\boldsymbol{\sigma}}$ and $\overline{\delta\hat{\mathbf{u}}}$. This property is used in all the internal products reported in this paper.

considering separately each term, and given that this expression has to be satisfied for different values of $\mathbf{k}$ and ω[2], then, the equation (D.19) is satisfied if:

$$\boldsymbol{\Sigma} = \langle \boldsymbol{\sigma} \rangle \qquad \text{and} \qquad \boldsymbol{P} = \langle \boldsymbol{p} \rangle \,. \tag{D.20}$$

ii) Performing arbitrary variations of $\delta\tilde{\mathbf{u}}$, expression (D.18) gives:

$$\left\langle \boldsymbol{\sigma} : \overline{\nabla_k \delta\tilde{\mathbf{u}}} - i\omega \boldsymbol{p} \cdot \overline{\delta\tilde{\mathbf{u}}} \right\rangle = 0 \qquad ; \qquad \forall \overline{\delta\tilde{\mathbf{u}}} \in \mathcal{V}_u \tag{D.21}$$

4. Lagrange Multiplier approach

In (D.21), to relieve the null average value constraint characterizing the functions in $\mathcal{V}_u$, and following to Roca et al. (2019), we introduce a Lagrange Multiplier approach. In this case, equation (D.21) can be rewritten as follows:

$$\left\langle \boldsymbol{\sigma} : \overline{\nabla_k \delta\tilde{\mathbf{u}}} - i\omega \boldsymbol{p} \cdot \overline{\delta\tilde{\mathbf{u}}} \right\rangle - \lambda \cdot \langle \delta\tilde{\mathbf{u}} \rangle = 0 \quad ; \quad \forall \ \delta\tilde{\mathbf{u}} \ \text{ periodic;} \tag{D.22}$$

$$- \langle \tilde{\mathbf{u}} \rangle \cdot \delta\lambda = 0 \quad ; \quad \forall \ \delta\lambda \ \in \ \mathbb{R}^{ndim}; \tag{D.23}$$

where $\lambda \in \mathbb{R}^{ndim}$ is the Lagrange Multiplier. In this formulation, the variations $\delta\tilde{\mathbf{u}}$ are not constrained to have a null average.

Taking the variational equation (D.22), and particularizing the variational displacement $\delta\tilde{\mathbf{u}}$ to be an arbitrary uniform vector $\mathbf{a} \in \mathbb{R}^{ndim}$, result:

$$\langle i\mathbf{k}\boldsymbol{\sigma} + i\omega \boldsymbol{p} \rangle = -\lambda \tag{D.24}$$

which, jointly with equation (D.19), provides a balance equation of averaged terms:

$$i\mathbf{k}\boldsymbol{\Sigma} + i\omega \boldsymbol{P} + \lambda = -\overline{\nabla_k} \cdot \boldsymbol{\Sigma} + i\omega \boldsymbol{P} + \lambda = \mathbf{0}. \tag{D.25}$$

The intermediate identity arises after considering that $\boldsymbol{\Sigma}$ does not depend on $\mathbf{x}$.

5. Microcell problem

Let the constitutive equation be given in terms of the periodic functions as follows:

$$\boldsymbol{\sigma} = \mathbb{C}\nabla_k \mathbf{u} = \mathbb{C}(\boldsymbol{E} + \nabla_k \tilde{\mathbf{u}}); \tag{D.26}$$

$$\boldsymbol{p} = \rho\dot{\mathbf{u}} = \rho(\dot{\boldsymbol{U}} + \dot{\tilde{\mathbf{u}}}) \tag{D.27}$$

where $\mathbb{C}$ is the elasticity tensor and ρ the density. Replacing both expressions in (D.22) and (D.23), result:

[2]The wavenumber $\mathbf{k}$ and frequency ω are not arbitrary. They have to be consistent with the dispersion curves of the material.

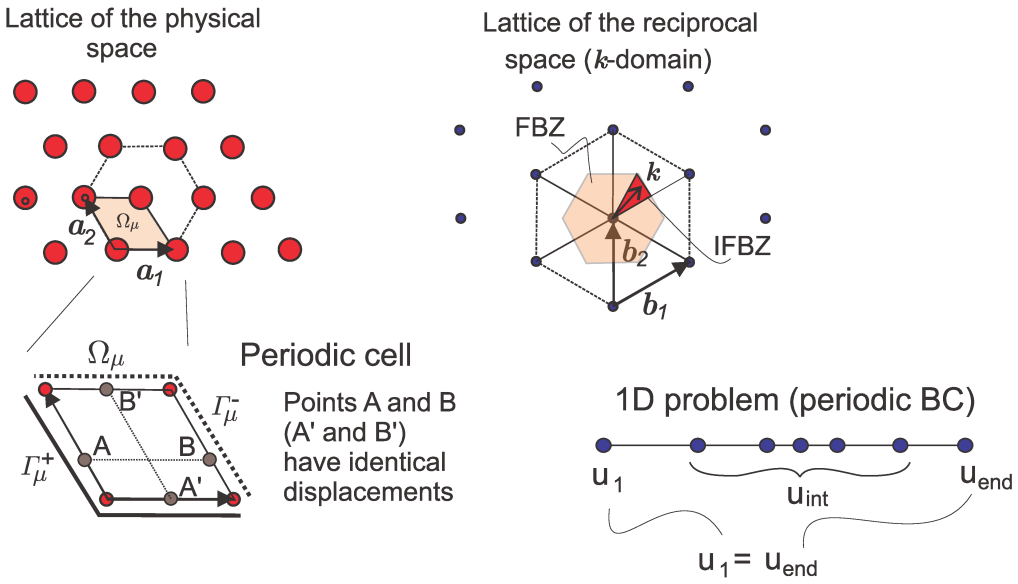

Figura D.2: Lattices of the physical and reciprocal spaces. Microcell Ω_μ with the boundaries Γ_μ^+ and Γ_μ^-. The points A and B (as well as A' and B') have identical displacements.

$$\left\langle \mathbb{C}\nabla_k\tilde{\mathbf{u}} : \overline{\nabla_k\delta\tilde{\mathbf{u}}} - \omega^2\rho\tilde{\mathbf{u}}\overline{\delta\tilde{\mathbf{u}}}\right\rangle - \lambda\left\langle\delta\tilde{\mathbf{u}}\right\rangle = -\left\langle \mathbb{C}\boldsymbol{E} : \overline{\nabla_k\delta\tilde{\mathbf{u}}} - i\omega\rho\dot{\boldsymbol{U}}\overline{\delta\tilde{\mathbf{u}}}\right\rangle \tag{D.28}$$

$$-\left\langle\tilde{\mathbf{u}}\right\rangle\delta\lambda = \mathbf{0} \tag{D.29}$$

$$\forall\ \delta\tilde{\mathbf{u}}\ \text{periodic} \quad ; \quad \forall\ \delta\lambda\ \in\ \mathbb{R}^{ndim}$$

Numerical implementation

The dispalcements $\tilde{\mathbf{u}}$ in Ω_μ are interpolated through a conventional FE approach:

$$\tilde{\mathbf{u}}(\mathbf{y}) = \boldsymbol{N}(\mathbf{y})[\tilde{\mathbf{u}}]; \tag{D.30}$$

$$\nabla_k\tilde{\mathbf{u}} = \mathbf{B}[\tilde{\mathbf{u}}] + i\mathbf{k}\otimes^s\boldsymbol{N}[\tilde{\mathbf{u}}] = \mathbf{B}_k[\tilde{\mathbf{u}}]; \tag{D.31}$$

where $\boldsymbol{N}$ is the matrix of shape functions and $[\tilde{\mathbf{u}}] \in \mathbb{R}^{ndof}$ is the vector gathering the full nodal displacement set of the finite element mesh. The total number of Degrees Of Freedom (DOFs) is denoted $ndof$. The matrix $\mathbf{B}$ is the conventional finite element strain-displacement matrix. Also, for notation consistency, we call $[\lambda] \in \mathbb{R}^{ndim}$ the Lagrange multiplier vector.

Introducing this approach into equations (D.28) and (D.29), they result in the following discrete equation system:

$$\begin{bmatrix} \mathbb{K}_{dyn} & -\left\langle\boldsymbol{N}\right\rangle^T \\ -\left\langle\boldsymbol{N}\right\rangle & \mathbf{0} \end{bmatrix}\begin{bmatrix}[\tilde{\mathbf{u}}] \\ [\boldsymbol{\lambda}]\end{bmatrix} = \begin{bmatrix} -\left\langle\overline{\mathbf{B}_k}^T\mathbb{C}\boldsymbol{E} - i\omega\rho\boldsymbol{N}^T\dot{\boldsymbol{U}}\right\rangle \\ \mathbf{0}\end{bmatrix} \tag{D.32}$$

where $\mathbb{K}_{dyn} = (\mathbb{K}(k) - \omega^2\mathbb{M})$ is the sum of an averaged stiffness matrix $\mathbb{K}(k) = \left\langle\overline{\mathbf{B}_k}^T\mathbb{C}\mathbf{B}_k\right\rangle$ and an averaged mass matrix $\mathbb{M} = \left\langle\rho\boldsymbol{N}^T\boldsymbol{N}\right\rangle$.

The periodicity of the field $\tilde{\mathbf{u}}$ requires that the nodal values of $[\tilde{\mathbf{u}}]$ on the boundary Γ_μ^-, of

Ω_μ, are identical to those of the nodes on the boundary Γ_μ^+. This restriction is imposed via the following expression:

$$[\tilde{\mathbf{u}}] = \mathbb{P}[\tilde{\mathbf{u}}]_r \tag{D.33}$$

where $[\tilde{\mathbf{u}}]_r$ is the vector gathering the displacement d.o.f's of the interior nodes of Ω_μ plus the nodes on the boundary Γ_μ^+ of Ω_μ, see Figure D.2. For one-dimensional (1-D) system, equation (D.33) is written as follows:

$$[\tilde{\mathbf{u}}] = \begin{bmatrix} u_1 \\ u_{int} \\ u_{end} \end{bmatrix} = \mathbb{P}[\tilde{\mathbf{u}}]_r = \begin{bmatrix} 1 & \mathbf{0} \\ 0 & \mathbb{1} \\ 1 & \mathbf{0} \end{bmatrix} \begin{bmatrix} u_1 \\ u_{int} \end{bmatrix} \tag{D.34}$$

where, as schematized in Figure D.2, the u_1 d.o.f is on the boundary Γ_μ^+, u_{end} is the d.o.f on the boundary Γ_μ^- and u_{int} are the full set of interior d.o.f's.

Using the reduced d.o.f's, equation system (D.32) is rewritten as follows:

$$\underbrace{\begin{bmatrix} \mathbb{P}^T \mathbb{K}_{dyn} \mathbb{P} & -\mathbb{P}^T \langle \boldsymbol{N} \rangle^T \\ -\langle \boldsymbol{N} \rangle \mathbb{P} & 0 \end{bmatrix}}_{\mathbb{D}} \begin{bmatrix} [\tilde{\mathbf{u}}]_r \\ [\boldsymbol{\lambda}] \end{bmatrix} = \begin{bmatrix} -\mathbb{P}^T \left\langle \overline{\mathbf{B}_k}^T \mathbb{C} \boldsymbol{E} - i\omega\rho \boldsymbol{N}^T \dot{\boldsymbol{U}} \right\rangle \\ 0 \end{bmatrix} \tag{D.35}$$

Thus:

$$\begin{bmatrix} [\tilde{\mathbf{u}}] \\ [\boldsymbol{\lambda}] \end{bmatrix} = \begin{bmatrix} \mathbb{A} & \mathbb{F} \\ \mathbb{G} & \mathbb{I} \end{bmatrix} \begin{bmatrix} \boldsymbol{E} \\ \dot{\boldsymbol{U}} \end{bmatrix} \tag{D.36}$$

where:

$$\mathbb{A} = -\overbrace{\mathbb{P}(\mathbb{D}^{-1})_{11}\mathbb{P}^T}^{\mathbb{Q}} \left\langle \overline{\mathbf{B}_k}^T \mathbb{C} \right\rangle = -\mathbb{Q} \left\langle \overline{\mathbf{B}_k}^T \mathbb{C} \right\rangle \ , \tag{D.37}$$

$$\mathbb{F} = +i\omega\mathbb{Q} \left\langle \rho \boldsymbol{N}^T \right\rangle \ , \tag{D.38}$$

$$\mathbb{G} = -(\mathbb{D}^{-1})_{21}\mathbb{P}^T \left\langle \overline{\mathbf{B}_k}^T \mathbb{C} \right\rangle \quad , \tag{D.39}$$

$$\mathbb{I} = +i\omega(\mathbb{D}^{-1})_{21}\mathbb{P}^T \left\langle \rho \boldsymbol{N}^T \right\rangle \ , \tag{D.40}$$

where $(\mathbb{D}^{-1})_{11}$ and $(\mathbb{D}^{-1})_{21}$ are the corresponding sub-blocks of the inverse matrix $(\mathbb{D}^{-1})$ which multiply the non-null right hand side of (D.35) to provide $[\tilde{\mathbf{u}}]$ and $[\boldsymbol{\lambda}]$, respectively.

The expressions (D.36) are replaced in equations (D.26) and (D.27); and the resulting stress and momentum terms are finally replaced into equation (D.20), giving:

$$\begin{bmatrix} \boldsymbol{\Sigma} \\ \boldsymbol{P} \end{bmatrix} = \begin{bmatrix} \langle \mathbb{C}(\boldsymbol{E} + \mathbf{B}_k[\tilde{\mathbf{u}}]) \rangle \\ \left\langle \rho(\dot{\boldsymbol{U}} - i\omega \boldsymbol{N}[\tilde{\mathbf{u}}]) \right\rangle \end{bmatrix} = \begin{bmatrix} \mathbb{C}^* & \mathbb{S}_1 \\ \mathbb{S}_2 & \boldsymbol{\rho}^* \end{bmatrix} \begin{bmatrix} \boldsymbol{E} \\ \dot{\boldsymbol{U}} \end{bmatrix} \tag{D.41}$$

where the matrices $\mathbb{C}^*$, $\mathbb{S}$ and $\boldsymbol{\rho}^*$ are:

$$\mathbb{C}^* = \langle \mathbb{C} \rangle + \langle \mathbb{C}\mathbf{B}_k \rangle \, \mathbb{A} = \langle \mathbb{C} \rangle - \langle \mathbb{C}\mathbf{B}_k \rangle \, \mathbb{Q} \left\langle \overline{\mathbf{B}_k}^T \mathbb{C} \right\rangle \quad ; \tag{D.42}$$

$$\mathbb{S}_1 = \langle \mathbb{C}\mathbf{B}_k \rangle \, \mathbb{F} = i\omega \, \langle \mathbb{C}\mathbf{B}_k \rangle \, \mathbb{Q} \left\langle \rho \boldsymbol{N}^T \right\rangle \quad ; \tag{D.43}$$

$$\mathbb{S}_2 = i\omega \, \langle \rho \boldsymbol{N} \rangle \, \mathbb{Q} \left\langle \overline{\mathbf{B}_k}^T \mathbb{C} \right\rangle \quad ; \tag{D.44}$$

$$\boldsymbol{\rho}^* = \langle \rho \rangle \, \mathbb{1} - i\omega \, \langle \rho \boldsymbol{N} \rangle \, \mathbb{F} = \langle \rho \rangle \, \mathbb{1} + \omega^2 \, \langle \rho \boldsymbol{N} \rangle \, \mathbb{Q} \left\langle \rho \boldsymbol{N}^T \right\rangle ; \tag{D.45}$$

Note that $\mathbb{D}$ is a Hermitian matrix, as well as its inverse ($\mathbb{D}^{-1}$) and the sub-matrix $\mathbb{D}_{11}^{-1}$. Therefore, the matrix $\mathbb{Q}$ is also a Hermitian matrix which determines real matrices $\mathbb{C}^*$ and $\boldsymbol{\rho}^*$.

Dispersion curves

We observe in the present model that the average balance equation (D.25) jointly with the microcell equation (D.21) result equivalent to solve the microcell variational problem (D.21), with admissible displacement variations $\delta\tilde{\mathbf{u}}$ being not necessarily spatial functions with null average. Thus, these equations can be similarly written as follows:

$$\left\langle \boldsymbol{\sigma}(\mathbf{u}) : \overline{\nabla_k \delta \mathbf{u}} - i\omega \boldsymbol{p}(\dot{\mathbf{u}}) \cdot \overline{\delta \mathbf{u}} \right\rangle = \mathbf{0} \qquad ; \qquad \forall \overline{\delta \mathbf{u}} \text{ periodic} \tag{D.46}$$

and the discrete problem is:

$$\mathbb{P}^T \mathbb{K}_{dyn} \mathbb{P} [\mathbf{u}]_r = \left[\mathbb{P}^T (\mathbb{K}(k) - \omega^2 \mathbb{M}) \mathbb{P} \right] [\mathbf{u}]_r = \mathbf{0} \, . \tag{D.47}$$

The solution of this eigenvalue problem provides the dispersion curves of the periodic material.

It is important to remark that even when the matrix $\mathbb{P}^T \mathbb{K}_{dyn} \mathbb{P}$ is singular for every pair $(\omega - \mathbf{k})$ lying on the dispersion curves, the matrix $\mathbb{D}$ in equation (D.35) is not singular for these pairs, and therefore, it can be inverted. A good condition number of this matrix $\mathbb{D}$ requires that the column vectors $-\mathbb{P}^T \langle \boldsymbol{N} \rangle^T$ and the row vector $-\langle \boldsymbol{N} \rangle \mathbb{P}$ be scaled. We suggest to multiply both vectors by the scalar factor $\alpha = \omega^2 \langle \rho \rangle$.

6. Homogenization model numerical assessment

In this Section, we validate the homogenization model. First, we solve two 1-D wave propagation problems with symmetric and non-symmetric multilayer configurations (sub-Sections 6.1 and 6.1, respectively). The obtained solutions are compared with reported results.

In the last sub-Section, we solve a two-dimensional (2-D) problem whose band structure has also been reported in several works. Therefore, these results allow us to validate the computation of dispersion diagrams in 2-D cases. The homogenized properties obtained with our model are finally plotted.

6.1. Effective properties of one symmetric layered composite

We evaluate the effective properties of the layered composite whose unit cell is depicted in Figure D.3. It consists of a heavy and stiff layer (Layer 3) placed between two soft and light layers (Layers 2). These layers are embedded into a pair of stiffer layers (Layers 1). The effective properties of this composite have been reported by Nemat Nasser et. al (see Nemat-Nasser y Srivastava (2011)). The objective that we pursue in this case is to validate our model by comparing our results with those reported in Nemat-Nasser y Srivastava (2011)[3].

The first two modes of the dispersion curves are shown in Figure D.3-b. Figure D.3-c depicts the effective compliance $(1/C^{eff})$ which is computed by following to Nemat-Nasser et al. (Nemat-Nasser y Srivastava (2011)):

$$C^{eff} = \mathbb{C}^* - \frac{\omega}{k}\mathbb{S}^1 \ . \tag{D.48}$$

This identity is derived by assuming 1-D conditions, as well as, that [4] $\dot{U} = -(i\omega)E/(ik)$ which is replaced in the first equation of (D.41). Identically, In the second equation of (D.41), the term E is replaced by $E = (ik)/(i\omega)\dot{U}$ to obtain the effective density

$$\rho^{eff} = \boldsymbol{\rho}^* - \frac{k}{\omega}\mathbb{S}^2 \ , \tag{D.49}$$

that is depicted in Figure D.3-d.

These results have been plotted for different FE mesh refinement. Three curves are plots for Nelem=5, Nelem=15, and Nelem=21 (Nelem: number of finite elements used to discretize the microcell). The finite elements in the case of Nelem=21 are distributed as follows: 6 elements for each Layer 1, 3 for each Layer 2, and 3 for Layer 3. In the remaining cases, the number of finite elements is uniformly distributed in the layer domains.

In Figure D.3-d, effective density vs. frequency plot, we copy the results taken from the reference work. Note the good agreement between both solutions.

6.2. Effective properties of one asymmetric layered composite

For asymmetric unit cells (i.e. when the phases are not disposed in a symmetrical spatial pattern), the out-of-diagonal terms $(\mathbb{S}_1, \mathbb{S}_2)$ in the matrix on the right hand side of equation (D.41) are complex-valued and introduce the fully coupling complex-relationship between $(\boldsymbol{E}, \dot{\boldsymbol{U}})$ and $(\boldsymbol{\Sigma}, \boldsymbol{P})$.

[3] The approach adopted in Nemat-Nasser y Srivastava (2011) to evaluate the effective properties consists on formulating the microscale problem through a pair of integral equations involving the eigenfields σ and $\tilde{\mathbf{u}}$. Then, instead of seeking a point-wise solution of these field, as we do, they calculate their volume averages in terms of the average stress and velocity: Σ and $\dot{\boldsymbol{U}}$.

[4] The identity: $-i\omega E = ik\dot{U}$ results from the kinematical relation at the macroscale (averaged variables): $\dot{\hat{\boldsymbol{E}}} = \nabla_{\mathbf{X}}\dot{\hat{\boldsymbol{U}}}$.

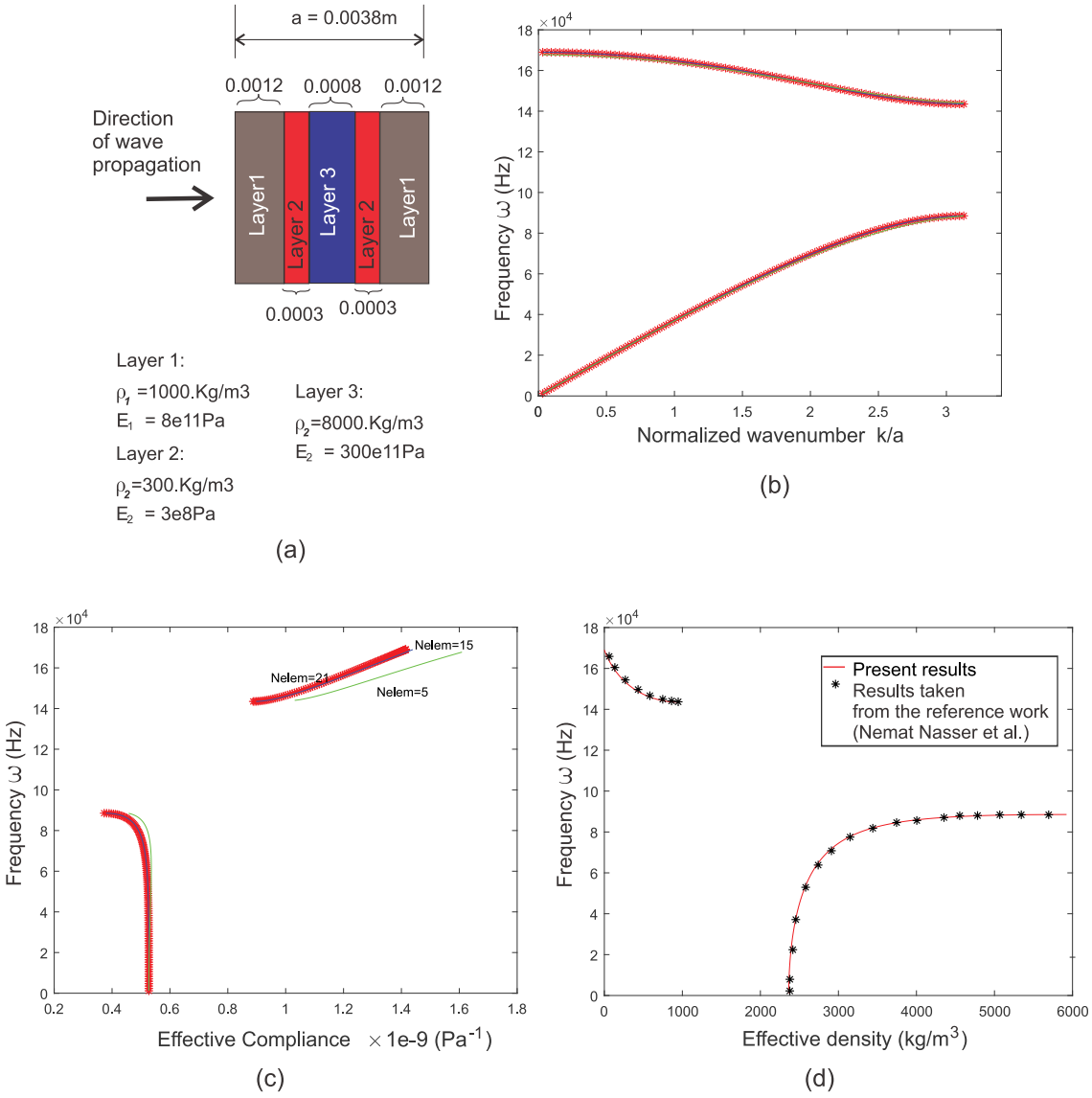

Figura D.3: Effective properties of one symmetric layered composite. a) Configuration of the composite multilayer and the wave propagation problem; b) Dispersion curves of the first two modes; c) Effective compliance; d) Effective density.

Following Nemat Nasser et al. (Nemat-Nasser y Srivastava (2011)), we present the results of the unit cell displayed in Figure D.4-a. Note that the material parameters are similar to the previous multilayer case, however, the thicknesses of the Layers 2 are dissimilar, introducing a non-symmetrical distribution of layer thicknesses.

The following results have been obtained with a finite element mesh of 21 finite elements (6 elements for each Layer 1, 3 for each Layer 2, and 3 for Layer 3).

Figure D.4-b displays the dispersion curves of the first two modes. Figure D.4-c displays the effective compliance $(1/\mathbb{C}^*)$ which is comparable to the plots reported by the reference work. Also, to compare the results of the reference work we plot in Figure D.4-d and Figure D.4-e the out-of diagonal terms $(-\mathbb{S}_1/\mathbb{C}^*)$ and $(\mathbb{S}_2/\mathbb{C}^*)$, respectively. As can be noted, our results compare very well with those of the reference work.

6.3. Composite with square scatterers

We analyse a wave propagation problem in a composite medium with an homogeneous host material and a regular distribution of square scatterers. The scatterer material (Phase 2) is chosen to be stiff and heavy and the host material (Phase 1) is compliant and light with a Young modulus ratio between both phases: $E_2/E_1 = 5$ and density ratio: $\rho_2/\rho_1 = 2$. The microcell is displayed in Figure D.5-a. This case is similar to the one reported in Sigmund y J.J. (2003).

A structured finite element mesh of 30×30 bilinear quadrilateral finite elements is used.

Discussion of results

The evaluated dispersion diagram is plotted in Figure D.5-b. The six bands with lower-frequencies are shown. They have been obtained using 100 wavenumber points along the path $\Gamma - X$ of the IFBZ perimeter, in the $\mathbf{k}$-space. The band structure for these wavenumbers compares very well with the ones reported in Sigmund y J.J. (2003).

Pictures in Figure D.5c-k display, as vectorial fields, the shape of the modes associated to the points A_1, A_2, ..., D_1, C_2, C_3, in the band diagrams. The first band is a transversal mode, the second one is a longitudinal mode, and the third band corresponds to wave propagation involving scatterer rotations. The second band intersects the third band. This characteristic can be noted in the behaviour of the effective properties at the intersection point I in Figure D.6.

Figure D.6 plots the effective elastodynamic properties of the composites vs. angular frequency for the three bands with lower frequencies. The plots correspond to the effective elasticity tensor components, $\mathbb{C}^*_{11}$, $\mathbb{C}^*_{22}$ and $\mathbb{C}^*_{12}$, respectively, defined in equation (D.42) and the effective density component, $\boldsymbol{\rho}^*_{11}$, defined in equation (D.45)

The computational cost demanded in a laptop to perform the present evaluation (mesh 30x30

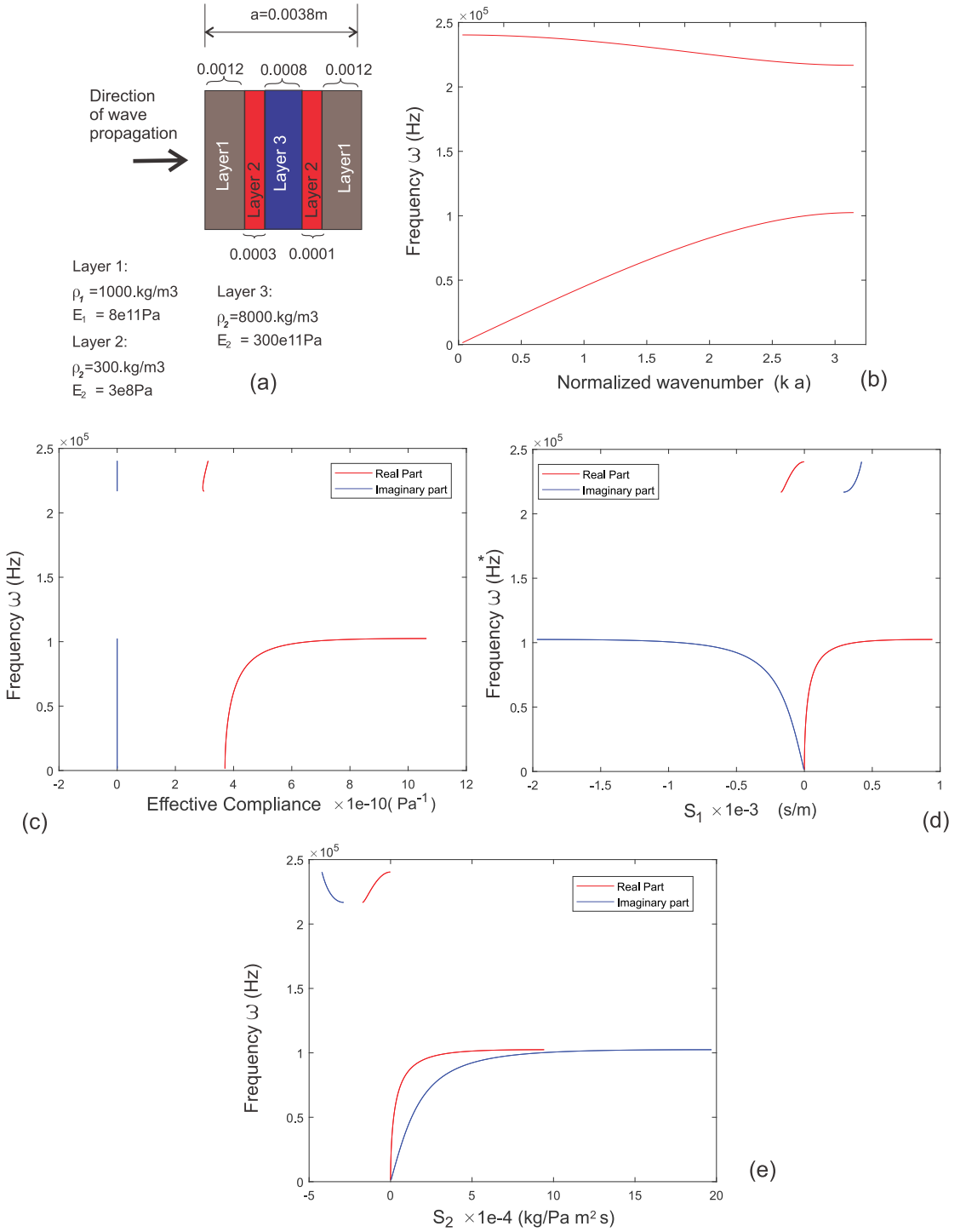

Figura D.4: Effective properties of an asymmetric layered composite obtained with (Nelem=21). a) Schematic diagram of the composite multilayer and the wave propagation problem; b) Dispersion curves of the first two modes; c) Effective compliance; d) Effective density.

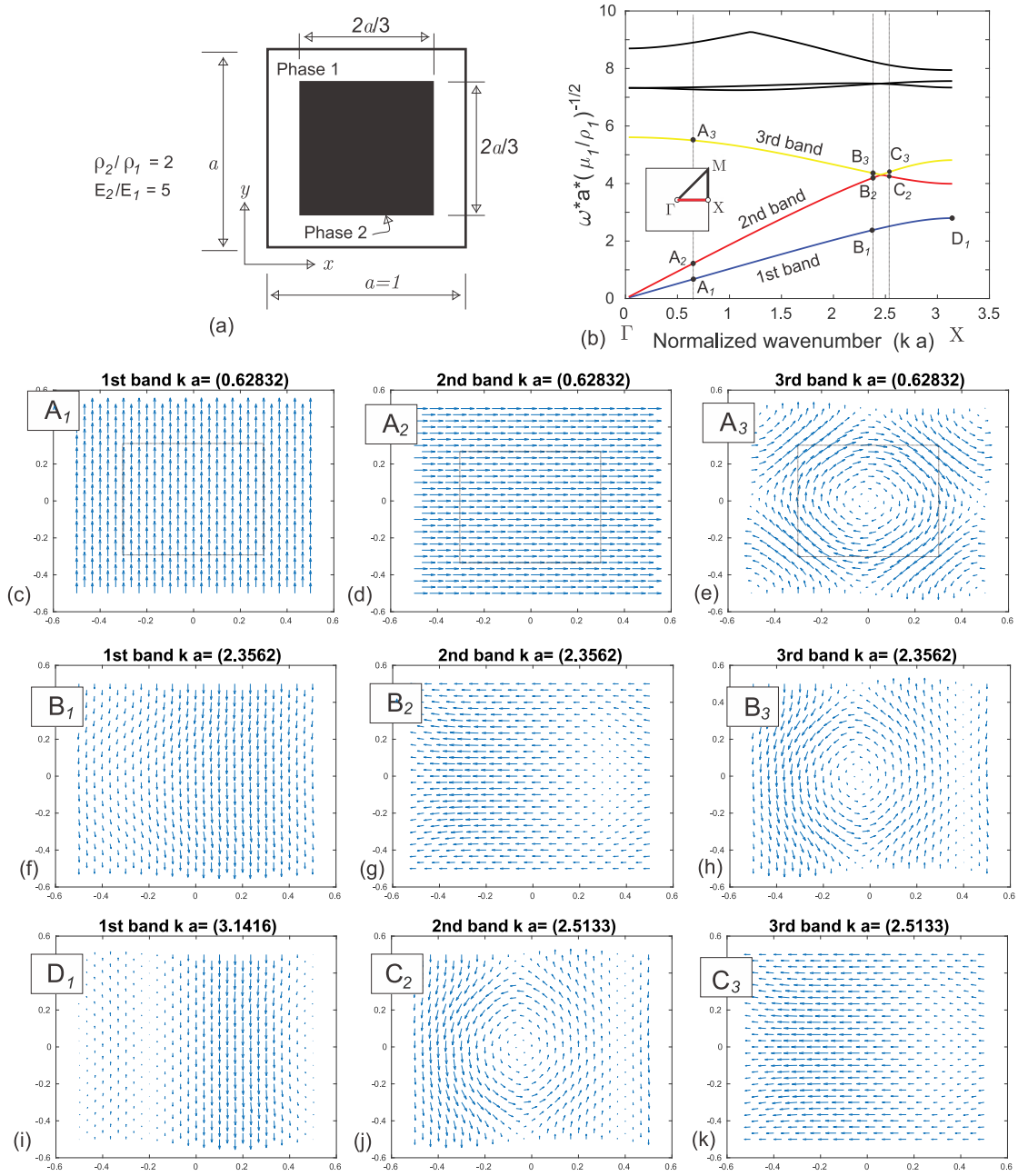

Figura D.5: Composite with square scatterers. a) Microcell geometry; b) Band structure for the six lower frequencies in the region $\Gamma - X$ of the IFBZ; d-k) vector fields of the modes for the points A_1, A_2, ..., D_1, C_2, C_3, displayed in the band structure.

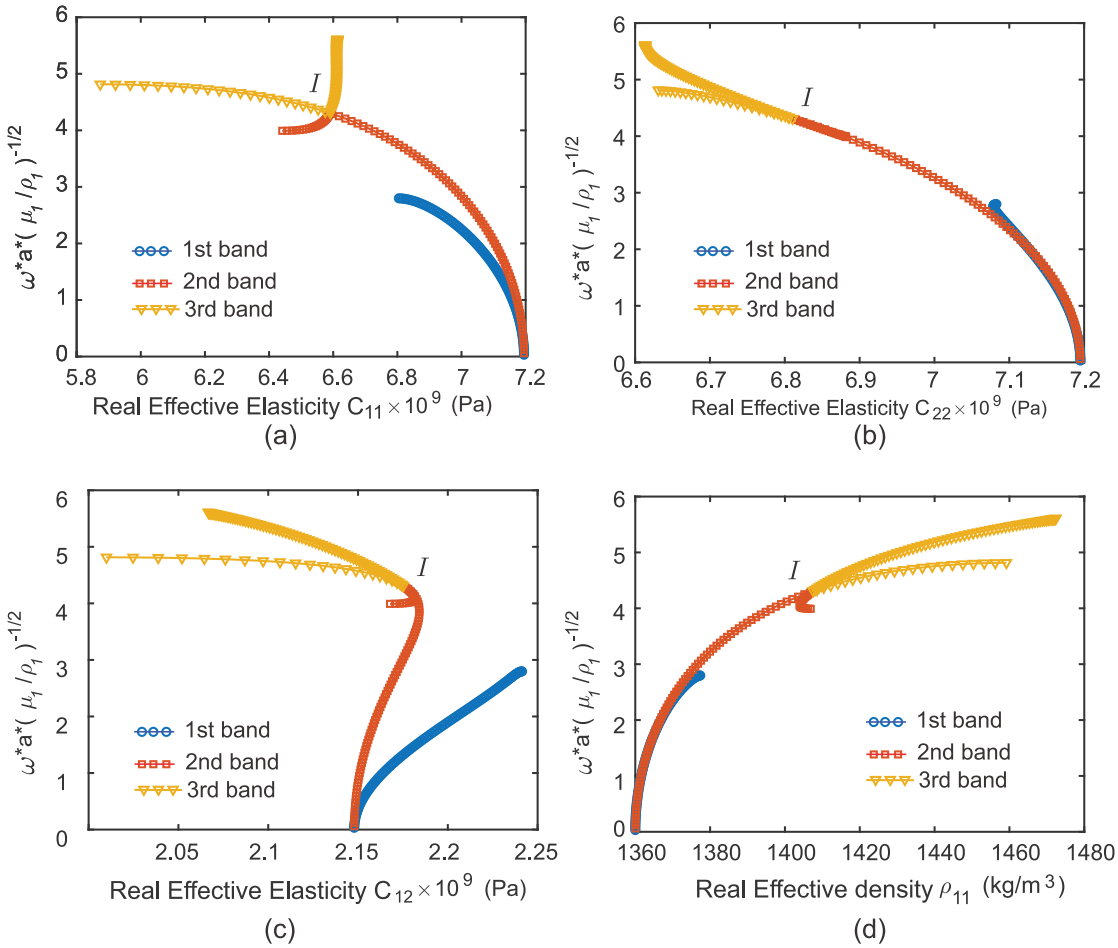

Figura D.6: Composite with square scatterers. Effective elastodynamic properties. Elasticity tensor componentes: a) $\mathbb{C}^*_{11}$; b) $\mathbb{C}^*_{22}$; c) $\mathbb{C}^*_{12}$; effective density component: d) $\boldsymbol{\rho}^*_{11}$.

and 100 points in the path $\Gamma - X$) is 22.sec for computing the band structure and 1169.sec for evaluating the effective properties. The high computational cost to determine the effective properties, relative to the band structure calculation, is due to the evaluation of the inverse matrix $\mathbb{D}$ in equations (D.37)–(D.40). We note that computational cost efficiency has not been pursued in the present work.

7. Conclusions

In this paper, we have presented a homogenization model which evaluates the effective elastodynamic properties of acoustic metamaterials. The model predicts the effective properties of the constitutive equation described in terms of averaged quantities. In this sense, the approach follows very closely the original ideas introduced by Willis and posteriorly reported in works of Nemat-Nasser and coauthors, Nassar et al., etc.

The distinctive characteristic of our approach is that we have written the microscale equations in the spatial domain with a pointwise determination of the eigenfields. As consequence of this

feature is that the numerical technique for solving the equations can be directly formulated with the finite element method, if compared with the ones based on specifying the equations in the Fourier space or using integral equations to find the eigenfields. The results that we attain with this model have been contrasted with those published in the literature (Nemmat-Nasser et al.). The agreement between both solutions is almost exact. Therefore, we consider that these outcomes validate the present model. Furthermore, a 2D analysis is also discussed.

The model reported in this work could be used for the topology design of acoustic metamaterials (see for example Dong et al. (2017)). The evaluation of effective parameters, in addition to the dispersion curves, would be an additional ingredient that could help to determine some specific design criteria.

Bibliografía

D. Krattiger M.H. Generalized bloch mode synthesis for accelerated calculation of elastic band structures. *Journal of Computational Physics*, 357:183–205, 2018.

Dong H., Zhao S., Wang Y., y Zhang C. Topology optimization of anisotropic broadband double-negative elastic metamaterials. *Journal of the Mechanics and Physics of Solids*, 105:54–80, 2017.

Gazalet J., Dupont S., Kastelik J., Rolland Q., y Djafari-Rouhani B. A tutorial survey on waves propagating in periodic media: Electronic, photonic and phononic crystals. perception of the bloch theorem in both real and fourier domains. *Wave Motion*, 50(3):619–654, 2013.

Hussein M., Leamy M., y Ruzzene M. Dynamics of phononic materials and structures: Historical origins, recent progress, and future outlook. *Applied Mechanics Reviews*, 66(4), 2014.

Milton G. y Willis J. On modifications of newton's second law and linear continuum elastodynamics. *Proceedings of the Royal Society A: Mathematical, Physical and Engineering Sciences*, 463(2079):855–880, 2007.

Nassar H., He Q.C., y Auffray N. Willis elastodynamic homogenization theory revisited for periodic media. *Journal of the Mechanics and Physics of Solids*, 77:158–178, 2015.

Nassar H., He Q.C., y Auffray N. A generalized theory of elastodynamic homogenization for periodic media. *International Journal of Solids and Structures*, 84:139–146, 2016.

Nemat-Nasser S. y Srivastava A. Overall dynamic constitutive relations of layered elastic composites. *Journal of the Mechanics and Physics of Solids*, 59(10):1953–1965, 2011.

Nemat-Nasser S., Willis J., Srivastava A., y Amirkhizi A.V. Homogenization of periodic elastic composites and locally resonant sonic materials. *Physical Review B*, 83(10):104103, 2011.

Roca D., Yago D., Cante J., Lloberas-Valls O., y Oliver J. Computational design of locally resonant

acoustic metamaterials. *Computer Methods in Applied Mechanics and Engineering*, 345:161–182, 2019.

Sigmund O. y J.J. S. Systematic design of phononic band–gap materials and structures by topology optimization. *Philosophical Transactions of the Royal Society of London. Series A: Mathematical, Physical and Engineering Sciences*, 361(1806):1001–1019, 2003.

Srivastava A. Elastic metamaterials and dynamic homogenization: a review. *International Journal of Smart and Nano Materials*, 6(1):41–60, 2015.

Srivastava A. y Nemat-Nasser S. On the limit and applicability of dynamic homogenization. *Wave Motion*, 51(7):1045–1054, 2014.

Willis J. Dynamics of composites. En *Continuum micromechanics*, páginas 265–290. Springer, 1997.

Willis J. The construction of effective relations for waves in a composite. *Comptes Rendus Mécanique*, 340(4-5):181–192, 2012.

Doctorado en Ingeniería

mención mecánica computacional

Título de la obra:

Diseño computacional de metamateriales mecánicos y acústicos

Autor: Rolando Yera Moreno

Lugar: Santa Fe, Argentina

Palabras Claves:

Metamateriales, optimización topológica, diseño inverso de materiales, derivada topológica, propiedades efectivas, cristales fonónicos, propagación de ondas en medios periódicos, análisis de estructura de bandas, diseño multiescala de materiales, simetría de cristales.